General Disclaimer

One or more of the Following Statements may affect this Document

- This document has been reproduced from the best copy furnished by the organizational source. It is being released in the interest of making available as much information as possible.

- This document may contain data, which exceeds the sheet parameters. It was furnished in this condition by the organizational source and is the best copy available.

- This document may contain tone-on-tone or color graphs, charts and/or pictures, which have been reproduced in black and white.

- This document is paginated as submitted by the original source.

- Portions of this document are not fully legible due to the historical nature of some of the material. However, it is the best reproduction available from the original submission.

DOE/NASA 0017/2

NASA CR-165197

DDA EDR 10383

CERAMIC APPLICATIONS IN TURBINE ENGINES

Progress Report for 1 January 1980 to 30 June 1980

Joseph A. Byrd

Michael A. Janovicz

Franklin A. Rockwood

Detroit Diesel Allison Division

General Motors Corporation

November 1980

TABLE OF CONTENTS

LIST OF ILLUSTRATIONS

Figure	Title	Page

LIST OF TABLES

I. INTRODUCTION AND SUMMARY

This report relates progress made from 1 January 1980 to 30 June 1980 on the National Aeronautics and Space Administration (NASA) Contract DEN3-17, funded by the Department of Energy (DOE). This contract, to apply ceramic materials to an existing Allison 404 industrial gas turbine (IGT) engine, has continued to show excellent progress in building a ceramic materials design data base, establishing design approaches for ceramic components in turbine engines, involving the ceramics industry in fabricating high-technology ceramic components, and defining the true structural, thermal, and chemical environment of ceramic components in turbine engines by rig and engine testing of selected ceramic components. These elements are essential to the highway vehicles. The development of the high-temperature ceramic materials allows increased (relative to metal components) engine-operating temperatures in gas turbine engines. This increased temperature capability yields a more efficient engine that has the potential of reduced fuel usage per mile (by more than 20%). Furthermore, the ceramic components can potentially reduce cost from that of metal parts and help to make feasible a production vehicular (truck, bus, or passenger car) gas turbine.

Detroit Diesel Allison (DDA) with its 404/505/605 series industrial gas turbine engines presented a unique opportunity to explore specific fuel consumption (SFC) improvement since it is a highly developed gas turbine engine with near term production potential for introduction into truck, bus and generator set markets. These markets use approximately 21% of the transportation petroleum products. Consequently, using this engine as a test bed for ceramic application is a logical first step to the broad automotive marketplace. Technology developed in this program is readily transferred to the passenger car gas turbine engines.

Contract activities were initiated to demonstrate ceramic components in an Allison IGT 404-4 engine in 1976. Initial work provided studies and analysis of the IGT 404-4 engine defining the parametric sensitivities and identifying the candidate components for ceramic application and efficiency improvement. The initial activity also included fabrication and test of selected ceramic components, ceramic material characterization and qualification, and conversion of two contractor-owned engines to an initial ceramic configuration capable of operating at 1038°C (1900°F).

The analysis and studies explored operating temperatures of 1002°C (1835°F) turbine inlet temperature (TIT)--current IGT--to 1371°F (2500°F) TIT. These studies concluded that a configuration at 1241°C (2265°F) with component efficiency improvements would be the optimum approach. Ceramics would be introduced to the following components: gasifier turbine nozzle vanes, gasifier turbine tip shroud, gasifier turbine blades, power turbine nozzle vanes, inlet plenum, combustor, and regenerator disks. Component efficiency improvements would be made in compressor, plenum flow uniformity, power turbine (two stage), gasifier turbine nozzle and tip shroud, and gasifier turbine tip and wall losses. These components would be introduced at three discrete TIT steps--the 1038°C (1900°F), 1132°C (2070°F), and 1241°C (2265°F). The project plan that included ceramic material test and characterization, rig testing, engine performance and durability, and vehicle demonstration at each of the temperature levels was published as NASA CR-135230 dated May 1977. Subsequently, this plan became the basis for the project now in progress at DDA.

DOE/NASA Reports DDA EDR 9519, DDA EDR 9722, DDA EDR 9951, and DDA EDR 10156 (NASA CR-159865) previously issued, cover the ceramic materials characterization, component design, and rig and engine test activities of the project from January 1978 through December 1979. Through that period, 6270 h of engine operation to truck and bus operating cycles were accomplished on initial ceramic parts at TIT of 1038°C (1900°F) some 36°C (65°F) above that of the all-metal baseline engine. These initial tests of ceramic parts indicated the chemical and structural stability of silicon carbide nozzle vanes, sintered silicon nitride, and silicon carbide turbine tip shrouds and alumina silicate regenerator disks. In addition, reaction-bonded silicon carbide nozzle vanes and alumina silicate regenerator disks have successfully withstood 7660 km (4760 mi) of over the road engine use in a turbine-powered truck including exposure to rigorous road hazard test courses. This truck experience has served as a demonstration of the utility and durability of ceramic parts operating in a turbine engine under actual vehicle application operating conditions. During this time, activities were conducted to characterize ceramic material candidates; improve realized strength of ceramics in part configurations; define ceramic design methodology; explore nondestructive evaluation (NDE) techniques applicable to ceramic materials; qualify parts with rigs simulating critical engine conditions; design a configuration to operate at 1132°C (2070°F) using the data, experience, and methodology being obtained to utilize ceramics effectively in a turbine engine configuration, and fabrication and process development leading to the initial compliment of 2070°F-configured ceramic parts.

This reporting period is characterized by the phase out of development activities on 1900°F-configured ceramic parts, qualification and development testing of ceramic parts of the 2070°F-configuration, preparation of associated metal engine subsystems for 2070°F-configuration engine operation, and initiation of the third generation ceramic parts design for eventual operation of the engine at 1241°C (2265°F). The current project master plan, shown in Figure 1, further illustrates the relationship of the activities of this reporting period with the overall project.

Activities of note during this reporting period include successful thermal shock and vibration qualification of the 2070°F-configuration ceramic gasifier nozzle assembly, successful spin tests of the ceramic blades required for the 2070°F-configuration gasifier turbine rotor, rig operation with the initial 2070°F-configuration regenerator disk and seals at anticipated worst case operating temperature, completion of silicon carbide ceramic part process development and initial part compliment delivery, completion of engine block cooling tests leading to the concept to be used under the conditions anticipated in the 2070°F-configuration, development test on an engine of the T-6 microprocessor control of the 2070°F-configuration engine verifying all essential modes, successful demonstration of photoaccoustic spectroscopy and accoustic microscopy NDE equipment applicable to high-technology ceramic materials, and build completion and functional check out of engine C-4, which will become the first 2070°F-configured engine upon incorporation of the ceramic parts during the next reporting period.

CY	1978	1979	1980	1981	1982	1983	1984
Materials Development							
1900 Configuration							
Design							
Process Development							
Fabrication							
Rig Test							
Engine Test							
Vehicle Demonstration							
2070 Configuration							
Design							
Process Development							
Fabrication							
Rig Test							
Engine Test							
Vehicle Demonstration							
2265 Configuration							
Design							
Process Development							
Component Performance							
Fabrication							
Rig Test							
Engine Test							
Vehicle Demonstration							
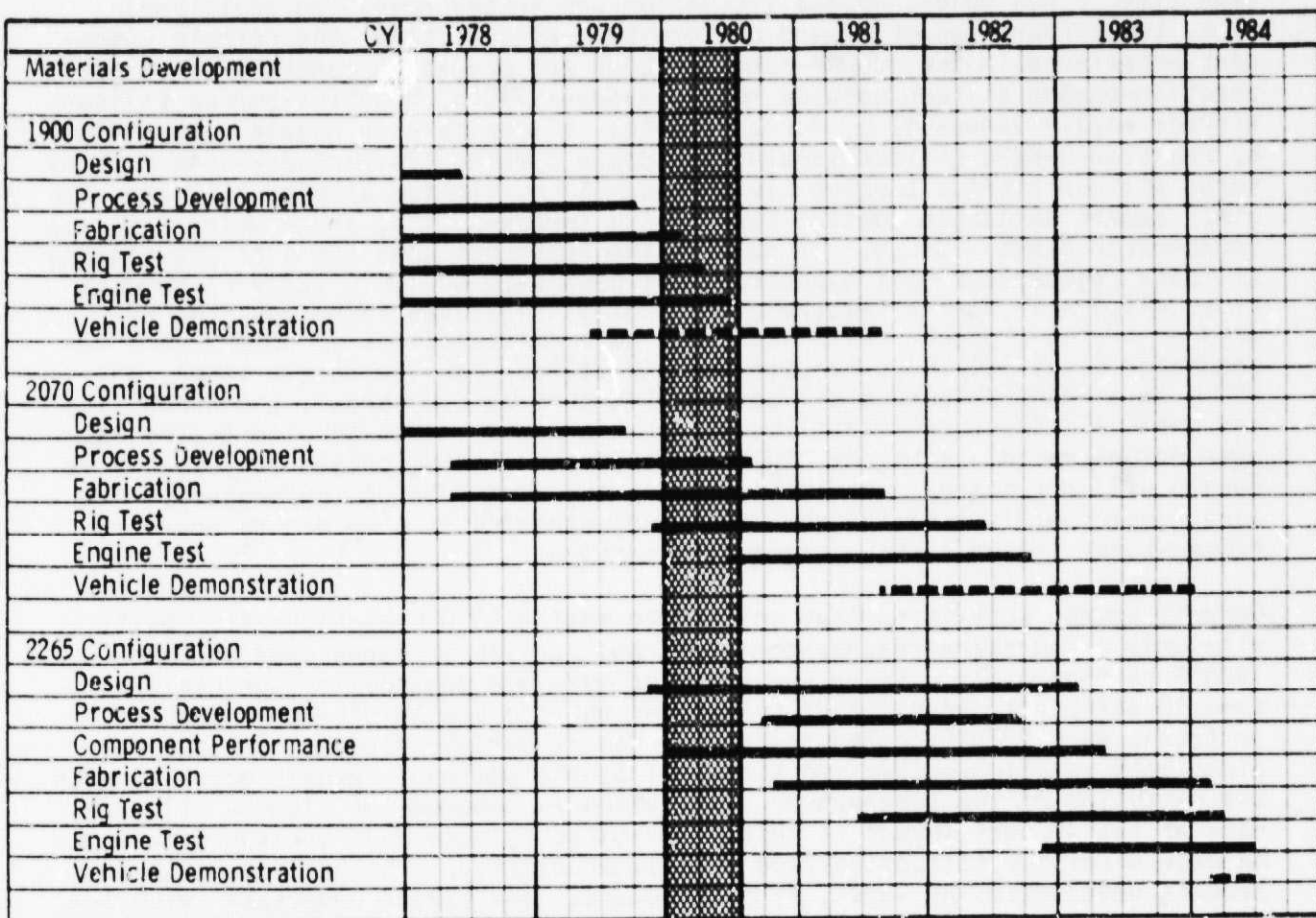
TE-80-1021

Figure 1. CATE project master plan.

Engine testing continued with three project engines (C-1, C-2, and C-4) used for an additional 215 h of ceramic component operating experience bringing the project total to 6439 hr. Engine C-1 was just used to conduct a series of T-6 microprocessor control tests at 1038°C (1900°F) TIT, where parametric correlation was achieved between the T-6 and T-4 (former control location) and the functions of a breadboard microprocessor was verified. In addition, this engine was operated in the project truck over the road for 3053 km (1897 mi) bringing the total road experiences with ceramic vanes and regenerators to 10,713 km (6657 mi). Engine C-2 was operated at 1038°C (1900°F) TIT with a prototype ambient air block cooling system with instrumentation that disclosed both reduction in wall temperatures and more room temperatures distribution. With this disclosure, it was concluded that temperatures would be within design limits and block distortion reduced when operating under 1132°C (2070°F)

3

TIT conditions. Engine C-4 was built as a new engine and successfully operated with 1900°F-configuration gasifier nozzle and regenerators. It now stands ready to accept the 2070°F-configuration gasifier nozzle for initial operation of this configuration at the reduced temperature--1038°C (1900°F)--to serve as the first step in achieving 1132°C (2070°F) TIT operation. At the same time, a new mold-in-place insulation was tested revealing additional block temperature reduction and uniformity. At this time, the ceramic component experience in the 1900°F-configuration and operating conditions follows: reaction-bonded silicon carbide nozzle vanes--2740 h, reaction-bonded silicon nitride nozzle vanes--81 h, Puribide Refel silicon carbide nozzle vanes--415 h, reaction-bonded silicon carbide abradable turbine tip shrouds--1546 h, sintered silicon nitride turbine tip shroud--113 h, lithium alumina silicate with glass cement abradable coating turbine tip shroud-- 11 h, and alumina silicate regenerator disks--7340 h. Of note is the fact that some 569 h of the alumina silicate regenerator disk experience has been with a 1100°C (2012°F) composition, which will have a temperature capacity to be used throughout the remainder of the project. With high time part accumulations of 3050 h on a regenerator disk, 1512 h on reaction-bonded silicon carbide nozzle vanes, and 985 h on a reaction-bonded silicon carbide turbine tip shroud, the durability and chemical/structural stability of ceramic parts in the turbine engine have been demonstrated. With the 1900°F-configuration being phased out, the above record will not change perceptibly during the remainder of the project. Future reports will emphasize the utility of ceramics at even higher operating temperatures in the turbine engine application.

Ceramic source activities have shifted to making 2070°F-configuration parts with only a few spare regenerator parts and one lot of vanes open on the 1900°F configuration. Seven ceramic suppliers are engaged in fabrication of some 10 different ceramic part shapes, which form the 2070°F-configuration. In total, each 2070°F-configured engine has 80 ceramic pieces. Silicon carbide (both reaction-bonded and sintered) is the dominant ceramic material with the exception of the regenerator disk, which is composed of alumina silicate. Each of the 10 part shapes is being fabricated by more than one source and may be made of either silicon carbide or silicon nitride. The major ceramic part process development of vanes, ring structures, and blades undertaken with the Carborundum Company for both sintered alpha and reaction-bonded silicon carbide parts has been completed. Ceramic process development is still continuing on the plenum and plenum inner annulus. The initial lots of parts have been delivered. A second development program with GTE Laboratories to produce a sintered silicon nitride blade continues as planned. It is expected to conclude at years end. New process development activities have been initiated based upon needs evidenced during fabrication of the initial lot of parts. The first process development program covers the alpha silicon carbide plenum and inner annulus required for the 2265°F-configuration to correct shrink and minimize distortion of these large slip cast parts. Another process development project seeks to improve silicon carbide ring structures where a high incidence of circumferential silicon-filled cracks was evidenced in the initial lot because of spring back after warm compression molding. Another series of process development activities is directed at continuing improvement of ceramic material abradability in the turbine tip shroud application, particularly in the gasifier section where a ceramic blade is to operate with a ceramic shroud at low operating clearance. In summary, the ceramic parts of the 2070°F-configuration engine being fabricated as the initial lot include: gasifier turbine nozzle inner support ring--silicon carbide by two sources, gasi-

fier turbine nozzle outer support ring--silicon carbide by two sources, gasifier turbine nozzle vanes--silicon carbide by two sources, gasifier turbine tip shroud--silicon carbide, gasifier turbine nozzle vane retaining ring--silicon carbide by two sources, gasifier turbine nozzle support strut shells--silicon carbide by two sources, gasifier turbine blades--sintered alpha silicon carbide and sintered silicon nitride, gasifier turbine inlet plenum--silicon carbide by two sources, gasifier turbine inlet plenum inner annulus--silicon carbide by two sources and silicon nitride, and regenerator disks--alumina silicate.

In-house ceramic machining process development has been completed with the machining of at least a portion of each of the above parts underway. The fact that initial sets of each component have been successfully fabricated and evaluated by NDE is deemed a significant accomplishment leading to the 2070°F-configuration engine.

The most significant accomplishments this reporting period are qualification testing of 2070°F-configured ceramic parts preparatory to engine installation. Thermal shock testing of the gasifier nozzle assembly was conducted under 1038°C (1900°F) conditions. The gasifier nozzle assembly consisting of 36 ceramic parts, the regenerator assembly, and a trial lot of gasifier turbine blades have successfully been qualification tested. The gasifier nozzle assembly was tested as a unit on thermal shock, cold flow, and vibration rigs yielding 55 silicon carbide vanes, six silicon carbide strut shells, two silicon carbide retaining rings, and one each of the three ring structures.

The regenerator disk and three-piece hot seals were operated on the regenerator rig at temperatures through 981°C (1800°F). Leakage was higher than design but seal cross distortion during manufacturing was evidenced with corrective design and processing changes integrated into subsequent seals. Blade testing advanced to the 2070°F-configuration blade after previous successful spin test coupon tests of sintered alpha silicon carbide and sintered silicon nitride, and prototype blades of sintered alpha silicon carbide. The gasifier turbine rotor consists of 40 individual ceramic blades in a Waspaloy rotor. Fourteen blades were spun (13 at room temperature and one at the 704°C (1300°F) operating temperature) at the dovetail averaging 120% of maximum rotor speed. The first compliment of blades manufactured by the final developed process is available for qualification test early in the next reporting period. Only the inlet plenum and its inner annulus have not undergone testing because of fabrication difficulties, which resulted in parts not dimensionally usable. The engine configuration development will proceed with a sheet metal plenum with the gas path side coated with NASA Lewis Research Center-developed yttria-stabilized zirconia to form a thermal barrier sufficient for limited life and a plenum inner annulus. Both metal components have now been successfully fabricated and will be tested early in the next reporting period.

Integrated into these intense rig qualification activities have been complete rebuilding of both the thermal shock and regenerator hot performance rigs to give them adequate temperature capacity to test ceramic components under operating conditions required for the remainder of the CATE project. The hot regenerator performance rig is now capable of testing a regenerator assembly at an inlet temperature of 981°C (1800°F). Under these conditions, thermal effectiveness, pressure drop, and leakage can be measured providing the basic data to establish regenerator performance. The thermal shock rig has been

updated to sustain temperatures of up to 1241°C (2265°F). It is capable of operating steady state for combustor development and under thermal transients to produce thermal shock in the ceramic parts installed including the gasifier nozzle and plenum. Later in the program, the combustor and the power turbine nozzles will also be tested in the rig. Finally, a hot engine simulator rig has been designed and fabricated to permit gasifier rotor (ceramic bladed) testing at speed and temperature under realistic engine conditions before actual trial in the 2070°F-configuration engine.

The regenerator development has continued complimenting the previously discussed initial qualification test of 2070°F-configuration parts. Subscale and full-scale seal surface tests are underway to establish the optimum nickel oxide/calcium floride composition to be used. These tests are establishing temperature limits and evaluating the thermal distortion characteristics through the temperature range of the project. Based upon previously conducted strength parameter experiments and statistical treatment of results, a baseline for regenerator core NDE was established. During this period, experiments were conducted using X-ray, hot wire anemometry, and vibration/holography. Out of this has come adoption of X-ray as an acceptance criteria with the other techniques still held as viable long-range alternatives.

Ceramic material activities in-house support the entire ceramic part development. During this reporting period the major activity was supporting the nondestructive evaluation (NDE) of 2070°F-configuration ceramic parts being received from ceramic suppliers and establishment of strength-limiting factors present in ceramic parts failed during qualification/development tests conducted on test rigs. Characterization activities have established strength of WESGO SNW-1000 sintered silicon nitride, Kyocera sintered silicon carbide, NGK-Locke sintered silicon carbide and silicon nitride, and the second-generation CVD-coated silicon nitride over reaction-bonded silicon nitride. Regenerator disk material strength testing of the 1100°C (2012°F)-rated alumina silicate is significantly stronger then the previous 1000°C (1832°F) composition. Abradability testing of ceramic source samples silicon nitride and magnesium alumina silicate showed promising results. Likewise, in-house efforts to apply abradable layers to ceramic substrates hold promise with ceramic cements, ceramic-filled laminated fabrics, sintered compacts, and plasma-sprayed zirconia and mullite under test. NDE development has been concentrated on completion of scanning photoaccoustic spectroscopy (SPAS) and scanning laser accoustic microscopy (SLAM) test equipment. SPAS laboratory tests have been very successful with alpha silicon carbide specimens. Again SLAM has been found very effective in the dark field mode. SLAM, SPAS, and high-frequency ultrasonics appear at this point to hold promise for detecting flaws of critical size and extent in ceramic materials.

Design has been initiated for the third ceramic engine configuration of the project to be operated at a turbine inlet temperature of 1241°C (2265°F). The aerodynamics of a two-stage power turbine have been established with construction concepts of the associated power turbine ceramic nozzles and turbine tip shrouds under evaluation. The current effort is pointed to a design review and initiation of ceramic part fabrication at the close of 1980. Likewise, a combustor concept has been completed for this engine configuration and is currently being evaluated by the ceramics industry prior to initiating fabrication.

The overall results of design, analysis, ceramic process development, and ceramic component test continue to reflect favorable progress leading to the second generation of the ceramic gas turbine engine to be operated at 1132°C (2070°F) during the next report period. The rig and engine testing also has been instrumental in promoting realized strength improvement of the existing materials and assessing emerging alternative materials. Further reports on Contract DEN3-17 will be issued semiannually.

II. ENGINE ASSEMBLY AND TEST

INTRODUCTION

Engine activities during the reporting period included a vehicle demonstration with engine C-1 at the Fifth International Automotive Propulsion Systems Symposium, microprocessor T_6 control development with engine C-1, evaluation of the 2070°F configuration block cooling with engine C-2, assembly and shakedown of a new engine C-4 followed by installation of the 2070°F-configuration ceramic gasifier nozzle assembly in engine C-4. Other significant activities during the period include evaluation of regenerator seals at the 871°C (1600°F) temperature level and evaluation of test procedures on the motoring dynamometer test stand in preparation for the first engine test of the 2070°F-configuration gasifier nozzle assembly.

The component rig test activities during the reporting period included spin pit testing of blade coupons, prototype and final configuration ceramic blades, qualification of a 2070°F-configuration ceramic gasifier nozzle assembly, regenerator rig testing of the three-piece 2070°F-configuration inboard seals, and conversion of both burner and regenerator rigs to uprated high-temperature configurations. Fabrication of hardware for the hot engine simulator rig also occurred during this reporting period. This rig was designed to qualify for engine testing ceramic turbine blades in an assembly subjected to simulated engine gas-path conditions.

SUMMARY

The test activities that occurred were conducted on 1900°F-configuration ceramic components that successfully completed proof tests in rigs that simulated the most severe engine operating conditions. They were then tested in an engine. The engines used to evaluate the ceramic components were C-1, C-2, and C-4, which are IGT 404-4 models rated at 1038°C (1900°F) gasifier rotor inlet temperature, modified to accept the ceramic parts. The 1900°F-configuration ceramic component test activities are plotted in Figures 2 (engine test hours), 3 (gasifier turbine vanes and shroud), and 4 (ceramic regenerator). Table I is a summary of the total engine test hours accumulated since the start of testing.

The rig proof testing of the new 2070°F-configuration ceramic components started during this reporting period. Successful qualification of a gasifier nozzle assembly was completed, and assembly of these qualified parts in engine C-4 was in progress at the end of this reporting period. Table II summarizes the 2070°F-configuration ceramic gasifier nozzle components tested and those that qualified for engine testing.

ASSEMBLY AND LABORATORY TEST ACTIVITIES

Objective

The primary objectives of the engine test activities during the reporting period were threefold--develop the microprocessor T_6 control, which is required for operation at the 1132°C (2070°F) and 1241°C (2265°F) temperature levels; prepare for engine testing of the 2070°F-configuration by assembling and shaking down a new engine and developing an improved engine block cooling configuration.
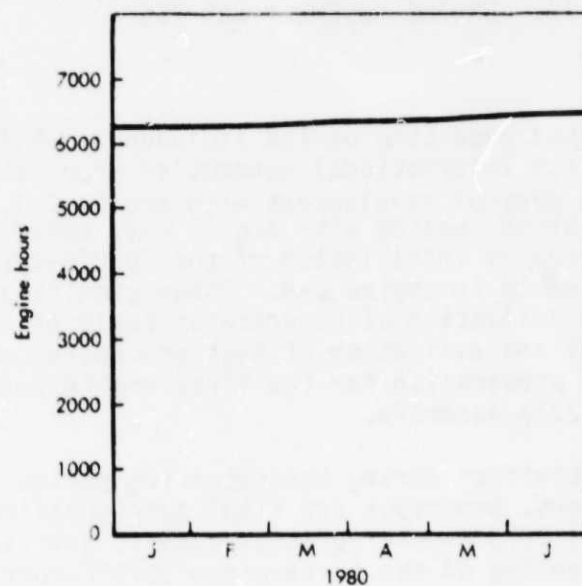
TE-80-1022

Figure 2. Engine test hour summary.
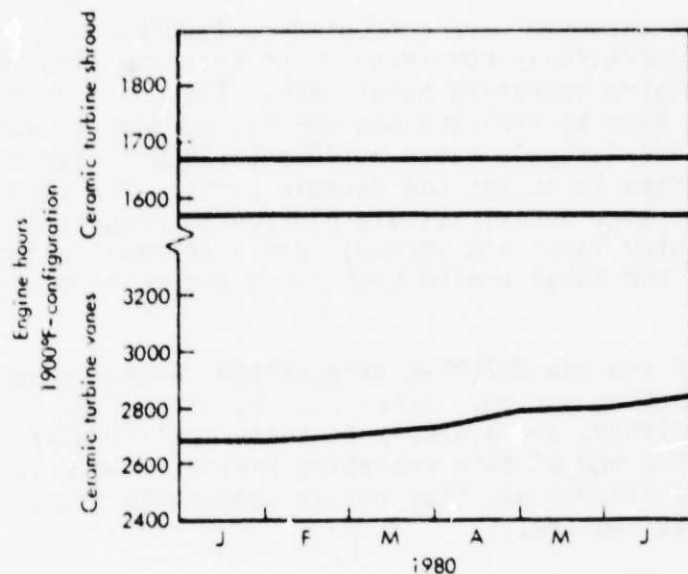
TE-80-1023

Figure 3. Gasifier turbine ceramic vane and shroud engine hours.
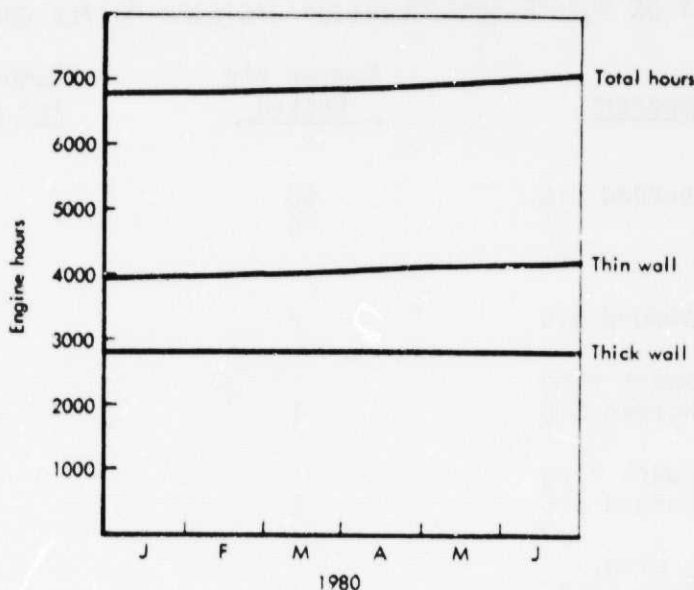
TE-80-1024

Figure 4. Ceramic regenerator engine hours.

TABLE I. ENGINE DURABILITY TIME OF CERAMIC COMPONENTS

Component	Maximum hours for one component	Total durability (hr)
Thick wall regenerators	1808	2833
Thin wall regenerators		
1000°C (1832°F) rated	3050	3938
1100°C (2012°F) rated	433	614
Gasifier turbine vanes		
Silicon carbide (Carborundum)	1512	2748
Silicon carbide (Pure)	435	435
Silicon nitride (AiResearch)	81	81
Gasifier turbine shroud		
Silicon carbide (Carborundum)	985	1546
Silicon nitride (GTE Sylvania)	113	113
LAS (Corning)	11	11

Discussion

Engine C-1

Engine C-1 accumulated 152 h of testing for a total test time of 3270 h. Silicon carbide (SiC) 1900°F-configuration gasifier turbine vanes from two vendors were tested. All ceramic regenerators tested were thin wall alumina silicate (AS) material; however, a new AS material rated at 1100°C (2012°F) was evaluated along with the original AS material rated at 1000°C (1832°F).

11

TABLE II. SUMMARY OF 2070°F-CONFIGURATION GASIFIER NOZZLE COMPONENT RIG TEST

Ceramic component	Number rig tested	Number qualified for engine test
Vanes		
Reaction-bonded SiC	50	45
SiC	4	4
Shroud		
Reaction-bonded SiC	2	1
Outer vane support ring		
Reaction-bonded SiC	1	1
Inner vane support ring		
Reaction-bonded SiC	2	1
Vane retaining ring		
Purehide Refel SiC	2	2
Strut shells		
Purehide Refel SiC	6	6
Alpha SiC	2	2

The inboard regenerator seals featured crossarm wearface material of 70% NiO/
30% CaF_2 or 85% NiO/15% CaF_2. The engine test activity consisted of test
stand evaluation of the T_6 microprocessor control and a vehicle demonstra-
tion at the Fifth International Automotive Propulsion Systems Symposium in
Dearborn, Michigan, followed by a road trip tour to NASA Lewis Research Cen-
ter, Cleveland, Ohio; Harrison Radiator Division, Lockport, New York; Corning
Glass Co., Corning, New York; Pure Carbon Co., St. Mary's, Pennsylvania; and
the return trip to Indianapolis. The engine accumulated 63.2 h and 3049 km
(1895 mi) during the vehicle operation. The ceramic parts in the engine dur-
ing vehicle operation were 10 SiC gasifier turbine vanes and two thin wall
1100°C (2012°F) AS material regenerators. The inboard seals used featured 85%
NiO/15% CaF_2 crossarm wearface material. Eight of the SiC vanes were manu-
factured by Carborundum Co. and two were supplied by Pure Carbon Co. The re-
mainder of engine C-1 testing consisted of test stand operation to prepare for
the vehicle installation and evaluation of the T_6 microprocessor control.
Several series of development tests and the control system have been com-
pleted. Successful starts, accelerations, decelerations, and power transfer
operation have been demonstrated with the T_6 control. Good correlation be-
tween T_6 and T_4 with the microprocessor logic calculating T_4 from T_6
measurements have been achieved. Software programming development continues
to refine the required functions to be acceptable for engine durability and
normal operation. During the control development testing, inboard regenerator
seals with 70% NiO/30% CaF_2 crossarm wearface material were introduced with
a noticeable improvement in engine performance. This change was attributed to
the improved seal leakage control the 70% NiO/30% CaF_2 seals have compared
to the 85% NiO/15% CaF_2 seals.

12

Engine C-2

Engine C-2 was active early in the reporting period evaluating the ambient
air-cooled block configuration required for 2070°F-configuration engine test-
ing. A total of 23 h were accumulated, bringing the total engine test time to
1367 h. During the block cooling test, the engine operating conditions were
allowed to increase regenerator inlet temperature (T_6) up to 871°C (1600°F).
The ceramic regenerators were thick wall 1000°C (1832°F) AS material, and the
inboard seals featured 85% NiO/15% CaF_2 crossarm wearface material. No det-
rimental affects on the ceramic disks or seals were evident after exposure to
the 871°C (1600°F) regenerator inlet temperature. The block cooling configu-
ration performance was very encouraging. The block bulkhead metal tempera-
tures in the critical areas were reduced by approximately 111°C (200°F). This
new cooling configuration combined with improved insulation should provide
adequate block cooling for the 2070°F configuration.

Engine C-2 is awaiting the availability of a 2070°F-configuration gasifier
nozzle assembly. The first 1132°C (2070°F) nozzle will be evaluated in engine
C-4, and the second available qualified nozzle will be used in engine C-2.

Engine C-4

Engine C-4 was assembled for the first time in late February. The test plan
was to perform an initial shakedown of the engine plus evaluate the first in-
board regenerator seals with 70% NiO/30% CaF_2 crossarm wearface material.
These seals were qualified for engine test on the regenerator rig and exhibit-
ed improved leakage control. The engine test data supported the regenerator
rig data because a measurable improvement in engine performance was evident
when data with 70% NiO/30% CaF_2 seals were compared to 85% NiO/ 15% CaF_2
seals. Engine C-4 was then installed on the motoring dynamometer and used to
develop test techniques and procedures to be used for testing the first ceram-
ic 2070°F-configuration gasifier nozzle and ceramic bladed gasifier rotor.
The procedures will be used to operate the hot engine simulator rig when the
first ceramic bladed gasifier rotor is tested.

Engine C-4 accumulated 40 h of shakedown testing after which the installation
of the the first rig qualified 1132°C (2070°F) ceramic gasifier nozzle assemb-
ly was completed. The planned test will be to evaluate the ceramic nozzle
during starting, engine performance over the entire freeshaft and power trans-
fer speed range, accelerations, and decelerations. A nozzle inspection is
scheduled after testing.

III. STRUCTURAL CERAMIC MATERIALS DEVELOPMENT

INTRODUCTION

The ceramic materials development this reporting period focused on the evaluation of new candidate materials for the fabrication of engine hardware including an examination of a new silicon nitride coating for reaction-bonded silicon nitride (Si_3N_4) called Inodelitun. A survey of oxidation behavior on the GTE SNW-1000 Si_3N_4 was also conducted. Ceramic regenerator seal material development continued with evaluation of friction/wear behavior and thermal distortion characteristics of the various wearface materials that have been developed. Turbine tip shroud abradability evaluation with both commercially supplied ceramics and DDA-generated materials continued in order to develop a viable seal system compatible with ceramic turbine blades. Nondestructive evaluation techniques for detecting strength-limiting flaws continued with the investigation of such techniques as scanning photoacoustic spectroscopy (SPAS), scanning laser acoustic microscopy (SLAM), and high-frequency ultrasonics. Ceramic machining processing techniques in creep feed grinding for blades and ultrasonic machining for rings were investigated. Improvement in tooling design and reduction in tool preparation time were also evaluated. Regenerator core material evaluation continued with the initiation of low-cycle fatigue (LCF) testing of thermally exposed regenerator disk samples.

MATERIALS BEHAVIOR AND CHARACTERIZATION

Summary

This reporting period effort focused on the evaluation of new candidate materials. Four new silicon-based materials were examined: sintered silicon nitride SNW-1000 (GTE-Westgo), SC-201 sintered silicon carbide (Kyocera International), a sintered silicon carbide (NGK-Locke), and a sintered silicon nitride (NGK-Locke). Inodelitun, a new CVD silicon nitride coating on reaction-bonded Si_3N_4 was also examined. The laboratory testing associated with the evaluation of new candidate materials consists primarily of an evaluation of microstructure and fast fracture strength. A cursory survey of oxidation behavior and the resulting effect on strength is also made. Particular attention is given to determining the nature of strength controlling flaws by fracture surface analysis.

Objective

The primary objective of this task is to establish appropriate material characteristics to support the design, development, and testing of hot section components for the 2070°F- and 2265°F-configuration engines. A secondary objective is to evaluate new candidate materials and compositions and to make an assessment as to which if any should be used in specific component development efforts. Work undertaken in this reporting period focused on the evaluation of such new materials.

Discussion

NGK-Locke Sintered SiC

The density of the NGK SiC material measured 2.57 g/cm³. The microstructure consists of a loose network of fine grains of silicon carbide with occasional small grains of carbon as shown in Figure 5. X-ray diffraction indicates that beta SiC is the major phase with some alpha SiC.

Its average modulus of rupture (MOR) at room temperature was 219.4 MPa (31.82 ksi) with a standard deviation of 17.4 MPa (3.98 ksi). Calcium carbide inclusions, shown in Figure 6, and pores were found to be the strength-controlling defects.

NGK-Locke Sintered Si_3N_4

The NGK-Locke Si_3N_4 material had an average density of 2.90 g/cm³ for the test bars. However, very large interconnected pores were found to be present throughout the microstructure as shown in Figure 7. The major phase of the material is beta Si_3N_4 shown in Figure 8. The average grain size is approximate 1.33 μm. Significant amounts of magnesium oxide (HgO) were also present throughout the microstructure.

Average room temperature MOR measured 355.94 MPa (52.63 ksi) with a standard deviation of 29.44 MPa (4.27 ksi). Surface pores were established as the strength-controlling defect.

Kyocera Sintered SiC

The SiC supplied by Kyocera International has a fine-grained structure. The average grain size is only 2.5 μm. Small micron size pores are uniformly distributed throughout the microstructure as shown in Figure 9. X-Ray diffrac-
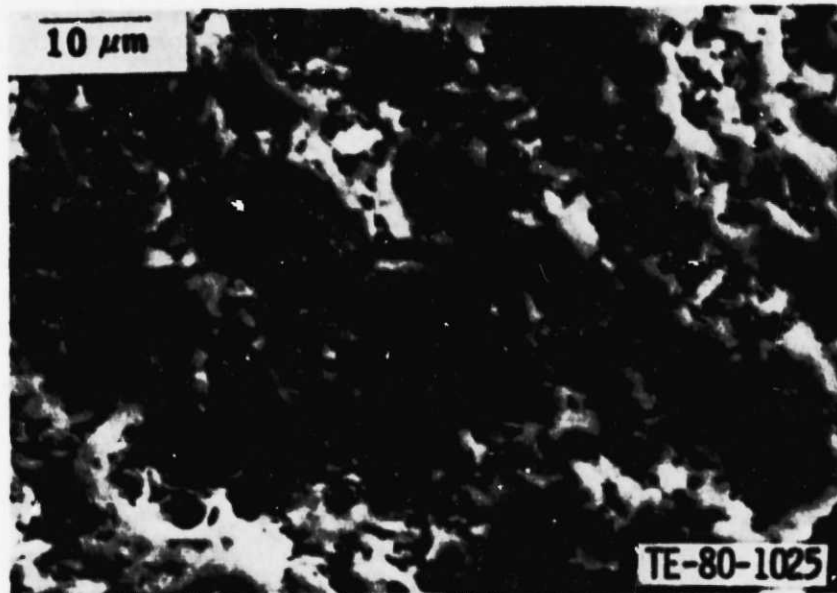
Figure 5. Photomicrograph of the fracture surface of NGK-Locke sintered SiC.
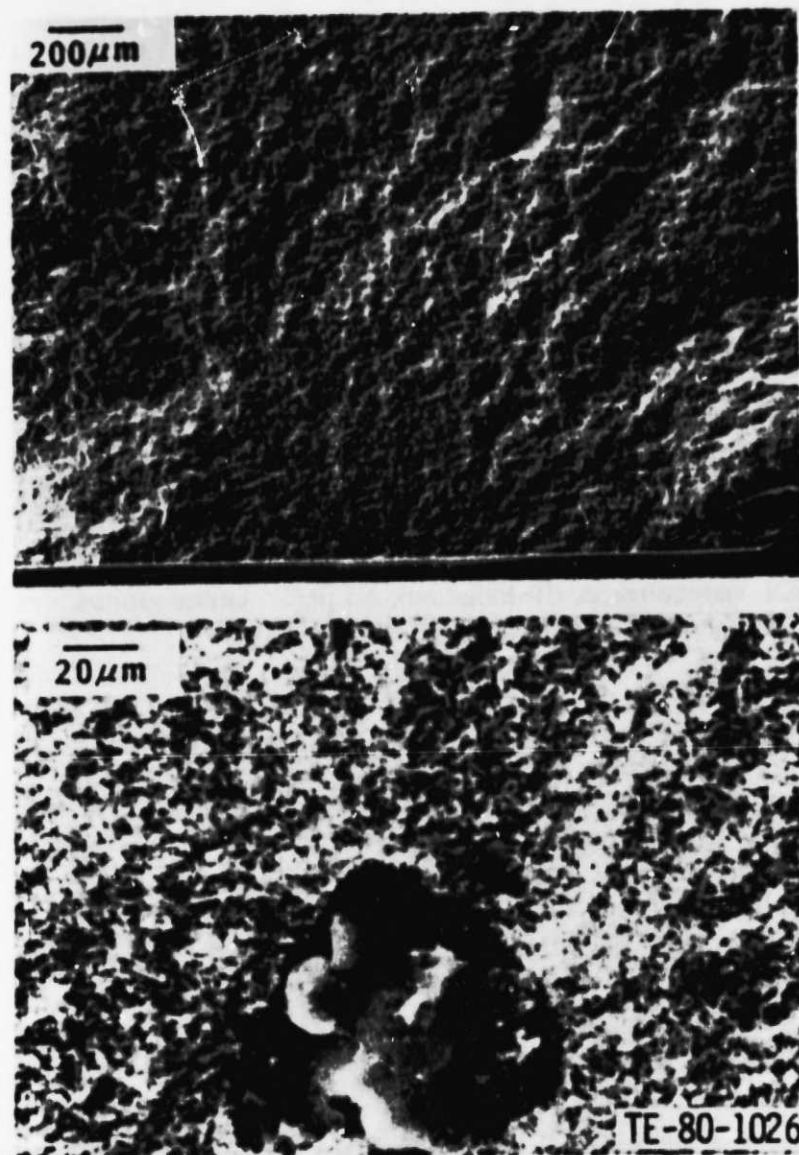
Figure 6. SEM fractograph of NGK-Locke SiC. The critical flow is a
calcium carbide inclusion.

tion indicates that equal amounts of alpha and beta SiC are present. Scat-
tered particles of titanium and vanadium could be seen throughout the materi-
al. Average material density was found to be 3.09 cm3.

Room temperature MOR averaged 352.96 MPa (57.00 ksi) for the as fired surface
and 350.70 MPa (50.87 ksi) for the machined surface of the bar. Critical de-
fects controlling strength in both cases were large pores. The squareness of
the large pore indicates that it may be the site for burnout organic binder as
shown in Figure 10. Two of the machined sample failed at the large deep crack
shown in Figure 11, which lowered the strength to 179.93 MPa (26.10 ksi).
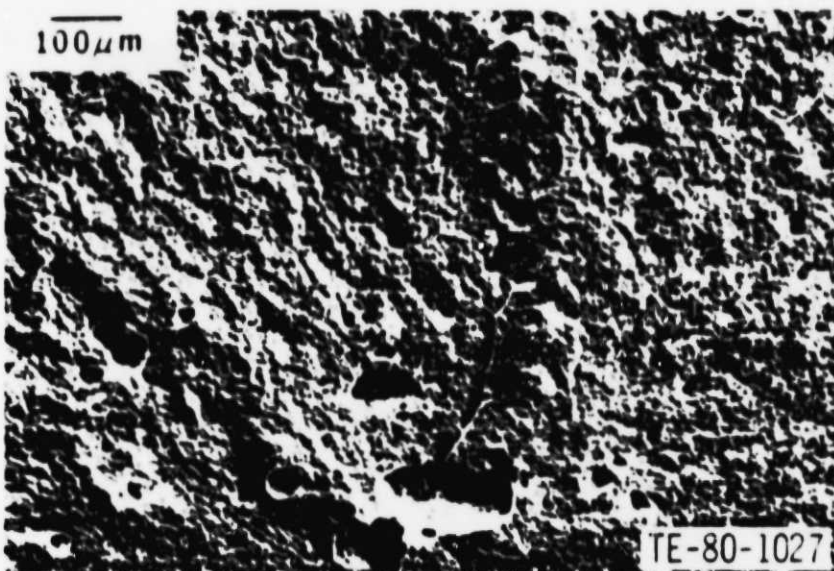
Figure 7. SEM fractograph of NGK-Lock Si$_3$N$_4$. Large pores are the strength-controlling defects.
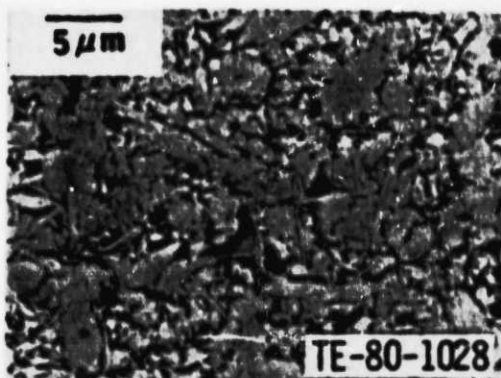
Figure 8. TEM replica micrograph of a polished and etched NGK-Locke Si$_3$N$_4$.

A second lot of test bars of the same material, had an average density of 3.13 g/cm^3 and room temperature MOR of 409.64 MPa (59.42 ksi) for the as fired surface condition and 410.12 MPa (59.49 ksi) for the machined surface condition.

Some of the as-fired surfaces in this lot were green machined prior to sintering. Several bars also had distinctly crystalline as-fired surfaces. Flake (or plate) crystals grew out of the top surface as shown in Figure 12. Spiral growth steps could be seen on some plates. Therefore, variability is evident in the test bars received.

An unusual fractured phenomenon which has not been observed in other carbide or nitride materials occurred several times in Kyocera material. In one test bar, for example, two fracture mirrors were recorded on one fracture surface as

18
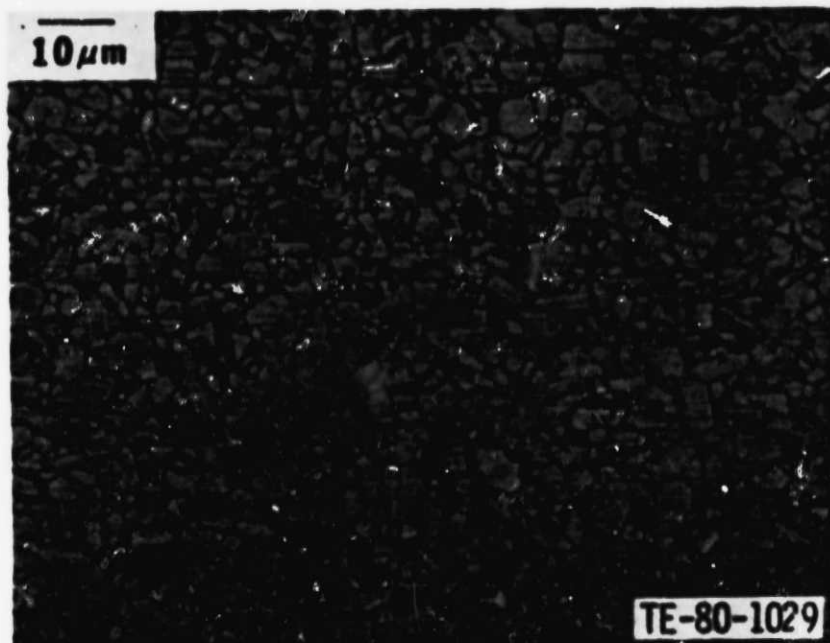
Figure 9. Microstructure of Kyocera SiC. Sample has been polished and etched.
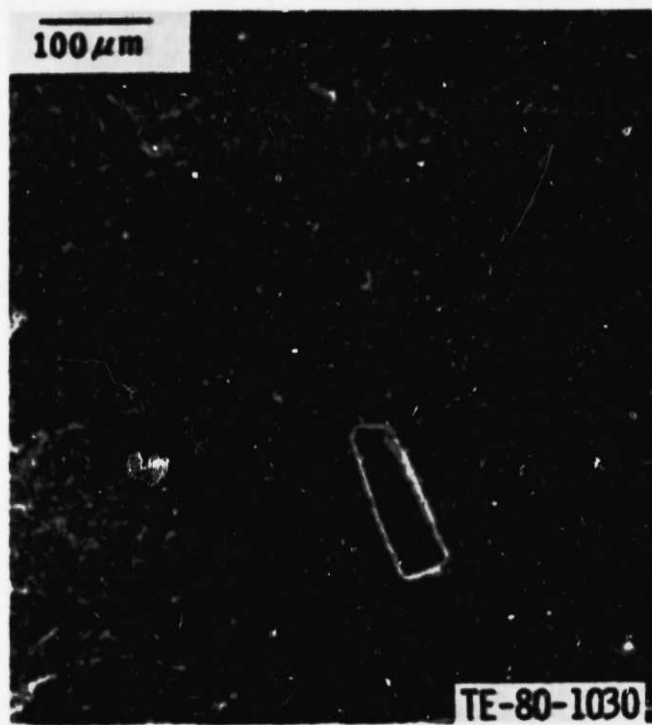
Figure 10. A typical critical flaw--large square pore--in Kyocera SiC.

19

Figure 11. Large deep crack that greatly reduced the specimen's strength to
179.93 MPa (26.10 ksi).

shown in Figure 13. Each mirror has its own defect. The primary origin at
the left-hand side is an open pore and the secondary origin in the middle of
the bar is a large internal pore. The fractural features (hackles and crack
branching) indicate that the crack front proceeded from left to right. How-
ever, the fact that both mirrors are perpendicular to the principle stress
direction indicates that the second mirror was formed before the primary crack
front passed. Further study is continuing.

CERAMIC COMPONENT CHARACTERIZATION

SNW-1000 Silicon Nitride

A preliminary evaluation of a Wesgo sintered silicon nitride (SNW-1000) has
been completed. The material was produced by cold pressing using GTE 502 sil-
icon nitride powder. It is similar in structure and chemistry to GTE 3502.

The fast fracture strength of both as-fired and ground surface conditions has
been determined both at room temperature and 1050°C (1922°F). Test results
are summarized in Table III.
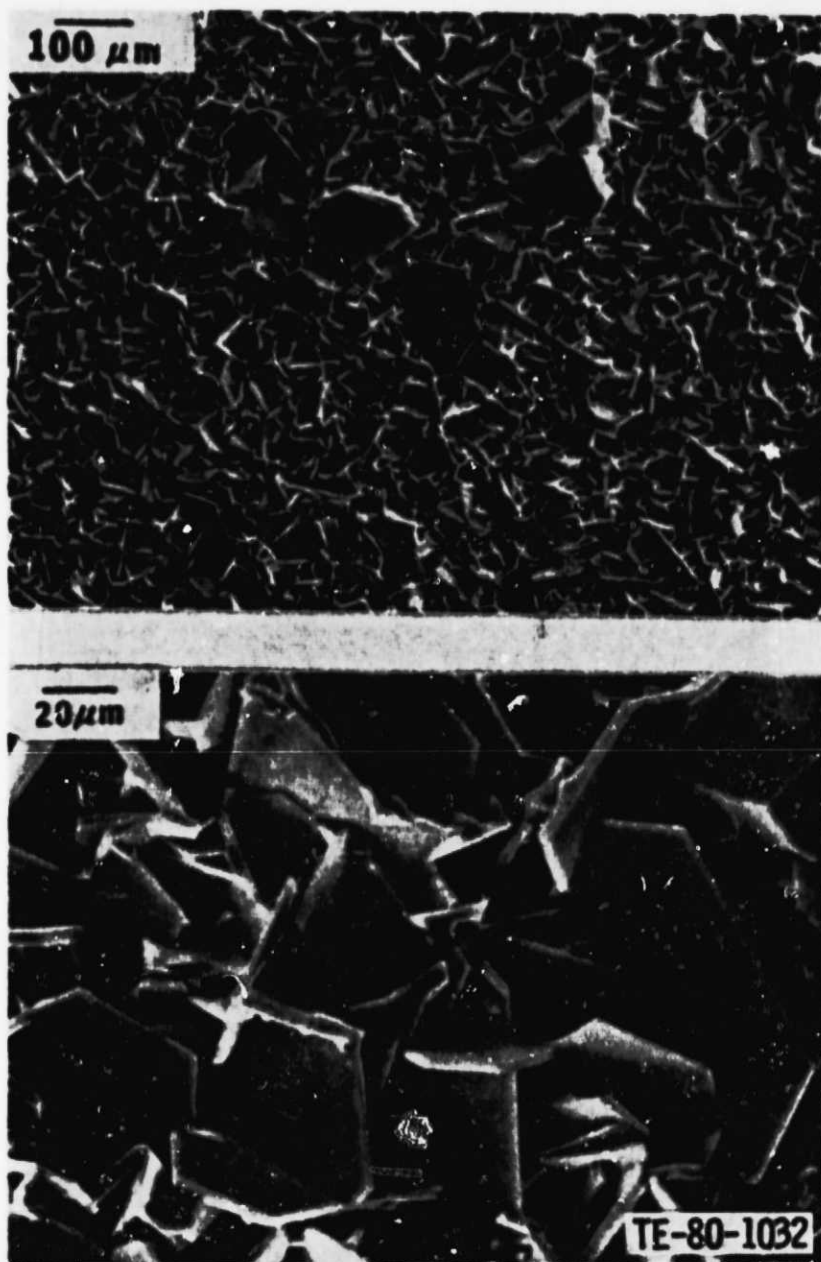
Figure 12. Photomicrographs of the as-fired surface of Kyocera sintered SiC.

TABLE III. FAST FRACTURE STRENGTH OF SNW-1000

Test temperature	Surface condition	No. of samples	MOR, MPa (ksi)
Ambient	As-fired	9	382 (55.4)
	Ground	10	643 (93.3)
1050°C (1922°F)	As-fired	5	416 (60.3)
	Ground	5	554 (30.4)

21
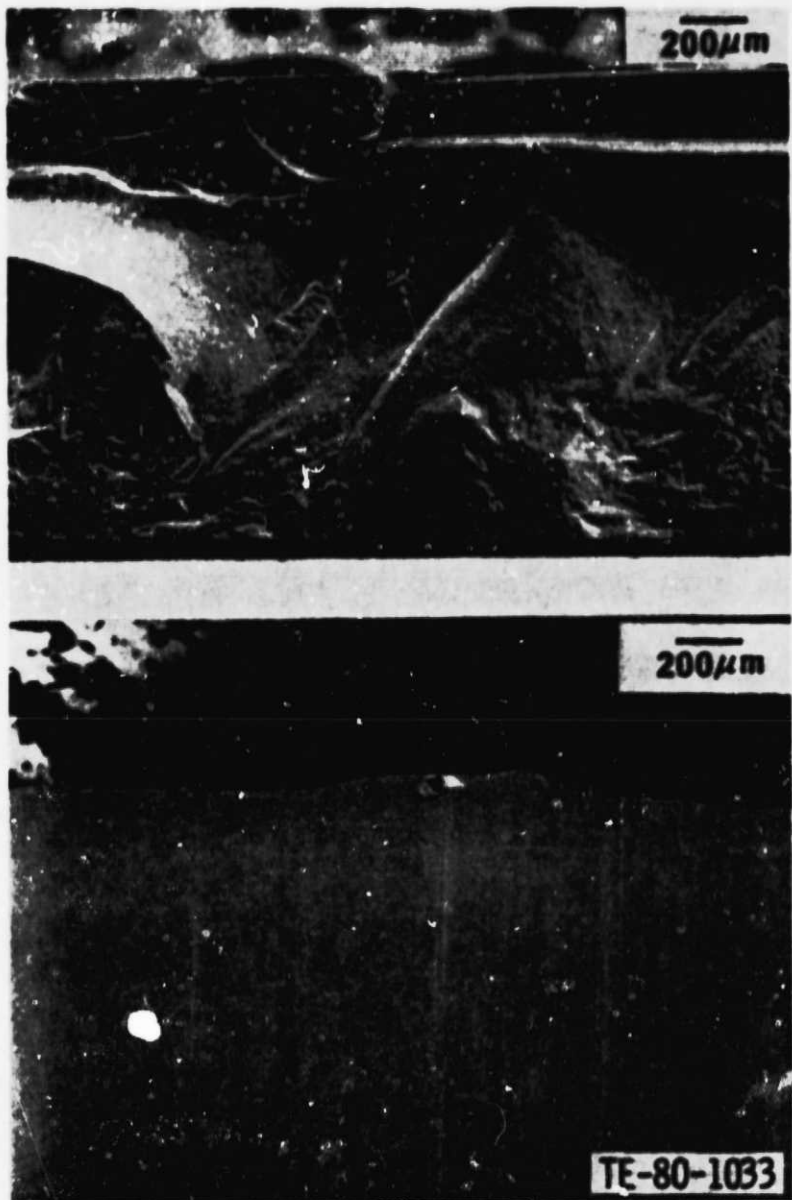
Figure 13. Fracture surface (top) and tensile surface (bottom)
of Kyocera SiC.

The average strength for the as-fired surface condition was found to be 382 MPa (55.4 ksi). For this case failure invariably originated from a surface connected pore as shown in Figure 14. Examination of the as-fired surface revealed numerous small pores of 40 μm or less in size as shown in Figure 15. Further, the general surface structure was very open, consisting in fact of loosely interwoven mesh of elongated silicon nitride.

22
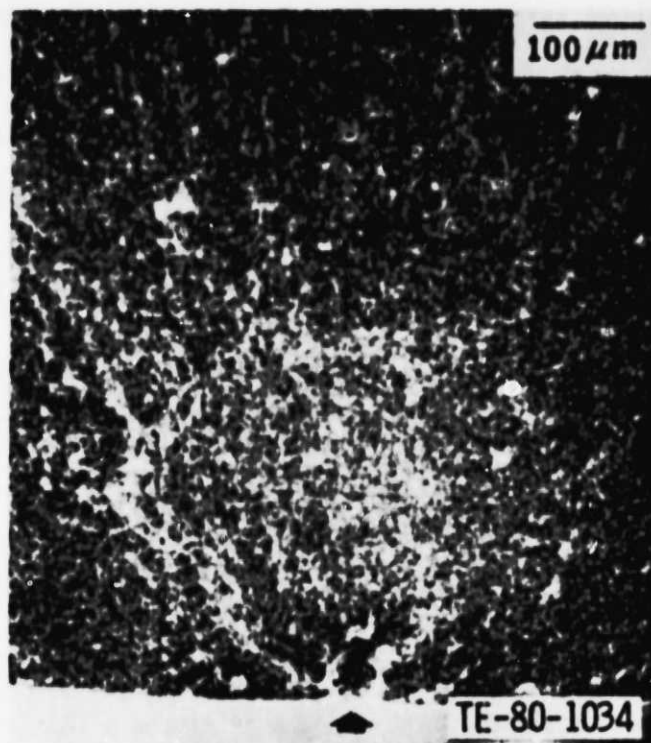
Figure 14.   Fracture surface of as-fired SNW-1000 showing surface pore at failure origin.
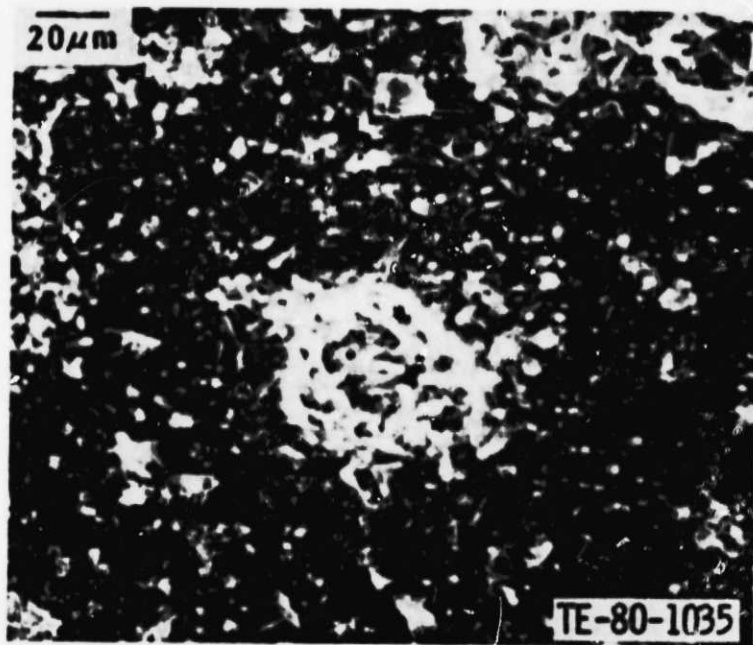
Figure 15.   Surface structure of as-fired SNW-1000 silicon nitride.

23

Removal of the as-fired surface skin by grinding markedly increased strength. The average strength for the as-ground surface condition was found to be 643 MPa (93.3 ksi). Somewhat less than half of the ground samples failed from machining-induced surface cracks. Figure 16 shows a typical example where failure originated from a surface scratch. The remaining samples failed from pores located at or just below the surface as shown in Figure 17. However, these pores are different in structure from those that initiate failure in as-fired samples. For example, most of these internal pores contain large grain inclusions. These large grains are richer in yttrium and may be yttrium silicate (Y_2SiO_5). General X-ray diffraction studies of as-fired SNW-1000 have shown small amounts of this compound to be present.

The strength for the as-fired surface condition at 1050°C (1922°F) was 416 MPa (60.3 ksi). This compares to a room temperature value of 382 MPa (55.4 ksi). (This represents a slight increase in strength at the $\alpha = 0.05$ significance level.) As was the case at room temperature, failure always originated from surface-connected pores. Figure 18 shows an example of such a pore which contains an included particle rich in yttrium. Also, such pores occasionally contain molybdenum-rich particles, as shown in Figure 19. However, most strength-controlling pore have been found to be free of foreign materials.

The strength for the ground surface condition was 554 MPa (80.4 ksi). This compares to a value measured at room temperature of 643 MPa (93.3 ksi). (Again this represents a significant change at the $\alpha = 0.05$ significance level.) The same type of defects that controlled strength at room temperature also prevailed at 1050°C (1922°F).
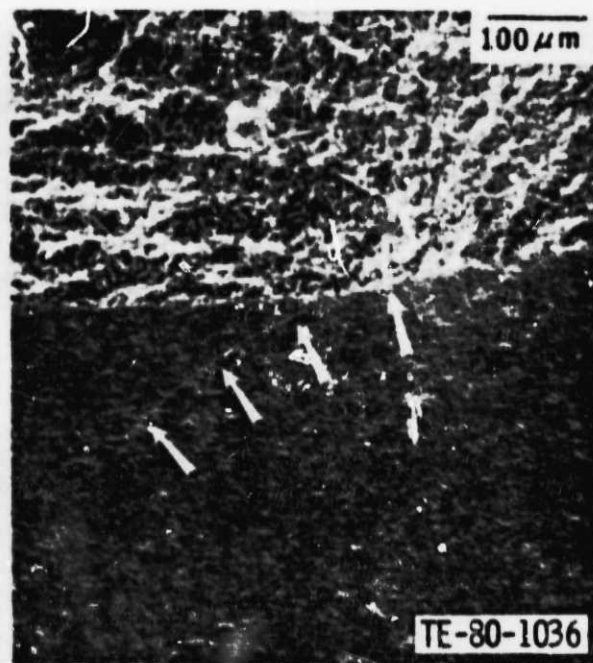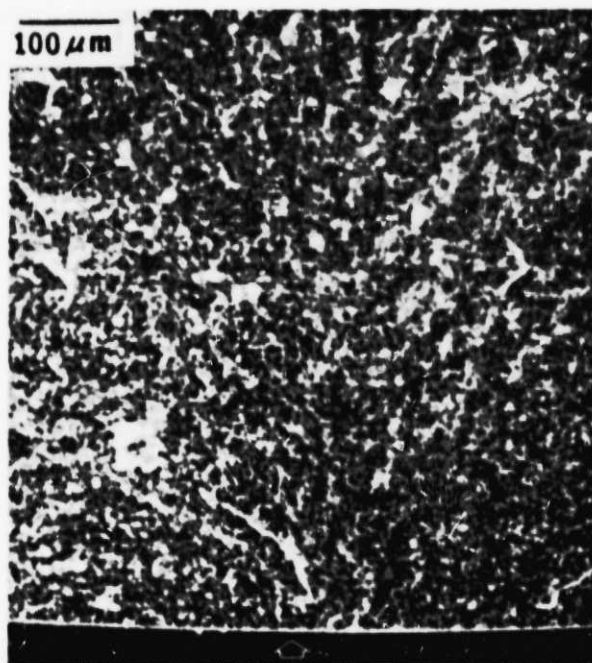
Figure 16. Fracture surface of ground SNW-1000 showing surface scratch at failure origin.
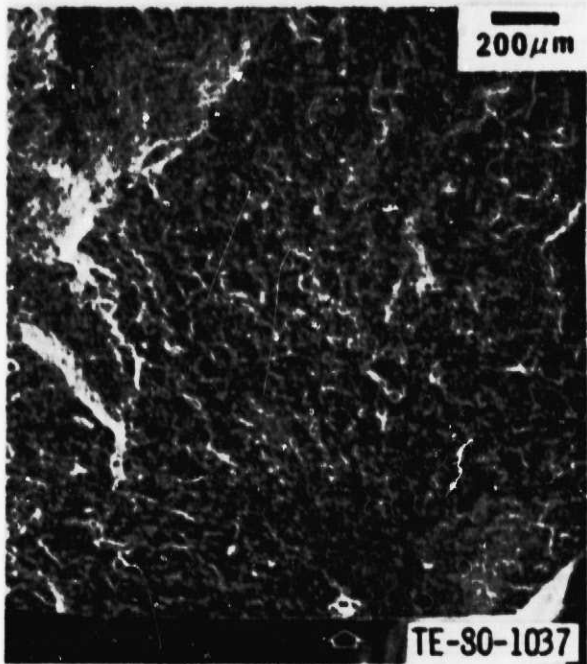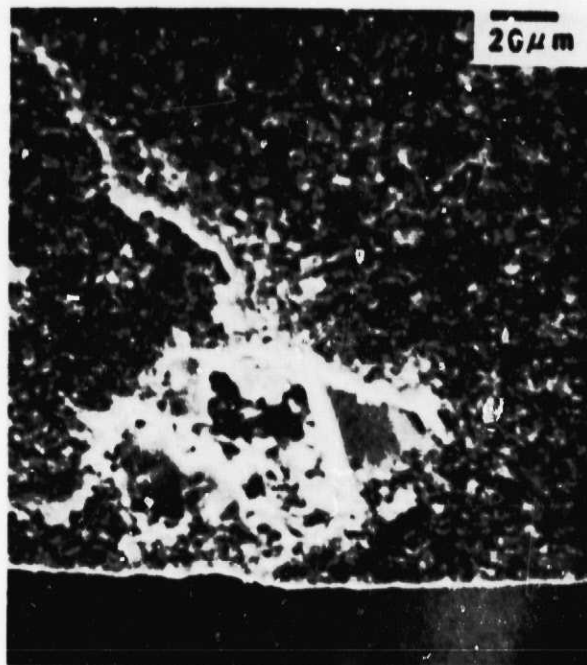
Figure 17. Fracture surface of ground SNW-1000 showing internal pore structure at the failure origin.
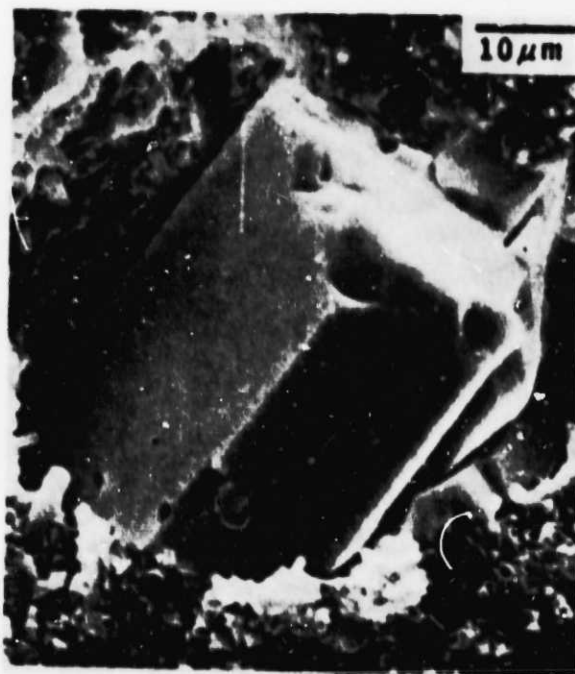
Figure 18. Photomicrograph of SNW-1000 silicon nitride showing a pore rich
in yttrium.

26

Figure 19. Fracture surface of SNW-1000 silicon nitride showing molybdenum particle in a surface connected pore at the failure origin.

Oxidation of SNW-1000 Si$_3$N$_4$

Preliminary testing to evaluate the effect of high-temperature oxidation on the strength of SNW-1000 has been completed. Standard MOR test specimens with both as-fired and ground surfaces were soaked for 100 h at temperatures of 875°C (1607°F), 1050°C (1922°F), and 1150°C (2102°F). In addition, the effect of thermal cycling (intermittant exposure) was examined for a test temperature of 1050°C (1922°F), where specimens were cooled to room temperature and re-heated every 24 h for a total of 500 h. After soaking, specimens were bend tested at room temperature using four point loading. The results of these preliminary tests are summarized in Table IV.

The weight gain observed after 100 h at 875°C (1607°F) was insignificant. Little evidence of oxidation could be found on as-fired surfaces, while a very thin glassy layer was evident on the machined surfaces as shown in Figure 20.

For this temperature, only the strength of the as-ground and oxidized surface condition was measured. The measured average strength of 610 MPa (88.49 ksi) is similar to that determined for as ground material.

At 1050°C (1922°F) significantly greater amounts of oxide were formed. The structure of oxide layer is similar for both the as-fired and ground surface

TABLE IV. ROOM TEMPERATURE FLEXURAL STRENGTH OF OXIDIZED SNW-1000

Oxidation temperature/time	Surface condition	No. of samples	MOR, MPa (ksi)
None	As-fired	9	382 (55.4)
	Ground	10	643 (93.3)
875°C (1607°F)/100 h	Ground	5	610.0 (88.49)
1050°C (1922°F)/100 h	As-fired	5	494.3 (71.70)
	Ground	5	499.4 (72.44)
1050°C (1922°F)/500 h	Ground	5	574.5 (83.33)
1050°C (1922°F)/500 h cycled	Ground	5	554.2 (80.13)
1150°C (2102°F)/100 h	As-fired	5	425.8 (61.77)
	Ground	4	507.3 (73.58)

conditions. Figure 21 shows an example of an as fired surface after oxida-
tion. The layer is approximately 4 μm in thickness and contains copious
amounts of a yttrium-rich crystals. This type of oxide structure was previ-
ously observed on early GTE 3502 material exposed at temperature of 1250°C
(2282°F) for 1000 h. The development of the type of oxide layer at 1050°C
(1922°F), however, is not consistent. Small samples subsequently exposed to
critical thermal conditions developed different scale morphologies. The rea-
son for this behavior is not known at present.

The strength after thermal exposure at 1050°C (1922°F) was found to be 494.3
MPa (71.7 ksi) and 499.4 MPa (72.44 ksi) for as-fired and ground surfaces,
respectively. This represents an increase in strength for the as-fired condi-
tion and a decrease for the ground condition. The major critical defect con-
trolling strength was glass-filled pores, Figure 22, particularly in the case
of as-fired and oxidized samples. In only one sample in ten (a ground sample)
did failure originate from a subsurface site.

SNW-1000 specimens subjected to 100 h at 1150°C (2102°F) showed less weight
gain than those exposed at 1050°C (1922°F). Surfaces of both as-fired and
ground samples were covered with continuous glassy film containing particles
of a yttrium-rich phase as shown in Figure 23. The crystalline structure is
much coarser and more well developed on as-fired surfaces. The results of
bend tests indicated a strength increase for the as-fired surface condition
and a strength decrease for the ground surface condition.

Cyclic exposure for 500 h at 1050°C (1922°F) resulted in the formation of
smaller amounts of oxide than observed during 100 h of continuous exposure.
Figure 24A shows the oxide morphology found on as-fired surfaces, whereas Fig-
ure 24B shows a typical structure developed on ground samples. The prismatic
grains of Si_3N_4 are split and rounded. Isolated areas of a white glossy
phase rich in yttrium, as shown in Figure 24C, are also present on as-fired
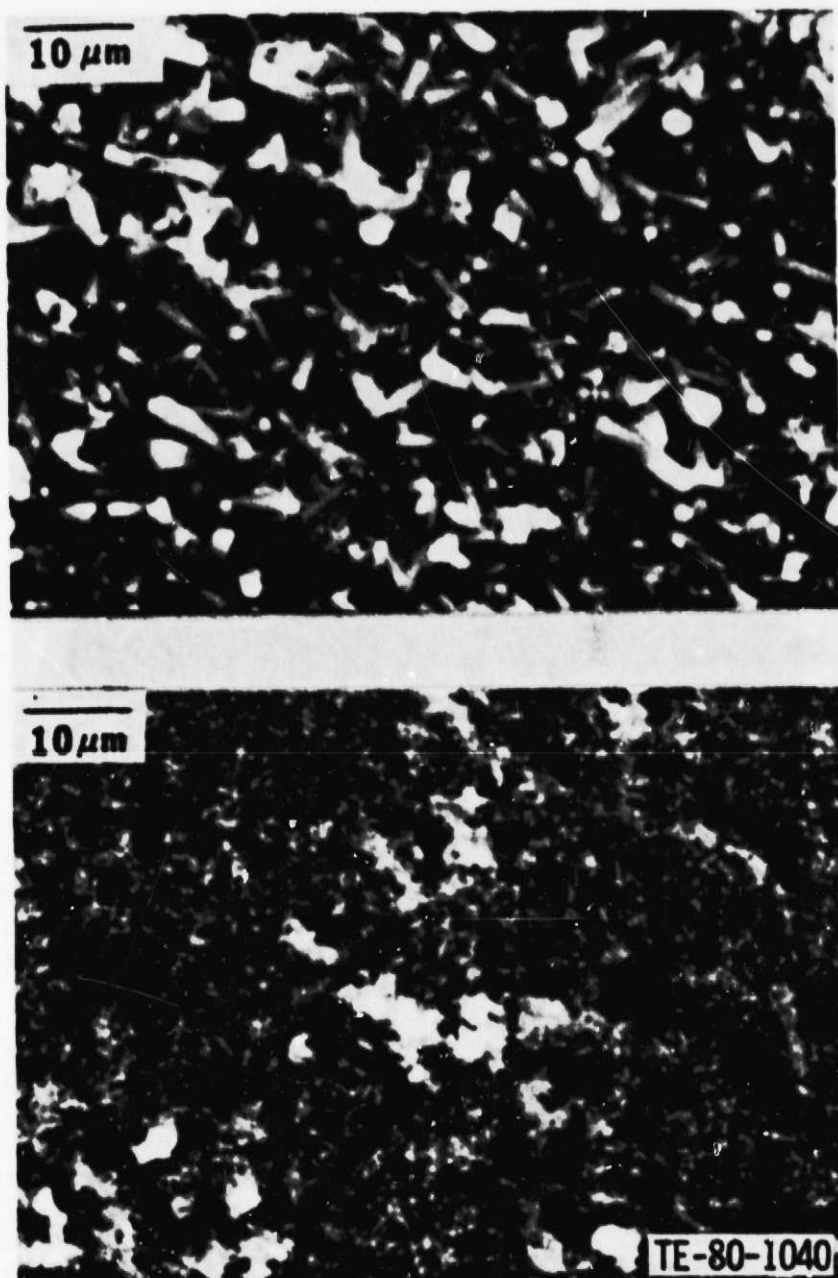
Figure 20. SNW-1000 Si$_3$N$_4$ heat treated at 875°C (1607°F) For 100 h.
Top: as-sintered surface; bottom: machined surface.

surfaces. That type of structure, regardless of whether or not a specimen was subjected to intermittent or continuous thermal exposure.

29
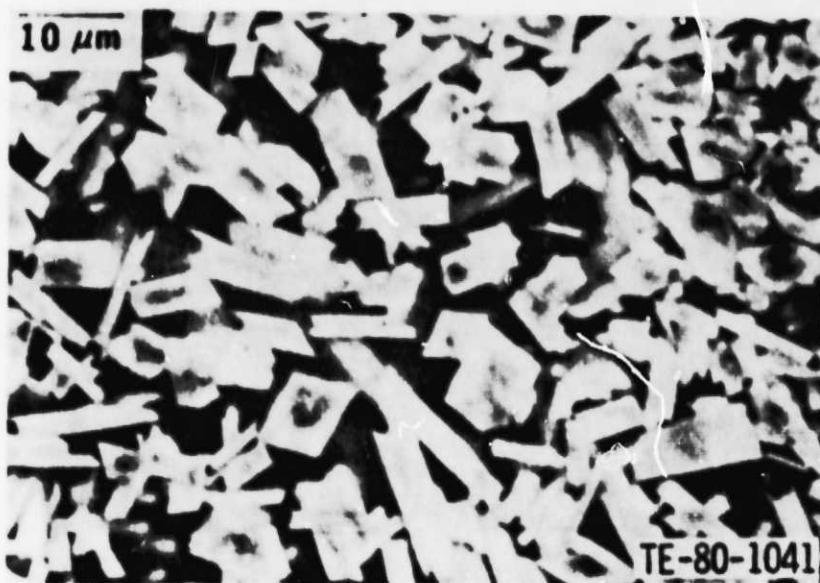
Figure 21.   SNW-1000 Si_3N_4 heat treated at 1050°C (1922°F) for 100 h.
A thick oxidized surface scale covers the original as-sintered surface.
Crystals are rich in yttrium.

The average measured strength of SNW-1000 continuously oxidized for 500 h at
1050°C (1922°F) was 574.3 MPa (83.3 ksi), while specimens cycled to room tem-
perature displayed an overall strength of 552.2 MPa (80.1 ksi). Thus the
limited thermal cycling caused neither a change in oxidation behavior nor
strength.

The preliminary evaluation of SNW-1000 has shown the material to have excel-
lent capability to temperature of at least 1050°C (1922°F). Oxidation testing
showed no unusual oxidation phenomena within the temperature range 875°C
(1607°F) to 1150°C (2102°F). In the short times considered, oxidation per-
formance is considered good. While some deterioration in the strength of as-
ground material after exposure at and above 1050°C (1922°F) occurred, residual
strength levels of 482.6-551.5 MPa (70-80 ksi) are still excellent for a mate-
rial of this type. Furthermore, data for as-fired surfaces generally re-
sulted in a modest increase in strength. The material remains a very viable
candidate for use on rotating structures.

Protective Coatings for Reaction-Bonded Si_3N_4 Materials

A small program was undertaken with the Chemetal Corp. to establish procedures
for coating reaction-bonded silicon nitride with an impervious, oxidation-re-
sistant layer of high-purity silicon nitride (Inodelitun) by chemical vapor
deposition. It was further hoped that the coating would be fine grained and
would display characteristics similar to the CVD SiC. RBN-122 silicon nitride
with an as-fired surface was used as a representative substrate material. The
results of the effort, which represents the second iteration, are summarized
next.

30

Figure 22. Fractographs of glassy pore and oxide film at the failure origin of as-fired SNW-1000 Si$_3$N$_4$ oxidized at 1050°C (1922°F) for 100 h.

Four groups of samples were coated by Chemetal using state-of-the-art coating procedures as of 6/79. Coating thickness (deposition time) was a major variable, and each of the sample groupings represented a different deposition time. Deposition times used were 25, 30, 45, and 60 min. Only material represented by the three stated times were evaluated. The general structural and strength characteristics are presented in Table V.

31
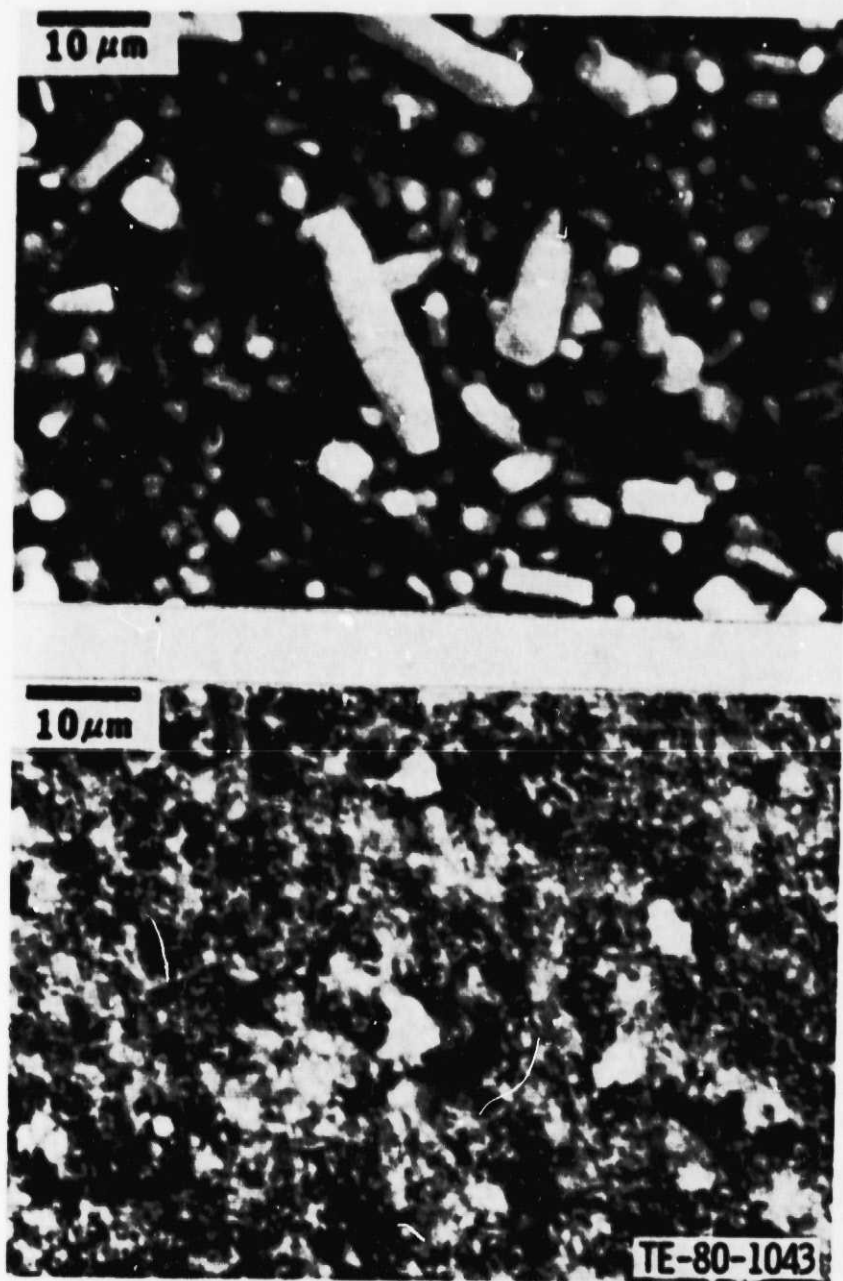
Figure 23. SNW-1000 Si$_3$N$_4$ heat treated at 1150°C (2102°F) for 100 h.
Top: as-sintered surface; bottom: machined surface.

The strength, in general, is significantly lower than the virgin RBN-122.
(The lot of RBN-122 in question has a typical strength level of approximately
241.3 MPa (35 ksi).) The strength reduction is attributed to the coating it-
self since all bars failed from the coating surface. Figure 25 shows a typi-
cal example of fracture surface where failure originated from the coarse sur-
face of the test bar.

Figure 24. SNW-1000 Si_3N_4 heat treated at $1050°C$ ($1922°F$) for 500 h. A and C: as-sintered surface; B: machined surface.

33

TABLE V. FLEXURAL STRENGTH AND MICROSTRUCTURE OF CVD Si_3N_4-COATED RBN-122.

Sample number	Strength,* MPa (ksi)	Failure origin	Thickness, μm	$\bar{\gamma}$, μm	Remarks
13.0368	173.3 (25.14)	Corner CVD surface	40	7.4	25-min run
13.0370	144.9 (21.02)	CVD surface	40	8.0	25-min run
13.0377	108.4 (15.73)	CVD surface	40	8.8	25-min run
13.0346	138.8 (20.13)	CVU surface	110	13.9	30-min run
13.0347	146.1 (21.19)	Corner CVD surface	160	19.4	30-min run
13.0350	128.9 (18.70)	CVD surface	220	18.3	30-min run
13.0360	---	Corner CVD surface	140	20.7	45-min run
13.0362	96.7 (14.02)	Corner CVD surface	140	15.2	45-min run
13.0363	122.1 (17.71)	Corner CVD surface	100	11.4	45-min run

*Uncoated strength, σ = 262.7 MPa (37.1 ksi)
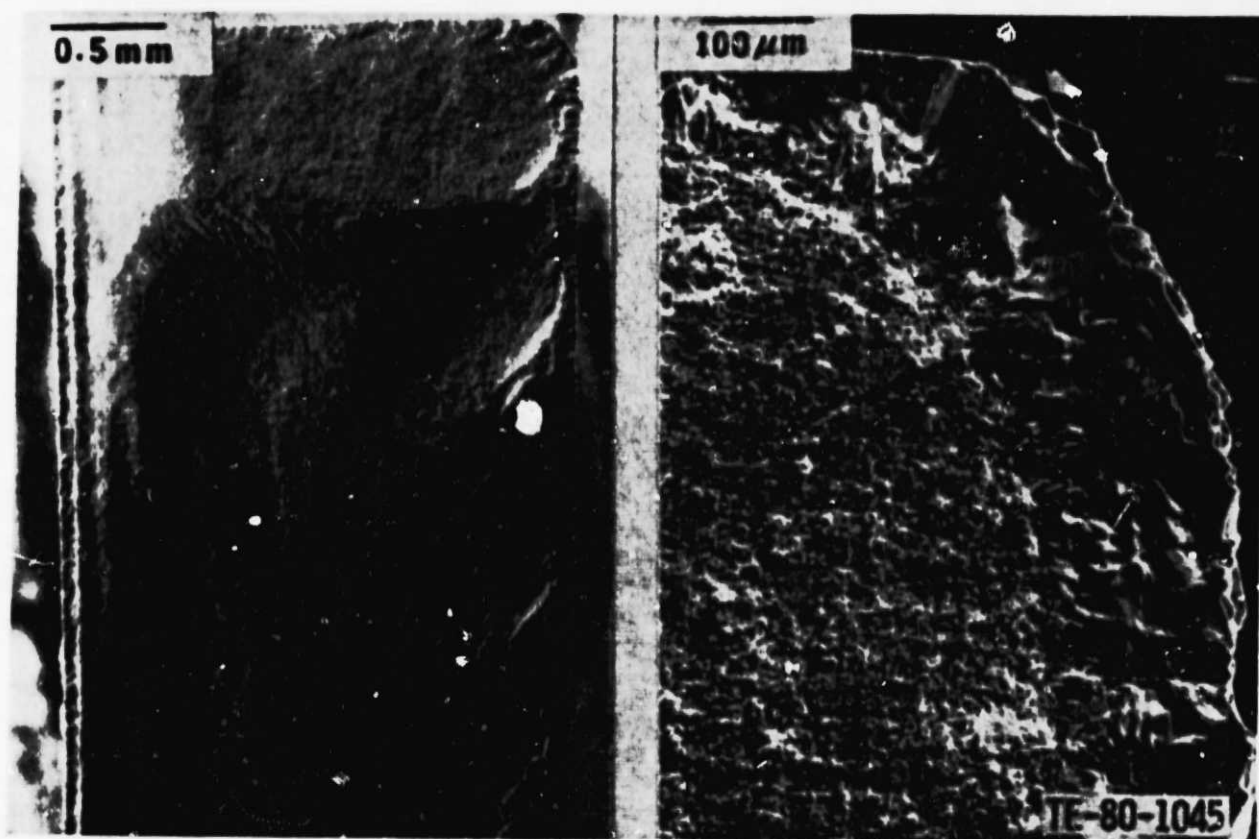
Figure 25. Fractograph of a CVD Si_3N_4-coated RBN-122 bar. Arrow identifies fracture origin.

The strength of the coating itself is considerably below the anticipated level. This is perhaps a result of the rough crystalline surface structure typically developed as shown in Figure 26 or to residual stresses associated with the columnar grain structure of the coating.

The achievement of a fine-grained coating has not been met. The present coating, while adherent and probably impervious, is low strength and not appropriate for the present application. The current assessment is that the realization of a fine-grained equiaxied microstructure in CVD silicon nitride requires an extensive development program, and this is clearly beyond the scope of the current effort.

TIP SHROUD ABRADABILITY

Summary

This task is directed toward the development of abradable seal materials that are compatible with ceramic blading. A dual-path approach is being taken. Both commercially supplied ceramics as well as DDA-generated materials are being investigated to develop a viable seal system.

Materials studies of silicon nitride abradable compacts have shown the basic concept to have merit. Further efforts are required to improve erosion resistance and to develop adequate bonding techniques. Abradable silicon carbide systems were reviewed, and several new approaches are being examined.

Buildup of a ceramic-bladed test rotor was completed, and preparations are being made for abradability testing on the high-speed rig. Plasma-sprayed abradable seals were installed in the 1900°F engine shroud for operation against metal blade tips. DDA-developed sintered mineral compacts and cement laminated refractory fabrics also appear promising for use on high-temperature abradable materials. Further testing will more fully assess their

100 μm

TE-80-1046

Figure 26. Topograph of the surface of the as-deposited CVD Si_3N_4.

35

potential. If solid body abradable structures continue to appear to be viable, effort will be given to implement their use through development of necessary joining techniques or mechanical capture systems.

Objective

The goal of this effort is to develop ceramic-based abradable seal materials with associated processing specifications that are compatible with metallic bladed turbines operating at temperatures of 1038°C (1900°F) and with ceramic bladed turbines operating at temperatures of 1240°C (2265°F). In addition to abradability, these seal materials must also demonstrate a high degree of resistance to hot gas particulate erosion. Resistance to thermal shock, fatigue, and oxidation are also essential for success.

Discussion

The development of abradable seal materials is a particularly difficult problem; therefore, a dual-pathed approach has been taken to provide increased probability of reaching a solution. Commercial sources of ceramic materials that have previously been selected to supply other turbine components for this program are also participating to varying degrees in the abradable seal development effort. These sources cover the range of materials that are considered to be potential candidates for turbine components and include such sources as Carborundum and Pure Carbon/BNFL for silicon carbide components, GTE Sylvania for silicon nitride and Corning and Coors for special silicate and other compounds. Each of these sources is investigating special formulations of its respective products as candidate abradable materials. To complement this external effort, DDA is conducting in-house studies of ceramics materials which are highly compatible with the engine structures being supplied by the previously mentioned suppliers. These materials investigations are extensions of DDA's basic work in areas of abradable seal and materials technology. They are directed toward the identification and modification of existing ceramics materials to improve properties that offer some potential for satisfying the requirements of abradability and erosion resistance. These materials include both free standing structures and coatings.

Candidate materials are extensively examined in a series of laboratory test rigs prior to committing the materials for engine testing. These test rigs subject the candidate materials to simulated operating conditions. Tests include low-speed abradability screening, high-speed, high-temperature abradability, aerodynamic/particulate erosion, permeability thermal shock and fatigue, and oxidation. In addition the data collected and the observations made during this testing, standard microanalysis is performed on coupon specimens and material microstructures are examined by optical and scanning electron microscope (SEM) techniques.

As previously reported in DDA EDR 10156 (NASA CR-159865), the acquisition of engine-type abradable turbine shroud rings was based on the results of abradability and erosion tests of vendor-supplied samples. Although good correlation was achieved in the test samples of abradability with particle size and specimen density for the silicon carbide material, the properties of the delivered shroud rings did not correspond to those of the test samples. The same was essentially true for the foamed LAS cement-type abradable shrouds.

It was apparent that the fabrication process for the shroud rings required further study in order to produce consistent and acceptable materials. Samples of silicon nitride, coordierite, and silicon carbide, as previously reported, were first generation-type specimens and required additional sample variations in order to form a more complete test matrix.

In the continuing program with Carborundum to develop abradable silicon carbide structure, it has been determined that the physical shape of the part plays a significant role in the final density and abradability. That is, the fabrication of a circular shroud ring requires different processes than a flat sample. These process variations, which include differences in pressing directions, are believed to have caused the difficulties leading to the poor abradability observed in the engine shroud rings.

To proceed with the development of abradable silicon carbide structures, a series of material systems has been proposed:

o Silicon matrix, SiC fiber reinforced--This is an impregnated carbon felt system molded to various densities, siliconized, and leached on the surface to expose abradable SiC fibers.

o Closed pore SiC foam on SKT backing--An SKT green body with cast-on green closed pore SiC foam is siliconized and leached on the surface layer. Variations would include hole size, hole proportion, and SiC material.

o Fine open pore SiC foam--This foam is very fine SiC open pore foam, silicon infiltrated and acid leached on the surface.

o Reaction-bonded SiC with free silicon in mix--This system is an existing CATE abradable shroud material with particulate silicon added, molded, siliconized, and leached on the surface. This would result in an increased green strength body with improved machining yields but would do nothing to improve the abradability over existing CATE materials already on bond.

Discussions held with various silicon carbide suppliers has resulted in almost opposite viewpoints as to the ideal powder size to be used in formulating an abradable surface. There is one point of view that adheres to a fine particle size approximately 10 μm whereas another viewpoint is to proceed with an appreciably coarser powder, perhaps up to 150 μm in size. Samples produced to date have been made from 10-μm and 45-μm powder sizes. The 10-μm type samples have generally been better performers than the 45-μm sample.

Previous investigations of silicon nitride compacts received from GTE Sylvania revealed that although these materials had good, homogeneous structures, they were too dense for satisfactory abradability performance. Additional test samples with lower density have been received from GTE Sylvania for evaluation.

As a part of the in-house investigations, ceramic cement-bonded systems have been explored over a wide range of variables. Initial work involved felts and papers in the alumina and aluminum silicate families with nearly simultaneous work with zirconia cements and rigidizers impregnating zircon and zirconia felts and fabrics. The aluminum silicate and zirconium silicate families appear to be attractive candidates for the CATE seal systems since their thermal expansion properties are compatible with SiC (α and possibly Si_3N_4) while possessing good thermal shock resistance. Figures 27 and 28 are examples of some of the systems examined where felts and fabrics were vacuum impregnated

with various cements. All such systems were dried to set the cement and then fired at temperatures as high as 1600°C (2910°F) to react and sinter the components.

More recent attention has been given to development of composite structures comprised of zirconia fabrics laminated and impregnated to form free-standing structures. Two basic fabrication methods have been employed. Thin flat specimens have been prepared through impregnation of individual fabric layers prior to lay-up, then pressure bonding of the assembly during initial curing through use of a vacuum bagging technique. Final fixing of the laminated ceramic fabric assemblies was usually carried out at 1400°C (2550°F). The fully fired thin laminate specimens measured from 1.5 mm (0.060 in.) to 2.2 mm (0.090 in.) thick depending upon the number of fabric layers used. Individual fabric layers 0.75 mm (0.030 in.) thick were used in the above composite structures. These specimens were prepared for testing by cementing a portion of the fabricated composites to metal coupons.

To permit evaluation of abradability into the "edge" of a layered composite, thick assemblies were prepared measuring approximately 2.5 cm^3 (1 in.^{3}). Some delamination of the specimens was experienced as a result of tooling limitations. New tooling was made and used in conjunction with a hydraulic press equipped with heated platens and temperature-controlled clam-shell heaters surrounding the bond fixture. Mechanical loading at 6894 kPa (1000 psi) yielded a laminate stack that was reduced to 46% of the original stacked laminate height.
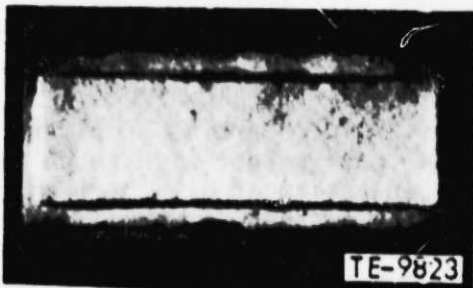
Figure 27. Aluminum silicate coating bonded to silicon carbide coupon. (1.1X)
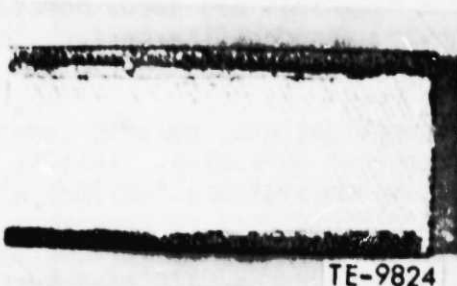
Figure 28. Zirconium silicate coating bonded to silicon carbide coupon. (1.1X)

Cross-sectional slices were made of the above green-fired specimens. All were then fired in a tube furnace to 1400°C (2550°F).

One phase of the abradable seal material development effort has been the investigation of fabricated free-standing sintered ceramic structures. A mixture of equal parts of fine (325 mesh) and coarse (80 mesh) silicon dioxide (SiO_2) powder and fine zirconium silicate (600 mesh) powders were subjected to a plasticizing coating process. The powder mix was subsequently cold-pressed into pellets, then transfer molded into a pattern die at 162°C (325°F). The molded shapes were then burned out at temperatures in excess of 1100°C (2012°F) in a slow programmed cycle to burn out the plasticizer and cause interparticle sintering of the ceramic particles. The process is readily adaptable to the fabrication of near-net shape abradable structures. Figure 29 is a SEM cross-sectional view at 75X and shows the large fused SiO_2 particles within the sintered matrix of the finer particles.

A preliminary test button was fabricated by blending zircon powders from equal parts of 80, 325, and 600 mesh particles with a plasticizing binder. Additionally, a test button was fabricated using 200-mesh yttria-stabilized zirconia powder with a plasticizing binder. The above specimens were sintered at 1400°C (2560°F).

Application of plasma-sprayed ceramic materials for seal applications requires innovation to reduce the material density and achieve abradability. One approach seeks to lessen the apparent density through a post-spray burn-out for removal of a low-temperature material co-sprayed simultaneously with the ceramic matrix material. A second approach traps and retains a second phase material that is compatible with the selecter matrix yet permits mechanical surface incursions to fracture the lower strength or lower apparent density composite.
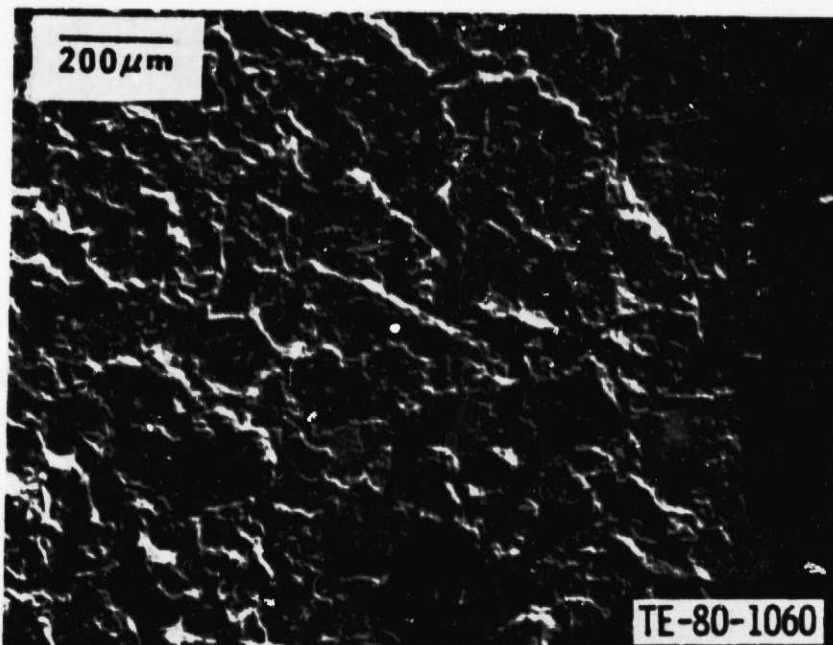
Figure 29. Sintered mineral (ceramic) compact SEM micrograph showing fused silicon oxide particles in fine powder matrix. (75X)

This concept builds on the highly successful thermal barrier coating technology developed at NASA Lewis Research Center and becomes, in effect, an "abradable thermal barrier." The use of ceramic and glass microballoons was explored to a limited degree since the growth of the 2070 and 2265°F CATE engines would push seal service temperatures above the softening point of those materials.

Several other mineral powders were evaluated for potential suitability as "fillers" or alternate matrix ceramics. Some fine powder minerals were spray agglomerated by Stork-Bowan Engineering Co. to yield particle size distributions suitable for plasma spray application. Wollastonite, kaolin, zirconium silicate, and mullite were among those powders found and agglomerated.

Vendor-Supplied Materials

The silicon nitride compacts produced by GTE Sylvania were intended to provide a "super" abradable lower limit to the series, as previously discussed. The results were exactly as desired: The samples investigated were extremely abradable, and very clear, distinct rub paths were produced when tested in the low-speed screening rig. In all cases, blade tip loss was minimal, with maximum losses of 0.001 mm (0.0004 in.), zero, and 0.005 mm (0.0002 in.) measured for rubs with the "A", "B", and "C" systems, respectively. All the tests were conducted at an infeed rate of 0.025 mm/s (0.001 in./sec). The blade tips were all extremely clean, with no blemished or damaged areas. Rub depths were unusually deep, accentuating the extreme abradability of this particular group of samples. Figures 30 through 32 show the rub paths made in each of the silicon nitride specimens. Superficial Rockwell hardness (R15Y) values varied from the low 40's to the low 50's. These are significantly softer then previous samples, which were in the high 70's. Dimples created by the hardness measurements are evident in Figures 30 and 32.

Preliminary oxidation tests were conducted on the silicon nitride samples to assess the initial effect in weight gain and any changes in hardness levels. These disks were run at 1093°C (2000°F) for a total of 27 h with the results shown in Figure 33. Sample B failed as a result of the abradable layer separating from the silicon nitride base. Hardness levels were virtually the same at the completion of the test as at the beginning, i.e., R15Y = 59 for sample "A" and 57 for sample "C".

Continuing investigations into Coordierite (MAS) structures supplied by Coors has resulted in a marked improvement in abradability performance over previously tested coordierite samples. The abradability test at a slow infeed rate of 0.025 mm/s (0.001 in./sec) resulted in the rub shown in Figure 34. The path was very well defined with no evidence of distress to the blade tips. Striations shown in the photograph of the rub path were presumably caused by entrapped abraded material, which was dragged along by the blade tip. However, no blade tip loss could be measured. Erosion testing resulted in considerable damage to the material during the first 30 min of exposure. The eroded specimen is shown in Figure 35.

As an aid in further characterizing the microstructure of the ceramic materials under investigation, SEM and optical micrographs were made to permit examination of the grain structure and the interface between the abradable and base materials.

40
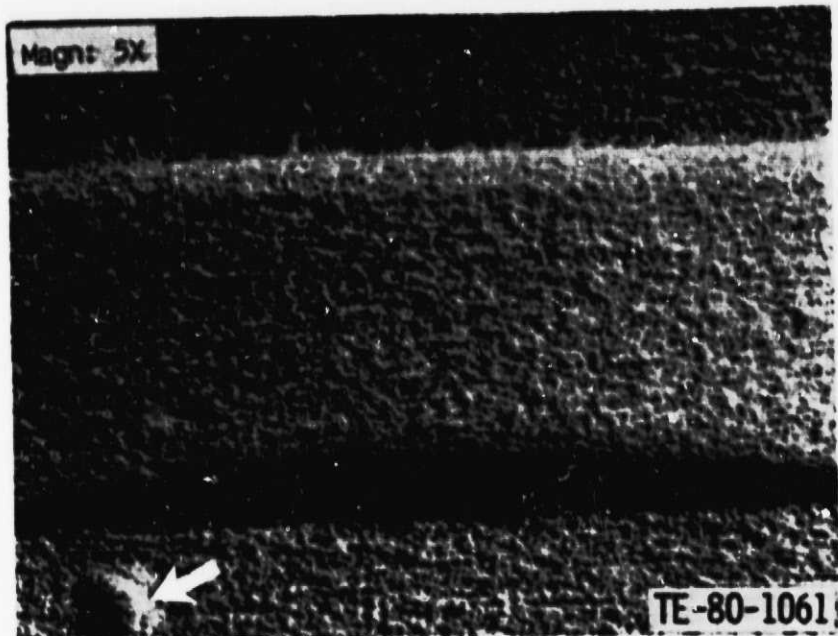
Figure 30.   GTE Sylvania 82-46A with silicon nitride rub depth
1.35 mm (0.053 in.) and R15Y avg = 52.
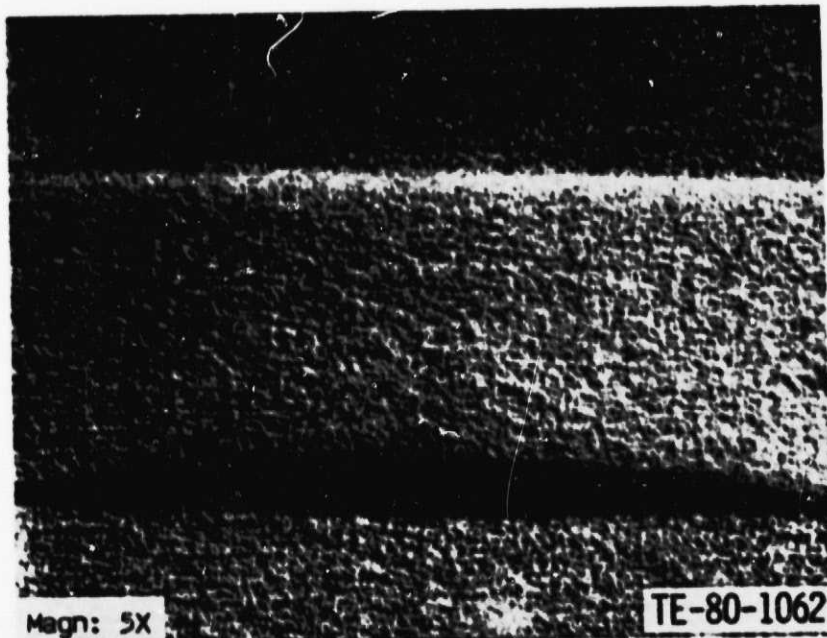
Figure 31.   GTE Sylvania 82-46B with silicon nitride rub depth
1.14 mm (0.045 in.) and R15Y avg = 43.
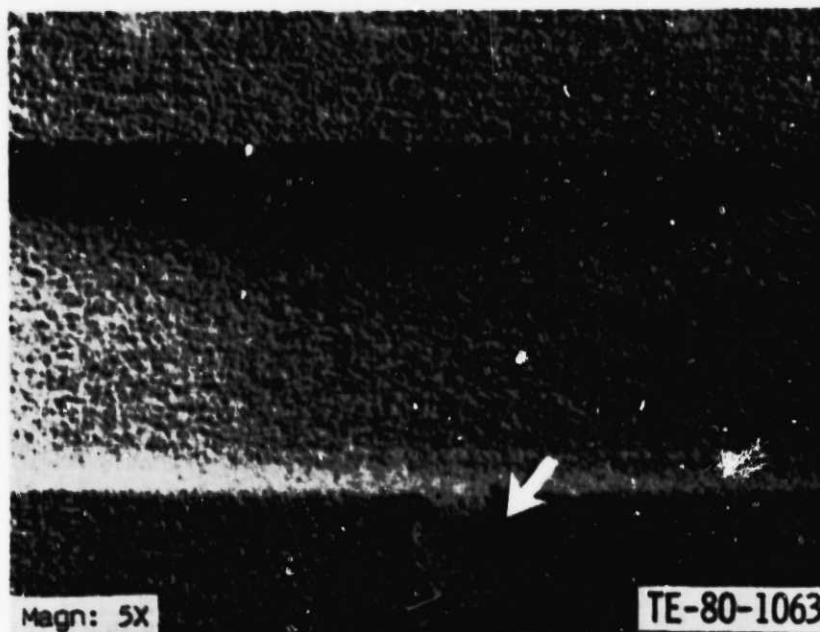
Figure 32. GTE Sylvania 82-46C with silicon nitride rub depth
1.70 mm (0.067 in.) and R15Y avg = 51.

TE-80-1066
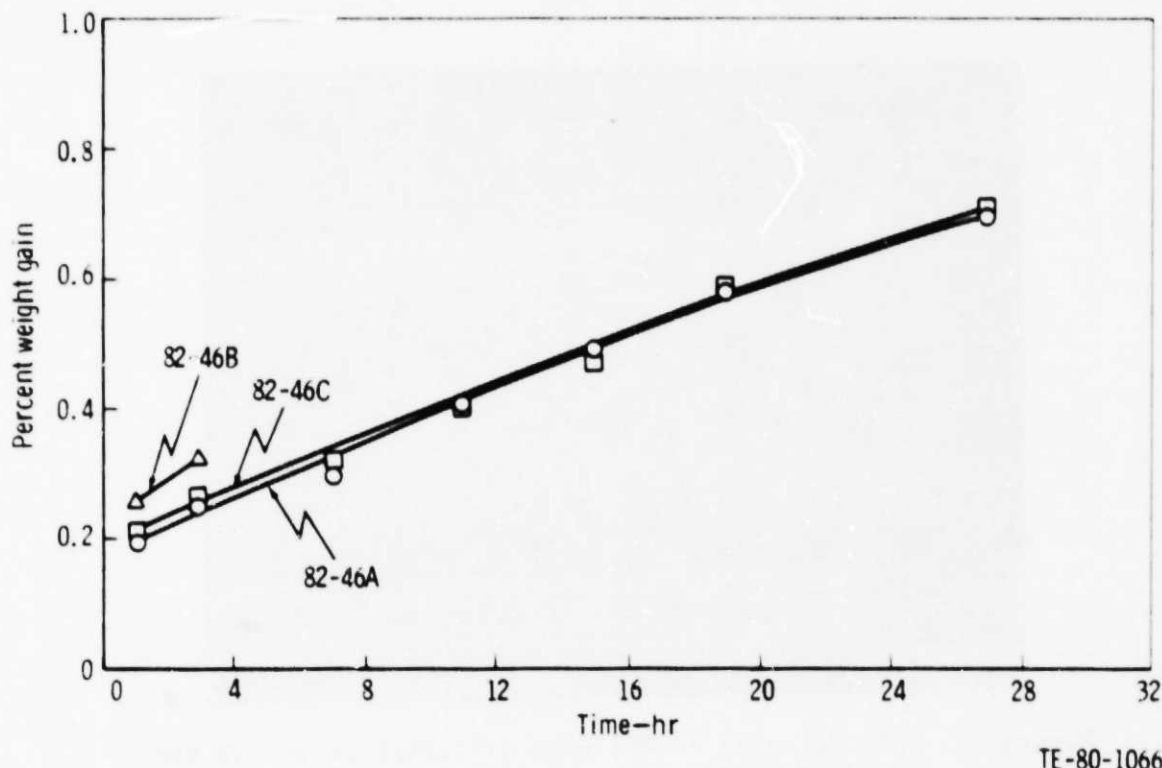
Figure 33. Oxidation of silicon nitride compacts at 1093°C (2000°F).

42

The GTE Sylvania silicon nitride revealed a very porous abradable material bonded by sintering to the base silicon nitride structure. The abradable silicon nitride had a larger grain size and lower yttrium concentration than the base material. The larger grains of the abradable layer had grown slightly into the fine-grained base silicon nitride. An optical microgaph of a typical silicon nitride coating is shown in Figure 36, and the comparable SEM photograph is shown in Figure 37. In Figure 38, the large silicon nitride grain can be seen growing into the fine grain base.

Figures 39 and 40 show the Coors Coordierite matrix with distinct grains distributed uniformly throughout the material. Both phases are MAS with impurities of barium and some iron. However, the matrix phase has a higher aluminum concentration than the grainy phase.

The Pure Carbon silicon carbide abradable specimens were made from reaction-bonded silicon carbide. All samples had a silicon-rich surface layer in which the free silicon was partially leached out to form the abradable structure. The resulting abradable layer was thus solely dependant on the microstructure of the silicon-rich surface layer. Sample I-3 shown in Figures 41 and 42 had a somewhat reduced free silicon content in the surface layer, resulting in increased density. Sample II-1 shown in Figures 43 and 44 had the highest

Magn: 5X   TE-80-1064
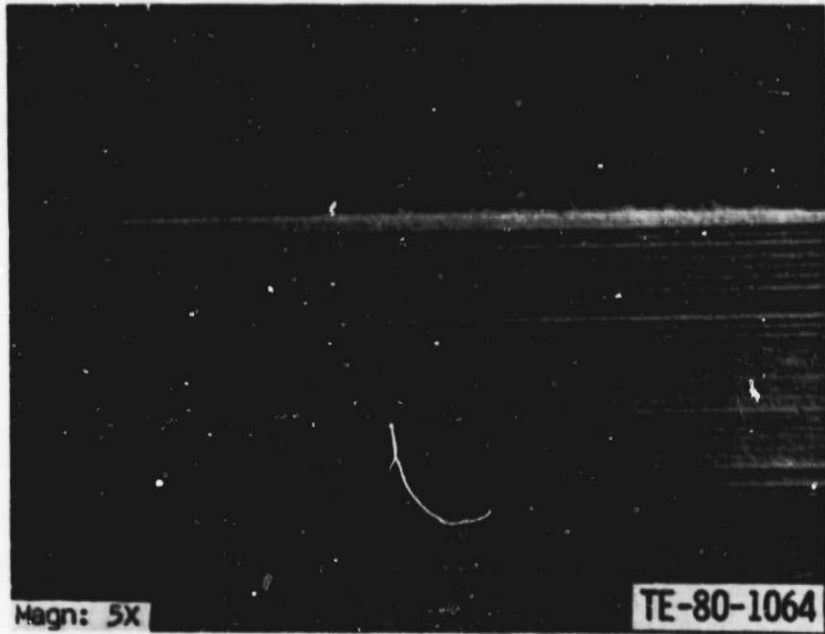
Figure 34. Coors 8H3 with Coordierite (MAS) rub depth 0.91 mm (0.036 in.)

43
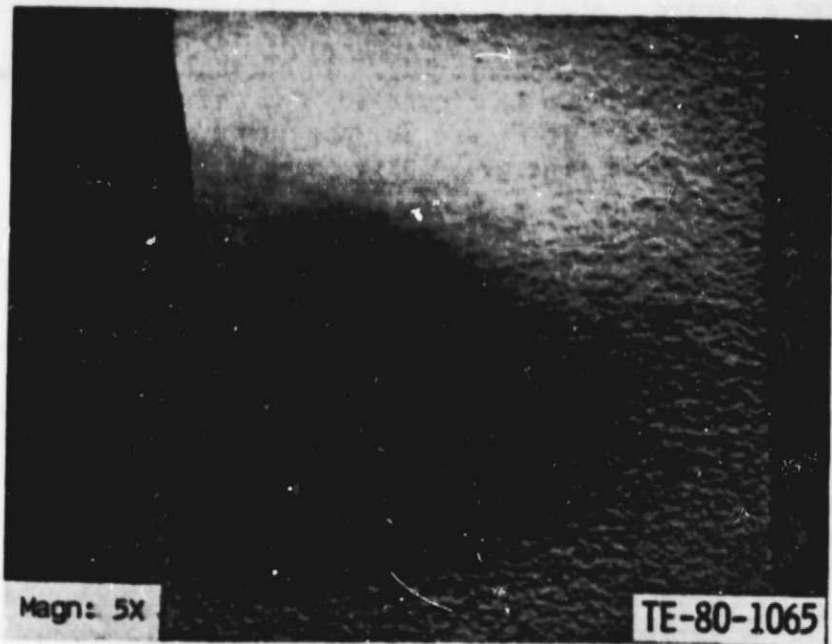
Figure 35. Coors Coordierite (MAS) with 30-min erosion and 45-deg impingement.
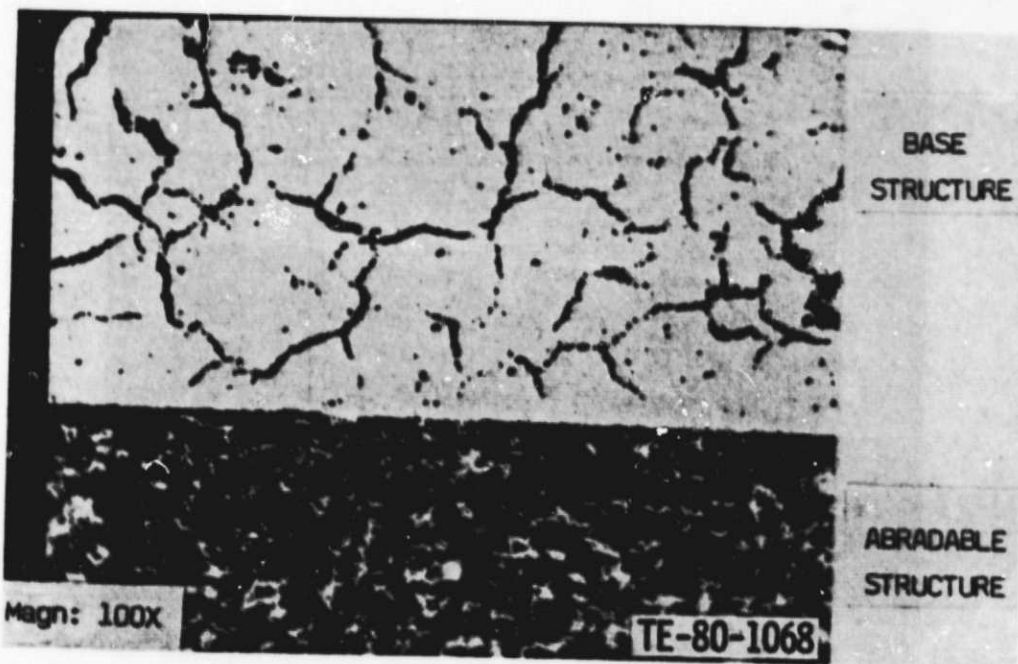
Figure 36. Si3N4 optical micrograph.

44
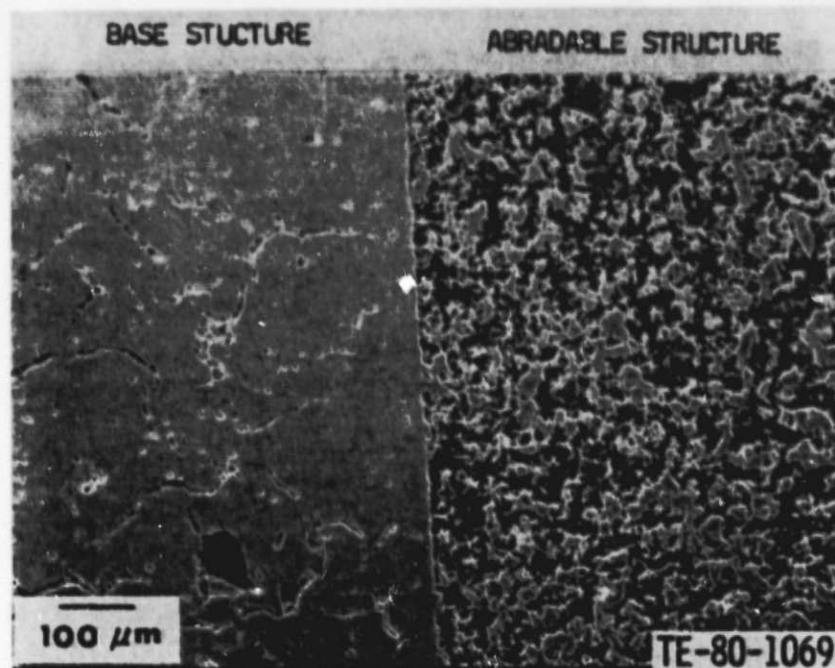
Figure 37.   Si$_{3}$N$_{4}$ SEM micrograph.

Figure 38.   Growth of large silicon nitride grain into fine-grained base.
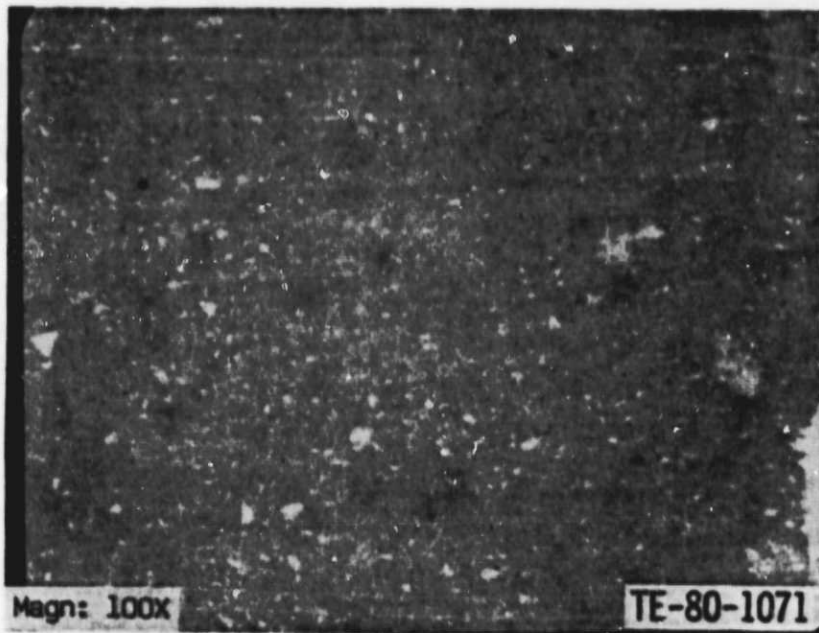
Figure 39.   Coors Coordierite (MAS).
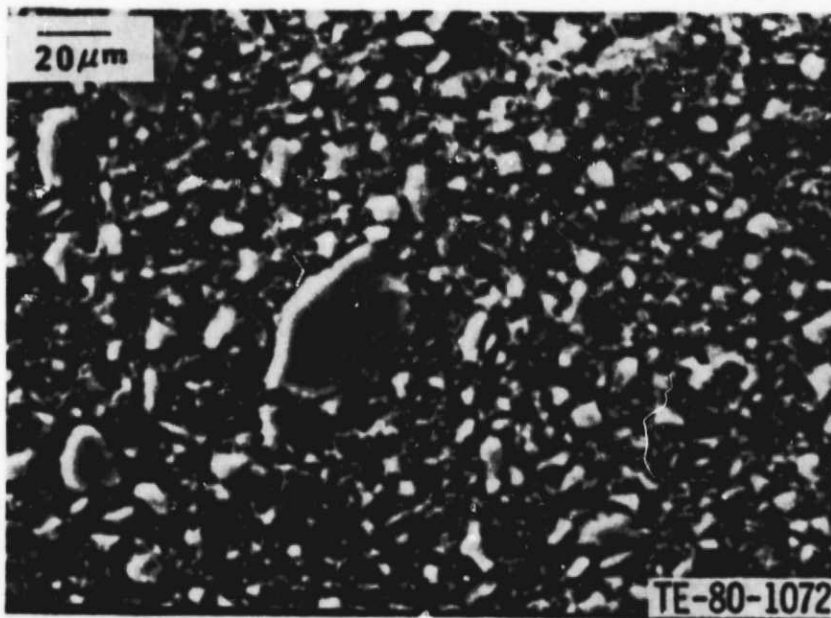
Figure 40.   Coors Coordierite (MAS).

LEACHED
SURFACE
LAYER

Magn: 100X   TE-80-1073

Figure 41.   Pure Carbon silicon carbide sample I-3.

LEACHED
SURFACE
LAYER

Magn: 500X   TE-80-1074

Figure 42.   Pure Carbon silicon carbide sample I-3.
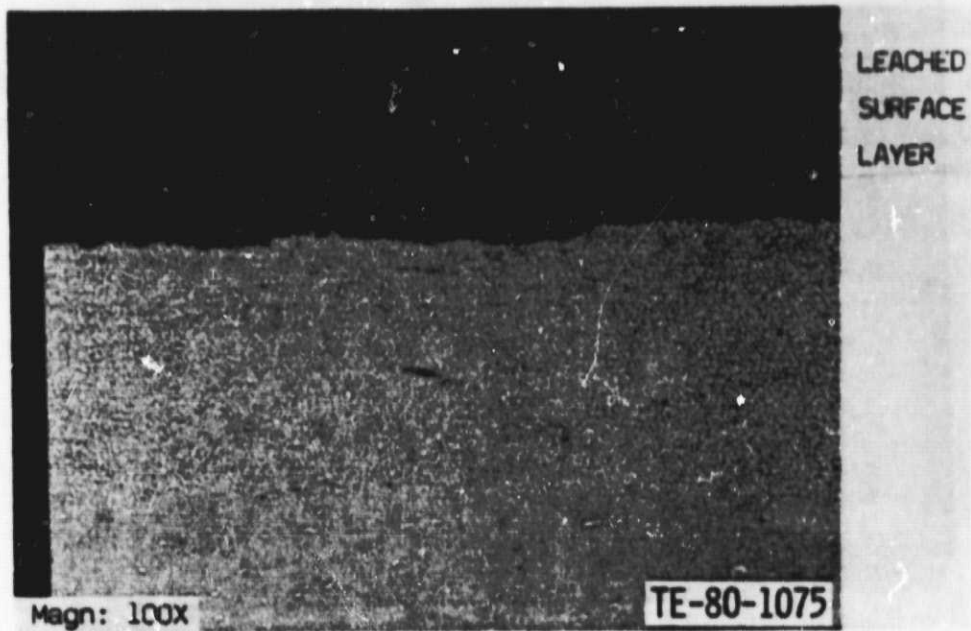
Figure 43.   Pure Carbon silicon carbide sample II-1.
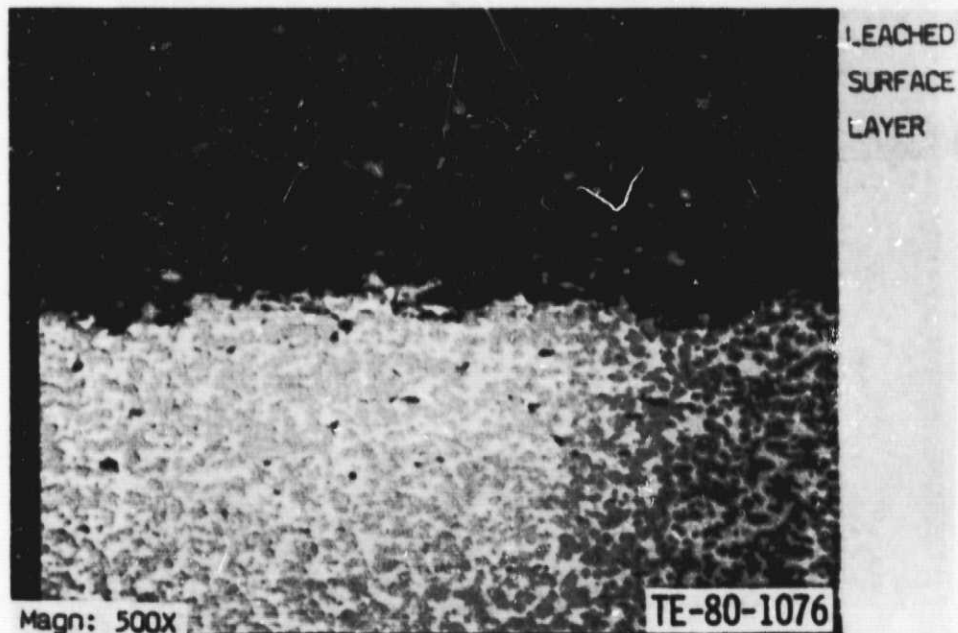
Figure 44.   Pure Carbon silicon carbide sample II-1.

48

free silicon content of the samples investigated and, consequently, possessed the lowest density abradable layer.

Development efforts with abradable material suppliers will be continued with emphasis on formulating abradable shroud materials within the limits established in the samples evaluated to date. In addition, emphasis will be placed upon the reproducibility of the abradable material from sample to sample.

DDA-Developed Materials

Cemented/Laminated Systems

The cemented systems using zirconia felts and papers seemed to be brittle and hard and lack mechanical integrity when compared to the composites fabricated from the zirconia fabrics. Figure 45 is a magnified view of one of the thin ZrO_2- laminated fabric assemblies, which was bonded to a metal coupon and subjected to abradability testing. The rub depth was 0.965 mm (0.038 in.) with an incursion rate of 0.025 mm/s (0.001 in./sec) using a Mar-M246 blade test wheel. The rub track was clearly abraded with very little metallic transfer. The blade tips were in excellent condition and evidenced no surface distress. The ZrO_2 0.75 mm (0.030 in.) thick fabric used in this assembly shows that the fabric reinforced composite withstands well the mechanical abuse of the rub. (Thinner fabrics to be used in future tests should lessen the tendency to exhibit topographic steps in rub pattern.)

Results of erosion testing of a comparison coupon are indicated in Figure 46. Thirty minutes of exposure in the erosion chamber produced no evidence of damage to the laminated structure surface.

Magn: 5X   TE-80-1077
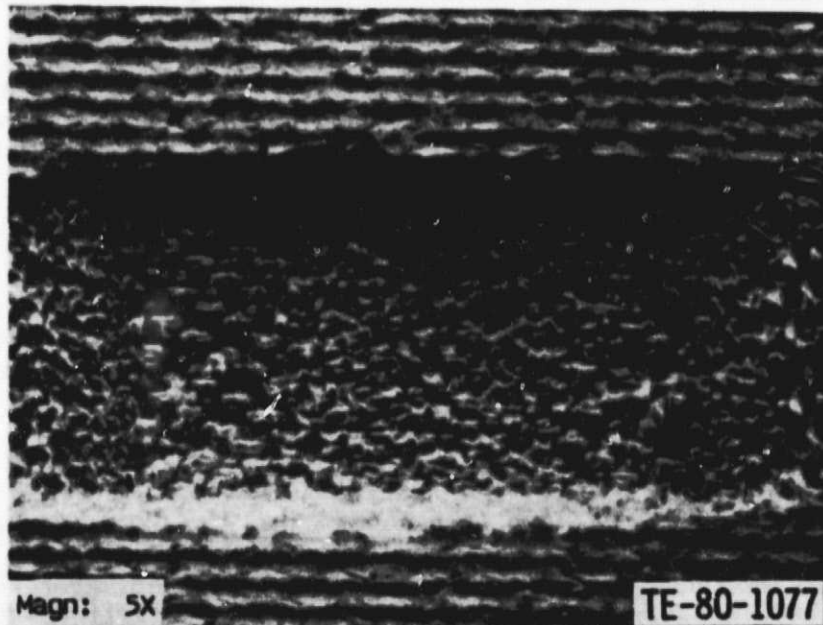
Figure 45. Zirconia fiber system with rub depth of 0.97 mm (0.038 in.)
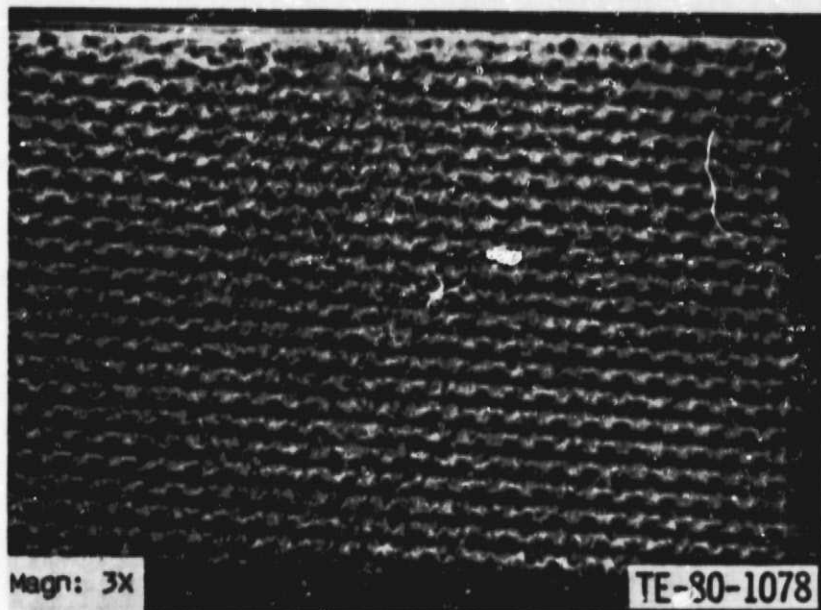
Figure 46. Zirconia fiber system with 30-min erosion and 45-deg impingement.

Sintered Mineral (Ceramic) Compacts

Results of abradability testing of a surface-machined specimen ($ZrSiC_4$) that was rubbed by a Mar-M246 blade tip is shown in Figure 47.

The blade track produced in the abradability test coupon was well defined and free of thermally induced crazing. The blade tips showed no evidence of damage no evidence of damage after the rub incursion to a depth of 0.737 mm (0.029 in.)

Specimen segments have been soaked in water and subjected to thermal shock in a 1038°C (1900°F) furnace with no observed damage. Additional test segments were soaked in JP-4 fuel and thrust into a test furnace. Burning soot was observed, but upon inspection after cool-down, no distress to the material was evident. These results imply that engine hot-starts should not damage the seal material.

Plasma-Sprayed Abradable Systems

Dual-density zirconia coatings have been successfully plasma sprayed on the surface of silicon carbide coupons. The dense ceramic intermediate layer interlocks with the substrate surface to provide a transition layer for the low-density outer layer. The initial coating of Metco 202 NS (yttria-stabilized zirconia) was applied 0.006 cm (0.015 in.) thick, followed by a low-density 0.010-cm (0.025-in.) coating of Metco 202 NS codeposited with Metco 600 polyester powder. The polyester powder "filler" has been used in other DDA abradable seal programs where the polyester has been burned out in a postspray operation.

50

The dual-density coating has been applied to an NC-400 coupon and is shown in Figure 48.
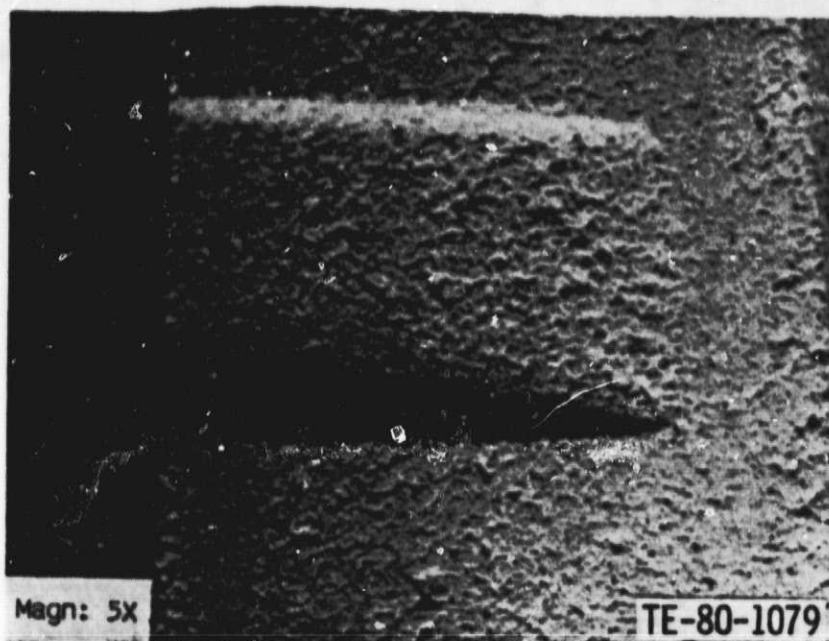
Figure 47. Injection-molded, sintered zirconia silicon oxide ($ZrSiO_4$) with rub depth 0.74 mm (0.029 in.)
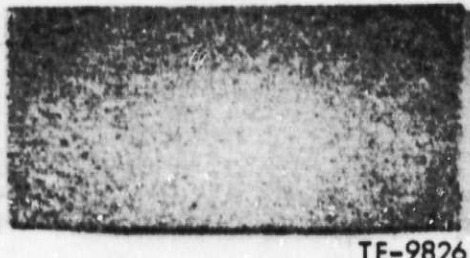
Figure 48. Dual-density zirconia coating on silicon carbide coupon C-7. (1.2X)

A similar dual-density coating was made by substituting mullite ($3 Al_2O_3 \cdot 2 SiO_2$) powder for ZrO_2. Figure 49 and 50 display the rub and erosion tests on the mullite-sprayed specimens. The excessive rub depth of 0.5 mm (0.020 in.) penetrated completely through the abradable layer and into the higher density mullite bond coat and caused slight metallic transfer from the Mar-M246 wheel. Erosion performance of this material was poor; the low-density mullite layer suffered severe erosion from the 30 min dust exposure at 45-deg impingement angle.

TE-80-1080
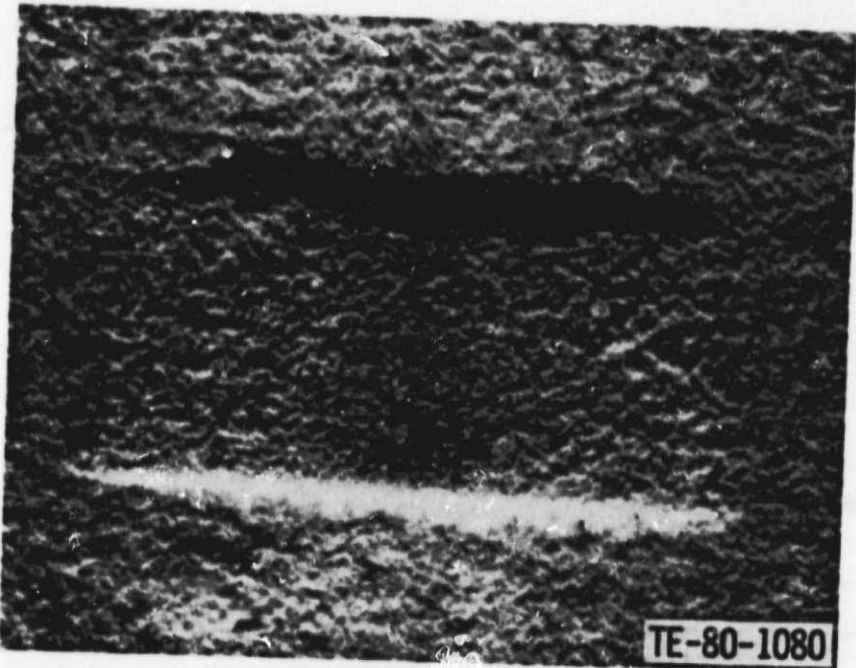
Figure 49.   Plasma-sprayed Mullite on SiC abradability test.   (5X)

TE-80-1081
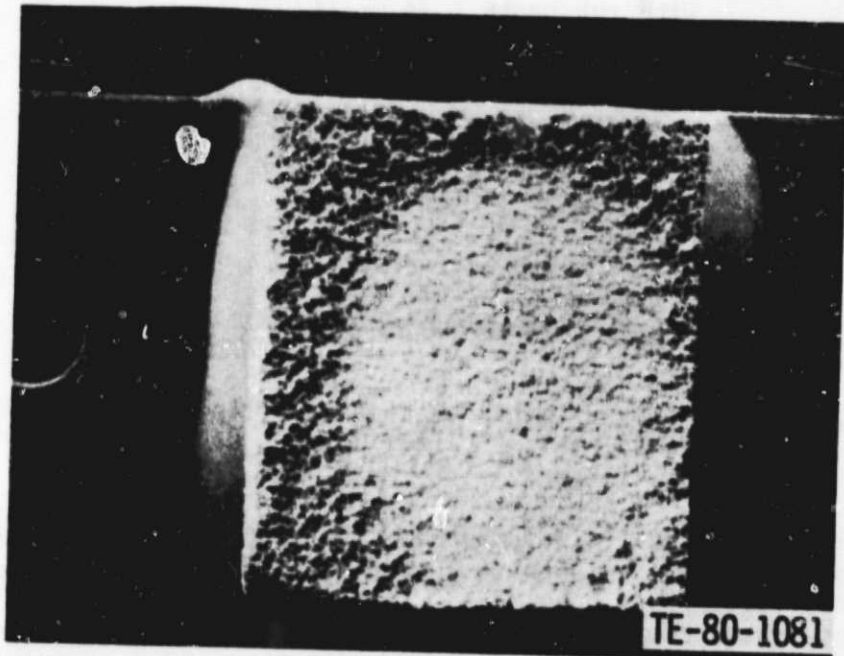
Figure 50.   Plasma-sprayed Mullite on SiC erosion test.   (3X)

52

In an engine test of the plasma-sprayed zirconia/ceramic ecosphere dual-density system, the gasifier nozzle diaphragm for the 1900°F-configuration engine design was selected for evaluation. An abradable coating consisting of Zircoa 8% yttrium-stabilized zirconia cosprayed with ceramic ecospheres was deposited in the blade track. After 9.5 h of engine service, this part was removed and found to have severely worn the blade tips, as shown in Figures 51 and 52 with attendant metallic buildup on the abradable surface as shown in Figure 53. Examination of the abradable surface showed the coating to be extremely hard, approximately R15Y = 74-80. Bench testing of the shroud on the low-speed abradability rig with a Mar-M246-bladed wheel resulted in a very similar metallic deposit being produced as shown in Figure 54. A detailed study of the plasma spray process led to changes in the powder spray rates, spray distresses, and powder feeder system. A new shroud was sprayed with these new parameters and installed on engine C-1 for evaluation in the next reporting period.

Buildup and balance of a ceramic-bladed test rotor system was completed. This rotor, shown in Figure 55, uses the ceramic blading intended for the 2265°F-configuration engine design and will be run in the high-speed/high-temperature abradability testing. A Mar-M246 stylized blade is also available for use in place of the ceramic blades.

NDE DEVELOPMENT AND EVALUATION

Summary

Three techniques--SPAS, SLAM, and high-frequency ultrasonics--are currently under investigation to assess their applicability for characterizing ceramic materials. Recent efforts have concentrated on the SPAS and SLAM techniques.
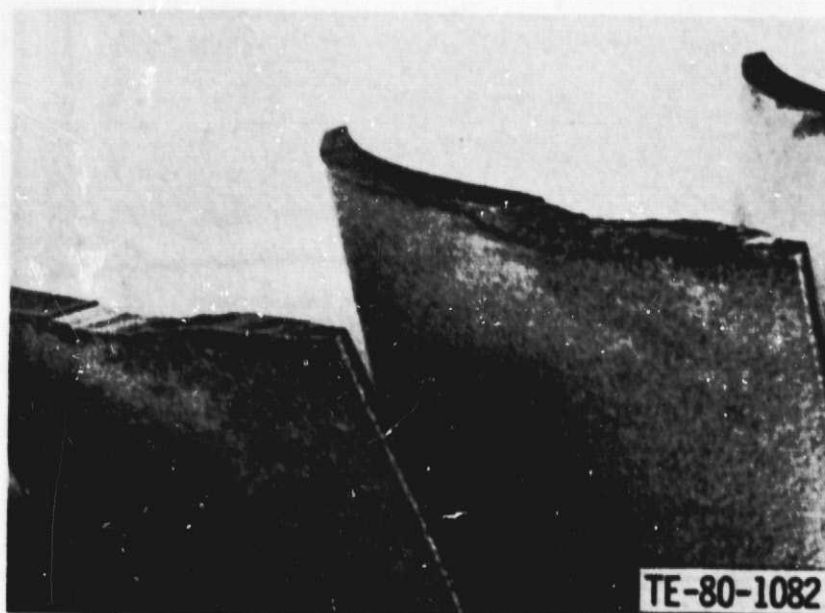
Figure 51. Worn blade tips--CATE test.

53

Figure 52. Worn blade tips--CATE test.
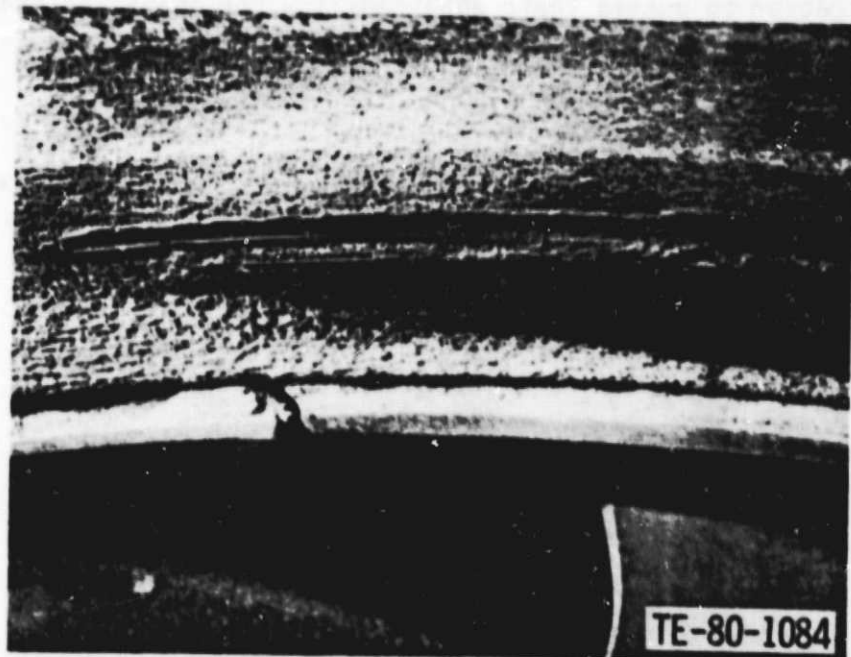
Figure 53. Plasma-sprayed gasifier shroud--CATE test, engine rub. (3X)

54
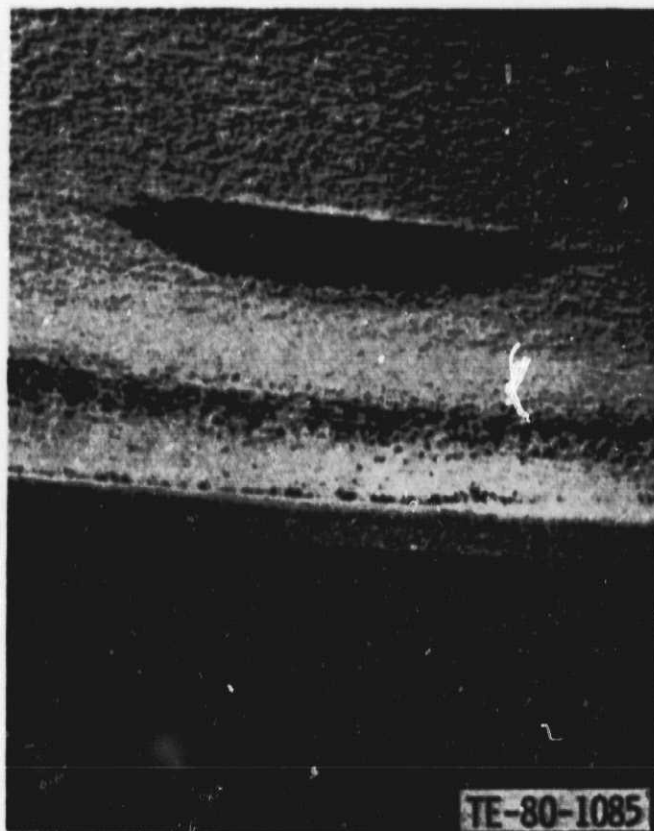
Figure 54. Plasma-sprayed gasifier shroud--CATE test, rig rub. (3X)

Experimental experience gained during early work at Gilford Instruments Laboratories Inc, was used to design and assemble, during this reporting period, a laboratory PAS set-up. Both simulated crack-like flaws, and small pores have been readily detected in alpha silicon carbide using this new PAS arrangement.

Preliminary work using the SLAM technique in the dark field mode has shown that simulated cracks (hardness indents) are readily detectable. Furthermore, certain other types of natural flaws can also be detected. It is concluded that both techniques offer real potential for both detecting and characterizing strength-controlling flaws, and that the additional work needed to quantify key detection parameters should be undertaken.

Objective

The objective of this task is to develop one or more NDE techniques capable of detecting and characterizing critical fracture-controlling flaws in silicon-based structural ceramic materials. Effective flaw detection can improve process control by eliminating the strength-limiting defects and assisting in establishing as probabilistic accept/reject criteria for the qualification of ceramic components.

TE80-1086
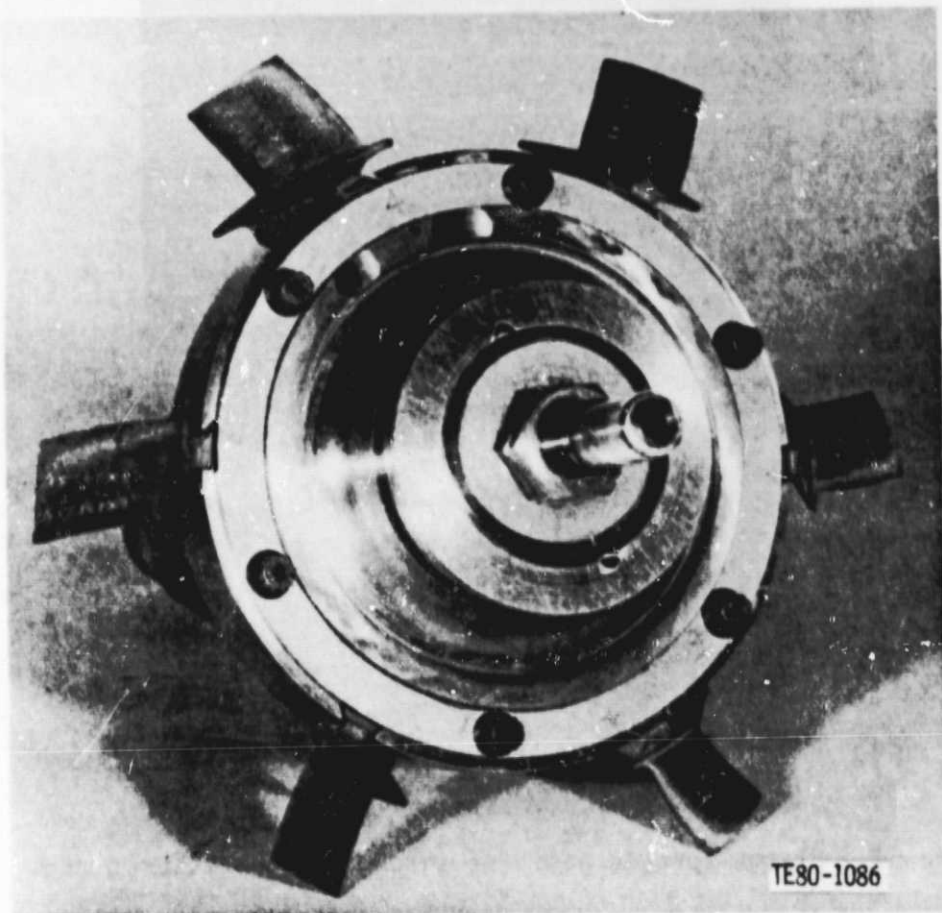
Figure 55. Ceramic bladed abradability rig test rotor.

Three techniques (reflective ultrasound, SPAS, and SLAM) were identified (NASA CR-159865) to have the sensitivity and resolution required for effective flaw detection. The following paragraphs describe the progress made in the development of these techniques during this reporting period.

Discussion

Scanning Photoacoustic Spectroscopy (SPAS)

To establish the feasibility of SPAS to detect surface and near-surface flaws, an experimental study was initiated at Gilford Instruments. This study was conducted on simulated surface flaws (Knoop indentations). Initial results indicated that this kind of tight surface defect could be readily detected.

Because of this initial success and in view of the extensive data base needed to reliably establish the detection sensitivity of this technique to a wider range of flaw types, it was decided to establish an in-house capability to further study and implement the SPAS technique. Subsequent sections review the final phases of Gilford work and initial phases of the DDA work.

Preliminary Study

Two additional specimens were evaluated at Gilford using the SPAS flaw detection system described in NASA CR-159865 (see p. 142). One specimen was of reaction-bonded silicon carbide and the other of densified silicon carbide (NC 430). Both specimens, 12.7 x 6.35 x 1.5 mm (0.5 x 0.25 x 0.06 in.), had artifically induced flaws (Knoop indentations) intended to simulate surface cracks. The specimens were scanned perpendicular to the major axis of each flaw.

Figures 56 and 57 show the resulting SPAS along with the SEM micrograph of the detected flaws. The photomicrographs of the polished surfaces of reaction-bonded and NC 430 did not reveal any apparent radial cracks at the surface enamating from the contact zone. Indenter induced surface spalling was observed only in reaction-bonded SiC. The length of the indentations was 175 μm for reaction-bonded SiC and 150 μm for NC 430. The surface finish of both the specimens was 1-2 rms.

The SPAS signals from the indentations was larger in NC 430 than in reaction-bonded SiC, even though the diffusivity of NC 430 is greater than in reaction-bonded SiC. It is hypothesized that the indenter-induced subsurface damage in NC 430 is substantially more than in reaction-bonded SiC and has a major effect on the SPAS signal. The SPAS signal is dependent on the spatial average surface temperature of the solid, which is governed by the diffusive nature of the material at the point of interest. It is, therefore, believed that subsurface microcracking in NC 430, which has bimodal grain size distribution, is more than that in reaction-bonded SiC. These microcracks internally reflect the optical light more in NC 430 when compared to reaction-bonded SiC, and thermally have a localized insulating effect to give a higher photoacoustic signal.

Follow-on Effort

The experimental arrangement established at DDA is shown in Figure 58. It consists of a 2.0-W argon laser. The laser light is modulated by a mechanical chopper and guided by two mirrors and a beam steerer toward an objective lens, which focuses the light onto the specimen surface. The focal length of the objective lens is 25.4 mm (1 in.). The specimen is positioned in the PAS cell, which is mounted on a two-dimensional translational stage. The entire specimen/cell assembly is scanned in the X-direction and incremented manually in the Y-direction. The minimum scanning speed is 250 μm/s with an incremental resolution of 25 μm. The photoacoustic signal is detected by a minature microphone that is amplified by a lock-in amplifier and displayed on an X-Y recorder. The entire system is arranged on a Newport Research honeycomb suspension table. This table is supported by four vibration isolation mounts to eliminate any noise resulting from floor motion that might contribute to the PAS signal.
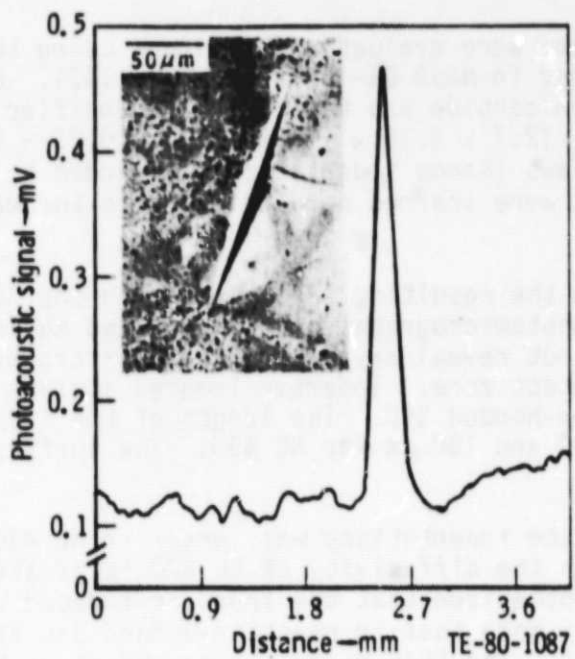
Figure 56. Photoacoustic signal from a microhardness indentation in densified silicon carbide (NC 430).
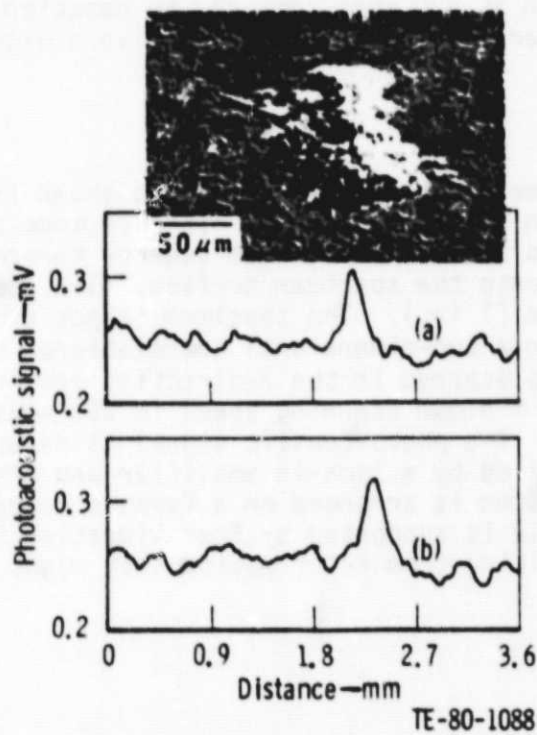
Figure 57. Photoacoustic signals from successive scams of a microhardness indentation in reaction-bonded silicon carbide.

Figure 58. Experimental set-up at DDA of scanning laser photoacoustic
spectroscopy for flaw detection in ceramic materials.

A modular photoacoustic cell was designed and fabricated at DDA for the char-
acterization of standard MOR specimens. A schematic of this cell is shown in
Figure 59. The cell has three parts: an aluminum outer shell, a lucite in-
sert with a cavity within which to place the MOR specimen and an aluminum lid
with a 25.4 mm (1 in.) diameter window of optically polished fused silica.
The lid is attached to the outer shell with three allen screws. An O-ring is
used in the top lid to make an airtight seal. This seal prevents the loss of
the photoacoustic signal. The air gap between the surface of the specimen and
the window is 0.5 mm (0.02 in.). The total volume of the air within the cell
is approximately 0.2 cm^3 (0.01 in.^{3}). The microphone is located in the
insert as shown.

Initial work has concentrated on studying alpha SiC, the primary blade materi-
al. A MOR specimen of this material, 5.08 x 0.635 x 0.317 cm (2 x 0.25 x
0.125 in.), was polished to surface finish of 6 rms. Two 2.5 kg (5.5 lbm)
knoop microhardness indentations were placed on the polished surface to eval-
uate the sensitivity of the experimental arrangement. The indenter-induced
damage was not removed.

A parametric study was conducted to obtain optimum scanning conditions. Fig-
ure 60 shows a scan of the area containing two hardness indentations. Test
parameters used for this mapping were laser power level-- 600 mW, modulation
frequency--200 Hz, scanning speed--250 μm/s, and focal spot size--less than
30 μm. The specimen was incremented 25 μm after each scan. The accompanying
pictures show the microstructural features corresponding the observed SPAS
signal peaks. Note that features in addition to the indentations are readily
detected. For example, at location 2, there is a single peak present only in
a single pass. This peak arises from a small pore where major surface dimen-

PAS CELL

LUCITE
INSERT

OUTER
SHELL

QUARTZ WINDOW

TOP
LID

'O' RING

MICROPHONE
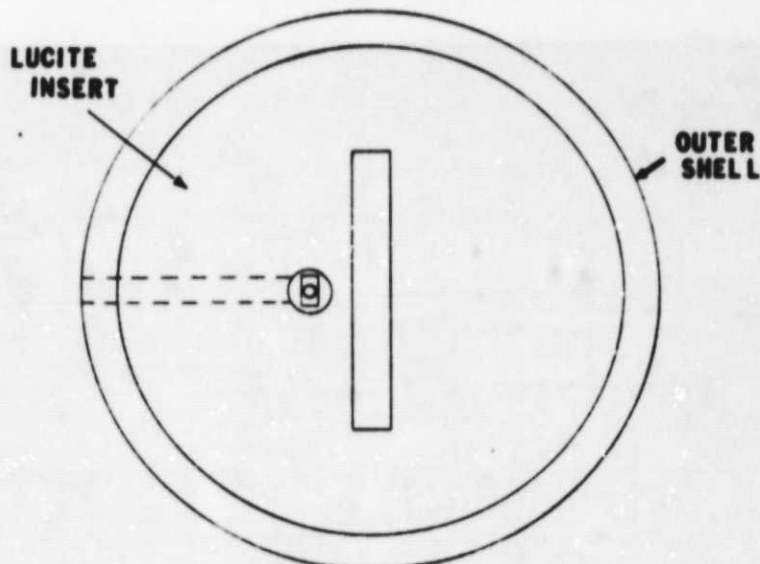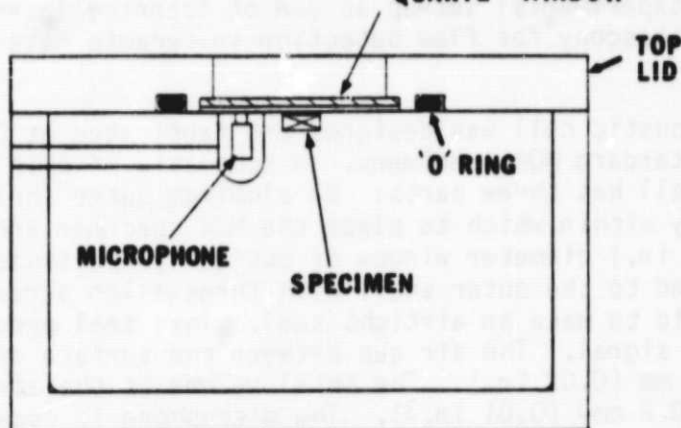
SPECIMEN

SECTION VIEW

TE-80-1090

Figure 59. Schematic of photoacoustic cell for MOR specimen.

sion is 30 μm and where depth is estimated to be about 6 μm. At location 1 a pair of peaks originate from a pair of pores 20 μm in diameter and 6 m in depth. These two pores are separated by 25 μm. Finally, the pair of relatively large knoop indentations with major axis of 148 μm was detected in five successive scans.
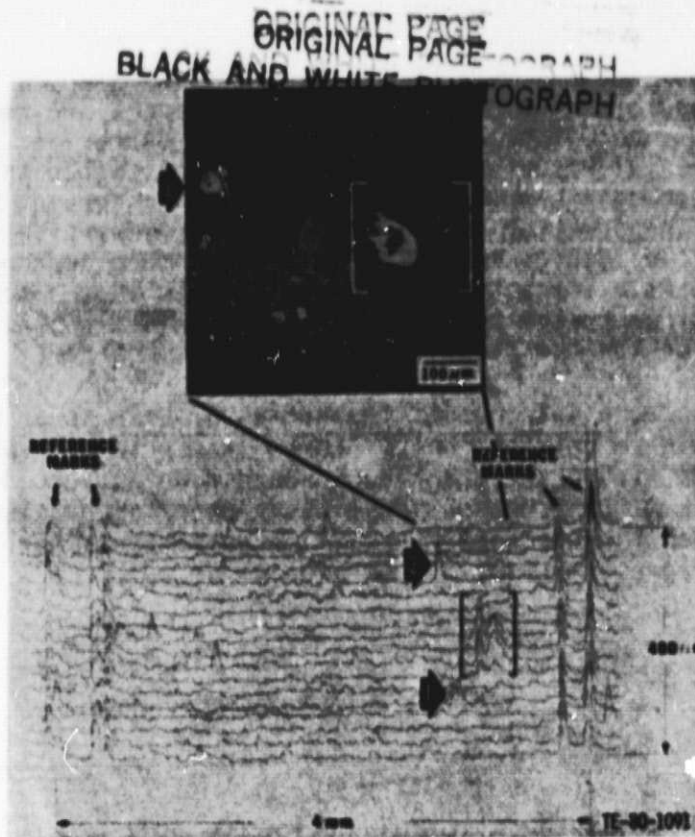
Figure 60. Photoacoustic signals from microhardness Knoop indentations and natural surface pores in alpha SiC.

The reproducibility of detecting all of the flaws both in terms of their SPAS signal and location was excellent. The observations made here confirm that the focal spot size of the laser beam is indeed less than 30 μm. This initial study also shows that both the detection sensitivity and spatial resolution of SPAS for polished alpha silicon carbide is 20 μm for naturally occurring surface pores at 250 μm/s scanning speed. It should also be noted that the Knoop indentations were detected over a length of 125 μm, which is within one focal spot diameter of the laser beam when compared to the measured length of 148 μm. There is therefore an excellent quantitative correlation between the major surface dimension of the flaw and distance up to which it is detected by SPAS.

Scanning Laser Acoustic Microscopy (SLAM)

Acoustic microscopy is a technique for imaging localized changes in the elastic properties of materials. The physical properties that govern sound propagation are modulus and density. The variability in these two properties directly affects the acoustic properties (attenuation, velocity, and impedence) of the material. The variation in the acoustic properties changes the microstructural insonification behavior of the specimen. Microstructural variations and presence of flows (voids, inclusions, and cracks) both in the bulk and on the surface of the specimen are observed as perturbations in the transmitted acoustic amplitude. The sensitivity and resolution capability of the technique depends on the relative acoustic properties of the parent material and the anomaly.

To establish the feasibility of this technique to detect and resolve defects an experimental study was initiated at Indianapolis Center for Advanced Research (ICFAR). Initial results were encouraging and showed that small bulk flaws could be detected in sintered silicon carbide in through transmission. However, this mode of operation was found to be less sensitive to surface flaws. The dark field imaging mode was found to be more appropriate for studying surface flaws. Consequently, recent efforts have concentrated on applying this technique to the study of surface flaws in alpha SiC. Subsequent paragraphs describe the technique and results obtained.

In the dark field mode, a specimen is insonified by bulk shear waves at a pertinent incident angle to generate bulk skinning waves on the specimen surface. These waves interact with a surface flaw and are mode converted to produce a reflected surface wave. These two waves interface coherently to produce ripple pattern, which is detectable in the acoustic microscope. Figure 61 shows a schematic representation of this phenomenon.

Scanning laser acoustic microscopy

Coherent ripple pattern → Defect — Top

Dynamic ripple (scattered surface wave)

Dynamic ripple (bulk shear wave) → Defect — Side

Transducer

TE-80-1092
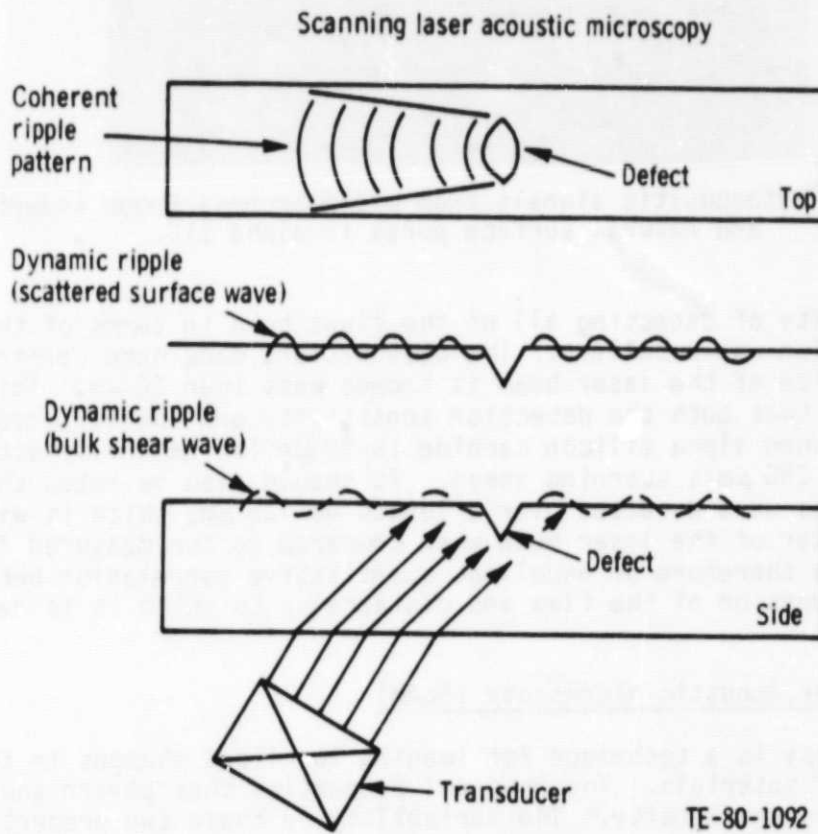
Figure 61. Schematic showing resultant interference pattern between bulk shear (skimming) waves and reflected surface waves.

The dark field condition is achieved by turning the frequency of the local oscillator within the microscope so that reflected surface waves are detected by the scanning laser system at about the same amplitude as the bulk wave. Because both of these waves produce surface ripples (Figure 62) and propagate with different acoustic velocities, a different frequency (spatial) is observed where the surface waves are coherent. One very useful feature of this detection method is the angular dependence of the coherent wave on the alignment of the flaw, e.g., a crack with respect to the incident bulk wave. Although the crack may be below the resolution limit of the system, the angular charactersitic of the interference pattern may provide information on the dimensions of the crack producing the surface wave.

Figure 62 is an example of a coherent ripple pattern generated by a pair of hardness indents on a polished specimen of alpha SiC. Note that this paired defect cannot be resolved but that its presences is easily detected. These indents are the same ones that were examined by SPAS and appear in Figure 60. This very strong constructive interference pattern results from the interaction of the scattered surface waves from each defect with the incident wave. The extent of reinforcement depends on the distance between the two scattering centers.

The intent of the initial studies was to establish the detectability of tight crack-like defects. Specimens of alpha SiC were polished with 6 μm diamond. Microhardness indentations were placed on the polished surfaces using loads of 2.4 and 1.4 kg (5.3 and 3.1 lbm). The exact positions of each indentation with respect to reference marks was then determined. Finally, the indentation itself was removed by further polishing leaving what was hoped to be a tight penny-shaped crack.
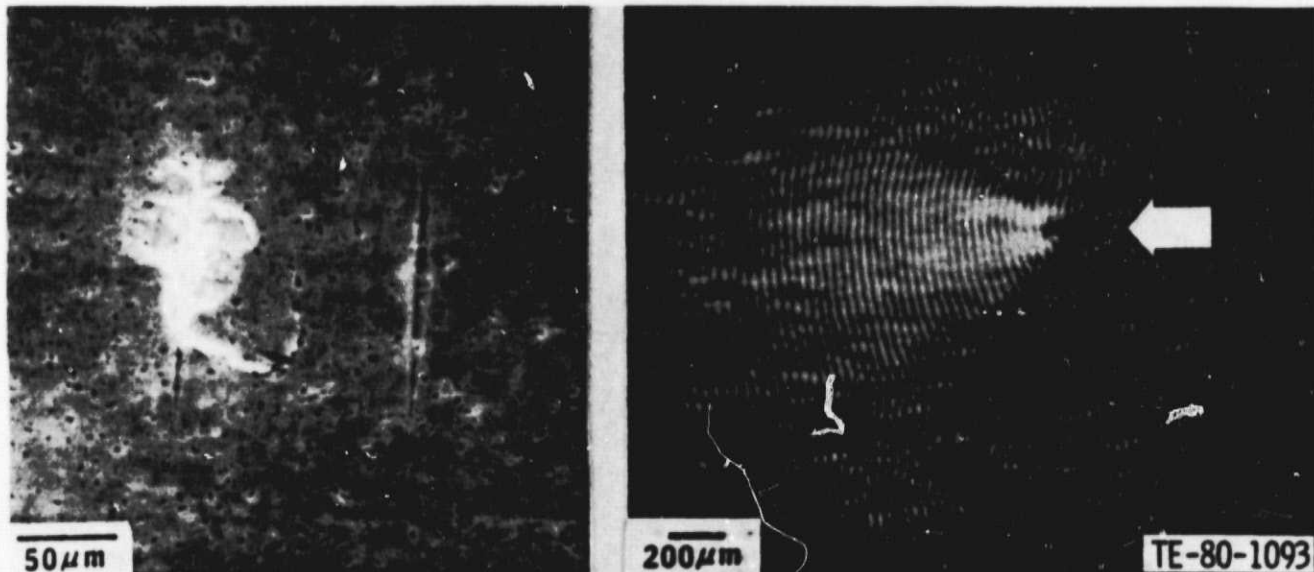
Figure 62. SEM and dark field acoustic interprogram of two microhardness indentations in alpha silicon carbide.

63

The two optical micrographs in Figure 63 show an indentation before and after polishing and one scanning electron micrograph of the final defect. The location of the indentation after removing the surface damage was revealed using a mapping technique with the aid of a transparent film before and after removing the indenter-induced surface damage. Figure 64 shows that subsurface microcracks (lateral) propagating parallel to the major axis of the indentation were present. Such microcracks have been observed by other workers both as a result of the process of indentation as well as the grinding/polishing operation. Figure 65 shows the dark field image generated by this flaw. The microscope seemed to be detecting some feature of this defect, which differed from others surrounding it. The SEM picture clearly show large number of micropores all around the indentation. It is believed that the combined effect of

Figure 63. Optical and SEM micrographs of 2.4 kg (5.3 lbm) Knoop microhardness indentation.

Figure 64. SEM micrograph showing microcracks in alpha silicon carbide specimen after polishing.
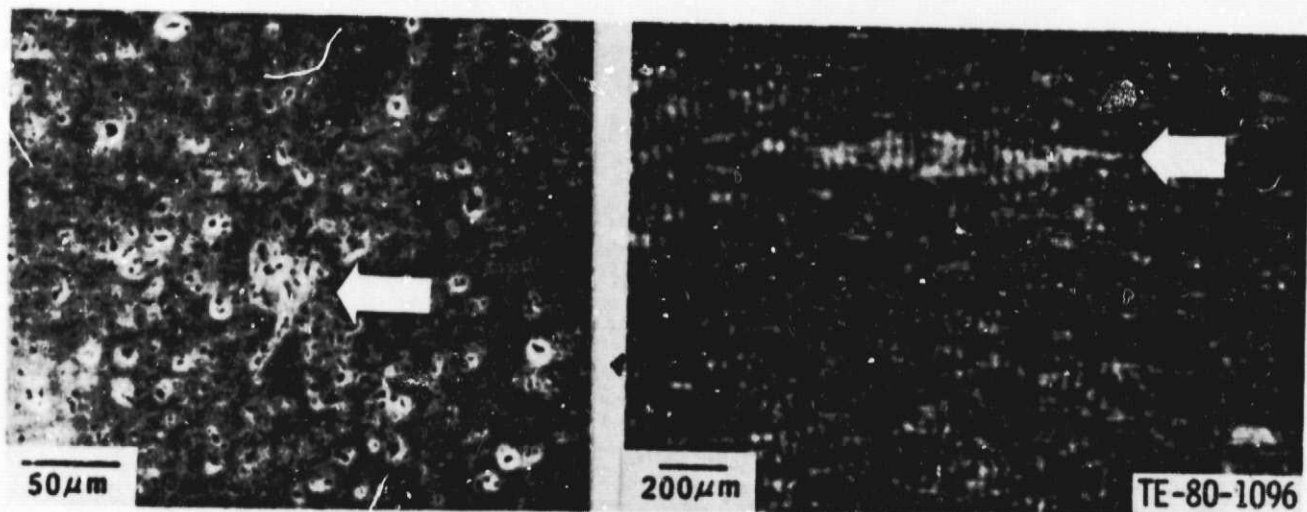
Figure 65. SEM and dark field acoustic interferogram from a microhardness indentation after removing surface damage.

65

both the microcracks and width (~1 μm) of the indentation is probably respon-
sible for such a distinguishable feature. In any event, the microscope in the
dark field mode appears to find flaws much below the expected detection limit.

This particular MOR specimen was tested in three-point bending with the inden-
tation at the peak stress location. The fracture strength was 206.8 MPa (30
ksi). Figure 66 shows an optical micrograph of the two mating tensile sur-
faces and a SEM photograph of the fracture plane at the origin of failure.
Failure originated from the polished indentation.
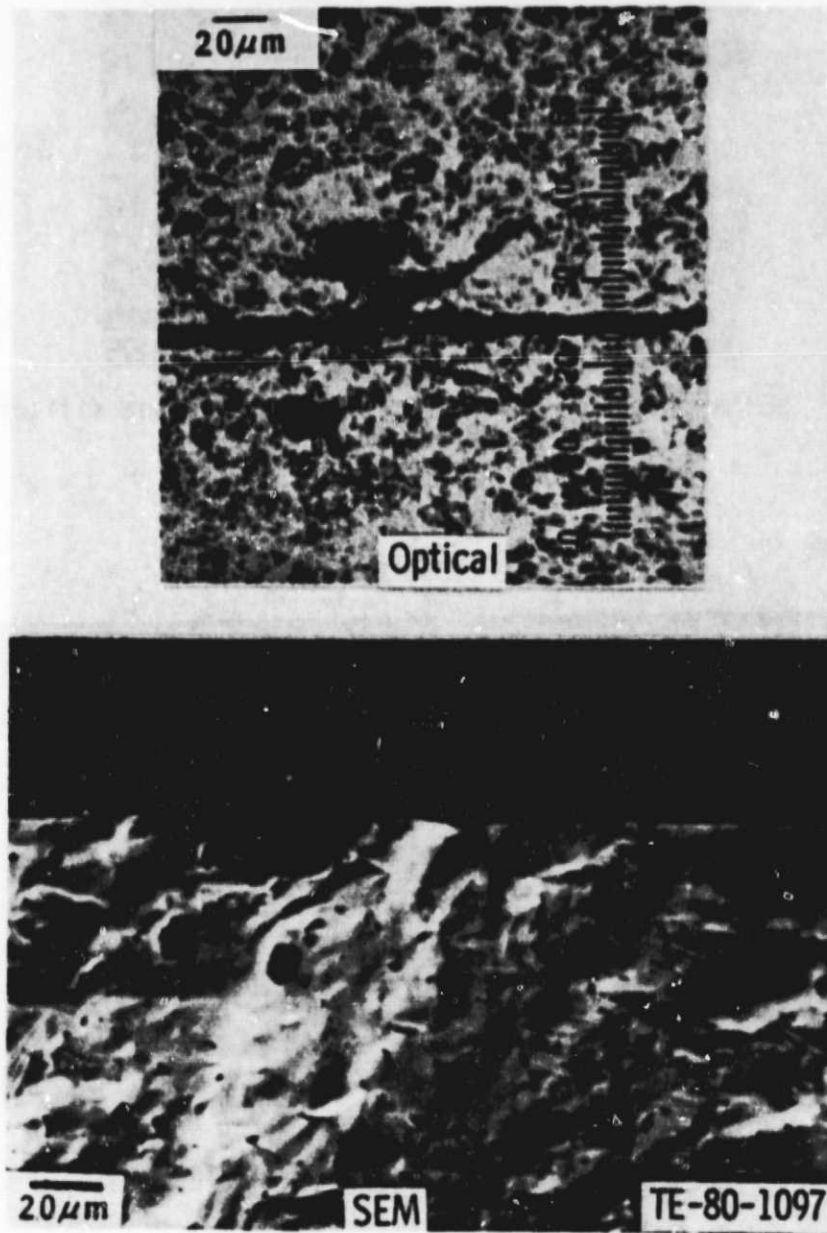
Figure 66. Micrographs of fractured alpha silicon carbide specimen with
a microhardness indentation.

A second specimen with a 1.4-kg (3.1-lbm) load Knoop indentation was evaluated after removing the surface damage. In addition to detecting the indentation, a naturally occurring flaw was also detected as shown in Figure 67. Both the optical and SEM analysis confirmed it to be pore. No other surface feature was detected. The bar was the tested in three point bending to determine the subsurface nature of the flaw. Figure 68 shows the SEM micrographs of two mating fracture surfaces. The fracture origin was positively identified as the detected pore. Fracture stress was 389.5 MPa (56.5 ksi). Depth of the bore was measured to be 32 μm and width 85 μm. (Presuming that this flaw acts like a sharp elliptical crack, the critical stress intensity factor is computed to be 4.37 MN/mm$^{3/2}$ (3.97 ksi/in.$^{3/2}$). This is in good agreement with previously measured values obtained on double torsion specimens.)

It is concluded from this preliminary study that SLAM in the dark field mode is capable of detecting tight surface cracks and small surface pores. Since the technique is new, its detection and resolution limits are not known at this time. Future work under the CATE program is directed toward determining the limits of detectibility using simulated surface flaws.

CERAMIC MACHINING DEVELOPMENT

The machining of fired ceramic components during this reporting period has provided verification of processing techniques and definition of the best tool selection.

The main effort in machining development has been directed at defining the potential of creep feed grinding accurately. Efforts to improve the efficiency of the ultrasonic machining process have been made.
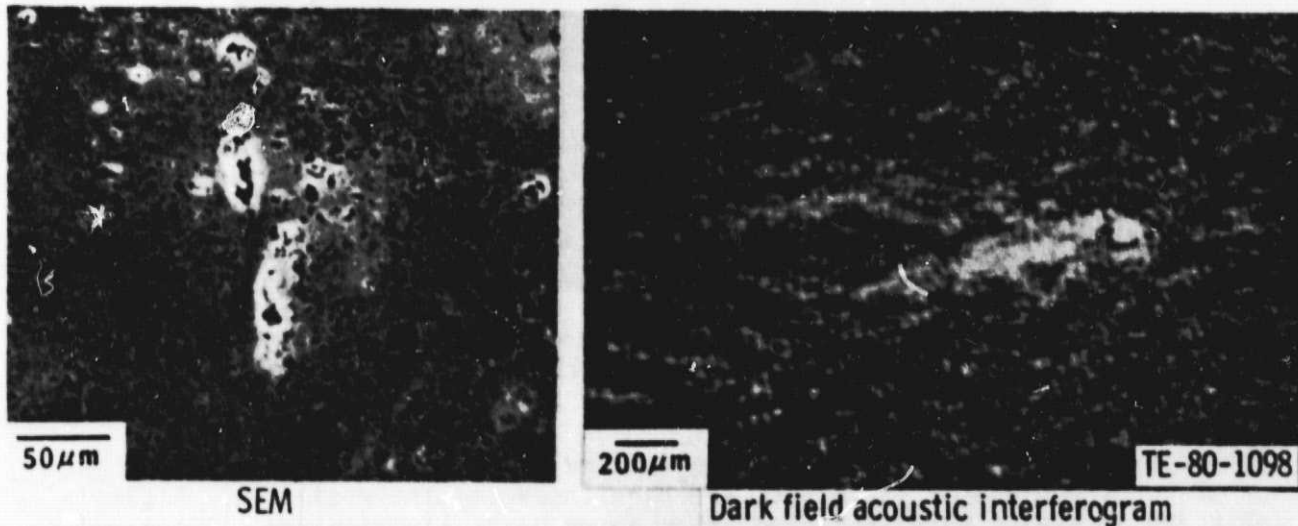
Figure 67. Micrographs of a natural flaw (pore) on the surface of alpha silicon carbide.
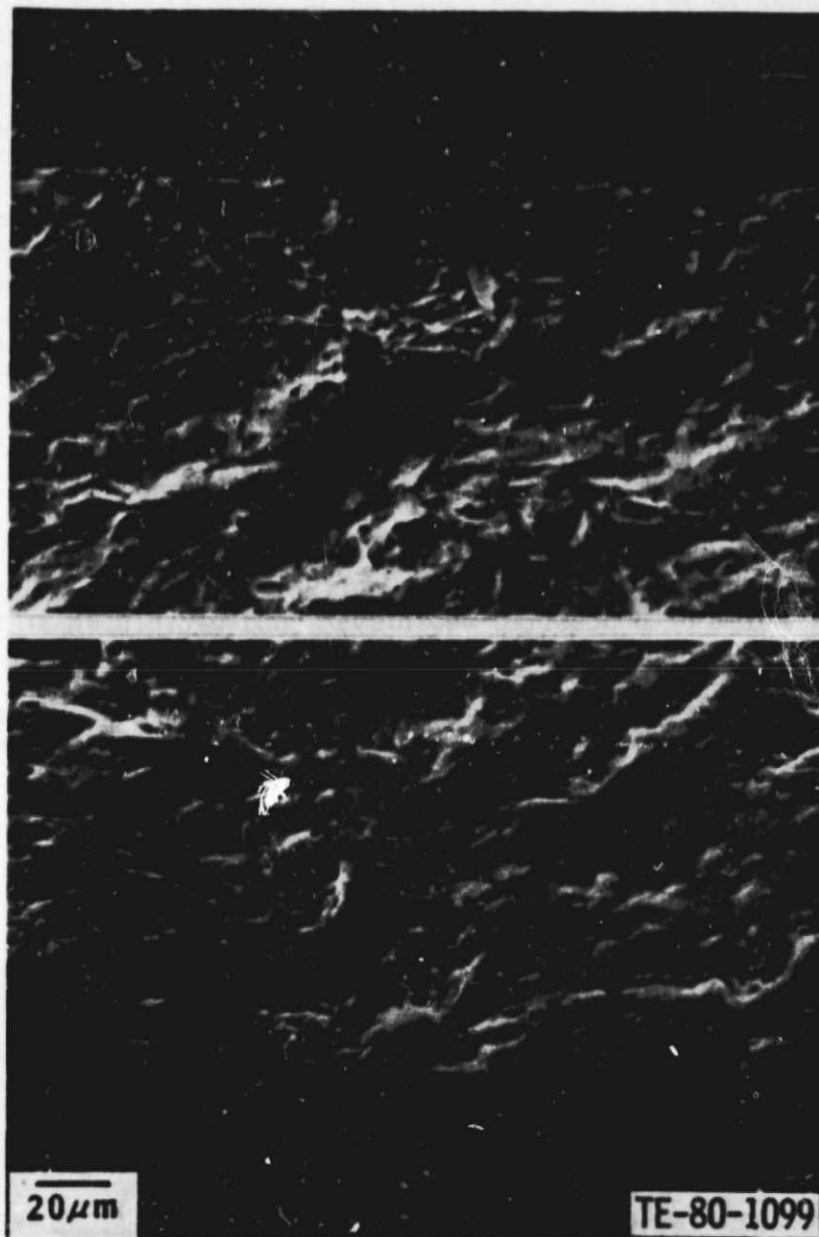
Figure 68. SEM micrograph showing failure origin (pore)
in alpha silicon carbide.

The study of creep feed grinding involves the machining of the dovetail shape
of 30 turbine blades. The blades are then inspected and evaluated. A sample
of these 30 blades were inspected after being partially machined. Two samples
had Zyglo indications that indicated the possibility of a faulty fixture set-
up. The fixture set-up has been modified and the machining is to be resumed.
Additional evaluation will be done after all of the machining is complete.

68

The efforts to improve the ultrasonic machining process have been directed at two areas--machining and tooling preparation. Considerable improvement in the machining times has been made by the machine set-up and fixturing. These changes were made to reduce the time required in handling the cutting slurry.

The efforts to reduce the tooling preparation times have had only limited success. Tooling designs that are mechanically joined to the toolholders are being studied. These designs would eliminate the need to braze tools to toolholders and thereby save time. New tool designs have shown very short effective work lives.

IV. CERAMIC TURBINE COMPONENTS

INTRODUCTION

Ceramic turbine component development continued with the assessment of the gasifier nozzle ceramic component at a 1900°F-configuration. This assessment included rig and engine testing at 1038°C (1900°F). The components tested were the gasifier nozzle vane and the turbine tip shrouds. The 2070°F-configuration design and development effort continued with the completion of the revised design analysis of the ceramic vane and outer vane support ring, process and component fabrication development, and component rig testing of the ceramic gasifier nozzle assembly.

Ceramic gasifier turbine blade developmental effort continued for the 2070°F-configuration with design and analysis process development work, and spin testing of the available components. Process development work was completed at Carborundum involving silicon carbide material and blade process development work was initiated at GTE Sylvania involving silicon nitride material. Spin testing included test coupons made from silicon carbide and silicon nitride to evaluate blade attachment and prototype ceramic blades from Carborundum.

Fabrication of the gasifier turbine plenum continued at both Norton and Carborundum. Norton has produced and shipped one plenum, and Carborundum (CBO) is currently involved with further process development work. The conceptual design of the ceramic combustor was initiated, and a layout of the mechanical design features has been completed.

GAS TURBINE NOZZLE

Assessment of Ceramic Components at 1038°C (1900°F)

Thermal Shock Rig Testing of 1900°F-Configuration Gasifier Nozzle Ceramic Components

Burner rig testing of 1900°F-configuration ceramic nozzle components consisted of building and testing two sets of 1900°F ceramic vanes made from material variations developed in Task IV of Carborundum's process development subcontract. The test consisted of five thermal cycles from 260°C (500°F) to 1038°C (1900°F) with a peak overshoot of 1177°C (2150°F). To expose the nozzle equally to the hot spots in the burner pattern, it was rotated 180 deg and cycled five more times. Those parts passing a posttest Zyglo inspection were qualified for use in engine testing.

The material variations in the vanes tested (previously discussed in DDA EDR 9951) were a Bimodal grain size for the first set of 10 vanes and a high purity silicon in the siliconizing cover mix for the second set of 10 vanes. There were no failures for the bimodal vanes and only one failure for the high-purity silicon vane.

Engine Testing of 1900°-Configuration Ceramic Components

Two CATE engines, C-1 and C-4, were used this period to test 1900°F-configuration ceramic components. The ceramic vanes in engine C-1 accumulated 152 hr, including 63.2 hr in a vehicle. In the initial build of C-4, an attempt was made to evaluated a lithium alumina silicate (LAS) turbine tip shroud.

During operation of engine C-1, the metal nozzle assembly progressively distorted causing four ceramic vanes to be mechanically loaded. The high time first-generation Carborundum vane (over 1500 hr), two second-generation Carborundum vanes (over 850 hr), and one fourth-generation Carborundum vane (over 300 hr) were chipped when removed from the nozzle. It was not determined if the vanes were chipped before removal from the nozzle or if the removal process resulted in the chipping. The chipped vanes were replaced by vanes that had been engine tested in previous builds. The entire set was installed in a new metal nozzle assembly, and the engine was used for development testing and vehicle demonstration.

2070°F Gasifier Nozzle Design and Development

Summary

The results of the design and development effort on the 2070°F-configuration gasifier turbine nozzle for the current reporting period has resulted in a full ceramic 2070°F-configuration nozzle assembly being successfully qualified and ready to begin engine testing. This effort included completion of a revised design analysis on the ceramic vane and outer vane support ring, ceramic process and component fabrication development, and component rig (thermal shock, cold flow capacity, and vibration) evaluation. Engine testing and additional rig component qualifica- tion are the activities planned for the next reporting period.

Previous progress reports have documented the initial ceramic component probability of survival analyses. A summary of the results of these analyses appears in Table VI.

In the current reporting period, several design modifications to the vane and the outer vane support ring were analyzed and found to have revised the component probability of survival. The survival rate for the vane was recomputed from 0.98592 to 0.98281, and that for the outer vane support ring was raised from 0.76317 to 0.99967. Although the calculated probabilities of survival of the vane and two support rings do not meet the design production-based goal, they are more than sufficient to operate the CATE development program.

Objective

The objective of the 2070°F-configuration design analysis is to predict the probability of survival of the ceramic gasifier nozzle components that are subjected to the most severe thermal transients of a typical vehicle operation schedule. This predicted probability is compared to the development goal of $P_s = 0.9$ and against a production warranty cost-based probability design goal as presented in Table VI. This production warranty cost-based probability is different for each component depending on the estimated number of failure sites per component.

72

TABLE VI. SUMMARY OF GASIFIER TURBINE NOZZLE CERAMIC COMPONENT ANALYSES

Component	Calculated probability of survival*	Maximum principal stress, MPa (ksi)	Thermal transient generating stress	Design goal**
Vane	0.985918	368.18 (53.40)	Heat-up, dynamic braking to 100% power	0.999974
Shroud	0.999999	77.70 (11.27)	Heat-up, dynamic braking to 100% power	0.999941
Inner vane support ring	0.998901	114.04 (16.54)	Heat-up, dynamic braking to 100% power	0.999757
Outer vane support ring	0.762592	381.62 (55.35)	Cool-down, 85% N_G to dynamic braking	0.999757

*Based on a reaction-sintered silicon carbide material strength represented by a MOR of 366.80 MPa (53.2 ksi), m = 8.0.
**Design goal is based on production reliability and warranty requirements.

The objective of the work for this specific work period was to predict a new probability of survival rate for the revised design and analysis procedure defined in the approach.

Discussion

Vane

The initial analysis of the vane was made with insulated vane platforms (both inner and outer) as a worst case. Subsequent secondary flow analysis has determined that from 0.4 to 1.4% of the primary gas flow can pass over just the outer vane platform as shown in Figure 69. This flow does not result in an insulated vane platform. Based on these flows, new heat transfer coefficients on the vane platform ends were determined, and the two transient heat transfer conditions were reanalyzed. The rest of the procedures in the analysis were the same as used initially.

Table VII presents the results of the original analysis and the revised analysis. The effect of secondary flow heating the vane platforms was to reduce the peak stress from 368.2 MPa (53.4 ksi) to 316.8 MPa (46.0 ksi). The stress field for the revised case is redistributed over a larger volume with the net result that the Weibull probability of survival does not change significantly, 0.98592 for the original and 0.98281 for the revised analysis. The overall result is little change in probability of survival, but the analysis boundary conditions are more realistic.

73

TABLE VII. SUMMARY OF 2070°F-CONFIGURATION VANE PROBABILITY OF SURVIVAL
(Transient analyzed rapid heat-up from 500 to 2070°F design point conditions.)

Boundary conditions	Peak stress, MPa (ksi)	Probability of survival of a single vane
Original analysis with no vane platform heat transfer	368.2 (53.4)	0.98592
With vane platform heat transfer	316.8 (46.0)	0.98281
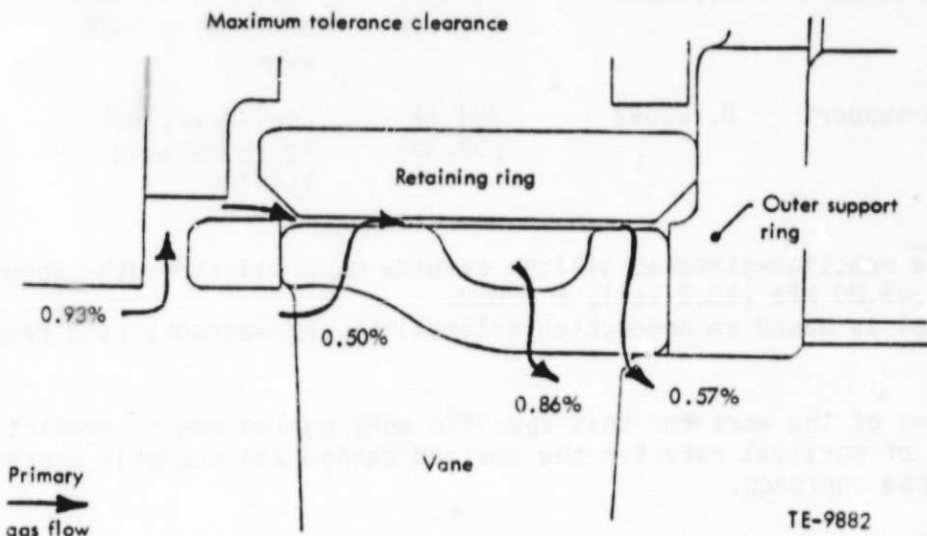
Figure 69. Secondary gas flow over 2070°F ceramic vane and outer support ring.

Included in the CATE development program is a burner rig thermal shock proof test that simulates the worst case thermal transient used in the analysis. The predicted vane failure rate of P_f = 0.01719 (P_f = 1.0 - P_s) would be expected in rig testing only. By using only successfully proof-tested vanes in the engine, the predicted engine vane failure rate would be zero. This is based on fast fracture failure theory only and does not consider slow crack growth failure phenomenon.

Outer Vane Support Ring

Study of the results of the initial outer vane support ring analysis has determined that its low probability of survival (0.762592) was due to different thermal response rates between the front and rear portions of the ring. The thin front edge responds to flow path gas temperature changes faster than the more massive rear flange. The resultant differential thermal expansion pro-

duces the internal loads and stresses that yield the low survival rate. Three modifications to the outer support ring have been investigated to address this problem.

The first modification to the vane outer support ring was to block the secondary flow over the front edge of the ring (Figure 69). This reduces the heat input to the less massive front edge and tends to equalize the thermal response rates of the two ring sections. The second and third modifications were to slot the ring using two different techniques (7 and 28 equally spaced cuts) on the front edge at the vane through-hole, which is the peak stress point (Figure 70). This breaks up the hoop integrity of the front section of the ring and allows differential thermal expansion without creating the internal loads.

Stress relief
slot (28 places)

TE-9883
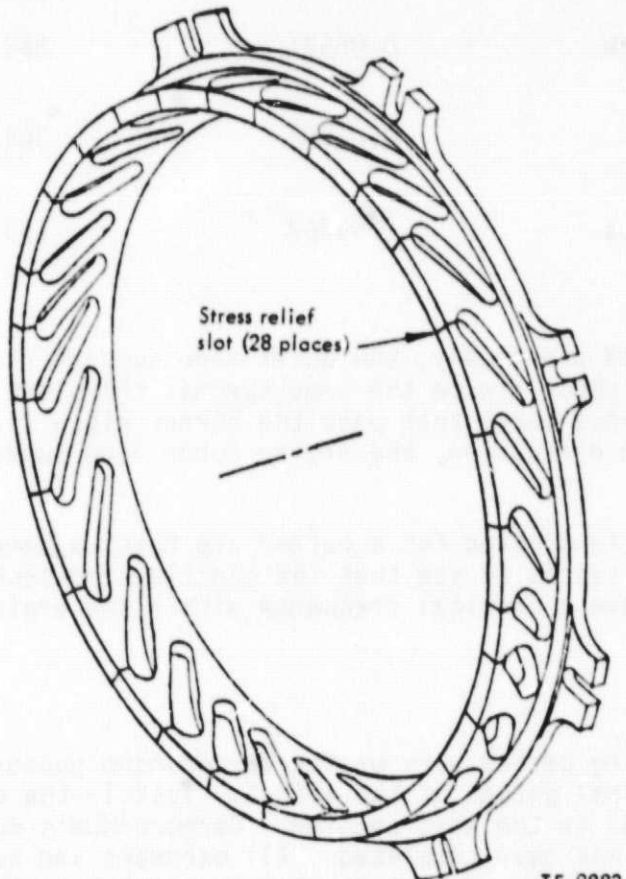
Figure 70. Outer vane support ring (split in 28 places).

Table VIII presents the results of the probability of success analysis conducted for the previously described modifications. On the original unslotted ring, the lowest probability of survival ($P_S = 0.76317$) was for cool down from 85% N_G power transfer to 85% N_G dynamic braking. The most effective variation analyzed was with the ring slotted in 28 places. The cool-down thermal transient probability of survival increased to $P_S = 0.99967$ with a peak stress of 193.1 MPa (28.00 ksi). The heat-up transient probability survival was also higher for the fully slotted ring at $P_S = 0.99994$, well above the design goal of $P_S = 0.999757$.

TABLE VIII. OUTER VANE SUPPORT RING STRESS ANALYSIS SUMMARY
(85% N_G power transfer to dynamic braking)

Model	Probability of survival	Maximum principle stress, MPa (ksi)
Original unslotted	0.76317	397.2 (57.61)
With secondary flow blocked	0.86531	362.25 (52.54)
Every fourth vane pocket slotted	0.86092	365.97 (53.08)
All 28 vane pockets slotted	0.99967	193.1 (28.00)

Like the vane described previously, the outer vane support ring will be proof tested in the thermal shock rig to the same thermal transient cycle used in the analysis. Only those parts that pass the burner rig will go to engine test. As per the vane discussion, the engine outer vane support ring will thus have a $P_S = 1.0$.

Before the outer ring is slotted for a burner rig test, a sample ring will be slotted and vibration tested to see that the cantilevered sections between vane pockets do not have a critical frequency within the engine operating range.

Process Development

In the current reporting period work on the Carborundum subcontract continued with completing the final phases of the effort. Task I--the ceramic blade development is reported in the next section. Carborundum's major work on Tasks II, III, and IV has been completed. All hardware and technical data has been delivered to DDA, and the only open item to resolve is the component process routings. Relative to ring structures considered under Task III--abradability evaluation, porosity and residual stress cracks still exist as technical problems that have not been resolved.

Objective

The purpose of activities to be performed under the Carborundum subcontract is to apply silicon carbide materials, processes, and nondestructive evaluation to produce ceramic parts required for the 2070°F-configuration gasifier turbine in the CATE 404 engine.

To achieve this objective, four tasks were established. Three of the tasks involved components and the fourth concentrated on variations to the basic silicon carbide material. These tasks are defined:

Tasks	Items
I	Blades--Gasifier Turbine Rotor
II	Vanes--Gasifier Turbine Nozzle
III	Rings--Gasifier Turbine:
	a. Rotor shroud
	b. Inner vane support
	c. Outer vane support
IV	Material Variations Investigation

Each of these tasks involved design coordination, tooling, process optimization, fabrication, and delivery of parts for evaluation at DDA. Progress on the gasifier turbine rotor blade, Task I, is reported in the next section. The final development efforts on Tasks II, III, and IV are reported in the following discussion and results. Work on each task is complete except for the final process routings.

Discussion

Task II Vane

The previous progress report, NASA CR-159865, documented the results of the process development and the strength characterization. The final 56 vanes were made per the final process routing and delivered to DDA. These vanes were inspected and accepted for evaluation. The vanes were also shortened per the latest engineering design change and are ready for thermal shock rig evaluation.

Additional reaction-bonded silicon carbide vanes have been ordered from Carborundum per the same process routing.

Task IIIa Shroud Ring

In previous reporting periods, Carborundum and DDA abradability data was used to select a material density of 2.84 g/cm3 (0.103 lbm/in.3) for the reaction-bonded silicon carbide shroud material. For this selected density, CBO had characterized and reported the material strength as 389.76 MPa (56.53 ksi) at 21°C (70°F) and 510.14 MPa (73.99 ksi) at 1100°C (2012°F). For the current reporting period, five shrouds have been delivered to DDA for evaluation, and CBO completed a final material characterization.

Three of the shrouds received at DDA have undergone NDE, with the remaining in process. Two of the three shrouds had no significant defects, but the third had numerous low density areas appear on the X-ray film. It was this shroud that broke through the low density area during thermal shock testing. One other shroud was successfully thermal shock proof tested. The remaining shrouds will be proof tested in the next reporting period.

Several visual discrepancies were noted between the first two abradable shroud rings delivered to DDA. A color variation (green to gray) and a variation in the uniformity of the abradable surface were noted. The color variation was traced to the fact that the starting silicon carbide powder used to make the molding mixture comes in two varieties. The gray powder has an aluminum additive in the silicon carbide to modify its electrical properties. The green powder does not have the aluminum additive. When components made from either of these powders are siliconized, the silicon metal masks the color of the base powder. Leaching of the silicon from the abradable surface returns the color of the surface to that of the base powder. Carborundum has been using either powder depending on availability. Carborundum has stated that, to the best of its knowledge, the aluminum additive does not affect the strength or quality of the final component.

In regard to the nonuniform abradable surface, Carborundum believes that it is a result of a thermal breakdown of the epoxy mask used to prevent acid leaching of nonabradable surfaces. Carborundum states that the leaching process is exothermic and that heat breaks down the epoxy mask. Some of the broken-down epoxy in the acid bath redeposits on the abradable surface being leached and prevents complete leaching of the surface. Carborundum is looking at several techniques to correct this. These involve investigating a wax mask and using agitation and cooling on the acid bath. On the last three shrouds delivered, the abradable surface was uniform in texture and green in appearance.

The final material characterization was planned to evaluate any changes in the material processing that were required in the component fabrication effort. Since no process changes were felt necessary by Carborundum, this final material characterization is a repeat of the effort previously documented in previous reports.

Fifty room temperature and 20 1100°C (2012°F) four-point bend tests (span 3.81 x 1.27 cm (1.5 x 0.5 in.)) in air were done on test bar specimens cut from warm compression molded 6 x 6 x 0.95-cm (2.5 x 2.5 x 0.375-in.) billets of reaction-bonded SiC. Photo microstructures on low and high-strength samples were done. Critical flaw identification using an SEM were done and compared to corresponding nondestructive test results. The NDI included visual, Zyglo, and X-ray.

Table IX presents and compares the results of final shroud material characterization against previously reported results. Note that there is an across-the-board drop in average strength and the Weibull modulus Carborundum has identified porosity as the major strength-limiting type of material defect. Approximately one-fourth of the bars made for this final material characterization had Zyglo indications or porosity. The comparison below of room temperature test data clearly shows the detrimental effect of porosity:

Average strength of 37 bars with no porosity indications	Average strength of 13 bars with porosity
399.90 MPa (58.0 ksi)	264.07 MPa (38.3 ksi)

Carborundum is investigating the possible causes of porosity and currently feels that furnacing conditions affect this problem. It should be noted that in the previous report, NASA CR-159865, porosity was found to be a problem in the characterization of Task IIIb and c component materials.

TABLE IX. CARBORUNDUM COMPRESSION-MOLDED, REACTION-SINTERED SILICON CARBIDE STRENGTH CHARACTERIZATION

4-point bend test summary,* MPa (ksi)

	Preliminary		Final	
	Room temp	1100°C (2012°F)	Room temp	1100°C (2012°F)
Mean value	389.76 (56.53)	510.14 (73.99)	340.46 (49.38)	433.89 (62.93)
Standard deviation	44.13 (6.40)	105.56 (15.31)	77.91 (11.30)	92.87 (13.47)
Weibull modulus	9.59	5.38	4.56	4.76
Number of bars	20	20	50	20
High-strength value	454.71 (65.95)	695.75 (100.91)	454.71 (65.95)	615.15 (89.22)
Low-strength value	277.58 (40.26)	368.04 (53.38)	165.49 (24.03)	268.27 (38.91)

Note: 2.84 g/cm^3 (0.103 lbm/in.^{3}) material density used for abradability
*Carborundum test data--bar size 3.18 x 6.35 x 50.8 mm (0.125 x 0.250 x 2.0 in.) 1/3 point loading, with center span of 12.70 mm (0.5 in.).

Task IIIb and c   Inner and Outer Vane Support Rings

Carborundum has completed all deliveries of reaction-bonded silicon carbide inner and outer ring structures under Tasks IIIb and c. Examination of these rings by NDE has disclosed that porosity and circumferential silicon-filled cracks are two types of defects that were prevalent in over half of the rings. The porosity is similar to that discussed in the abradable shroud section. Carborundum is working to resolve this problem. The silicon-filled crack problem is unique to Task IIIb and c.

The desired final density for the support rings is 2.95 to 3.00 g/cm^3 (0.106 to 0.108 lbm/in.^{3}), in the belief that the highest density gives the highest material strength. By comparison, the shroud is fabricated to a 2.84-g/cm^3 (0.103-lbm/in.^{3}) density for abradability. To achieve the higher final densities, the pressure used to mold the green bodies is increased. Carborundum stated that the circumferential cracks and Zyglo indications found in finished parts were a result of the high pressure used in molding the green body. It is speculated that the high pressure results in residual stresses that create cracks in subsequent processing steps. In the final siliconizing step, these cracks fill with silicon as shown in Figure 71. It is Carborundum's position that these silicon-filled cracks do not detract from the part strength.

The shroud rings, pressed to a lower density (2.84 g/cm^3 (0.103 lbm/in.^{3})) do not exhibit the cracking tendency. The 2.84-g/cm^3 (0.103 lbm/in.^{3}) shroud material has strength equivalent to the 2.95 g/cm^3 (0.107 lbm/in.^{3}) plus material if made without porosity (ref Table XIII--2.84 g/cm^3 (0.103 lbm/in.^{3}) material and Table XVII--2.97 g/cm^3 (0.107 lbm/in.^{3}) material in previous report, NASA CR-159805). On future vane support rings, Carborundum feels that these cracks could be overcome by pressing the green body at a lower pressure and hence a lower density.

Figure 71. Black light photograph of silicon-filled cracks in outer vane
support ring--FX 23815.

Task IV Material Variation Investigation

The purpose of Task IV was to evaluate test bars and material properties made
from variations to the basic reaction-sintered silicon carbide material used
in Task II. Vanes fabricated from the materials showing the most promise will
be burner rig tested. In a previous reporting period, eight variations were
evaluated in four-point bend tests of tests bars at room temperature (ref to
Table X in semiannual report DDA EDR 9951). Fifteen vanes of each of three
variations showing promise have been made into 1900°F vanes and test bars for
evaluation. Twenty out of 45 of these vanes have been proof tested in the
thermal shock rig test.

It was clear from the results of these eight variations that several varia-
tions were promising. The strength-testing results indicated that a hammer
milling step added to the standard mix preparation improved strength by elimi-
nating microstructural nonuniformities. Another variation used a bimodal sil-
icon carbide filler resulting in a higher Weibull modulus and a slightly lower
strength. These discoveries were used as the basis for this second material
matrix of five new materials and a control, which is summarized in Table X.

After their optimum molding conditions were found, all six of the material
variations were molded. This latest matrix used the 2070°F vane mold in which
test bars and vanes were molded together. The previous material investigation
matrix used a separate four-cavity test bar mold. Less molding difficulty was
experienced with the new tool, and it is believed the gating configuration
differences were responsible for this improvement. Since different test bar
molds were used for the two matrices, it was felt that comparisons between the
material strengths might not be valid. Variation 5 of the first matrix was
repeated as a control to ascertain the effect of mold changes with the new
tool.

TABLE X. REDEFINED MATERIAL VARIATION MATRIX

Variation	Purpose
5--Control group--microstructural improvement, hammer milled	Repeat of Variation 5 for a control group
9--Bimodal grain size 400-1000, hammer milled	Improve microstructure uniformity of bimodal material
10--Microstructural improvement, hammer milled, air impact milled	Improve microstructure uniformity more than hammer milling
11--Bimodal grain size 400-1000, hammer milled, air impact milled	Improve microstructural uniformity of bimodal material more than hammer milling
12--Bimodal grain size 400-1000, low free silicon, hammer milled, air impact milled	Lower free silicon than Variation 11
13--Variation 12--acid treated to remove all free silicon	Reduce manual labor of cleaning excess silicon from part surfaces

Variations 9 and 11, both bimodal mixes, did not siliconize very well. X-Ray inspection indicated density variations resulting from incomplete silicon infiltration. The other four variations were siliconized satisfactorily.

Variation 13 was acid treated with the same technique as used for Task IIIa-- Abradable Shrouds, and some difficulty was experienced. The acid treatment did not remove the silicon from small areas in the center of the bars, apparently, because they were not left in treatment long enough. The X-ray inspection clearly shows the silicon-rich core as does the fracture surface.

Twenty room-temperature four-point bend tests in air were done on transfer molded test bar samples for each of the six material variations. Table XI presents the results of the four-point bend test for the materials produced in the last matrix. The two bimodal mix compositions that did not siliconize completely, Variations 9 and 11, resulted in mean material strengths that were quite low; 168.2 MPa (24.39 ksi) and 223.0 MPa (32.34 ksi). This correlation between poor siliconization, low density areas, and low strength has been seen with both warm compression-molded and transfer-molded materials. These variations will not be discarded until siliconization and low density problems are more readily understood.

The bimodal material that gave a low free silicon (Variation 12) had the highest Weibull modulus (12.0) of the six variations tested. The bimodal composition in the previous matrix also had the highest Weibull modulus. This may indicate that additional development of bimodal materials might be worthwhile.

81

TABLE XI. RESULTS OF FOUR-POINT BEND TEST

Material variation	Mean strength,* MPa (ksi)	Standard deviation, MPA (ksi)	Weibull modulus, m (ft)
5--Control, 1000 mesh, hammer milled (442-38)	400.8 (58.13)	51/8 (7.51)	8.11 (2.47)
9--Bimodal, hammer milled (442-40)	168.2 (24.39)	54.9 (7.96)	3.26 (0.99)
10--1000 mesh, hammer milled, air impact milled (442-36)	391.2 (56.74)	56.9 (8.25)	6.24 (1.90)
11--Bimodal, hammer milled, air impact milled (442-41)	223.0 (32.34)	76.3 (11.07)	3.21 (0.98)
12--Bimodal, low free silicon, hammer milled, air impact milled (442-39, 43)	378.1 (54.85)	33.2 (4.81)	12.00 (3.66)
13--Variation 12, acid treated to remove free silicon (442-42)	56.2 (8.15)	5.2 (0.76)	10.35 (3.31)

---

*Carborundum test data--bar size 3.18 x 6.35 x 50.8 mm (0.125 x 0.250 x 2.0 in.) 1/3 point loading, with center span of 12.70 mm (0.5 in.).

The additional air impact milling step did not result in any strength improvement (Variations 5 and 10). The acid-treated material (Variation 13) was very weak 56.2 MPa (8.15 ksi); however, the elimination of the difficult step of removing excess silicon from siliconized vanes might aid in the commercialization of reaction-sintered silicon carbide engine components.

At the close of this reporting period, vanes from Variation groups 5, 10, and 12 have been burner rig proof tested to 1038°C (1900°F) with no failures to date (see the next section).

Rig Evaluation of 2070°F-Configuration Ceramic Hardware

The rig tests performed with the 2070°F-configuration hardware this reporting period consisted of thermal proof test qualification of ceramic components, determination of nozzle cold flow capacity, and evaluation of nozzle vibratory response to excitation frequencies expected from engine operation. Successful completion of the rig tests resulted in qualification of a complete 2070°F-configuration gasifier nozzle assembly for engine use. This nozzle was being installed in engine C-4 at the end of the reporting period.

Thermal Shock Rig

The test activities in the burner rig involved qualification of the components for the first 2070°F-configuration ceramic gasifier nozzle assembly. There were three builds, of which two were successfully run for five thermal cycles from 260 to 1038°C (500 to 1900°F) with a peak overshoot of 1204°C (2200°F).

The initial build of the burner rig was conducted in February, see Figures 72 and 73. On the initial rig shakedown run, the thermal cycles were limited from 260 to 682°C (500 to 1250°F) with a peak overshoot to 816°C (1500°F). The gas conditions at both the high and low values were held for a minimum of 5 min to stabilize the temperatures of the ceramic components. After five cycles of these conditions, the nozzle assembly was removed from the rig for inspection. By visual examination, the outer vane support ring was found fractured in three locations, the inner ring was fractured at one point, and two vanes were fractured as shown in Figure 74. Teardown of the nozzle assembly found three more vanes fractured and additional fractures on the outer ring.
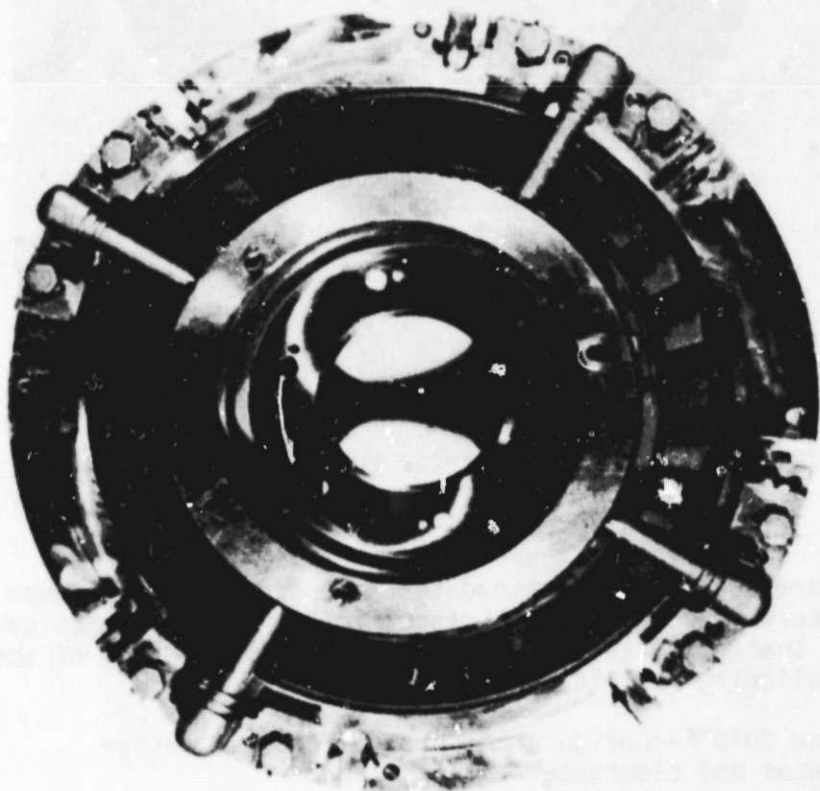
TE80-1322

Figure 72. 2070°F-configuration gasifier turbine nozzle assembly without plenum (front view).
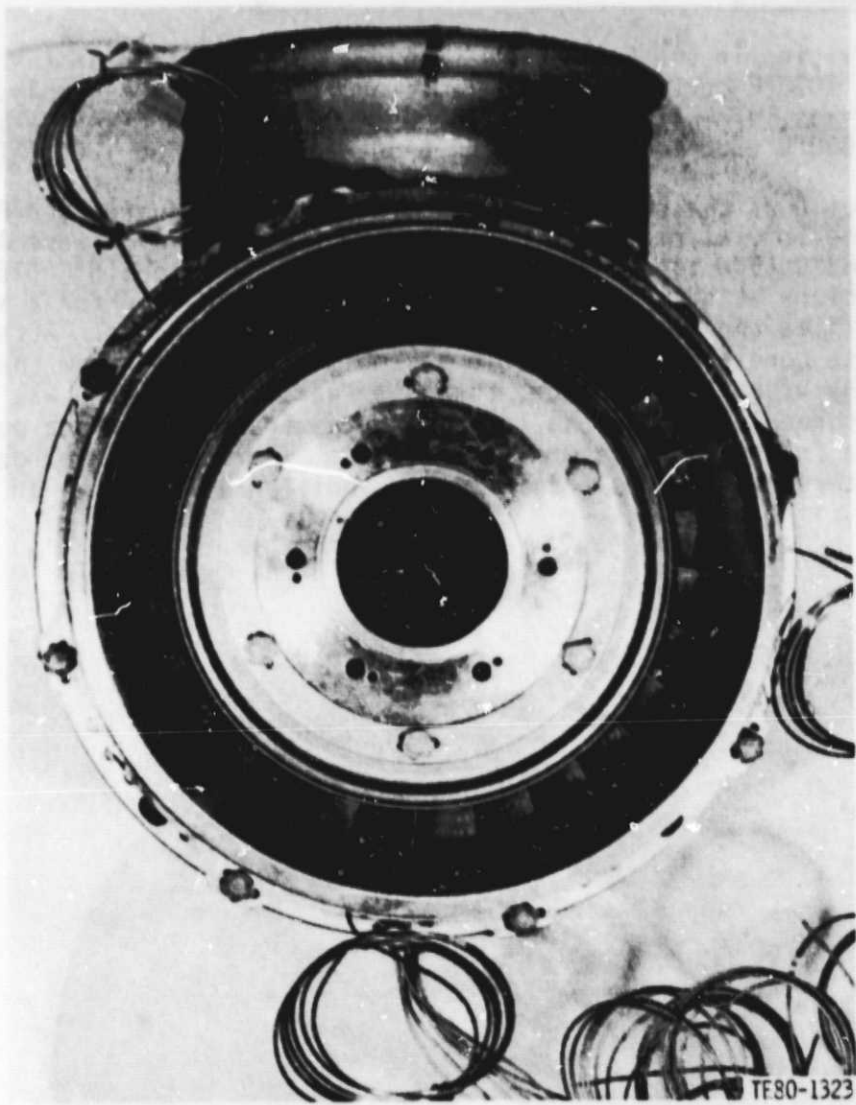
Figure 73. 2070°F-configuration gasifier turbine nozzle assembly with plenum installed (rear view).

Subsequent failure analysis determined that the most probable cause of the failure of the ceramic components was mechanically induced loads caused by a misalignment of the nozzle assembly and the rig. As a result of the failure analysis, the following activities were initiated:

o Review of the 2070°F-configuration gasifier nozzle design
    o Tolerances and clearances
o Review of the burner rig design
    o Alignment repeatability
    o Degree of compliance to misalignment
o Review of assembly procedures
    o Gasifier nozzle
    o Thermal shock rig
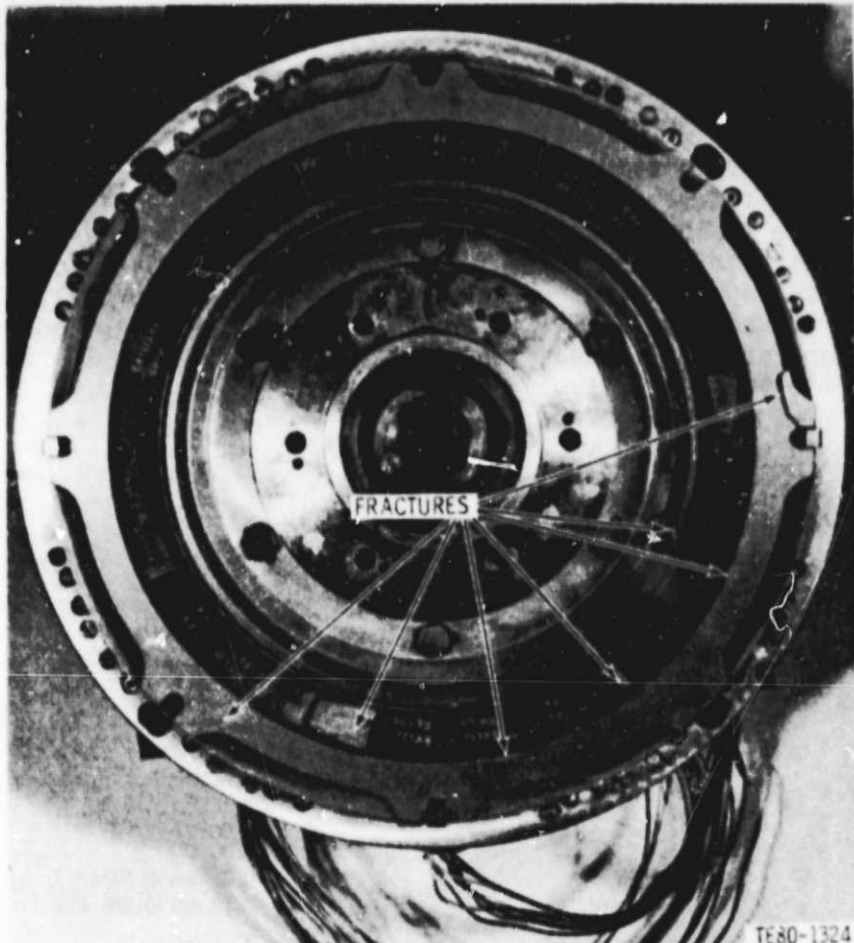
84

Figure 74. 2070°F-configuration gasifier turbine nozzle assembly after rig failure (rear view).

o Special tests
    o Load-deflection test
    o Thermal stability test

Based on these activities, several changes were made to the rig and the nozzle design. On the nozzle assembly, the only change was to increase the ceramic vane radial clearance by 0.38 mm (0.015 in.). On the rig, the interface between the nozzle assembly and the rig was redesigned to give more compliance to possible rig and nozzle misalignment. In addition, the fits and positional locating features on the rig were revised to reduce the degree of misalignment that could occur. The assembly and test procedures were established and reviewed by engineering, material, and test personnel. Deflection tests and calculations were completed to determine the dimensional shift between the metal support structure holding the inner and outer ceramic rings under design loads.

During assembly of the reworked nozzle assembly, measurements were taken to determine the degree of freedom of the ceramic components to comply with the deflections of the metal support structure. Figure 75 presents the results of the metal structure deflection versus degrees of freedom of the ceramic components. In all cases, there is at least a 2 to 1 factor between the available freedom and the required freedom. Based on this data, it was determined that under normal design loads the ceramic vanes would not bind or become loaded.

The second thermal shock rig build occurred after all of these tests, reworks, and evaluations were completed. Initial testing limited the thermal shock upper temperature limit to 649°C (1200°F). After each five thermal cycles at a given temperature limit, there was a complete teardown and Zyglo inspection. Successive increases in temperature limit with satisfactory Zyglo inspections led to an upper steady-state temperature limit of 1038°C (1900°F). Five thermal cycles from 260 to 1038°C (500 to 1900°F) with a peak overshoot of 1204°C (2200°F) were conducted. The peak temperature was reached in 1 s with steady state reached in a total of 2 s.

Deflections: Movement of metal structure supporting ceramic rings resulting from normal operating conditions

Freedom: Ability of ceramic rings to comply with deflections without binding ceramic vanes

Axial
Deflection—Aft   0.56 mm (0.022 in.)
Freedom—Fwd   1.12 mm (0.044 in.)
Aft   1.57 mm (0.062 in.)

Circumferential
Deflection   0.09 mm (0.003 in.)
Freedom   2.18 mm (0.086 in.)

Radial
Deflection   0.03 mm (0.001 in.)
Freedom   1.63 mm (0.064 in.)

Inner ring held stationary

2070°F CATE ceramic vane support rings
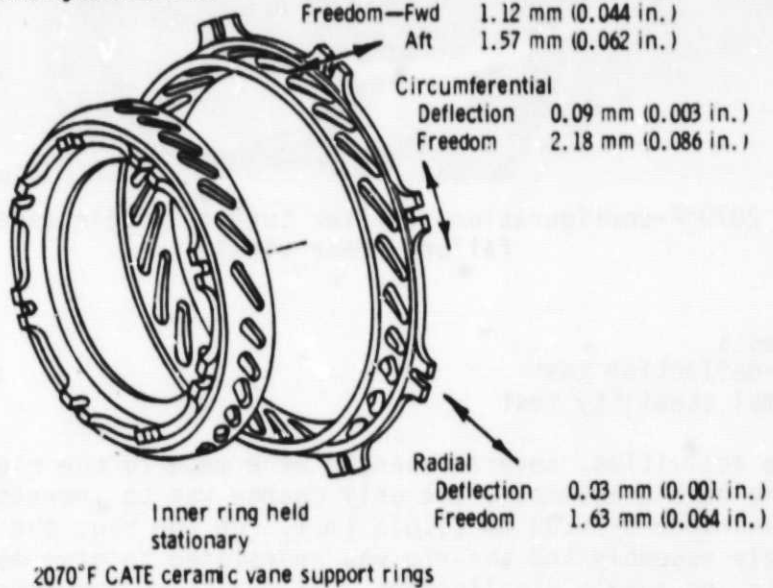
TE80-1325

Figure 75. Nozzle deflection versus ceramic component degrees of freedom.

Examination of the hardware after the second burner rig proof test revealed that two vanes were cracked and that chipping occurred at the leading edge of one pocket in the outer support ring. Both vanes were fabricated from reaction-bonded silicon carbide delivered under the Carborundum subcontract and were located in adjacent positions within the assembly.

Vane number FX23718 (315 deg CW VFR--ClockWise Viewed From Rear, looking upstream) failed at the midspan section. Fracture was initiated at the trailing edge, pressure side and progressed forward to the leading edge as shown in Figure 76. No obvious flaw could be identified. However, the surface of the airfoil on the pressure side at the failed section contains large grains of silicon carbide.

Cracked vane

Fracture surface failure origin (marked by white arrow) is on the pressure side (middle)

TE80-1326

Figure 76. Failed reaction-bonded silicon carbide vane FX23718 from burner rig thermal proof test.

87

Vane number FX23707 (327 deg CW VFR) also failed from the trailing edge, mid-span location, as shown in Figure 77. No obvious defect could be associated with the failure origin. Again, however, a thin smooth layer of large grains of silicon carbide was present at the surface near the failure origin. While it is not possible to attribute failure directly at this time to the silicon carbide layer, it should be noted that very large granular silicon carbide layers were responsible for thermal shock failures in several early 1900°F-configuration vanes.

Black light photograph of cracked vane
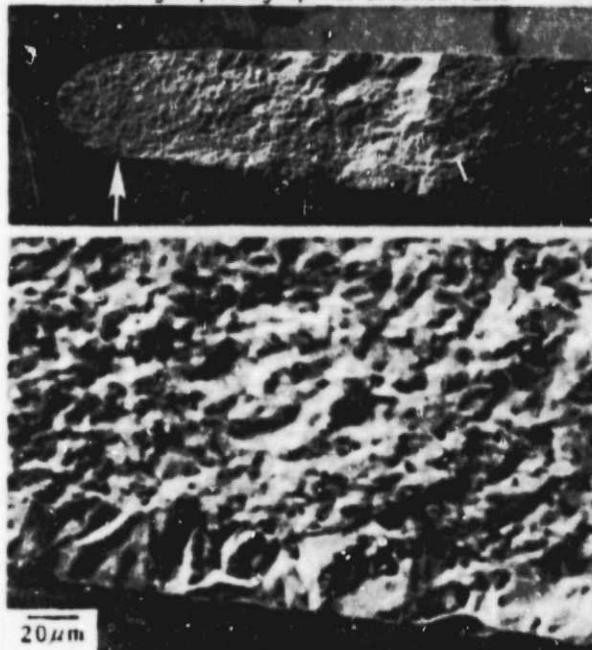
Fluorescent dye penetrated crack was revealed
under ultraviolet light (top). Failure origin
(pointed by white arrow) is on the pressure
side (middle), which is covered by a surface
layer of large silicon carbide grains (bottom)   TE8C-1327

Figure 77.   Failed reaction-bonded silicon carbide vane FX23707 from
burner rig thermal proof test.

88

A small fragment was spalled out of the leading edge of pocket No. 4 (327 deg CW VFR) at the outer diameter surface, Figure 78. This origin is at the interior surface of the pocket. The fracture surface indicated that contact stresses could account for the spalling. Review of the loading system can find no load that would create this type of contact stress. Further testing will be required to determine if this is an isolated failure.

The third build of the thermal shock rig qualified additional nozzle parts for use in an engine. Ceramic parts availability required that the same outer support ring from the second build be reused in the third build. In addition, two proof-tested vanes were located in the positions where the vanes had failed in the second build to see if the position was responsible for failure. This third build ceramic nozzle hardware set was exposed to five thermal cycles as defined previously. Posttest teardown found multiple fractures in both the turbine tip shroud (two fractures) and the inner vane support ring (five fractures). Zyglo inspection also found three vanes cracked.

Examination of the three cracked vanes showed that all three failed in a similar fashion. Fracture started at the trailing edge and proceeded forward toward the leading edge along a midspan plane. Arrest occurred at midchord as shown in Figures 79 through 80. No identifiable defect could be found at the

1000 μm

The milky mound outlined by white dotted line is SiO$_2$

100 μm
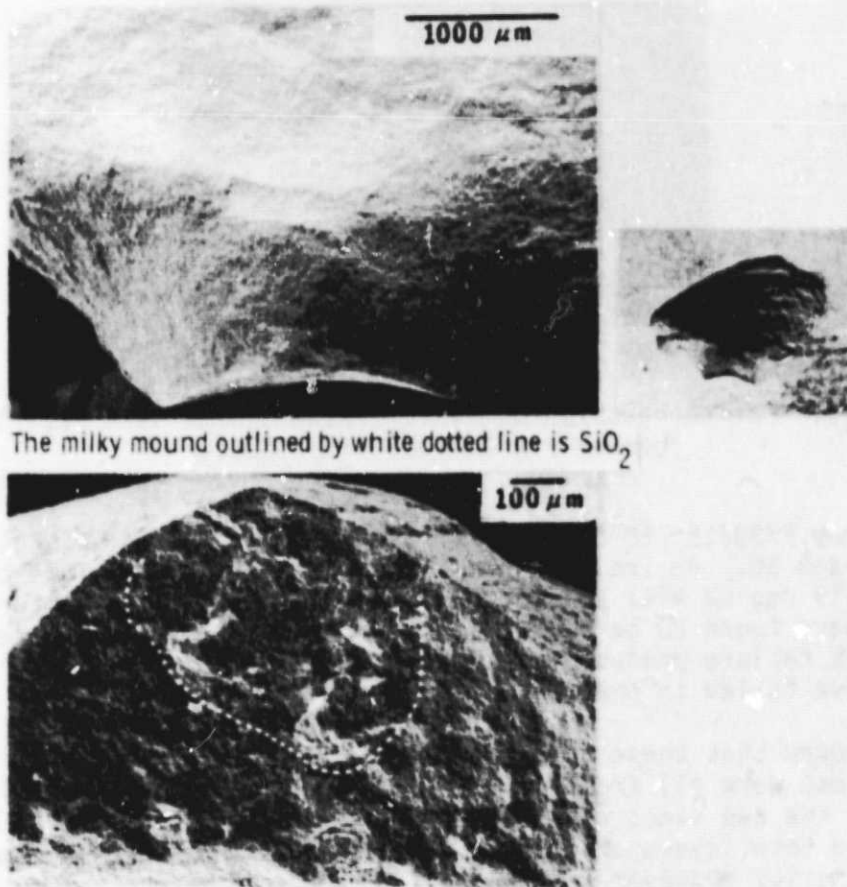
TE80-1328

Figure 78. Spall from No. 4 vane pocket of outer support ring from burner rig thermal proof test.

89

Black light photograph of cracked vane

100 μm
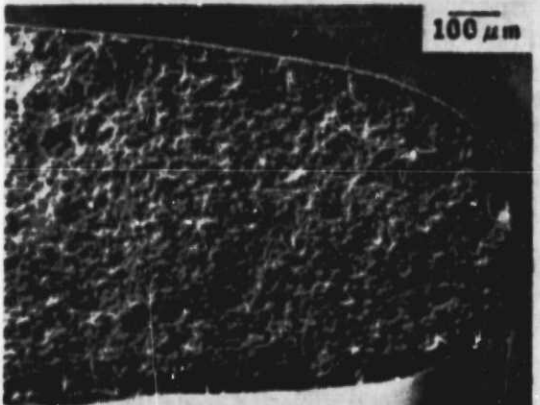
Fracture surface of vane   TE80-1329

Figure 79. Failed reaction-bonded silicon carbide vane FX23715 from
burner rig thermal proof test.

origins of vanes FX23715 (58 deg CW VFR) and FX23706 (32 deg CW VFR) and shown
in Figures 79 and 80. An inclusion was found to be present at the origin of
vane FX23708 (19 deg CW VFR) and is shown in Figure 81. The fracture surfaces
of this vane were found to be bluish with scattered calcium silicate deposits,
indicating that failure probably occurred early in the test. All three vanes
appeared to have failed in thermal shock.

It should be noted that these three cracked vanes as well as the two from the
previous rig test were all from the same lot delivered under Task II, Mile-
stone 5. Like the two vanes that failed in the second rig test, both FX23715
and FX23706 had thin layers of silicon carbide on the pressure side of the
respective airfoils. However, the present failures appeared to occur directly
at the trailing edge where no unusual surface structure existed.
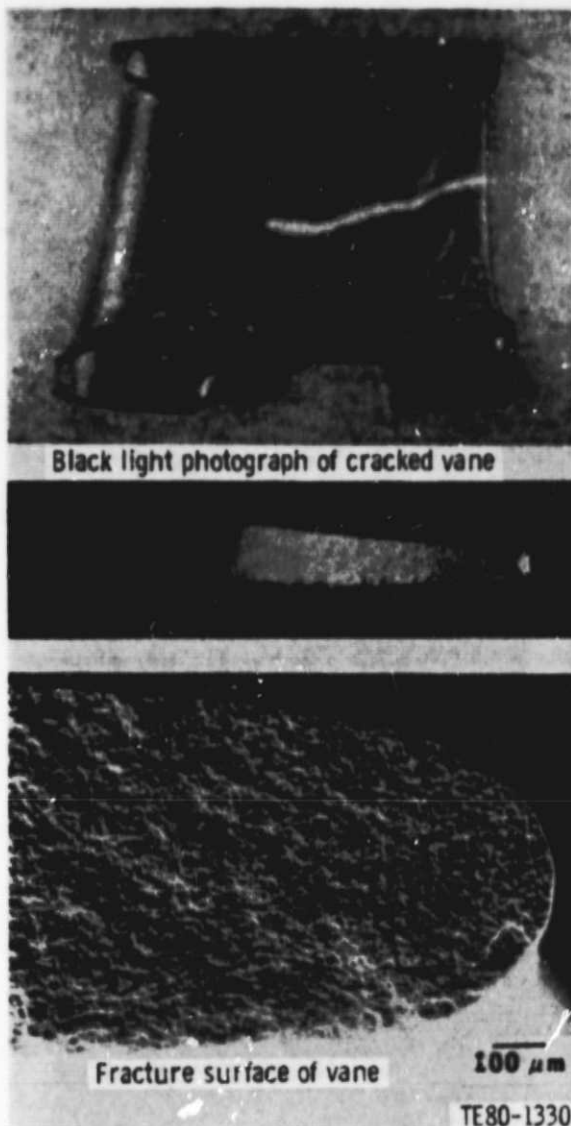
Figure 80. Failed reaction-bonded silicon carbide vane FX23706 from burner rig thermal proof test.

Examination of the vane inner support ring showed it to be broken in five locations. The fractures are close to vane pockets 354 deg, 302 and 289 deg, 238 deg, 135 deg, and 89 deg CW VFR as indicated in Figure 82. Among these fractures, three (354 deg, 302 and 238 deg, and 135 deg) started at the rear ID of the ring, one (135-deg CW VFR) at ID, and one (89-deg CW VFR) near the front corner at ID. All failure origins are free of any obvious defects, and their locations are coincident with the location of calculated maximum principal thermal stress of approximate 90 MPa (13.0 ksi).

Black light photograph of cracked vane

100 μm

Fracture surface of vane

TE80-1331
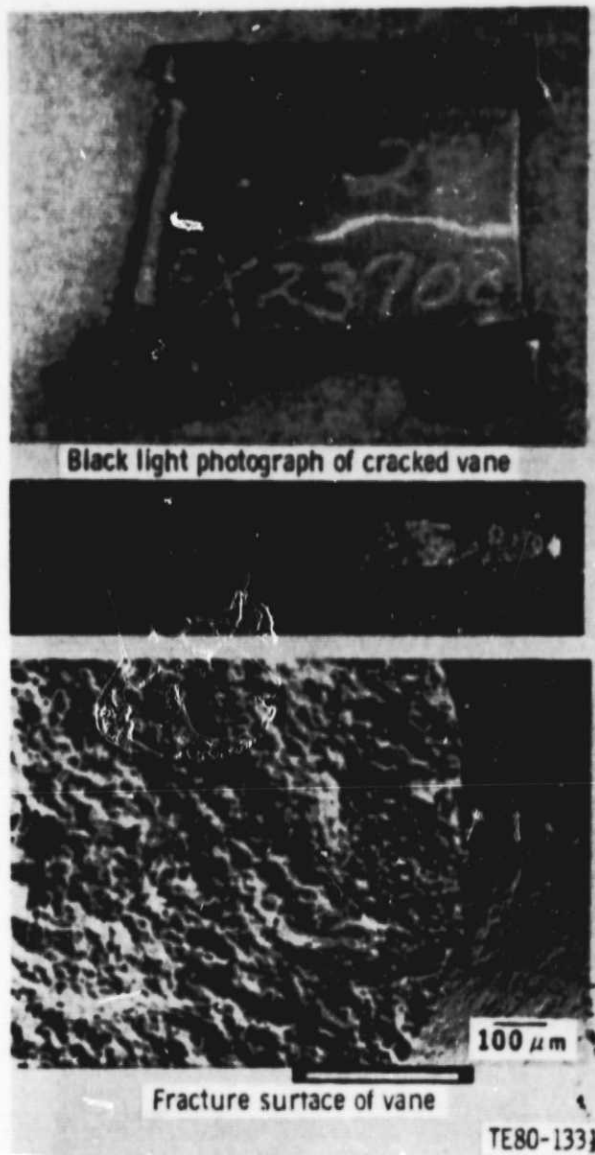
Figure 81. Failed reaction-bonded silicon carbide vane FX23708 from
burner rig thermal proof test.

No evidence suggesting a contact-type failure mode could be found. Whereas
failure appears to be thermal, the predicted stress levels are quite low rela-
tive to material strength. Subsize bars cut from the ring flange between
pockets at 45 deg and 354 deg and 264 and 251 deg CW VFR displayed three-point
bench strengths of 303.8, 378.0, and 406.1 MPa (44.07, 54.82, and 58.29 ksi).
Conversion of the average of the three-point bend data to four-point DDA bar
size (using an m = 8) yields a four-point bend strength of 290 MPa (42 ksi).

Furthermore, no microstructural abnormalities were found in the flange area.
Therefore, at present no causitive agents that could account for the failure
of the inner support structure have been identified. The predicted stresses
in this flange were no more than 117 MPa (17 ksi). MOR test bars cut from the
qualification billet of the fractured ring indicated a material strength of

92
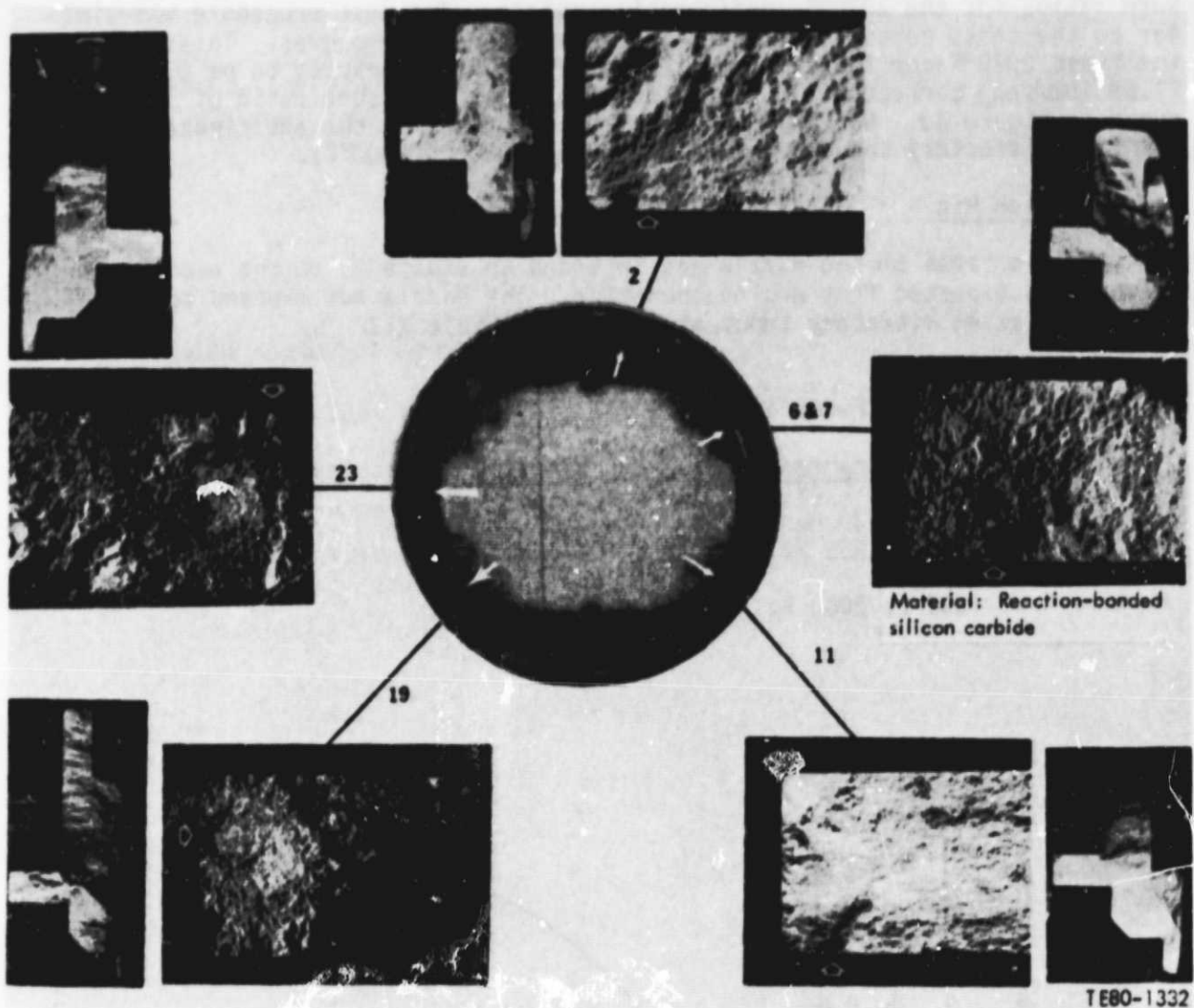
Figure 82. Fracture surface associated with failure location found on the inner support structure (arrows indicate failure origins at vane pocket numbers).

299.7 MPa (43.5 ksi). This is well above the peak predicted stress level. Investigation is continuing with a review of the stress prediction techniques.

Examination of the shroud found low density porous areas at each of the fracture sites. This porosity was identified in X-ray before testing, but after rig test it was verified to be a lack of complete siliconizing in the reaction-sintering process.

Cold Flow Rig

At the end of the third build of the burner rig, a complete set of ceramic components for a 2070°F-configuration gasifier nozzle had been proof tested. These parts were assembled and subjected to a cold flow capacity test. The

cold flow capacity test was used to determine the airflow at different pressure ratios for the 2070°F-configuration nozzle. The test procedure was similar to the tests conducted on the 1900°F-configuration nozzles. This test on the first 2070°F-configuration nozzle found the flow capacity to be 0.77 kg/s (1.69 lbm/sec) corrected flow at a total-to-static pressure ratio of 1.45, as shown in Figure 83. Nozzle flow capacity is 2.8% below the anticipated value but is satisfactory to operate the engine at 1038°C (1900°F).

Vibration Rig

The vibration test on the nozzle was intended to expose it to the excitation frequencies expected from engine operation. The nozzle was exposed to both radial and axial vibratory input as defined in Table XII.

TABLE XII. 2070°F-CONFIGURATION NOZZLE VIBRATION TEST INPUT SPECTRUM

Frequency range	Vibration input level
10 to 130 Hz	1g
130 to 652 Hz	0.76 cm/s (0.3 in./sec) average velocity
652 to 2000 Hz	5g
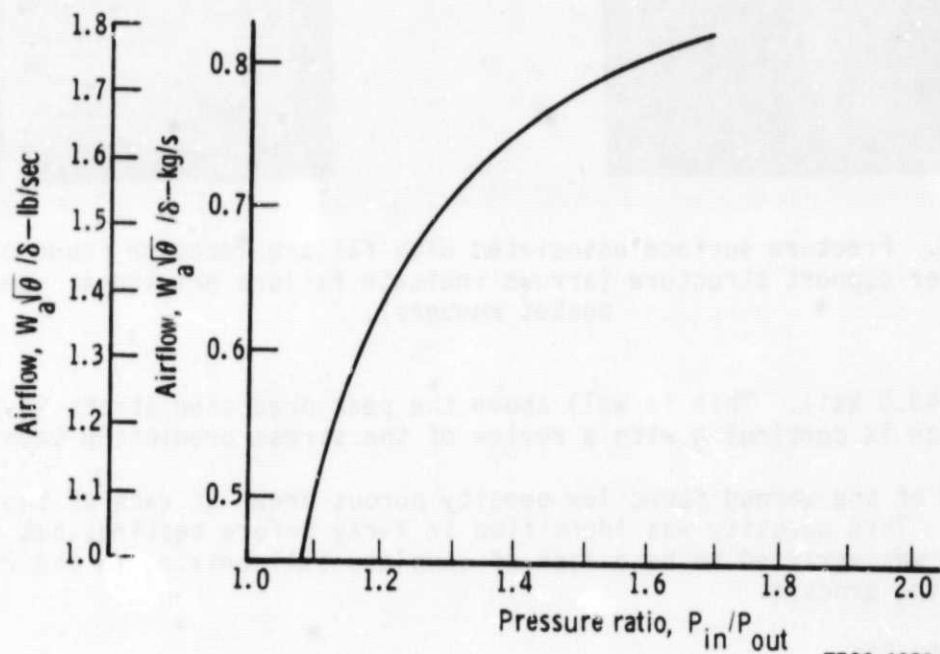
TE80-1333

Figure 83. Cold flow characteristics of first 2070°F-configuration gasifier turbine nozzle.

94

During the vibration test, vanes were spring loaded to simulate aerodynamic load, as shown in Figure 84. The results of this testing indicate that the 2070°F-configuration ceramic components and method of restraint are vibrationally acceptable for development engine testing. A total of 4.5 h of vibration testing was accumulated on the ceramic hardware. Zyglo inspection of the ceramic parts revealed no damage from either the cold flow or vibration tests.

The nozzle assembly was being installed into engine C-4 at the end of this period for test evaluation.
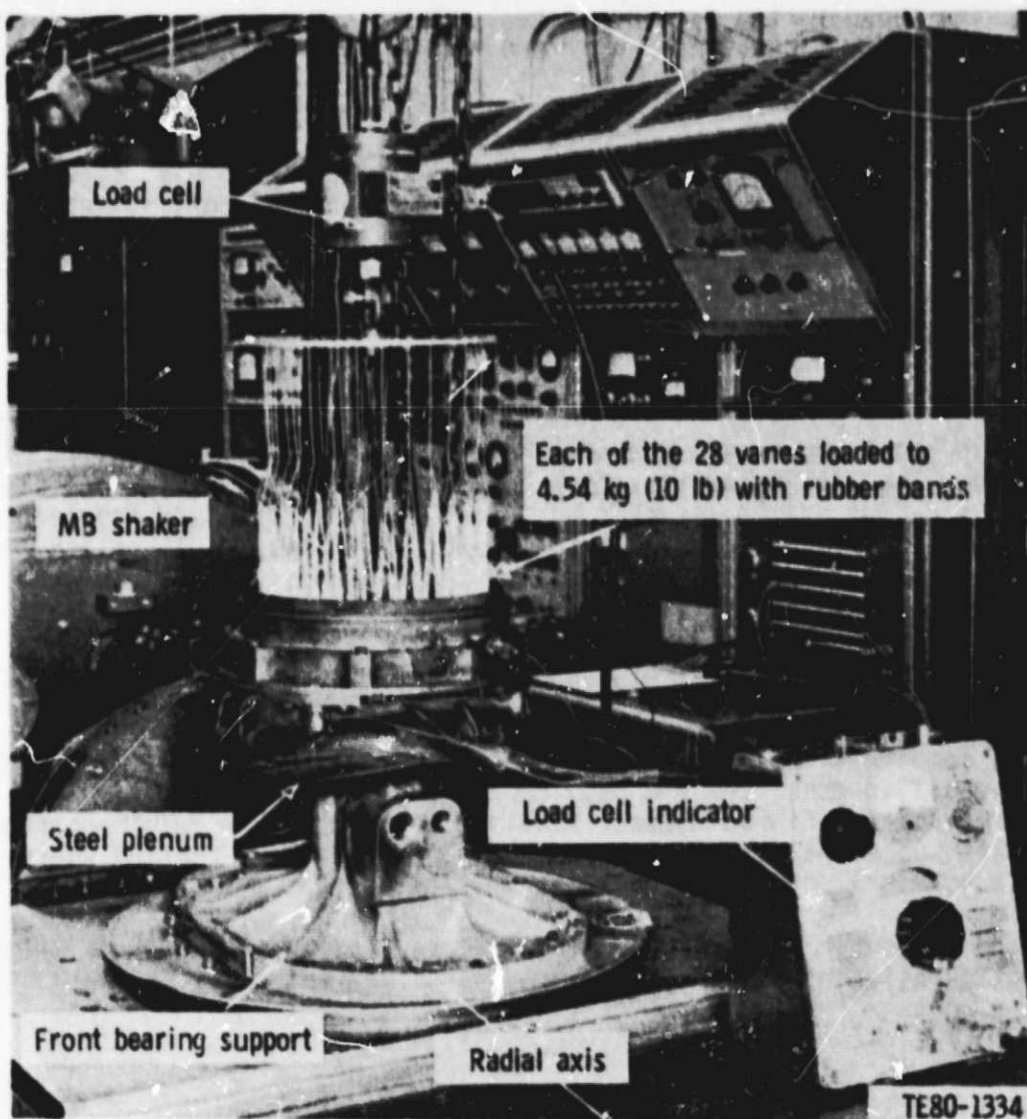
Figure 84. Vibration test rig with 2070°F-configuration ceramic gasifier nozzle assembly--radial axis excitation on an MB-C26H shaker.

2265°F-Configuration Gasifier Turbine Nozzle Design and Analysis

Summary

The preliminary 2265°F-configuration gasifier turbine nozzle design will use the 2070°F-configuration nozzle design as a baseline. The ceramic materials thermal capabilities have been reviewed, and the gasifier vane material has been upgraded from reaction-bonded silicon carbide to alpha-silicon carbide. A ceramic component probability of survival analysis for the vane, shroud, inner vane support ring, and outer vane support ring has been planned and implemented. The analysis procedure have been reviewed and revised where applicable. At the close of this reporting period, the analysis on the vane and the outer vane support ring were completed. Work on the inner vane support ring and the turbine tip shroud are in progress.

Objective

The objective of the preliminary design analysis on the 2265°F-configuration gasifier turbine nozzle is to calculate the probability of survival of the vane, tip shroud, and inner and outer vane support ring, when these components are exposed to 2265°F transient thermal conditions. The calculated probability of survival will be compared to the development goal of $P_s = 0.9$ to determine if any component design change or material strength improvement is required.

The philosophy of the design of the CATE 2265°F-configuration gasifier turbine nozzle design is to begin with the 2070°F-configuration design shown in Figure 85 as a base. The 2265°F-configuration cycle temperatures will expose the 2070°F-configuration nozzle assembly to a more severe thermal environment than was analyzed in the 2070°F-configuration component analysis. To select the appropriate ceramic materials, these higher temperatures will be reviewed and compared to the thermal capabilities of the ceramic materials.

To compute the Weibull probability of survival for the 2070°F-configuration ceramic components at 1241°C (2265°F) gas conditions, a transient heat transfer analysis will be done to determine what point in time the maximum ΔT exists in a component. The temperatures at this time will be used to determine the thermal stresses and the resultant probability of failure. This analysis will use the finite element models developed in the 2070°F-configuration analysis. The analysis procedure will be reviewed and revised where more appropriate boundary conditions data are available.

The vane and the outer vane support ring will be analyzed first since in the 2070°F-configuration nozzle these two components had the lowest probability of survival.

Discussion

Figure 86 presents the 1241°C (2265°F) cycle temperatures for the maximum engine steady-state operating point of 85% gasifier speed in power transfer with 85% power turbine speed. It should be noted that the temperatures in Figure 863 are circumferentially averaged for the hub, mean, and tip radial sections. As a result of the burner circumferential profile, hot spots of approximately 111°C (200°F) over the average can be expected. For the gasifier vane this can mean gas path temperatures of 1404°C (2560°F). The primary vane material

96

Metal strut four locations

Containment ring

Outer metal support ring
Outer metal retaining ring
Vane retaining ring
Rotor tip shroud
Outer vane support ring

Ceramic tube

Vane
Inner vane support ring
Retaining plate

Inner metal support structure
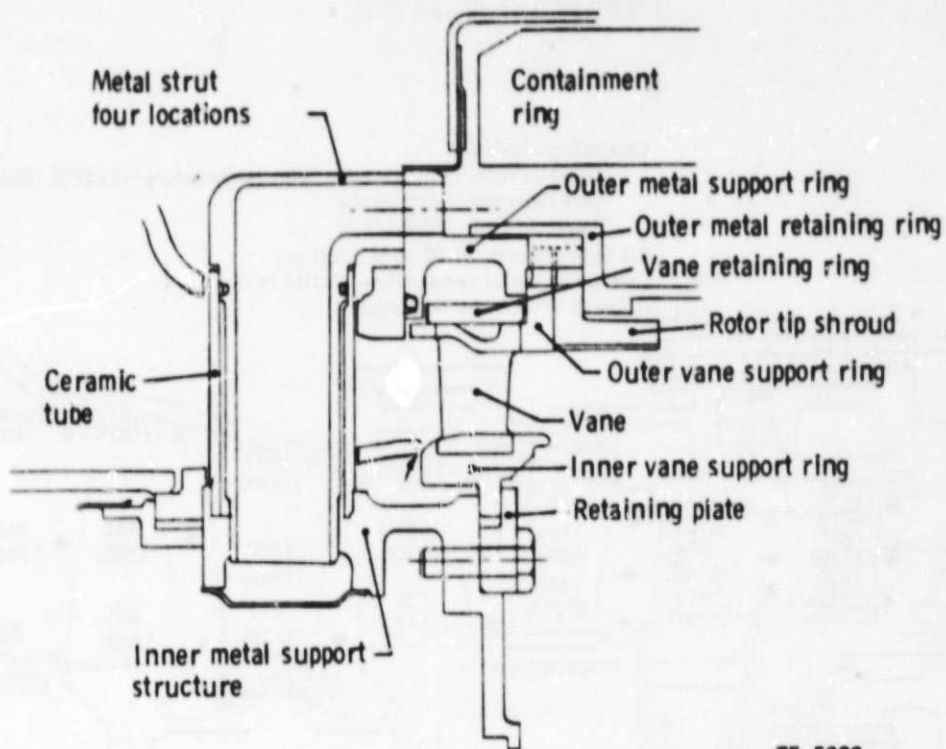
TE-5808

Figure 85.   2070°F-configuration ceramic vane assembly.

in the 2070°F-configuration nozzle design is reaction-bonded silicon carbide, and it has an upper temperature usage limit of approximately 1300°C (2372°F). For the 2265°F-configuration application, the vane material will have to be changed to sintered alpha-silicon carbide with a temperature capability of over 1700°C (3100°F). This material is already being evaluated in rig tests on the 2070°F-configuration gasifier nozzle design as an alternate material.

Based on previous CATE 1900°F and 2070°F-configuration analyses of ceramic components, it is the rapid gas path thermal transients that result in the critical probability of survival. For the 2265°F-configuration analysis, these thermal transients are presented in Figure 87. They represent the vehicle engine in dynamic braking at 85% gasifier shaft speed and the gas path temperature is 260°C (500°F). This is followed by a rapid rise in the gas path temperature as the engine goes from negative power to positive power and full design temperature of 1252°C (2286°F) mass averaged nozzle inlet temperature. The return to engine braking results in a rapid temperature drop back to 260°C (500°F). It is these two thermal transients that were analyzed for the probability of survival.

Operating condition:
  Gasifier rotor average total inlet temperature—1259°C (2265°F)
  Gasifier rotor—85% speed
  Power turbine—85% speed
All temperatures °C (°F) are relative.
Combustor radial temperature profile is included.
Dilution effects are included.

TE80-1335
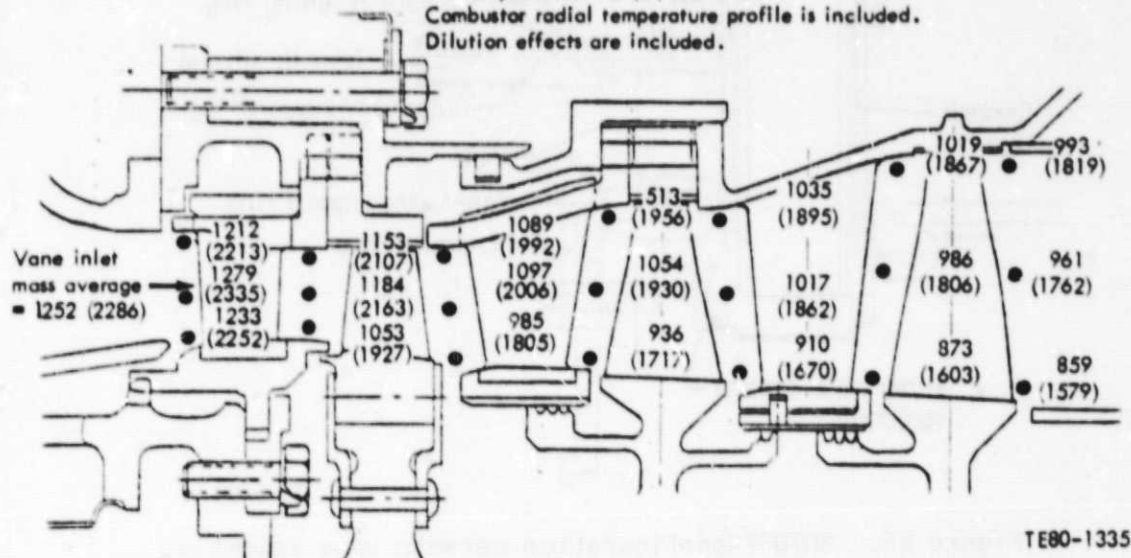
Figure 86.   2265°F-configuration gas path temperatures.

Vane

The procedures and finite element model used on the 2265°F-configuration vane
analysis are similar to the 2070°F-configuration analysis except that the heat
transfer and stress boundary conditions are changed to reflect the 1241°C
(2265°F) gas conditions.

Table XIII gives a comparison of the steady-state 2265°F-configuration vane
heat transfer analysis against the 2070°F-configuration analysis results.

TABLE XIII.   COMPARISON OF STEADY-STATE CERAMIC VANE DESIGN POINT TEMPERATURES

	2070°F configuration vane reaction-bonded silicon carbide	2265°F configuration vane sintered alpha-silicon carbide
Max temperature	1233°C (2251°F)	1346°C (2455°F)
Min temperature	1170°C (2138°F)	1247°C (2277°F)
Gradient	63°C (113°F)	99°C (178°F)
Max gas temperature	1267°C (2311°F)	1374°C (2506°F)
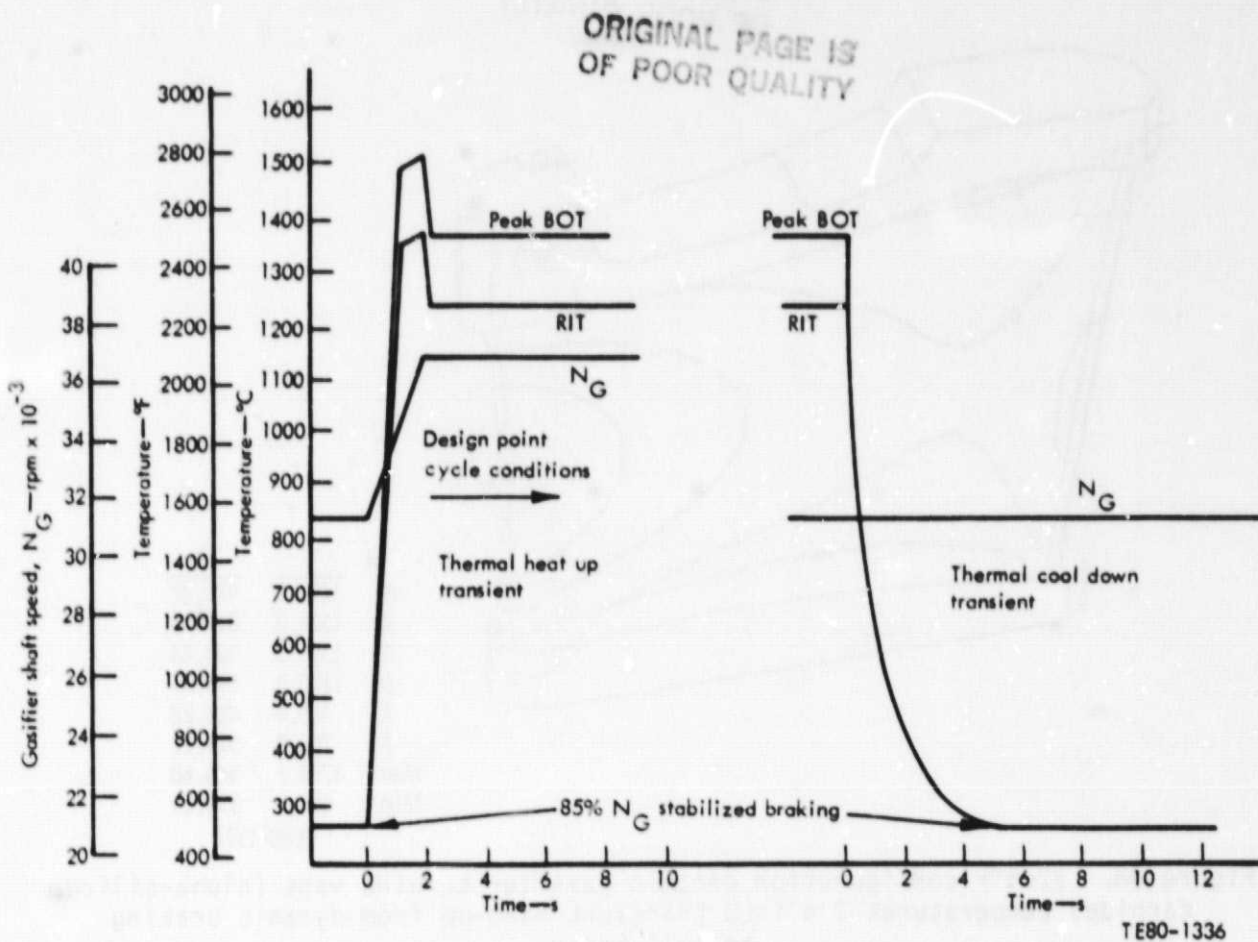
Figure 87.   2265°F-configuration gas thermal transients.

The 2265°F-configuration vane using alpha-silicon carbide has a peak tempera-
ture at the midspan trailing edge of 1346°C (2455°F) with a gradient of 99°C
(178°F) compared to the 2070°F-configuration vane at 1233°C (2251°F) and a
gradient of 63°C (113°F). The transient analysis resulted in the maximum
gradient occurring at 2 s into the heat-up thermal transient. At that time,
the 2265°F-configuration vane has a peak temperature of 947°C (1736°F) with a
gradient of 596°C (1072°F), as shown in Figure 88. This compares to the
2070°F-configuration analysis where the maximum gradient also occurs at 2 s
into the thermal heat-up transient where it has a peak gradient of 572°C
(1029°F). The cool-down transient was also analyzed, and the maximum gradient
occurs at 4 s into the transients. At this point, the gradient is 469°C
(844°F). The temperatures for these two transient conditions were used to
analyze the transient thermal stresses.

For the heat-up condition, the probability of survival was 0.96101 at 2 s into
the transient or four failures in 100 using alpha SiC material properties.
The cool-down transient probability of survival was 0.99994. The vane stress-
es for the most severe heat-up transient appear in Figure 89. The stress
field is very similar to the 2070°F-configuration vane with peak stress of
394.8 MPa (57.3 ksi) occurring at the midspan trailing edge and dropping off
rather sharply to less than 82.7 MPa (12.0 ksi) in the rest of the airfoil.
The alpha-silicon carbide material used in this analysis has a four-point bend
MOR strength of 342.7 MPa (49.7 ksi).

99
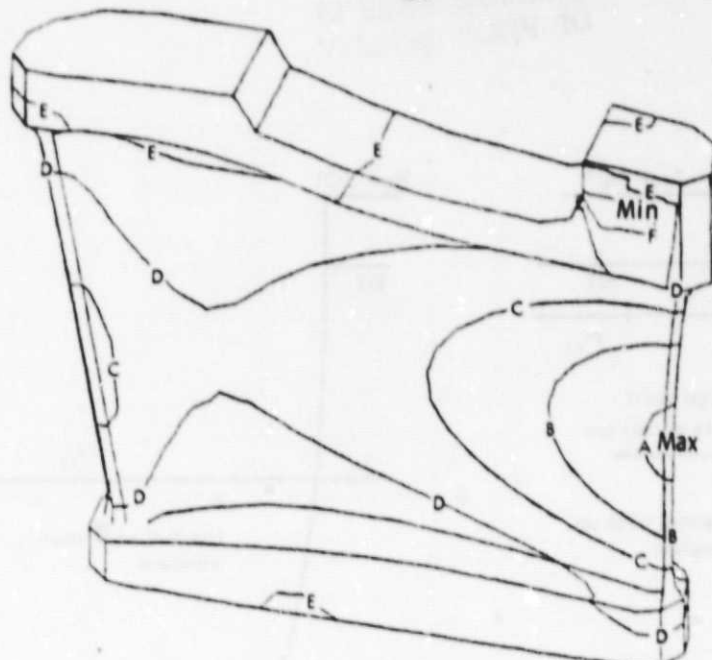
	°F	°C
A	1700.0	926.67
B	1500.0	815.56
C	1300.0	704.44
D	1100.0	593.33
E	900.0	482.22
F	700.0	371.11
Max	1736.2	946.80
Min	664.1	351.19

TE80-1337

Figure 88.   2265°F-configuration ceramic gasifier turbine vane (alpha-silicon carbide) temperatures 2 s into transient heat-up from dynamic braking to full power.

The P_S = 0.96101 for the vane does not meet the design production goal of P_S = 0.999974, but it is more than the development goal of 0.9 and is satisfactory for the CATE effort. The probability of survival for the cool-down transient was 0.99994 just less than the design production goal.

Outer Vane Support Ring

The analysis of the 2265°F-configuration outer vane support ring used the same finite element model used in the final 2070°F-configuration analysis. This model had the outer support ring split at each of the 28 vane holes, as shown in Figure 70. Based on the 2070°F-configuration component reanalysis, the split ring reduced the stress and significantly improved the probability of survival. It was felt that this split ring geometry was required for the 2265°F configuration and the greater thermal loads.

The analysis procedures used on the 2265°F-configuration outer vane support ring were the same as previously reported in the 2070°F-configuration work except for the endwall boundary conditions. The heat transfer boundary conditions have been recalculated based on the 2041°C (2265°F) gas conditions and using a revised technique for the endwall flow conditions. In the 2070°F-configuration analysis, the heat transfer coefficients were calculated based on channel flow theory. Since that time, DDA heat transfer rig data on vane end-

100
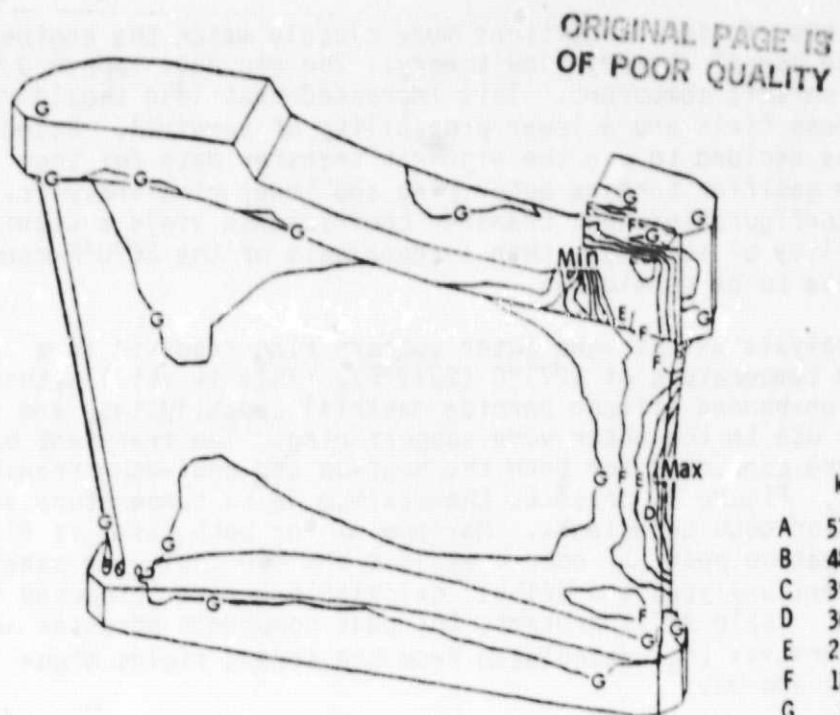
	ksi	mPa
A	57.0	393.00
B	48.0	330.95
C	39.0	268.90
D	30.0	206.84
E	21.0	144.79
F	12.0	82.74
G	3.0	20.68
H	-6.0	-41.37
Max	57.3	394.80
Min	-6.5	-44.52

TE80-3338

Figure 89.   2265°F-configuration ceramic gasifier turbine vane (alpha-silicon carbide) maximum principal stresses 2 s into transient heat-up from dynamic braking to full power.

walls have become available. The rig geometry was similar to the 2265°F-configuration nozzle, and data were run at similar Mach numbers and Reynolds numbers. Heat transfer coefficients calculated for the 2265°F-configuration analysis were based on the rig data and yielded significantly higher values than those calculated from channel flow theory. Table XIV compares a typical case.

TABLE XIV.   COMPARISON OF CONVECTIVE HEAT TRANSFER COEFFICIENTS AT NOZZLE INLET OUTER FLOW PATH MIDCHANNEL

Based on channel flow theory	Based on DDA rig data
h = 357.7 W/m² °C (63.0 Btu/hr-ft²-°F)	h = 545.7 W/m² °C (96.1 Btu/hr-ft²-°F)

101

It is believed that the rig test conditions more closely match the engine conditions than does the use of channel flow theory. The rig data impose a higher heat load on the ceramic component. This increased heat load should result in a more severe stress field and a lower probability of survival. Based on these reasons, it was decided to use the rig heat transfer data for the 2265°F-configuration gasifier turbine outer ring and inner ring analysis. If the revised 2265°F-configuration heat transfer coefficients yield a significantly lower probability of survival, then a reanalysis of the 2070°F-configuration rings will have to be considered.

The heat transfer analysis on the vane outer support ring resulted in a steady-state maximum temperature of 1271°C (2319°F). This is still within the capability of reaction-bonded silicon carbide material capabilities, and it will be retained for use in the outer vane support ring. The transient heat transfer analyses were conducted for both the heat-up and cool-down transient defined in Figure 87. Figure 90 presents the maximum delta temperature versus time calculated for both transients. Maximum ΔT for both cases is 611°C (1100°F); with the heat-up peak, ΔT occurs at 14 s and the cool-down peak T occurs at 24 s. Stress analyses and Weibull calculations were conducted for these two conditions. Table XXIII presents the peak component stresses and the probability of survival (P_s) calculated from the stress fields highlighted in Figures 91 and 92.

While both of the survival rates are below the production design goal of Table XV, they are still well above the development goal of 0.9. The maximum stresses for both transient cases are located at the back corner of the vane pocket. These stresses occur from a combination of the radial heating and/or cooling of the ring during transients and the stress concentration effect of the vane pocket.

As with all other components, the outer vane support ring will be burner rig thermal shock proof tested. Thus the probability of survival in engine testing should be 1.0 for all parts that pass the rig proof test.
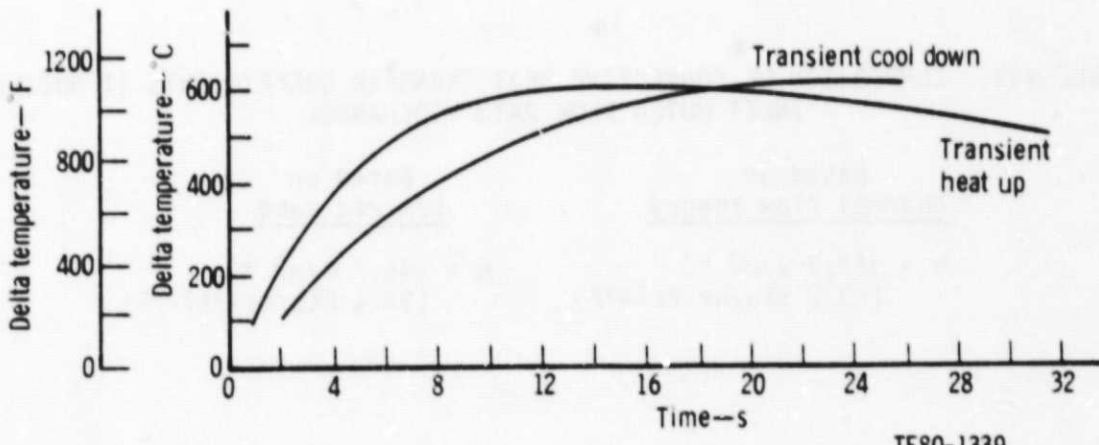
Figure 90. 2265°F-configuration outer vane support ring maximum ΔT on thermal transients (Material: reaction-sintered silicon carbide).

TABLE XV.   2265°F-CONFIGURATION OUTER VANE SUPPORT RING STRESS ANALYSIS
RESULTS AND PROBABILITY OF SURVIVAL ANALYSIS

	85% N_G dynamic braking to 100% N_G power transfer	85% power transfer to 85% dynamic braking
Maximum principal stress	200.43 MPa (29.07 ksi)	284.41 MPa (41.25 ksi)
Probability of survival*	0.99795	0.98764

*Based on using reaction-bonded silicon carbide with a MOR of 366.8 MPa (53.2 ksi) and M = 8.

GASIFIER TURBINE BLADE

Summary

The effort to develop a satisfactory ceramic turbine blade for the 2070°F-configuration engine has continued this period witn progress made in three areas: 1) design and analysis, 2) process development, and 3) spin testing.

o A simplified finite element model of the 2070°F-configuration blade has been established. Stress and reliability computed with this model are in agreement with the original, more complex model. The simplified model has been used to evaluate a nontilted airfoil and an alternate spin test configuration with a skewed broach wheel, which should improve proof test effectiveness.

o Ceramic blade process development was completed at Carborundum and injection-molded sintered silicon carbide blades are being made. Machining of attachment and other critical surfaces is being accomplished by two different grinding techniques.

o Ceramic blade process development at GTE Sylvania labs has been initiated. This effort will develop an injection-molded, sintered silicon nitride turbine blade of the 2070°F-configuration. Progress is being made in binder development plus blade tool design and construction.

o Spin testing of available components has continued and includes GTE sintered silicon nitride spin coupons, Carborundum injection-molded prototype blades, and Carborundum injection-molded 2070°F-configuration blades.

Design and Analysis

A simplified finite element computer model of the 2070°F-configuration turbine blade, which has reduced the number of elements from 649 to 263, has been established. Simplified model stress and reliability calculations compare favorably with those obtained with the original more complex model at the 3-s acceleration engine condition. The simplified modeling concept has been used to depict an alternate spin proof test configuration. A finite element model, which simulates the 2070°F-configuration blade mounted in a spin test wheel

Material: Reaction-bonded
silicon carbide

	ksi	mPa
A	41.0	282.68
B	35.0	241.32
C	29.0	199.95
D	23.0	158.58
E	17.0	117.21
F	11.0	75.84
G	5.0	34.47
Max	41.2	284.41
Min	-0.3	-1.89
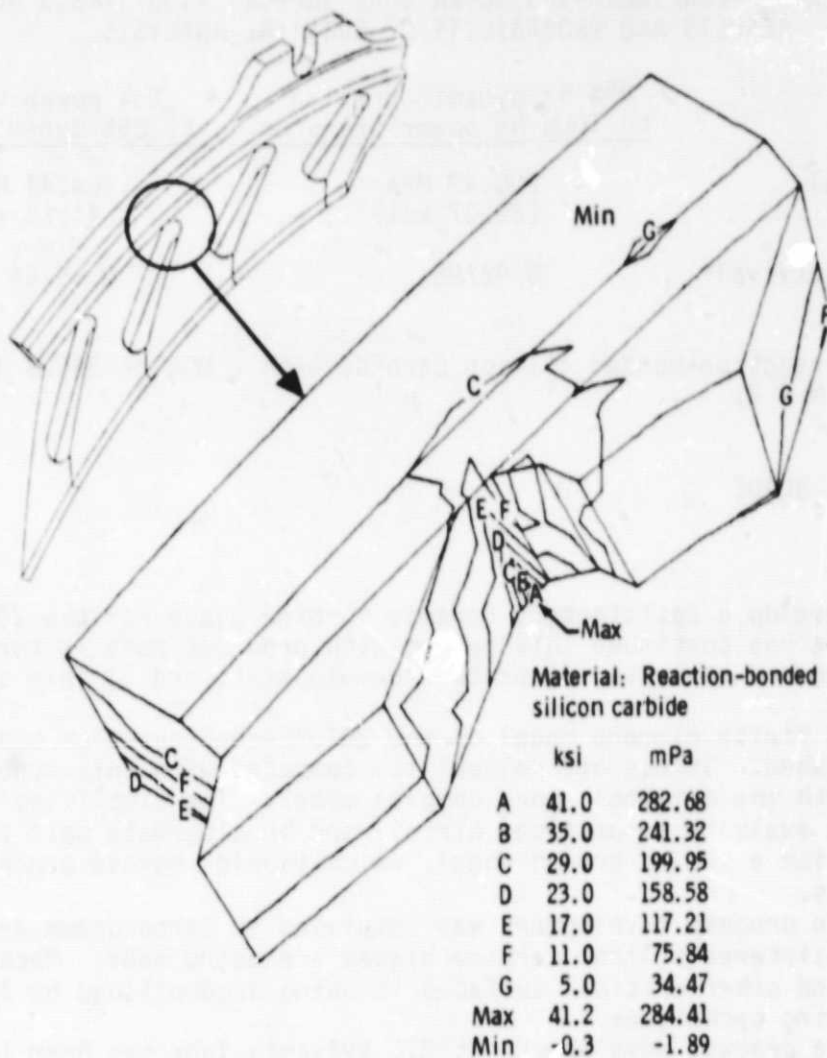
TE80-1340

Figure 91. Outer vane support ring maximum principal stress at 24 s into transient thermal cool-down from 85% N_G power transfer to 85% NG dynamic braking.

but in a skewed position, has also been established. This mounting position was selected to modify blade stress distribution during spin and improve the effectiveness of the proof test by better simulating engine operating conditions.

Objective

The objective in the design and analysis activities this period was to improve the capability of evaluating alternate blade configurations in a multitude of operating conditions. The high cost of analysis with the original finite element blade model prevents analyses of design variation at all desired conditions and then repeated after a proof test is completed. DDA intends to design a new blade configuration. This blade will feature a reduced hub setting

F

Min

G

C

D
B
E
F E
F E
C

Max

G

F

G

G

Material: Reaction-bonded silicon carbide

	ksi	mPa
A	29.0	199.95
B	24.0	165.47
C	19.0	131.00
D	14.0	96.53
E	9.0	62.05
F	4.0	27.58
G	-1.0	-6.89
Max	29.1	200.44
Min	-2.6	-17.92

TE80-1341
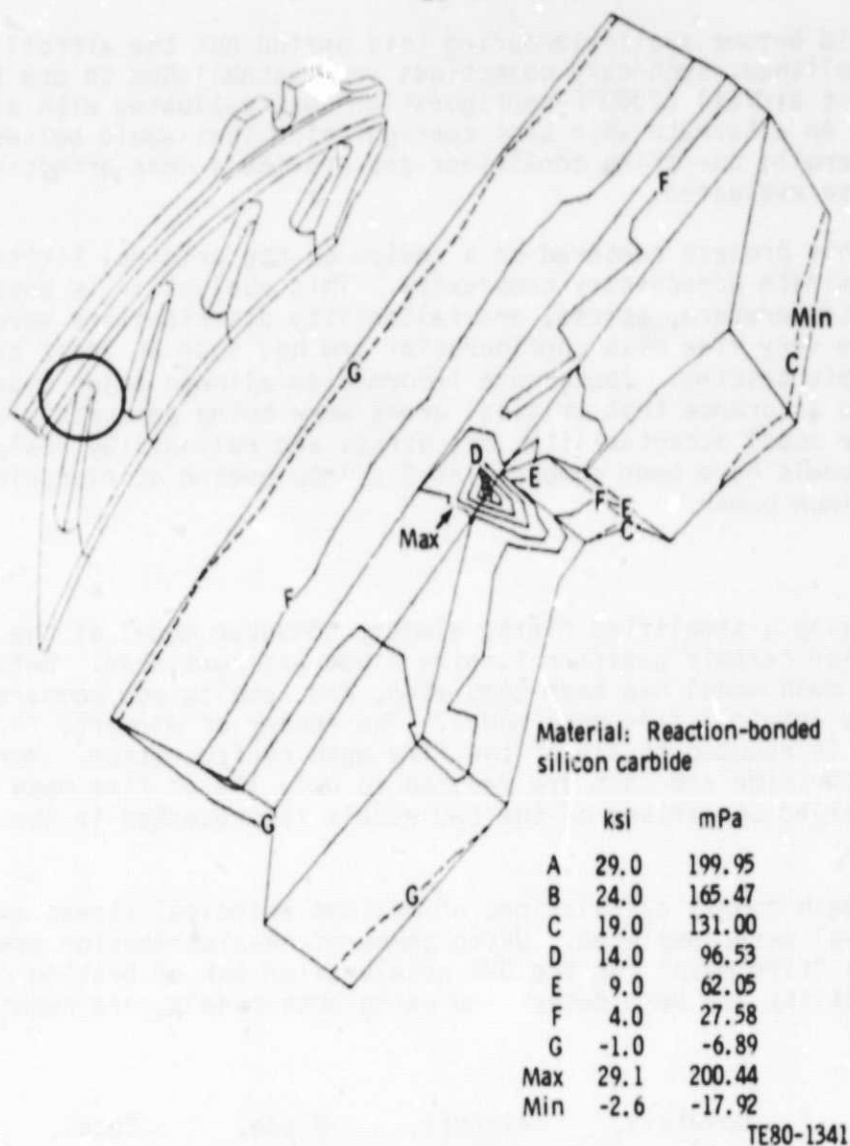
Figure 92. Outer vane support ring maximum principal stress at 14 s into transient thermal heat-up from 85% N_G dynamic braking to 100% N_G power transfer.

angle with resulting improved stress distribution in the attachment. The new concept will provide fundamentally imp ved attachment load distribution, but it will be challenging to establish an optimum blade attachment and airfoil stack (radial alignment), which addresses three engine operating conditions, each recognizing the effects of proof testing. This will require iteration on design and several stress/reliability computer runs once the temperature distribution is established. The objective in this period has been to complete evaluation of a simplified model, which will reduce computer operational cost while providing accurate analysis.

Since the model did become available during this period but the airfoil redesign was not established, secondary objectives were established to use the model. The current airfoil (2070°F-configuration) was evaluated with airfoil tilt eliminated. An alternate spin test configuration that would better simulate certain engine operating conditions and provide a more effective proof test was also evaluated.

The approach to this project centered on a review of the original finite element model to eliminate unnecessary complexity. This evaluation is possible only because the temperature, stress, and reliability distributions were established with the very fine mesh configuration and had been at least partially confirmed by spin testing. Background information allowed major changes in modeling with some assurance that critical areas were being adequately addressed. To prove model acceptability, the stress and reliability analysis results of both models have been compared at 3 s into engine acceleration out of braking to maximum power.

Discussion

The effort to develop a simplified finite element computer model of the 2070°F-configuration ceramic gasifier turbine blade was continued. Definition of the new coarse mesh model has been completed, and results now compare favorably with the original fine mesh model. The number of elements in the coarse mesh model is reduced to 41% of the fine mesh configuration. More significantly, computer time and cost are reduced to only 10% of fine mesh model cost. A more detailed comparison of the two models is presented in the last semiannual report.

Using the coarse mesh model, calculations of maximum principal stress and probability of survival were completed. Using temperature distribution previously determined with "fine mesh" for the 3-s acceleration out of braking condition, blade reliability has been determined using both models, and results compare favorably:

Model	Dovetail, P_s	Airfoil, P_s	Blade, P_s	Total, P_f
Fine mesh	0.9831	0.9992	0.9823	(0.0177)
Coarse mesh	0.9846	0.9995	0.9841	(0.0159)

The calculated maximum principal stress distribution as determined with each model is shown in Figure 93. Note that peak values of maximum principal stress as determined with the two models are also in near agreement and correlation between coarse and fine models is considered acceptable.

2070 F-configuration blade design

Three-dimensional analysis SiC material

3-s acceleration

100% rotor speed

Maximum principal stress—MPa (ksi)

Symbol	MPa	(ksi)
B	276	(40)
C	207	(30)
D	138	(20)
E	69	(10)
F	0	(0)
G	-69	(-10)
H	-138	(-20)

326.0 (47.35)   197.5 (28.65)

336.0 (48.73)   197.5 (28.65)
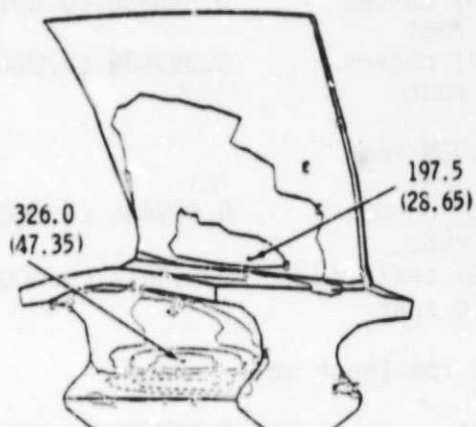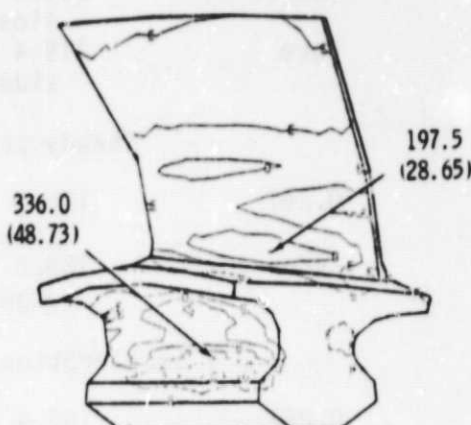
Fine mesh result

Coarse mesh result

TE80-1342

Figure 93.   Calculated blade stress using fine and coarse
mesh computer models.

Using the coarse model, an activity was initiated to study airfoil tilt as it
affects stress and reliability in various operating conditions. A version of
the coarse mesh model was established in which airfoil tilt of 0.257 in./in.
was reduced to zero (airfoil sections are stacked on a radial line). Four
conditions were evaluated:

1. Ambient temperature spin test, 100% rpm
2. Steady state, 2070°F, 100% rpm
3. 3-s acceleration (rapid heat up), 100% rpm
4. 5-s deceleration (rapid cool down), 85% rpm

A comparison of the blade airfoil stress (maximum principal) and reliability
in the tilted and nontilted geometries is presented in Table XVI. The blade
model as configured with a zero tilted airfoil was revised to provide a fully
moment-balanced blade (the platform is off-set), and attachment stresses are
not as uniform as possible. Therefore, only airfoil data are presented.

TABLE XVI. GASIFIER TURBINE BLADE AIRFOIL TILT STUDY

Model (coarse or fine mesh)	Airfoil tilt, mm/mm or in./in.	Peak airfoil stress and location, MPa (ksi)	Airfoil reliability, P_s (P_f)
		Spin test, 100% rpm	
Fine	0.267*	201.3 (29.30) convex side near root	0.998836 (0.0012)
Coarse	Zero	119.4 (17.31) convex side near root	0.999989 (0.000011)
		Steady state, 100% rpm	
Fine	0.267	170.2 (24.68) convex side near root	0.999486 (0.00051)
Coarse	Zero	189.6 (28.80) trailing edge at mid span	0.999617 (0.00038)
		3 s acceleration, 100% rpm (heat up)	
Fine	0.267	197.5 (28.64) convex side near root	0.999486 (0.00051)
Coarse	Zero	246.5 (35.75) concave side near root	0.997872 (0.0021)
		5 s deceleration, 85% rpm (cool down)	
Fine	0.267	263.5 (38.22) convex side near root	0.997173 (0.0028)
Coarse	Zero	205.2 (29.76) convex side near root	0.999584 (0.0004)

*2070°F-configuration blade tilt value.

The results indicate that zero tilt results in a significant change in stress distribution and reduced reliability for 3-s acceleration. In the spin test and 5-s deceleration conditions peak stress is reduced and reliability is improved. These results do not reflect the effects of proof testing on blade reliability. A complete optimization of airfoil tilt must be accomplished with full consideration of proof test effects on each operating condition at each considered airfoil tilt position. This is a costly iterative process. Therefore, it was decided to await the design of a new airfoil shape, which will allow a more axial blade attachment with inherently improved stress distribution in the attachment.

108

Another analytical effort was initiated to evaluate an alternate spin test mounting of the current 2070°F-configuration blade design. The current configuration features a tilted airfoil, which minimizes stress during engine operation but does not provide any significant load or "proofing" of airfoil concave surfaces during spin test. It may be possible to improve the effectiveness of spin proof testing if the entire blade is mounted in a skewed retaining slot as shown in Figure 94. This mounting position will increase loading of the airfoil concave surfaces during spin test and provide a proof of these surface elements. DDA envisions that two proof tests would be completed in series: one with a normal slot orientation and the second with a skewed slot configuration. The model with a blade mounted in a skewed position is complete but stress/reliability analyses are just beginning. Analytical results of this concept are anticipated in the next reporting period.
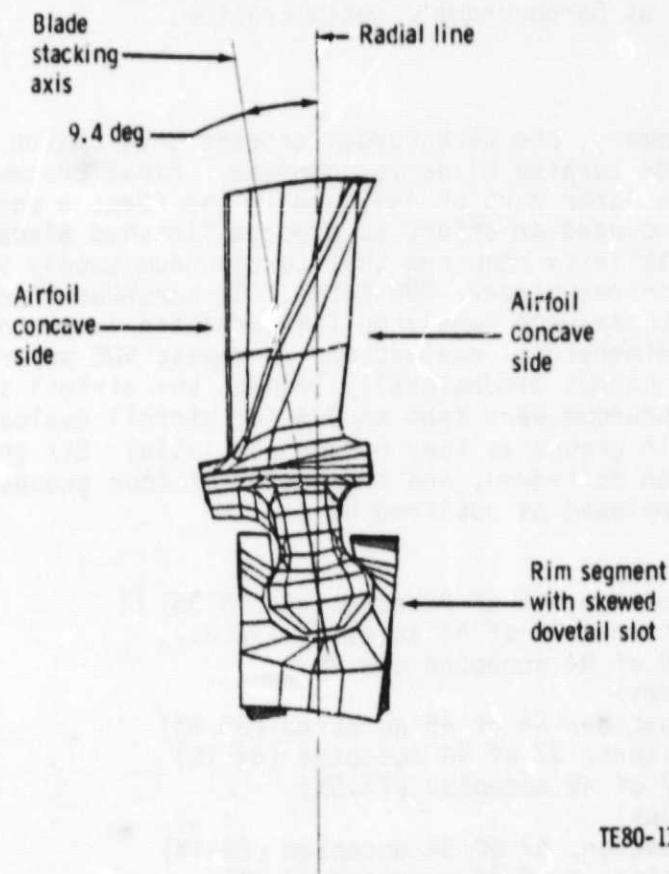
Figure 94. Spin proof test with skewed dovetail slot.

TE80-1343

Carborundum Process Development

Summary

Optimization of a process applicable to an injected, molded, sintered alpha-silicon carbide blade is completed. Established parameters are being used to make the first sets of engine blades. The process development contract with Carborundum required delivery of one set of completely finished blades; additional parts are on order. In total, Carborundum will supply 230 blades and of these, 90 are to be completely machined. DDA will machine or subcontract machine the remaining 140 blades.

To satisfy blade delivery requirements, Carborundum has injection molded 1250 blades and continued to process these blades in groups. DDA has received 431 nonmachined blades and completed inspection on 211 parts of which 92 were acceptable. These were returned to Carborundum for machining at a subcontractor. Fifty-one machined blades that have been received, inspected, and accepted by DDA. Inspection of nonmachined blades is continuing at DDA and machining continues at Carborundum's subcontractor.

Discussion

As stated in the summary, the Carborundum process development for a sintered alpha-silicon carbide turbine blade is complete. Final process parameters were selected in the later part of 1979 and in the first 6 months of this year. Activities included an effort to produce finished blades to this process. The planned activity required that Carborundum supply 90 finished blades and 140 unmachined blades--230 total. Carborundum injection molded 1250 blades and as these were completed (sintered and inspected), they were shipped to DDA for dimensional evaluation and repeat NDE prior to machining. Because Carborundum cannot dimensionally inspect the airfoil shape, all blades passing NDE at Carborundum were sent to DDA for airfoil evaluation. Blades have been supplied in groups as they became available. Six groups, totaling 431 blades, have been delivered, and inspection of four groups, totaling 211 blades, has been completed as outlined here:

o Group 1 (84 blades)
     Snape evaluation, 65 of 83 accepted (78.3%)
     NDE evaluations, 50 of 66 accepted (75.8%)
     Overall, 50 of 84 accepted (59.5%)
o Group 2 (49 blades)
     Shape evaluation, 44 of 49 accepted (89.8%)
     NDE evaluations, 37 of 44 accepted (84.1%)
     Overall, 37 of 49 accepted (75.5%)
o Group 3 (64 blades)
     Snape evaluation, 57 of 64 accepted (89.1%)
     NDE evaluation, 5 of 64 accepted (7.8%)
     Overall, 5 of 64 accepted (7.8%)
o Group 4 (14 blades)
     Shape evaluation, not accomplished
     NDE evaluation, none accepted

From the first two groups of parts, 87 of 133 blades were accepted, which is a 65.4% yield. This indicated that there would probably be no difficulty in obtaining the 230 blades desired from the 431 available (53% yield required); however, in the next two groups, totaling 78, only 5 were acceptable. Shape evaluation of these parts indicated an 89% yield, but NDE revealed a single problem causing rejection of most blades in three groups.

This problem is a depression and a fissure in the blade base resulting at the injection gate location. The injection stem normally separates from the blade at removal from the mold leaving a depression in the blade dovetail forward face about 1.5 x 0.75 x 0.75 mm (0.06 x 0.03 x 0.03 in.) deep. The depression varies somewhat in size, and many would not be removed completely by machining. The depression is formed by fracturing the green body, and a rough surface is formed which results in an FPI indication. The depression itself is not considered serious, but visual binocular examination revealed a fissure or crack at the bottom of the gate depression. Analysis indicated that a low stress level would be imposed on this area; however, it was decided not to use these blades.

After 550 blades were molded, the gate configuration was revised to add a fillet radius at the juncture to the blade base.

The remaining 700 molded blades featured the revised gate geometry. The first two groups of blades were part of the 700 revised gate blades actually molded last but delivered to DDA first. The remaining blades at DDA have been visually previewed and most are from the revised gate configuration.

Inspection of available blades is continuing. and proof testing of finished blades is planned.

GTE Process Development

Summary

A 1-yr development program with GTE Sylvania Laboratories began in February 1980. This program will establish processing parameters for a sintered silicon nitride (SNW 1000) turbine blade of the 2070°F-configuration engine and will yield a small number (15) of blades and 100 MOR bars at program completion. GTE has completed several milestones this period including:

o Submit a report defining the blade process development plan
o Complete an injection mold tool design concept and drawings
o Complete construction of the injection mold tooling and supply DDA with replicas of the blade and bar cavities
o Initiate development of a suitable binder including study of mixing, molding, and removal characteristics

GTE's activities also include a significant effort to furnish its laboratory with new equipment needed for binder/ceramic mixing, injection molding, and sintering.

111

Objective

The objective in GTE's program is to establish process parameters suitable for an injection-molded sintered silicon nitride (SNW 1000) blade in the 2070°F-configuration. This includes development of a suitable binder, injection molding parameters, binder removal, sintering, and inspection. The current program will demonstrate the total process, culminating in the delivery of sample blades and MOR test bars. Manufacturing sizable quantities of blades for engine test will be accomplished in a follow-on program.

Discussion

Significant progress has been made in the program to develop a process suitable for producing an injection-molded silicon nitride 2070°F-configuration turbine blade. GTE met the scheduled completion of the first milestone, which is a report defining the plan for development of an injection-molding binder and its removal. The submitted report discussed GTE's approach to the following major work steps:

o Powder preparation
c Binder selection and optimization
o Process parameters for powder/binder compounding
o Process parameters for injection molding
o Process parameters for devehicleization
o Sintering and inspection

Mold Tooling

The report also contains a proposed injection molding tool concept that provides the 2070°F-configuration blade and two MOR test bars. Design of the injection mold for the blade was modified after review by DDA personnel. The tool opens in three sections: a slide that forms the bottom half of the dovetail and two arms that pivot on a location equivalent to the turbine center-line. Each arm holds two insert blocks. The upper half forms the airfoil and the top half of the platform, the lower half forms the bottom of the platform and the dovetail down to the slide. The part is gated into the center front (leading edge) of the dovetail. A copy of the mold tool tailed drawings has been provided to DDA.

Mold tool construction was completed in June 1980, and plastic replicas of the blade and bar (2) cavities, as shown in Figure 95, have been received. Molding of blades and bars will be initiated.

Binder Development

GTE has been evaluating two binder systems that may be suitable for injection molding. One is wax-based and the other is based on a low density polyethylene. Both were developed by Battelle in its injection molding project. To mix these binders with ceramic powder, an instrumented mixer ("torque rheometer") made by Haake was evaluated and ordered. Before this unit arrived, compounding tests were run on a similar unit at the University of Lowell (Massachusetts). GTE's unit arrived in June 1980 and is presently in operation.

TE80-1344

Figure 95.   Plastic replica of GTE 2070°F-configuration blade mold cavities
(blade and two bars).

Work in the two powder/binder systems has progressed through binder removal
and sintering. In the wax-based binder system, a mix of 62% by volume ceramic
loading has been sintered to 99.5% theoretical. The sintered part was an ar-
row shape that is about 3 mm (0.124 in.) thick x 74 mm (2.9 in.) long x 23 mm
(0.9 in.) wide. In the polyethylene-based system, samples of 62 and 64% by
volume ceramic have been respectively sintered to 97 and 98% theoretical den-
sity. These are all very respectable results and indicate that thermal burn-
out is a viable technique and that simple shapes can be injection molded and
sintered to 98% theoretical density.

To study expansion characteristics during burnout, an expansion cell is being
designed for use on the dilatometer. The sample will be imbedded in glass
beads to allow expansion measurement above the softening point of the binder.
The expansion cell will also allow the escape of volatiles generated during
the cycle.

Carbon levels have been measured in as-received powder, ball milled powder, and an injection-molded part after burnout. The molded sample used the wax-based binder. The carbon levels were 0.017, 0.016, and 0.024% of weight, respectively. The results indicate no significant carbon contamination in the raw material or as a result of processing.

Thermal binder removal experiments have been run for the wax-based system only at solids loading levels of 62 and 64% by volume. The samples (about 25.4 x 6.2 x 3.2 mm (1 x 0.25 x 0.125 in.)) were small in cross-sectional area. One air atmosphere cycle comprised isothermal holds at 150°C (302°F), 250°C (482°F), 400°C (752°F), 530°C) (986°F), 620°C (1148°F) with climb rates of 10°C (18°F)/h between hold points. Following this cycle, selected parts had no cracks visible to the eye. They sintered respectively to 95 and 97.7% theoretical density. This initial result should be viewed with guarded optimism, i.e., the part cross section was small, it was compression molded not injection molded, and no final properties were evaluated. However, it does indicate that thermal binder removal is worthy of further study. That work is continuing.

Injection Molding

Initial molding experiments were accomplished on a small 50-cm^3 injection molder at Minute Man Technical High School (MMT). In these experiments, two molds were used, an arrow-shaped mold (MMT property) and a GTE Labs spiral mold. Both were used to evaluate the wax-based binder system at various ceramic solids loading levels. Samples of the injected compositions were used for subsequent thermal devehicleization tests.

Injection molding performance on the small injection molder was sporadic especially for the wax-based system. On some occasions the material ran from the nozzle exhibiting great fluidity; on the other occasions, no flow occurred with the same mix. It may be nonuniform heating, segregation of powder and binder at the nozzle, or some other problem that is causing nozzle bridging. Nevertheless, control on this injection molding unit is not good, and a transfer press at GTE Labs was retrofit for use with thermoplastic materials.

Once the retrofit of the transfer press was accomplished, small scale injection molding tests were discontinued at MMT, and transfer molding was accomplished at GTE Labs. A parametric study was established to evaluate mix and molding variables using spiral flow distance as an indicator. Batches were made using both the polyethylene and wax-based binder systems at loading levels of 60, 63, and 66% by volume ceramic. The batches were then molded at pressures from 8 to 30 MPa (1160 to 4361 psi) and at material temperatures from 125 to 175°C (257 to 347°F).

The results to date show increased flow for lower ceramic loading, high injection pressure, and increased material temperature. The results also indicate better flow in the wax-based binder system than in the polyethylene system.

Tests have also been made to evaluate the degree of flow enhancement by injecting into a heated mold. Spiral flow distances increased from 33 to 838 mm (1.3 to 33 in.) for a wax-based binder with 63.3% ceramic, when mold temperature was increased from room temperature to 150°C (302°F). The flow distance for the polyethylene binder with 60.8% ceramic increased from 19 mm (0.7 in.) at room temperature to 193 mm (7.6 in.) at 150°C (302°F).

The Van Dorn 0.074 cm^3 (2.5 oz) 75-t machine has been checked out using the MOR bar/disk mold and polyethylene. Mix containing ceramic will be used in that tool as soon as sufficient quantities of compound mix are produced from the Haake equipment. GTE has a two-cavity mold tool for this machine. The cavities include an end-gated bar 67.3 x 7.6 x 3.8 mm (2.65 x 0.30 x 0.15 in.) and an edge-gated-disk 50.8 mm in diameter x 1.02 mm thick (2 in. diameter x 0.04 in. thick).

Spin Testing

Summary

The spin test program continued during this 6-month period and included evaluations of spin coupons of sintered silicon nitride material, sintered silicon carbide prototype turbine blades, and the first 2070°F configuration blades (also of sintered silicon carbide).

Twelve spin coupons made of GTE 3502 (sintered Si_3N_4) were run overspeed to failure, and the average speed reached was 47,129 rpm, which is 153% of design speed. The tests were at ambient temperature except for two at 677°C (1250°F). Other test variations included two coupons with radially ground dovetail attachments, which reached 162% speed, and three polished attachment coupons, which averaged 154% speed.

Four prototype blades made of sintered silicon carbide blades were evaluated in the spin condition. These were the first injection-molded airfoil shape parts to be tested. Average speed of the four at failure was 134.9% of design engine speed.

The first 2070°F-configuration blades (sintered alpha-silicon carbide) were also tested this period. These blades were not of the final Carborundum process and were not all dimensionally correct. They became available as the result of machining trials ahead of final blades. Fourteen blades were tested in total. The first group of six averaged 116.0% of engine speed. These first six parts may have been affected adversely by a furnacing fixture error during a pretest heat treatment. The next group of eight parts reached an average 123.8% speed before failure.

Discussion

Spin testing was continued this period and included evaluations of GTE silicon nitride spin coupons plus Carborundum silicon carbide prototype and 2070°F-configuration turbine blades. Testing was accomplished in DDA's evacuated spin chamber, and the blades or coupons were run one at a time. In this test series, rotor speed is slowly increased until failure occurs. A portion of the attachment normally remains in the disk slot so that it can be removed for investigation and so that the failure initiation site can be established. Results of testing completed this period are presented here.

GTE Spin Coupons

Spin test coupons of pressed and sintered silicon nitride (GTE 3502) had been procured from GTE Sylvania. Evaluation of these coupons was desired. Based on hot cyclic spin results, L605 compliant layers with boron nitride spray coating were used in overspeed-to-failure testing. Recent failure speed data along with one previously available data point are presented in Table XVII. 100% attachment load speed is 30,800 rpm, and all coupons exceeded this speed by a considerable margin. The average failure speed for the two hot tests was 146% of design speed. The average speed of four room temperature tests was 152%, and the average for two radially ground coupons tested at room temperature was 162% of design load speed.

TABLE XVII.   Si$_{3N4}$ OVERSPEED TO FAILURE TESTING SUMMARY

Test temperature	Coupon number	Dovetail machine lay	Failure speed, rpm	Group avg, rpm (% of 30,800)
677°C (1250°F)	43580	Axial	46,350	45,050 (146)
677°C (1250°F)	43581	Axial	43,750	
Ambient	43584	Axial	46,500	46,250 (152)
Ambient	43585	Axial	46,850	
Ambient	43586	Axial	47,900	
Ambient	43587	Axial	47,500	
Ambient	43588	Axial	45,000	
Ambient	S4S	Radial	50,750	49,925 (162)
Ambient	Moore*	Radial	49,100	
Ambient	43589	Polished axial	46,350	47,283 (154)
Ambient	43590	Polished axial	47,250	
Ambient	43591	Polished axial	48,250	

*This coupon tested with IN-600 compliant layer.

Finite element analysis of the silicon nitride coupon was previously completed, and average (P_f = 0.5) failure speed of 49,601 rpm (161%) was predicted. Materials data used to determine the Weibull strength parameters were obtained from longitudinally ground MOR bars. Only two coupons (identified as S & S and Moore) had a radial machining lay on critical attachment features, which corresponds with the machining lay conditions of the test bars. Average failure speed of these two coupons is within 0.7% of prediction, which is very encouraging. Unfortunately cross-ground MOR bar data is not available to allow a valid prediction of failure speed for the other coupons that had axially ground attachments. As would be expected, the axially ground attachment coupons exhibited reduced failure speeds but were still well over the 100% load speed.

Because of the apparent material performance degradation resulting from an axial machining lay in the attachment, an attempt was made to improve the surface condition.

Three additional coupons originally produced with an axial machining lay were hand polished using diamond paste until all visible machining striations were removed as determined by 30X visual examination. These three polished coupons failed at an average of 47,283 rpm (154%), which is still below the radial ground coupons and within 2% of the as-finished axially ground parts. This implies that surface damage from the axial machining cannot be removed by surface polishing. The damage apparently extends below the visible surface.

Prototype Blades

Spin testing also included the first testing of injection-molded sintered alpha-silicon carbide turbine blades. Four prototype configuration blades were available for testing. These were the only acceptable quality parts in a group of 15 finished parts used by Carborundum in developing machining techniques. These parts were tested at room temperature in the evacuated spin chamber. These blades had axially ground dovetail surfaces but had been heat treated at 1250°C (2282°F) for 24 h in air to improve surface strength. Blade attachment was coated with boron nitride spray and L605 material compliant layers were used in all tests.

The first test blade (S/N 115) is shown in the disk slot prior to test, as shown in Figure 96. Note hand-blended area in trailing edge to remove a small chip and injection mold die part line flash evidence in the stalk area. A depression resulting from injection gate removal can also be seen. These are considered conditions that may be encountered in the injection-molded blade manufacturing process. It is hoped that some of these conditions can be tolerated in the interest of producing a low-cost reliable product.

Blade S/N 115 was first run for one min at 37,000 rpm, which is 100.3% of engine design speed. Condition of blade and compliant layer were satisfactory after this short test, and attachment contact pattern (Figure 97) was identical to patterns previously observed in spin coupon testing. S/N 115 was subsequently subjected to an overspeed-to-failure test, and 47,500 rpm was achieved. Failure apparently initiated in the attachment near the predicted peak stress location and fracture surface topograph is similar in nature to those observed in spin coupons as shown in Figure 97.

The four available blades were tested to failure with the following results:

Serial No.	Failure speed, rpm (%)
113	54,200 (146.9)
115	47,500 (128.7)
116	54,500 (147.7)
119	43,000 (116.5)
Average	49,800 (134.9)

Average speed reached by the four blades is 135% of engine 100% rpm. A complete reliability analysis of the prototype blade was not completed, and injection-molded SiC material properties representative of prototype blades is
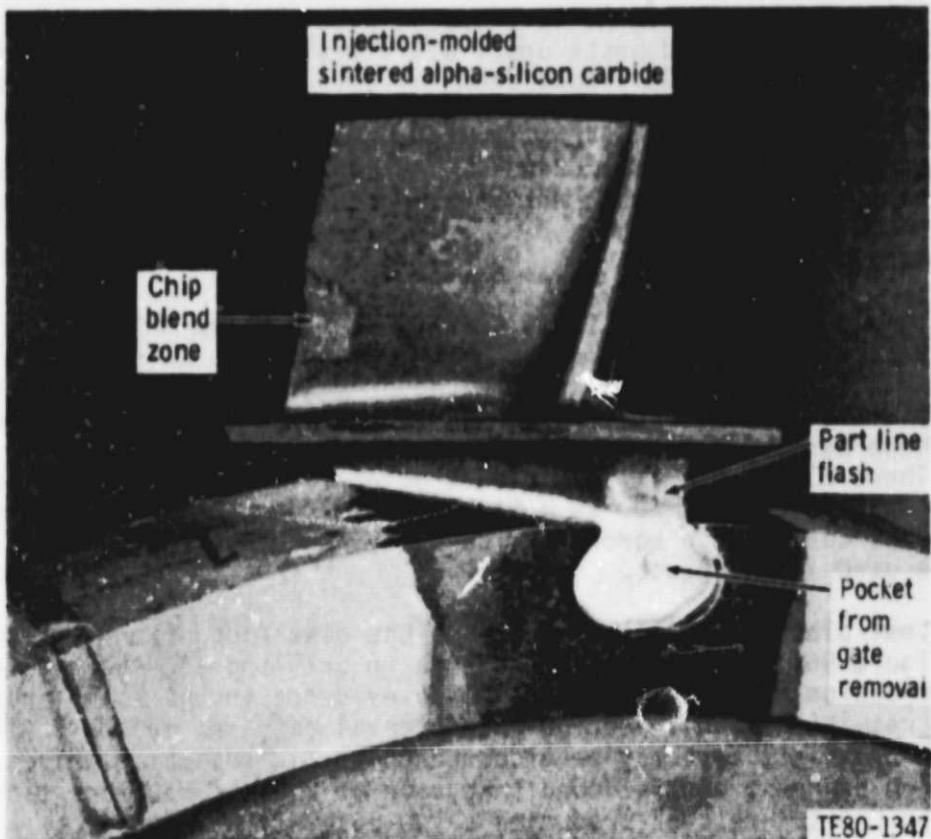
Figure 96.   Prototype blade ready for spin test.

not available. However, the predicted mean spin test failure speed of the
2070°F engine blade of 48,280 rpm (131% of engine speed) has been approximated
by the prototype blades. 2070°F-configuration blade analysis assumes material
MOR = 343 MPa (49.7 ksi) and Weibull is 7.9. This preliminary attachment
evaluation with the prototype blade is encouraging and provides a preliminary
indication that the blade design will be successful.

2070°F-Configuration Blades

From the outset of this program, it was recognized that the axial machining
lay selected for the blade dovetail would result in a material performance
decrease. This was demonstrated with the silicon nitride coupon spin test
program. This effect corresponds with lower MOR data obtained with transverse
ground bars when compared with that obtained with longitudinally ground bars.
A program that evaluates MOR bar strength with various thermal exposure treat-
ments has been completed. Improvement in the cross-ground sintered alpha-sil-
icon carbide test bar strength is shown in Table XVIII. The baseline strength
of 294 MPa (42.6 ksi) is nearly equal to that observed with cross-ground qual-
ification bars previously obtained with alpha-silicon carbide spin coupons and
is, therefore, considered typical. Improved strength is shown in the three
conditions tested. The average strength of two groups of bars tested at
1250°C (2282°F) for 24 h is 336 MPa (53.1 ksi), which is 124.6% of baseline
strength. Although data are limited, the improvement shown is significant,
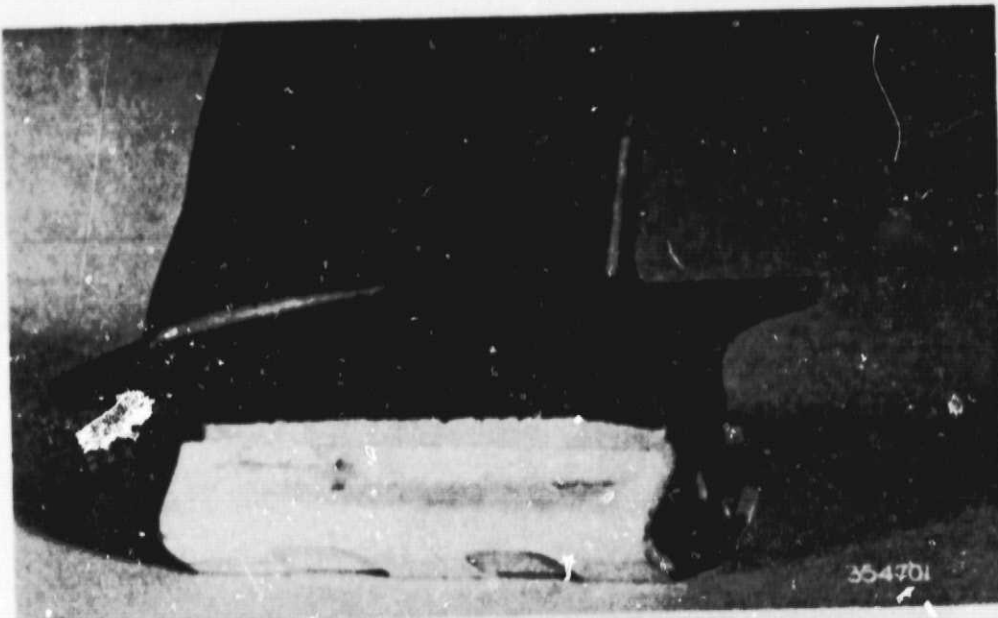
Compliant layer and blade condition
after spin to 37,000 rpm (100.3%)

Failure initiation site
failed at 47,500 rpm (128.7%)

TE80-1345

Figure 97. Spin testing of prototype SiC blade.

and the 1250°C (2282°F) 24-h condition was selected for further evaluation on test blades.

TABLE XVIII.   EFFECTS OF OXIDATION TREATMENT ON CROSS-GROUND ALPHA SILICON CARBIDE
(Room Temperature Testing of MOR Bars)

Exposure conditions (in air)	Number of samples	Average MOR, MPa (ksi)
Room temperature baseline	10	294 (42.6)
100 h at 1250°C (2282°F)	10	356 (51.6)
24 h at 1250°C (2282°F)	10	387 (56.1)
24 h at 1250°C (2282°F)	10	345 (50.1)
24 h at 1375°C (2500°F)	10	354 (51.3)

Ceramic turbine blade development this period centered on initial spin test evaluations of 2070°F-configuration silicon carbide blades. The blades tested were produced by Carborundum prior to completion of their process optimization and had been machined primarily to establish a machining source capability. However, the availability of these blades provided an opportunity for a preliminary evaluation of the 2070°F-configuration design in a spin test situation. Overspeed-to-failure testing has been completed on 14 of these development blades.

First tests were accomplished on a group of six blades, which had been preoxidized for 24 h at 1250°C (2282°F) in air as indicated desirable from the MOD bar evaluations. Two examples of these blades are shown in Figure 98. Each of the six were run overspeed-to-failure and results are listed in the upper portion of Table XIX. Five were tested at ambient temperature, and one blade (S/N 17) was evaluated at 677°C (1250°F). Failure speeds ranged from 105.7% (of 36,905 rated engine speed) to 127.4% with a mean of 116%. This average is below a predicted failure speed of 131%, which is based on material average strength of 342.7 MPa (49.7 ksi) and a Weibull modulus of 7.9.

The flaws found at fracture origins are similar in size and nature to those flaws that control strength in test bars and are not considered abnormal. The blades did have a glassy coating that may have affected part strength. Investigation revealed that the preoxidation treatment had been accomplished using Al_2O_3 furnace set plates. It is felt that this produced the thick glassy layers on these six blades. Silicon carbide furnace set plates have been used in heat treatment of all other silicon carbide bars, coupons, or blades.
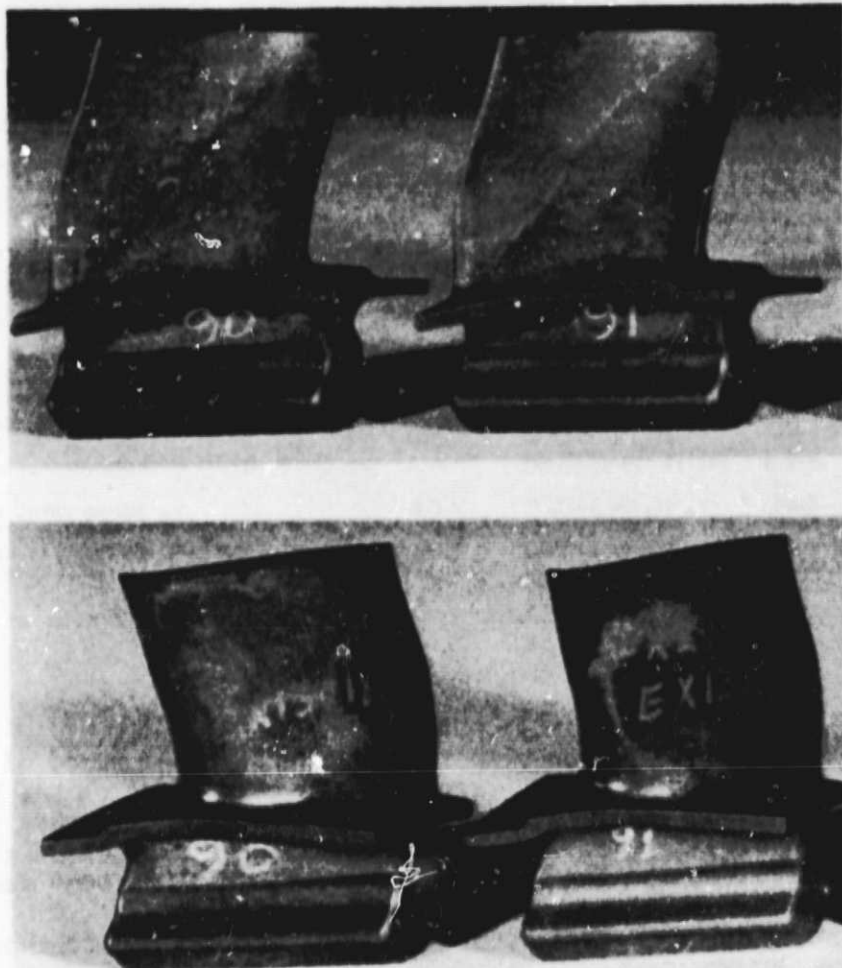
TE80-1346

Figure 98. 2070°F blades prior to spin test--S/N FX24890 and FX24891.

To further assess the effect of the heat treatment on blade performance in spin test, the remaining eight blades were divided into two groups of four each. One group was tested as supplied by Carborundum, and the second group was heat treated prior to test. Test results (Table XIX) indicate a slight advantage for the heat-treated parts. Average failure speed for non-heat-rated blades was 45,175 rpm (122.4% of 36,905 rpm) versus 46,200 rpm (125.2%) with heat treatment indicating a 3.2% rpm advantage, but because of the low sample size, there is no statistical significance to this indicated improvement. Both groups were significantly above the first six blades, which failed at an average speed of 42,875 rpm (116%). The limited spin data and the test bar results indicate a possible advantage to utilization of pretest heat treatment. At least initially, all 2070°F-configuration blades will be subjected to this thermal treatment prior to proof test and subsequent engine test.

TABLE XIX. OVERSPEED-TO-FAILURE TESTING OF 2070°F CONFIGURATION BLADES OF SINTERED SILICON CARBIDE DEVELOPMENT BLADES

Serial No.	Heat treat*	Test temp	Failure speed, rpm (%)	Failure location	Failure origin
12	Yes**	Room	39,000 (105.7)	Attachment	40-μm pore, volume
10	Yes**	Room	46,000 (124.6)	Attachment (cv)	100-μm pore, surface
17	Yes**	677°C (1250°F)	40,150 (109.8)	Stalk	200-μm pore, volume
FX24890	Yes**	Room	40,600 (110)	Attachment	24-μm pore, surface
FX24891	Yes**	Room	47,000 (127.4)	Airfoil at root Platform at acute corner	No flaws at initiations recorded airfoil TE flaws
FX24892	Yes**	Room	44,200 (119.8)	Attachment	Large grain, 70-μm pore, volume
			Avg 6 = 42,875 rpm (116%)		
FX24886	No	Room	45,100 (122.2)	Attachment	Surface, no flaw
FX24885	No	Room	40,500 (109.7)	Attachment	Surface, no flaw
FX24884	No	Room	45,650 (123.7)	Attachment	Surface, no flaw
FX24887	No	Room	49,450 (133.9)	Stalk	Surface, no flaw, looks like low strength failure
			Avg 4 = 45,175 rpm (122.4%)		
FX24880	Yes	Room	42,700 (115.7)	Stalk	100-μm pore, volume
FX24881	Yes	Room	49,800 (134.9)	Attachment	Surface, no flaw
FX24882	Yes	Room	47,300 (128.2)	Attachment	Surface, no flaw
FX24883	Yes	Room	45,000 (121.9)	Attachment	Surface, no flaw
			Avg 4 = 46,200 rpm (125.2%)		

*24 h at 1250°C (2282°F) in air
**Al_2O_3 furnace set plates

The best performing group of four blades reached an average speed of 125.2% of engine speed. Predicted average failure speed is 131% based on the three-dimensional finite element analysis and anticipated material strength (MOR = 343 MPa (49.7 ksi), M = 7.9). The 5.8% discrepancy between prediction and test result is being studied, and the following observations have been made to date:

o Flaws found in failed blade fracture surfaces are similar to those found in test bars.
o Failure initiation sites correspond to predicted zones of peak stress in attachment, stalk, or airfoil.
o The material strength properties of injection molded alpha-silicon carbide have not been established. (A large number of bars are being produced for evaluation.)
o The development blades tested do not represent the final process established for the 2070°F-configuration blade.
o The test blades have no dimensional variations (airfoil twist distortion), and the influence on stress distribution is not established.

GASIFIER TURBINE INLET PLENUM

Fabrication of a silicon carbide plenum is still in the development stage at two suppliers, the Norton Co. and the Carborundum Co. Norton, using a densified silicon carbide (NC 430) material, produced one piece that appeared to be dimensionally acceptable in the as-cast state and structurally sound. Subsequent plenum fabrication attempts resulted in a local area of porosity caused by air entrapment in the mold. A change was made in the mold and Norton is currently evaluating the results.

Carborundum, using a sintered alpha-silicon carbide material, has encountered a variety of problems. Several of the best pieces which were delivered to Detroit Diesel Allison have excessive distortion at inlet and outlet. They currently consider their casting operation to be acceptable, but a change in mix ratio of silicon carbide particles had to be made causing a change in shrinkage resulting in pieces that are 2% oversize. A new mold will be made to correct this. It will include features that Carborundum is confident will also reduce warpage.

2265°F-CONFIGURATION COMBUSTOR CONCEPTUAL DESIGN

The initial design and analysis of a ceramic combustor for the CATE engine has been completed. This includes an analysis of combustor operating conditions, design criteria, and a aerodynamic distribution study.

A layout study of the mechanical design features of the ceramic prechamber combustor was completed. This information has been sent to Norton Co. and Carborundum Co. for their evaluation with respect to manufacturing feasibility. The proposed basic design uses segmented cylindrical construction held in place with metal supporting bolts.

V. CERAMIC REGENERATOR DEVELOPMENT

INTRODUCTION

Ceramic regenerator disk development continued with disk failure evaluation, development of ceramic disk inspection techniques at Corning, disk process improvement using new manufacturing techniques, application of a new rim-finishing technique to reduce disk rim cracking, redesign of the gear adapters, and studies of alternate disk matrices. Regenerator seal development continued with the rig testing for leakage parameters of the three-piece high-temperature seal and friction wear testing of the inboard seal crossarm.

REGENERATOR DISK

Summary

Analysis of remaining portions of the fourth failed disk showed no weak areas as in previous failed disks. Inspection techniques are being evaluated to detect weak areas. New manufacturing processes show encouraging results for eliminating weak areas. Stress analysis shows that most stress is a result of pressure loads in the 1900°F-configuration engine. Disks employing the latest specified rim-finishing technique show no evidence of the previous rim-cracking problems. A new single rim coat shows improved resistance to handling damage and fewer voids. A new one-piece drive gear adapter design eliminates fit and rivet problems and provides disk protection. Discussions were held with NGK-Locke concerning failure of cement joints in their modular extruded disk and potential for further improvement in matrix performance.

Objectives

Objectives of regenerator disk development are to:

- o Improve manufacturing and inspection processes to eliminate weak areas and provide better resistance to handling damage
- o Increase temperature capability to 1200°C (2192°F)
- o Improve regenerator effectiveness, pressure drop and strain tolerance

The approach to achieving regenerator disk development objectives is to:

- o Vary disk manufacturing parameters to determine effect on weak spots
- o Combine most effective manufacturing parameters
- o Confirm strength improvement and repeatibility
- o Prove effectiveness of X-ray, microscopic, and pressue drop inspection to detect weak areas
- o Tighten internal leakage and cell slant limits as indicators of weakness
- o Use stress analysis for interpreting failures
- o Improve rim coating to reduce susceptibility to rim cracking and handling damage
- o Eliminate gear adapter fit and rivet retention problems by redesign
- o Provide guidance to manufacturers of extruded disks to improve performance and strain tolerance

Discussion

Disk Failure

A fourth disk failure occurred out of the 34 disks that have been run in the CATE and transit bus programs. Figures 99 through 101 show the failure. This and the first disk failure were adjacent to the hub, whereas the second and third were at 25- and 28-cm (10- and 11-in.) radii. All four failures were circumferential. Unlike the first three failures, which were short term, this disk failed after 460 h of engine operation. The first and second failures had occurred the first time those disks were exposed to full pressure in the regenerator rig with only 45 min at full pressure. Stress analysis shows that, for the 1900°F-configuration engine, maximum stress at the outside diameter is largely a result of the requirement that the disk rim support full compressor discharge pressure.

The first three disk failures were attributed to local weak areas caused by extreme thinness and/or distortion of the flat separator strip. The matrix is composed of a flat and a corrugated strip spirally wrapped together.

Extensive examination and MOR tests on surviving portions of the fourth failed disk have revealed no weakness responsible for its failure. In fact, this disk was unusually strong. No flat separator strip distortion or thinness was found. The separator strip thickness averaged 0.0125 mm (0.0005 in.) thicker than normal. The cold face was distorted by 50 firing supports resulting in distortion of the corrugated strip with locally high passage skew angles as high as 23 deg and an unusually high incidence of splits in the corrugated strip at joints. This distortion, however, did not cause low MOR. Section III provides additional details.

Disk Inspection

Corning (the disk vendor) is developing cost data for additional disk inspection and tighter limits to screen out weak areas in disks. Costs will include new X-ray and microscopic inspection and tighter limits on internal leakage and cell slant.

X-Ray Inspection

Corning has agreed to an X-ray inspection technique for detecting and rejecting disks with greater than 0.75-mm (0.030-in.) "S" shape in their passages. The "S" shape had been found to cause the flat separator strip distortion, which results in weak areas in the disk. It has been found to occur in about one out of nine disks. Since nine disks are fired at one time, Corning is trying to relate the "S" shape to kiln location.

Microscopic Inspection

After evaluating a DDA-proposed specification for microscopic disk inspection to detect thin separator strips, Corning is formulating an alternative technique.

126
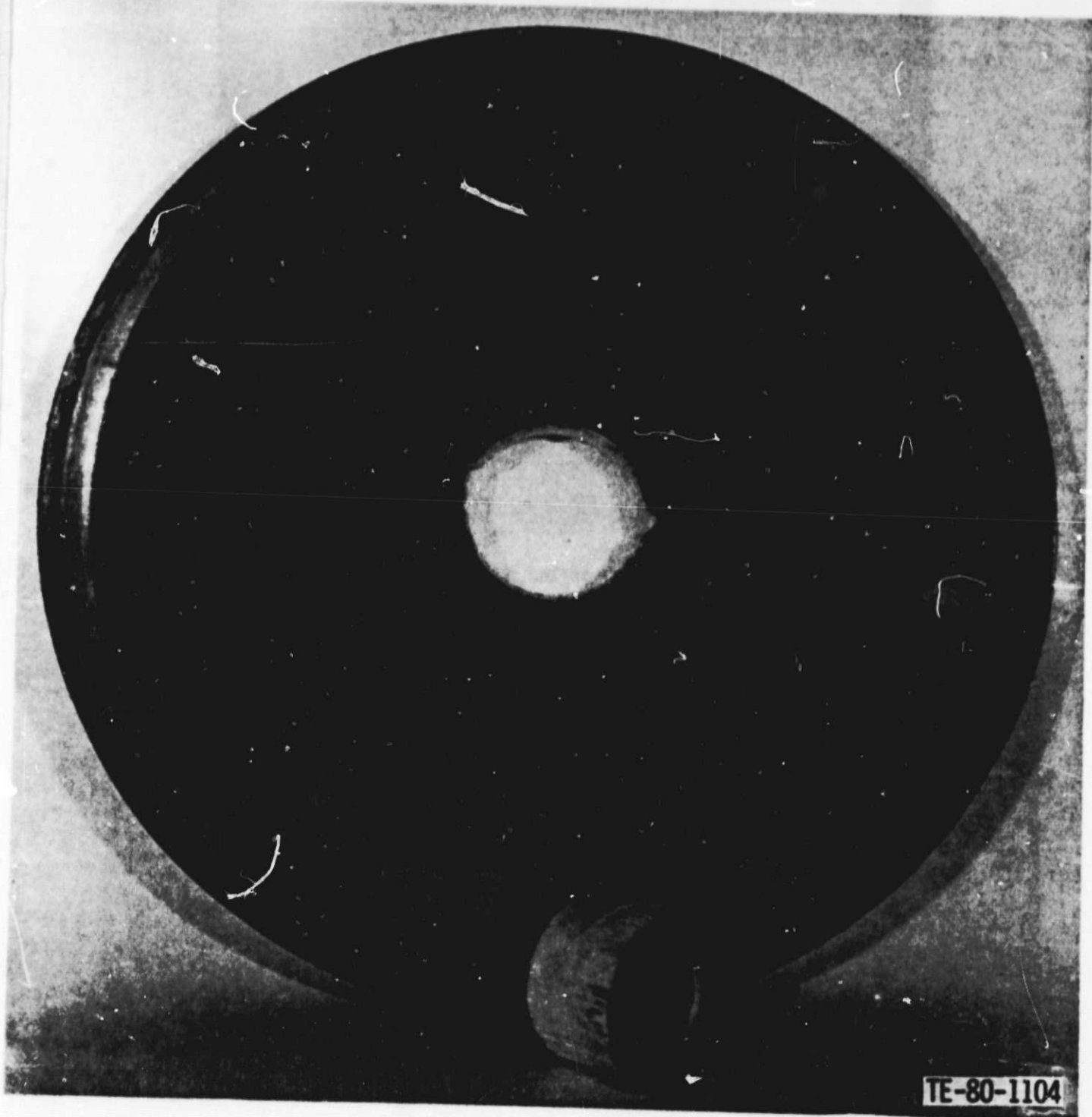
TE-80-1104

Figure 99.   Bus ceramic regenerator disk with hub breakout.
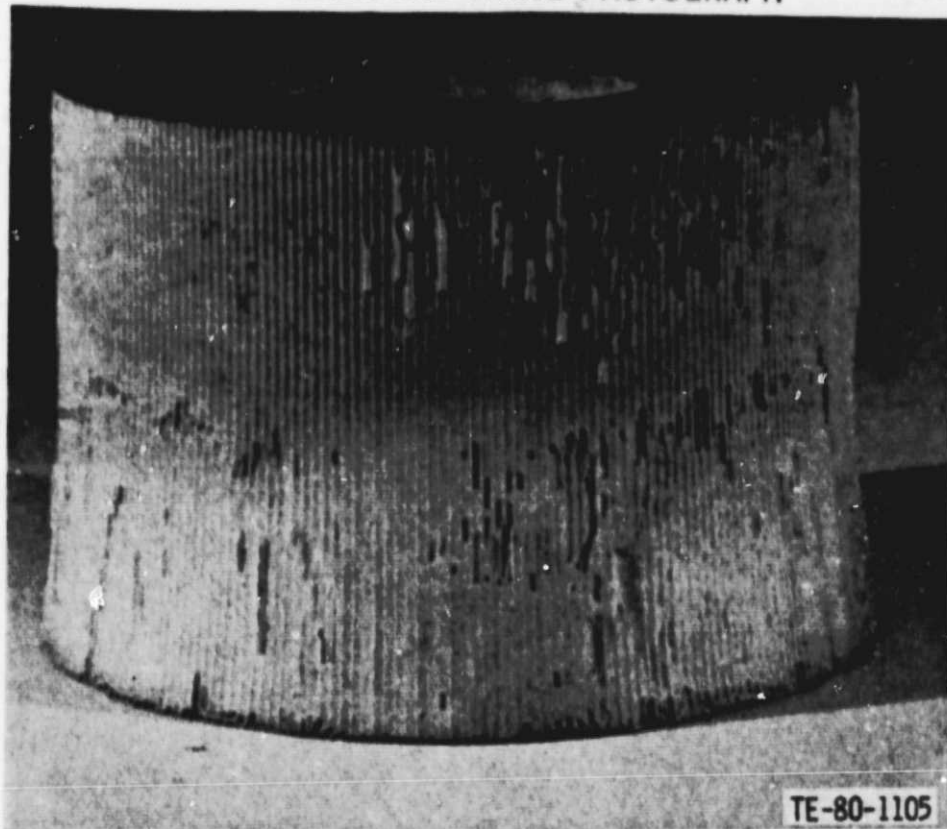
Figure 100. Hub broken out of bus ceramic regenerator disk.
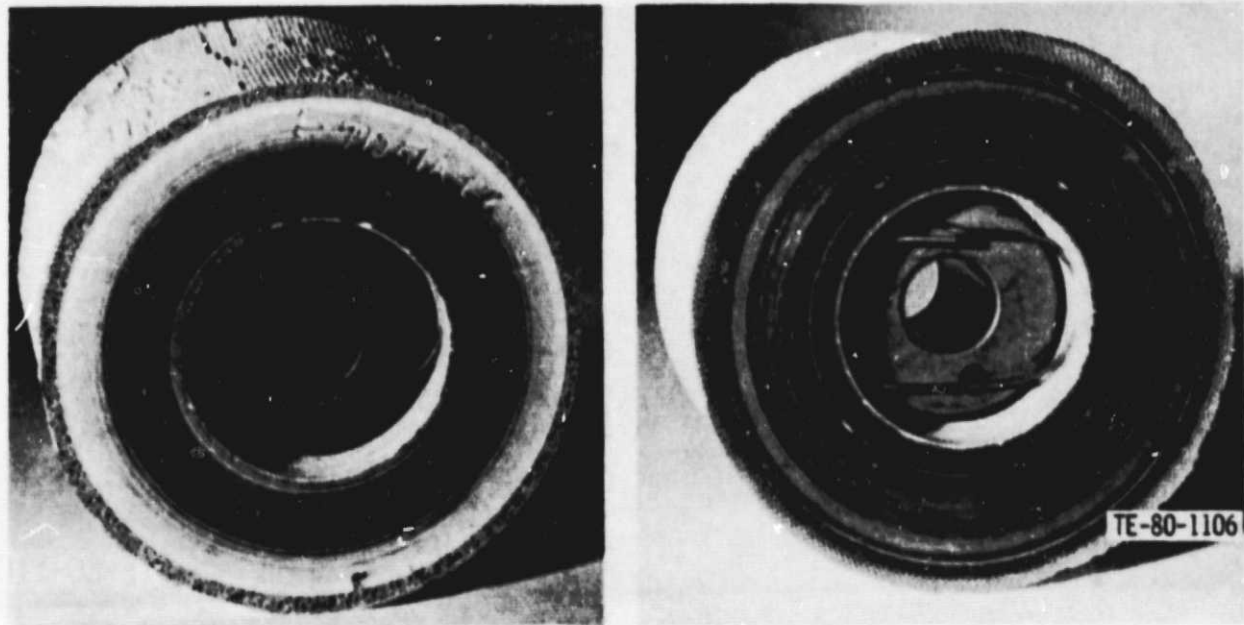
Figure 101. Hub broken out of bus ceramic regenerator disk.

128

Pressure Drop Inspection

Preliminary results using a sensitive anomometer with an 8-mm (0.25-in.) flow diameter suggest that either flow rate or pressure drop may be useful for detecting locally thin walls. Although a very strong correlation between wall thickness and flow has been shown, dispersion of the data is too great for control purposes. Correlation with a third variable, cell count, is being tried to narrow the dispersion. A prior hope that this test could detect distorted separator strips is not justified.

Pressure drop at several locations on the 18-cm (7-in.) radius is presently a part of Corning's acceptance test. At DDA's suggestion, Corning has agreed to perform the test at several radial locations; since the thin separator strips, which have caused failures, have been confined to various specific annular areas. DDA will attempt to establish a minimum limit on pressure drop by statistical analysis of the anemometer, separator thickness, cell count, and MOR data.

Natural Frequency Inspection

No further effort has been applied to use disk natural frequencies or mode shapes to detect weak spots. A disk, with visually verified thin separators for a positive correlation, has not been found. The success of other inspection techniques will determine whether this one is pursued.

Proof Test

Since three of the four disk failures are known to have occurred while operating at maximum pressure instead of maximum temperature, and stress analysis confirms that pressure produces most of the stress at current 1900°F engine conditions, 30% overpressure proof tests will be continued on new CATE disks in the regenrator hot rig. Consideration will be given to a pressure proof test on unfinished disks that would not conform as closely to engine conditions but would avoid high finishing costs on inferior disks.

Disk Process Improvement

Corning has made three disks with a revised process to prevent thin spots in the flat separator strip, which have been shown to cause severe loss in strength. Minimum separator thickness was held to 0.05 mm (0.0020 in.) where separators as thin as 0.02 mm (0.0003 in.) have been seen and 0.06 mm (0.0024 in.) is nominal. Maximum thickness was 0.10 mm (0.0040 in.) similar to previous disks. The new process was selected from an experiment with several process variables. Samples from these three disks will be tested to ensure that higher strength has been achieved. More disks will be made with the new process to verify repeatibility.

Disk Stress Analysis

Since three of the four regenerator disk failures were known to be at maximum pressure rather than maximum temperature, the stress model and program were extensively revised to represent more accurately true pressure loading and to define the effects of pressure loads better. At current 1900°F-configuration conditions, pressure loads were found to be the largest contributor to stress.

Thermal stress was only significant near the rubber gear attachment where rubber expansion causes stress. No failures have been related to this rubber expansion. Stress calculations are being analyzed with respect to matrix strength to interpret the failures. Details will not be presented until that analysis is completed.

Revisions to the stress program and model follow:

1. Circumferential pressure distribution imposed by the seal crossarm pressure drop was modeled.
2. Lateral pressure distributions across seal wearfaces and on the sides of the rubber gear attachment were modeled.
3. Local seal friction loads, gear loads and bearing reaction loads were modeled in their true direction instead of an approximation as unidirectional.
4. Drive torque was reduced to conform to test experience.

Disk Rim Cracking

Many disks have been rig and engine tested with a new technique for applying the rim coating cement and the face filler cement and with ground bevels on the rim corners. No cracks of the previous type have been seen; however, difficulty in joining the two cements has promoted experiments with a single cement for both rim coating and face filling. Two disks with the single cement have accumulated 600 and 329 h. The single cement appears superior, particularly in its resistance to handling damage, and has been specified in new orders.

Gear Adapter

Additional changes to the mounting adapter shown in Figure 102 have been made.

A rivet failure problem, which occurred when one rivet was substituted for another in the attachment of the gear, caused a disk to be damaged beyond further use. The mechanism of failure is shown in Figure 103. As shown in Figure 104 when rivet A is installed the head of the rivet "pull" shank is well trapped in the rivet collar. This head of rivet B is not well trapped, and it works loose when the disk assembly is used. When the disk is at room temperature, dimension X is too small to let the rivet head work into the space between the gear and matrix rim, but when the gear expands with temperature and is distorted further by action with the drive pinion, the rivet head can work its way into this space and dig into the core rim as shown in Figure 104. this caused failure of disk E77250A (GM15-14) as shown in Figure 105. The ring gear has been removed from the disk in order to show the damage to the core.

Rivet A is again being used in all new disk fabrication and all disks in which rivet B had been installed have been reworked to use rivet A. During repair of one of these disks, slight damage to the rim was encountered in which a rivet head was actually found lodged in the damaged area adding further credibility to the failure theory.

POOR FIT OF ADAPTER PIECES AND
PULL DOWN ACTION OF RIVET HERE
CAUSES DELAMINATION BETWEEN
DISK AND ELASTOMER HERE

24 GEAR RETENTION
PINS SLIP FIT INTO
GEAR AND WELDED TO
ADAPTER
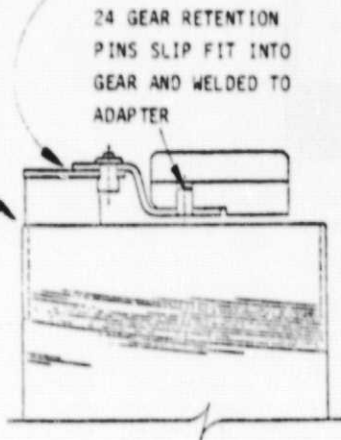
12 WELDED DOWN GEAR
RETENTION PADS

ELASTOMER TO BE
BACK FILLED FROM
ONE SIDE ONLY

A. CURRENT DESIGN
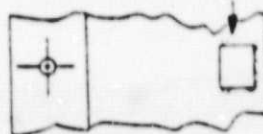
B. CHANGES PROPOSED TO
PROVIDE BETTER DISK
PROTECTION
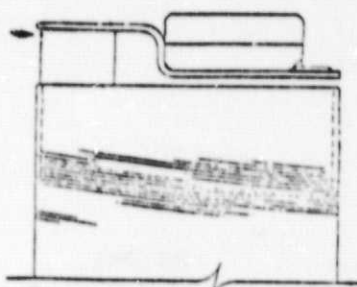
C. ONE PIECE RIVETLESS
ADAPTER DESIGN

TE-80-1108

Figure 102.   Evolution of ring gear mounting adapter to provide improved
matrix protection and eliminate rivet problems.
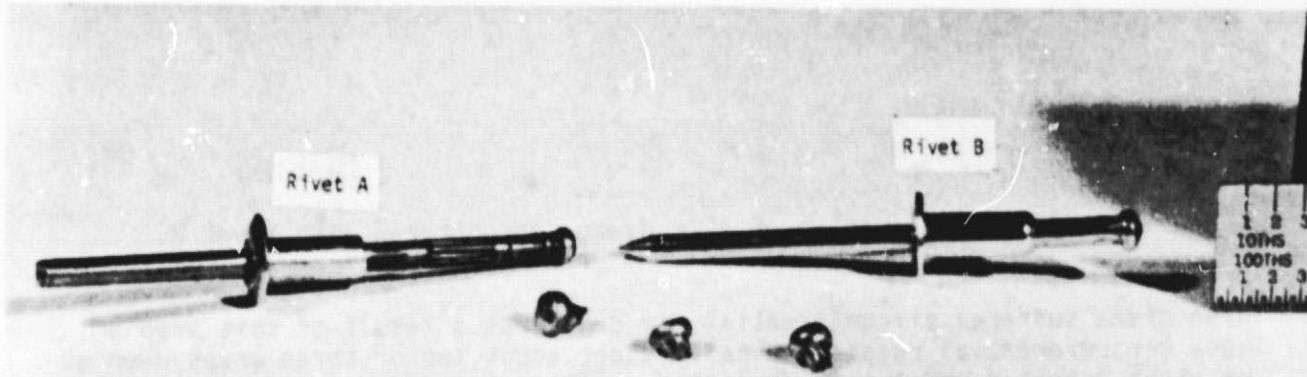
Rivet A

Rivet B

TE-80-1109

Figure 103.   Unused rivets A and B and rivet heads that came loose from
used type B rivets.

The second rivet-related problem encountered was a result of poor fit at the
rivet joint between the two metal pieces of the gear adapter as shown in Fig-
ure 102. On some disks, there is a gap between the adapter pieces that is
pulled closed by the rivet thus putting tension on the disk-elastomer joint.

RIVET A -

HEAD REMAINS

WELL TRAPPED
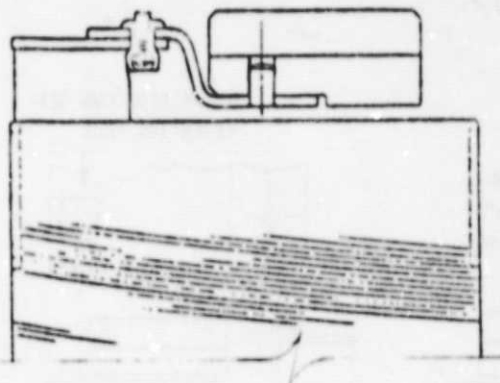
RIVET B

HEAD COMES

OUT OF COLLOR

AND GETS CAUGHT

BETWEEN DISK

AND GEAR
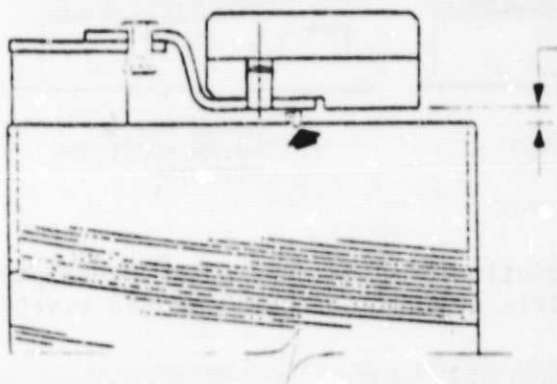
TE-80-1110

Figure 104. Mechanism of disk damage encountered with rivet B.

Three disks suffered circumferential rim cracks as a result of this problem.
These circumferential cracks typically start about two or three wraps deep at
the rivet location and extend about 2.5 cm (1 in.) in either direction to the
disk O.D. They are self limiting as rubber tension developed by the rivet
pull is relieved. Rubber tension holds them open, and little debris is gene-
rated. Unlike the earlier cracks resulting from rim cement mismatch, they
occur only on the cold side under the rubber. Some have been filled with RTV
rubber to maintain the attachment and prevent generation of debris. Subse-
quent operation has been satisfactory. Remaining assembly of two-piece adap-
ters will be subject to limits on adapter fit prior to riveting.

Damage caused by rivet heads as well as circumferential disk cracks caused by
a poor fit between the gear adapter pieces led to a design that eliminates the
rivet joint. This is shown in Figure 102. Having gained experience in
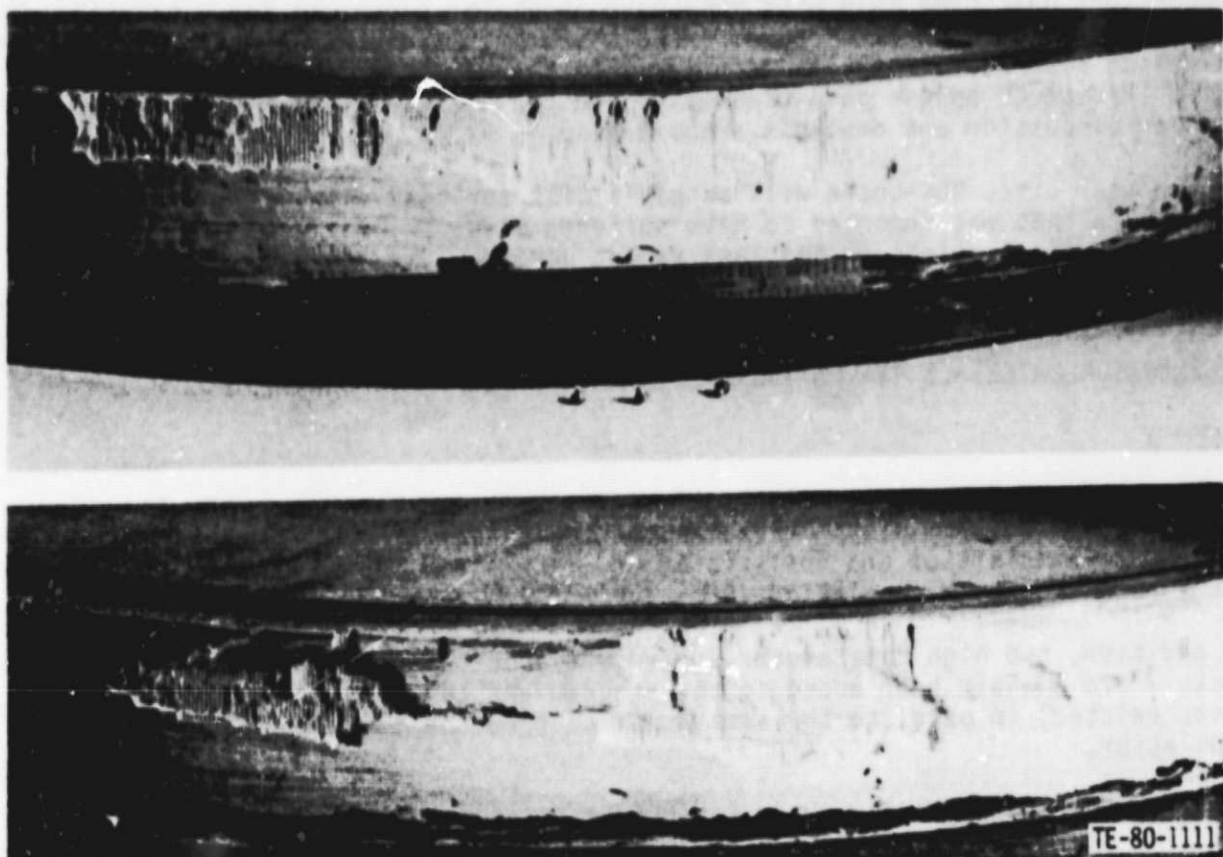
Figure 105. Damage caused to disk GM15-14 by heads of rivet type B.

elastomer application with the current design, it is felt that back filling the elastomer from one side only, as required with a one-piece adapter, is practical.

1100°C (2012°F) Disk Testing

A total of 614 h of testing have been accumulated on Corning 1100°C (2012°F) alumina silicate disks with 443 h on the highest time disk. These disks are rated 100°C (180°F) higher than previous Corning disks. No operating problems have been experienced to date.

When compared to Corning 1000°C (1832°F) disks, these disks have been observed to exhibit the following characteristics:

o 5% less open area
o 80% less internal leakage
o 11% more pressure drop
o 1.3% more effectiveness
o 85% more strength (based on one 1100°C (2012°F) disk)

133

Alternative Disk Matrices

Discussions have been held with NGK-Locke about the prospects for extruding matrices with thinner walls, greater heat transfer area, and greater strain tolerance than the triangular matrix, which they are currently supplying for test. Prospects appear good that NGK-Locke can produce an improved matrix. Further discussion and analysis are planned.

In the mean time, NGK-Locke will supply a disk for test with the same triangular matrix that was reported to have suffered premature failure because of defective cement joints in the last report period. The new disk will incorporate rectangular blocks cemented together rather than sector-shaped blocks. This arrangement will allow better control of the cement joints.

REGENERATOR MATERIALS EVALUATION

Summary

During the past 6 mo, the analysis of the as-received condition data for the first 1100°C (2012°F) disk matrix has been completed, and the same three variable data acquisition and analysis procedure was applied to the 1000°C (1832°F) disk sample population.

In addition, two high time engine and regenerator test rig exposed disks--disks 7 and 8--have been added to the program and the information from these disks related, in part, to the data acquired from the 1000°C (1832°F) disk population.

Finally, the transient-low cycle fatigue tests of thermally exposed 1100°C (2012°F) disk samples has been started with some 800 simulated truck-bus acceleration-deceleration cycles completed without fracture or visible cracking.

Objectives

The primary objective for this reporting period was to investigate mechanical behavior of the Corning 1100°C (2012°F) disk material. A second objective was to characterize the surface structure of high time engine tested disks.

The approach used to link the data base, acquired using randomly selected disks from the ongoing production from the supplier, to the engine exposed disk population consists of two parts. The first of these consists of disk failure analyses, the second part is made up of high time engine (or regenerator rig) disks, which are damaged or retired from service.

Discussion

Characterization of 1100°C (2012°F) Disk Material

The initial results for the 9461 disk material (rated temperature 1100°C (2012°F)) showed a marked increase in tangential MOR over the 9460 disk population. This has been fully confirmed for the four radial positions sampled. A comparison of the strongest 9460 disk with the 9461 disk is given at four radii in Table XX.

TABLE XX.   COMPARISON OF AS-RECEIVED MOR VALUES FOR 9460 AND 9461 MATRICES
(Mean minus two sigma (lower 95% confidence limits))

	Radial position, cm (in.)			
Disk	25.4 (10.0), MPa (lb/in.^{2})	20.3 (8.0), MPa (lb/in.^{2})	15.2 (6.0), MPa (lb/in.^{2})	10.1 (4.0), MPa (lb/in.^{2})
HRD-AB-3 (9460)	1448 (210)	1724 (250)	1276 (185)	1379 (200)
HRD-AC-1 (9461)	2193 (318)	1813 (263)	1786 (259)	1869 (271)

Clearly the strength of the 9461 disk is well above the highest strength 9460
matrix, sampled to date, at all radii.

A concentrated effort was made to identify the cause for the increase in
strength.   Simple comparison of the separator wall fracture plane thickness
established that the 9461 disk was well within the thickness distribution es-
tablished for the 9460 disk sample population.   Table XXI shows the compari-
son at a radius of 25.4 cm (10.0 in.).

TABLE XXI.   COMPARISON OF FRACTURE PLANE SEPARATOR WALL THICKNESSES AT
25.4 cm (10.0 in.)

Disk	Type	Mean thickness, mm (in. x 10^3)	Range, mm (in. x 10^3)
GM14A-23	9460	0.042 (1.66)	0.055/0.029 (2.17/1.15)
HRD-AD-3	9460	0.056 (2.20)	0.067/0.045 (2.62/1.78)
GM15-05	9460	0.057 (2.23)	0.084/0.029 (3.30/1.14)
GM15-01	9460	0.075 (2.94)	0.094/0.063 (3.71/2.49)
HRD-AC-1	9461	0.056 (2.22)	0.103/0.031 (4.04/1.21)

Similarly, the skew angle distribution was well within the distribution for
the 9460 disks.   Electron photomicrographs showed no significant differences
in grain size, although the amount of mullite crystals in the grain boundaries
are apparently lower in the 1100°C (2012°F) matrix than in the 1000°C (1832°F)
material.

Multiple correlation analysis, applied to the 1100°C (2012°F) matrix, shows
that the sensitivity of the MOR to wall thickness and skew angle, measured by
the regression coefficients, is very low.   The coefficients are ~43 for the
wall thickness and ~7 for the skew angle.   Figure 106 presents the correlation
as well as a three-dimensional plot showing the average and the range of the
two variables.

$Y = 303 + 42.8X_W - 7.1X_S$
X_W correlation at 0.025 to 0.01,
X_S correlation at 0.10 to 0.05 level

TE-80-1100
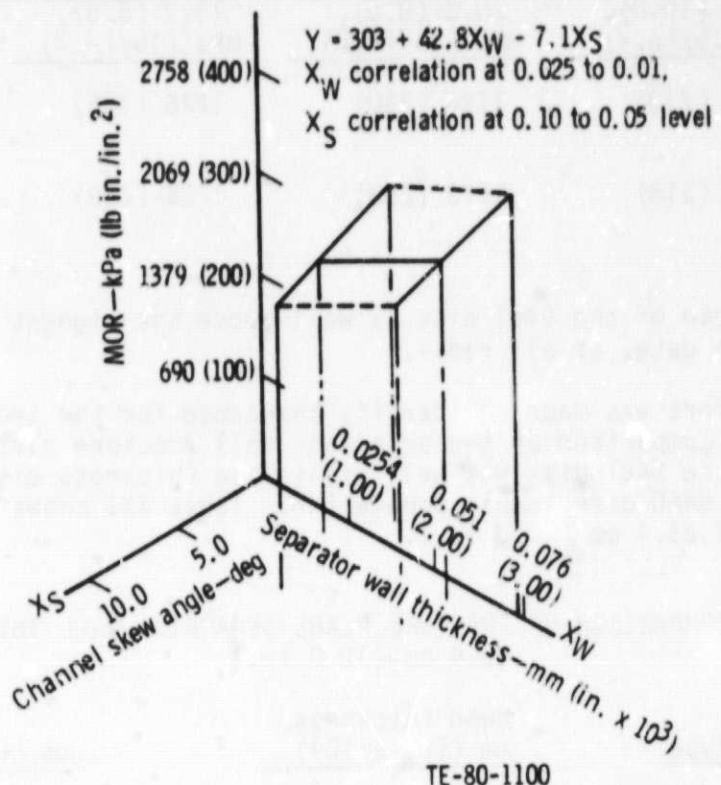
Figure 106. Multiple correlation of separator wall thickness, channel skew
angle, and tangential MOR for 9461 matrix, material HRD-AC-1,
radius = 20.32 cm (8.0 in.) as-received.

Structural Analysis of High-Time Disks

During the reporting period, two high-time engine and rig exposed 9460 disks
were added to the program. The first of these, Disk GM15-01, Disk 7, failed
after 460 h in the regenerator test rig where it accumulated 300 h of a tran-
sient cycle simulating a once per minute engine acceleration from idle and
return to idle, plus 160 h of steady-state 100% power. Analysis of the fail-
ure established that the MOR level is high overall, no radial strength grad-
ient is evident, the channel skew angle was in the normal range (11 to 2 deg),
and channel distortion was not present. No assignable cause was identified
for the failure, and the data plotted well within the one sigma band for all
9460 disks correlating wall thickness and MOR as shown in Figure 107.
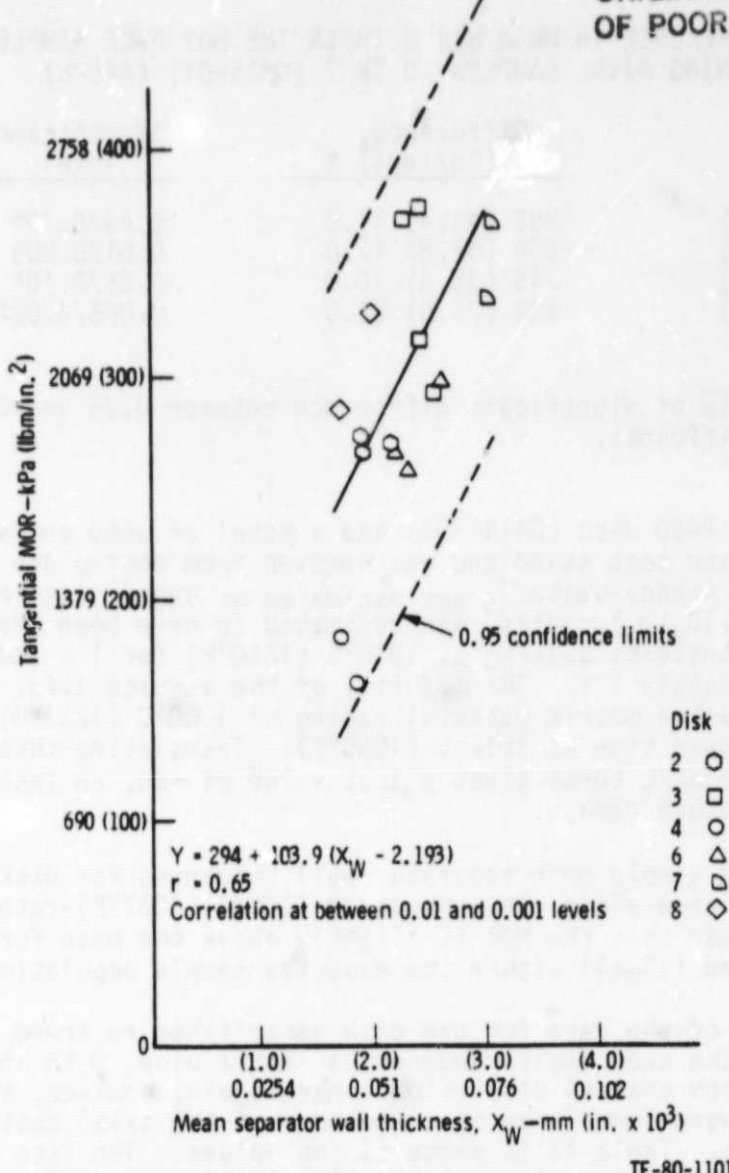
Figure 107. Correlation of sample mean separator wall thickness and MOR.

Inspection of the data showed, however, that the hot face axial position test bar MOR values were low when compared to the values for the remainder of the disk thickness at all radii. Accordingly, a simple test for difference in means was used to test for significance of the difference. Table XXII tabulates the difference between the remainder of the disk mean MOR and the hot face MOR. The analysis indicates that real differences exist at radii of 20.3 cm (8.0 in.) and 10.2 cm (4.0 in.).

TABLE XXII. DIFFERENCE IN MEAN MOR BETWEEN THE HOT FACE SAMPLES AND THE
REMAINING AXIAL SAMPLES--DISK 7 (GM15-01) (460 h)

Radius, cm (in.)	Difference, KPa (lb/in.^{2}) %		Significance level
25.4 (10.0)	285 (41.4)	11.0	0.25/0.10*
20.3 (8.0)	399 (57.8)	17.0	0.01/0.005
15.2 (6.0)	245 (35.5)	10.0	0.25/0.10*
10.2 (4.0)	524 (76.0)	21.0	0.005/0.001

*Probability of significant difference between 0.25 and 0.10
(not significant).

The second high-time 9460 disk (GM14A-07) had a total of 3050 engine hours
split between truck and test stand and was removed from engine use in service-
able condition. The steady-state T_6 was estimated at 788°C (1450°F). The
hot spot, at 25 cm (10 in.) radius, was estimated to have been 840°C (1550°F)
with acceleration transients peaking at 1010°C (1850°F) for 1 s and 954°C
(1750°F) for approximately 2 s. The majority of the service life, then, is
estimated to be below the matrix material rating of 1000°C (1832°F) with a
relatively short elapsed time at 1010°C (1850°F). Translating this time-tem-
perature history into $\Delta L/L$ terms gives a $\Delta L/L \times 10^6$ of ~50, an insignificant
level of thermal exposure damage.

When the mean MOR and sample mean separator wall thickness for disk 8
(GM14A-07) are correlated along with the other 1000°C (1832°F)-rated disks, in
Figure 107, it is clear that the MOR is slightly above the mean for the wall
thickness measured and is well within the expected sample population variance.

Detailed examination of the data for the disk established no trend for separa-
tor wall thickness, the skew angle range was a little wide, 0 to 15 deg, but
was not associated with channel distortion. Here again, however, the hot face
test bar MOR values were lower than the remainder of the axial test bars from
a given sample radius. Table XXIII presents the values. The loss in strength
is larger here, and the number of statistically significant differences is up
relative to disk 7.

TABLE XXIII. DIFFERENCE IN MEAN MOR BETWEEN THE HOT FACE SAMPLES AND THE
REMAINING AXIAL SAMPLES--DISK 8 (GM14A-07) (3050 h)

Radius, cm (in.)	Difference, KPa (lb/in.^{2}) %		Significance level
25.4 (10.0)	367 (53.3)	18.0	0.50/0.25*
20.3 (8.0)	643 (93.2)	20.0	0.10/0.05
15.2 (6.0)	1114 (161.5)	42.0	0.001
10.2 (4.0)	1009 (146.3)	36.0	0.005/0.001

*Not significant.

A series of tests were performed on the hot face samples with particular attention to elemental analysis and morphology of the friction and wear contact areas of the seal contacted surface. The results of an electron beam microprobe analysis of the hot face seal contact areas, and comparison probes run on the cold face of disk 7 (GM15-01), are shown in Table XXIV. The values listed are only an approximation since they are computed from relative counts.

TABLE XXIV. MICROPROBE ANALYSIS OF RELATIVE METALLIC ELEMENT COUNT--DISK 7 OF (GM15-01) (460 h)

Radius and test bar	Al	Si	S	K	Ca	Fe	Ni	Cr
10.2 cm (40 in.) B_1 cold face	14	86	--	--	--	--	--	--
10.2 cm (40 in.) B_1 hot face	7	45	1	--	1	--	45	1
10.2 cm (40 in.) C_1 cold face	14	86	--	--	--	--	--	--
10.2 cm (40 in.) C_1 hot face	6	42	1	TR	1	TR	50	--

Both the cold and hot face probe analyses reflect the expected mole ratio of alumina to silica in the 9460 matrix. The hot face data show the expected pickup of sulfur from the fuel and iron and chromium from the engine superalloy hot components. However, the high level of nickel and the low level of the calcium are both surprising in view of the very brief contact time of a given point on the matrix with the seal and the 70:30 wt % ratio of $NiO:CaF_2$ in the seal.

Accordingly, an experimental design was laid out for disk 8, specifying multiple samples and using the microprobe in 1) the point analysis mode on the seal/matrix contact surface, 2) in the scan mode in the axial direction to look for diffusion gradients, and 3) as an electron microscope for contact surface morphology. All samples were cleaned ultrasonically in distilled water to remove loose debris (recognizing that surface debris containing CaF_2 would lose the CaF_2 by dissolving it). Table XXV gives the results for the point analyses on the seal/matrix contact surface.

TABLE XXV. MICROPROBE ANALYSIS OF RELATIVE METALLIC ELEMENT COUNT--DISK 8 (GM14A-07) (3050 h)

Radius and test bar	Al	Si	S	Ca	Fe	Ni	Cr
25.4 cm (10.0 in.) B_2	No foreign material (no seal contact)						
20.3 cm (8.0 in.) T_1	2582	31608	1306	--	1765	155237	2936
15.2 cm (6.0 in.) B_1	11599	89575	641	--		44442	
B_1	5605	56074	694	--	892	82317	1207
10.2 cm (4.0 in.) T_2	No foreign material (no seal contact)						

The aluminum-silicon ratio has moved downward, compared to disk 7 and the expected value of the as received matrix, sulfur is present in all contact areas, and the superalloy constituents are present. Nickel, however, has increased significantly from the levels seen in disk 7. Calcium was not detected in the contact surfaces as sampled. The absence of all foreign material in the two sampled areas, at the outer and inner radii, where no seal contact was observed points up the findings of the electron photomicrographs.

The seal/matrix contact areas, in all areas where photomicrographs were made, were small fractions of the total projected area of the matrix. Figure 108 typifies the contact areas seen (the sliding seal material scuff marks can be discerned in the flattened area of contact). When this flattened area is examined at 1500X, the surface shown in Figure 109 is seen. The mosaic crack pattern is strongly suggestive of a remelted surface. Table XXV at the 15.2 cm (6.0 in.) radius gives the microprobe estimate of the cation chemistry. (Oxygen was the anion in all cases.)

Two things emerge from this data. First, significant transfer of nickel from seal to AS matrix is taking place, both at 460 and 3050 h. Second, both the mosaic crack pattern and approximate calculations indicate that temperatures well above ambient are generated by frictional heat at the areas of contact. The highly localized nature of this thermal effect is caused by the low thermal diffusivity of the AS matrix, 0.012 cm^2/s (0.04 ft^2/hr). The role of the calcium fluoride is not clear at this point.
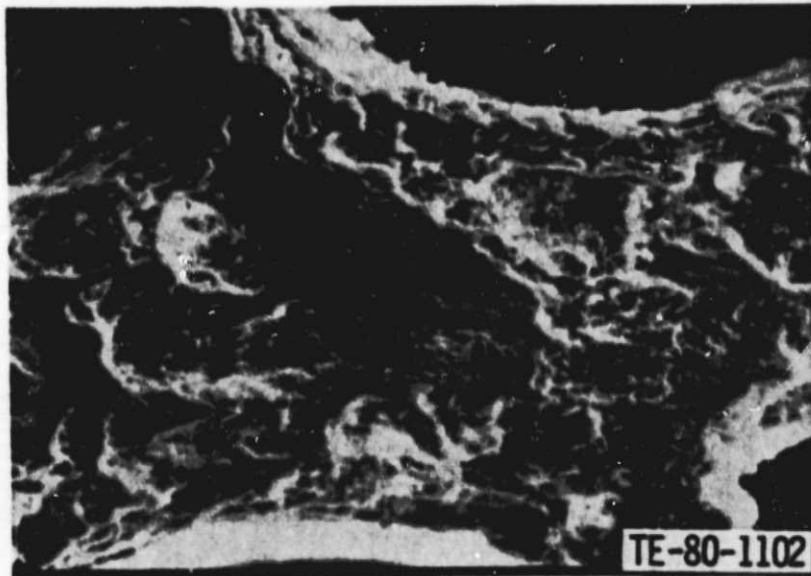
Figure 108.   Disk 14A-07, 3050 h, radius 15.2 cm (6.0 in.)
seal/matrix interface.   (300X)

Figure 109.   Disk 14A-07, 3050 h, radius 15.2 cm (6.0 in.)
seal/matrix interface. (1500X)

Based on the only 1100°C (2012°F) material disk sampled to date the 1100°C (2012°F) matrix is stronger than any 1000°C (1832°F) material disk tested. This increase in strength is the result of a variable that lies outside the channel skew angle/cell distortion and separator wall thickness variation, which account for a major portion of the scatter in disk strengths. Three more 1100°C (2012°F) disks are scheduled and must be tested before any final resolution can be made.

Two high-time 1000°C (1832°F) engine disks have been tested, and a statistically significant loss in strength noted in the hot face layer of both disks. The greatest loss in strength, found in the longest disk, was not significant when compared to the calculated stress. Electron beam examination of the seal/matrix interface shows a large transfer of nickel oxide to the matrix and indicates that high-temperature conditions exist at the interface because of friction, which causes an easily recognized mosaic cracking of the interface.

REGENERATOR SEAL

Summary

Testing the first three-piece high-temperature regenerator seals showed leakage problems resulting from weld distortion and adverse cooling effects. The nickel oxide-calcium floride crossarm wearface material has shown problems of

141

chemical stability at temperatures above 927oC (1700oF) resulting in high friction and wear under laboratory conditions but is capable of significant life at 982oC (1800oF) under engine conditions. Best friction and wear was achieved with 10% CaF_2, while best thermal expansion match was achieved with 30% CaF_2. One-piece seals with 30% CaF_2 showed less leakage in both rig and engine operation. The high-temperature regenerator rig experienced excessive oxidation requiring burner and liner modifications.

Objectives

Objectives of regenerator seal development are to:

o Develop an inboard seal capable of low friction, wear and leakage for operation at 982°C (1800°F) regenerator inlet gas temperature in the 2265°F-configuration engine
o Provide a regenerator rig capable of measuring seal leakage at 2265°F-configuration engine conditions

The approach to achieving regenerator seal development objectives is to

o Apply compressor discharge air to cool the inboard seal crossarm sufficiently to prevent creep but without introducing thermal warpage to cause leakage
o Try cooling crossarm wearface to provide chemical stability
o Seek a crossarm wearface compound that is more chemically stable and provides a better thermal expansion match with the substrate

o Alternately try a design with a flexible isolator between wearface and substrate
o Counteract thermal coning of seal rim to reduce leakage and concentrated wear

Discussion

Three-Piece High-Temperature Seal

Seal leakage data have been obtained on the first two three-piece high-temperature seals in the hot regenerator rig, which closely simulates engine operation. The engine conditions simulated were for the 2070°F-configuration engine. Table XXVI shows the percent leakage obtained for each seal at three engine speed conditions with and without cooling air admitted to the seal crossarm.

TABLE XXVI. SEAL LEAKAGE

Engine speed condition	With cooling air		Without cooling air	
	Seal H3048	Seal H3049	Seal H3048	Seal H3049
50% (idle)	16.6%	14.1%	14.2%	9.5%
80%	6.6%	4.0%	4.2%	2.3%
100%	6.4%	7.1%	4.9%	3.5%

Two causes of excess leakage are evident from Table XXVI.

1. Leakage is excessive at the 50% or idle speed condition. Prior tests in the static, cold leaf leakage rig, where leak paths can be identi- fied, showed that much of this leakage was a result of bow in the crossarm caused by weld distortion. This bow was concentrated near the ends of the crossarm where joints between the crossarm and rim pieces admit air to the wearface making it extremely difficult to blow the bowed seal wearface down against the regenerator disk for sealing. The processing of the second pair of three-piece seals is being altered to reduce this bow. The third pair of three-piece seals will incorporate a thinner platform in the weld area to reduce bow resulting from weld distortion.

2. The data also show that crossarm cooling air causes excess leakage. Figure 110 shows how compressor discharge cooling air is admitted to both ends of the crossarm and through holes at the center of the crossarm and is channeled along the crossarm by sealing leaves to exit ports in each half of the arm. The excess leakage with cooling is believed to be due to uneven cooling causing thermal distortion of the crossarm resulting in poor fit against the regenerator disk face. Tests, previously reported, showed tht the ends of the cross- arm are cooled to a lower temperature than the mid portion. Ports and baffles will be modified to better equalize crossarm temperatures and decrease thermal distortion. Designs that introduce cooling air into a porous compliant interlayer between the wearface and the structural platform are being considered to reduce thermal distor- tion further. This compliant arrangement has been successfully uti- lized without cooling air in the past.

Testing of these seals was limited to $886^{o}C$ ($1627^{o}F$) gas temperature until rig modifications were completed. Eight hours of endurance were run at $886^{o}C$ ($1627^{o}F$) gas temperature to check for permanent thermal distortion and wearface stability. No distress was evident.

Inboard Seal Crossarm Wearface

A reaction has been encountered between the CaF_2 lubricant in the inboard seal crossarm NiO/CaF_2 wearface and the AS regenerator disk material during laboratory friction and wear testing at $982^{o}C$ ($1800^{o}F$). The reaction re- sulted in very high seal and disk wear, which has not been encountered in full-scale rig or engine tests probably because of the cooling and self-clean- ing effects of airflow. The wear debris has been identified as calcium flouro silicate. In contrast, an 85% NiO/15% CaF_2 seal, which was run 15 h at $982°C$ ($1800°F$) gas temperature in the hot regenerator rig, simulating engine conditions, showed only slight chalking of the wearface, which was analyzed to be $Ca(OH)_2$. Drive torque was normal during the run. This test will be con- tinued to determine the life of the NiO/CaF_2 wearface at extreme CATE engine conditions. NiO/CaF_2 oxidation samples expanded and became very soft after standing one month at room conditions following 20- to 1000-h exposure at $982°C$ ($1800°F$) in air. CaF_2 heated in a platinum crucible formed CaO at a considerable rate in air at $982^{o}C$ ($1800^{o}F$) showing the basic instability of the CaF_2 lubricant. The laboratory friction and wear tests show that the lowest friction and wear are obtained with 90% NiO/ 10% CaF_2. No NiO/CaF_2

TE-7737

Compressor discharge air

Regenerated air side

Exhaust gas side

Section A - A

Inboard seal

Compressor discharge air

Enlarged sectional view of hub region
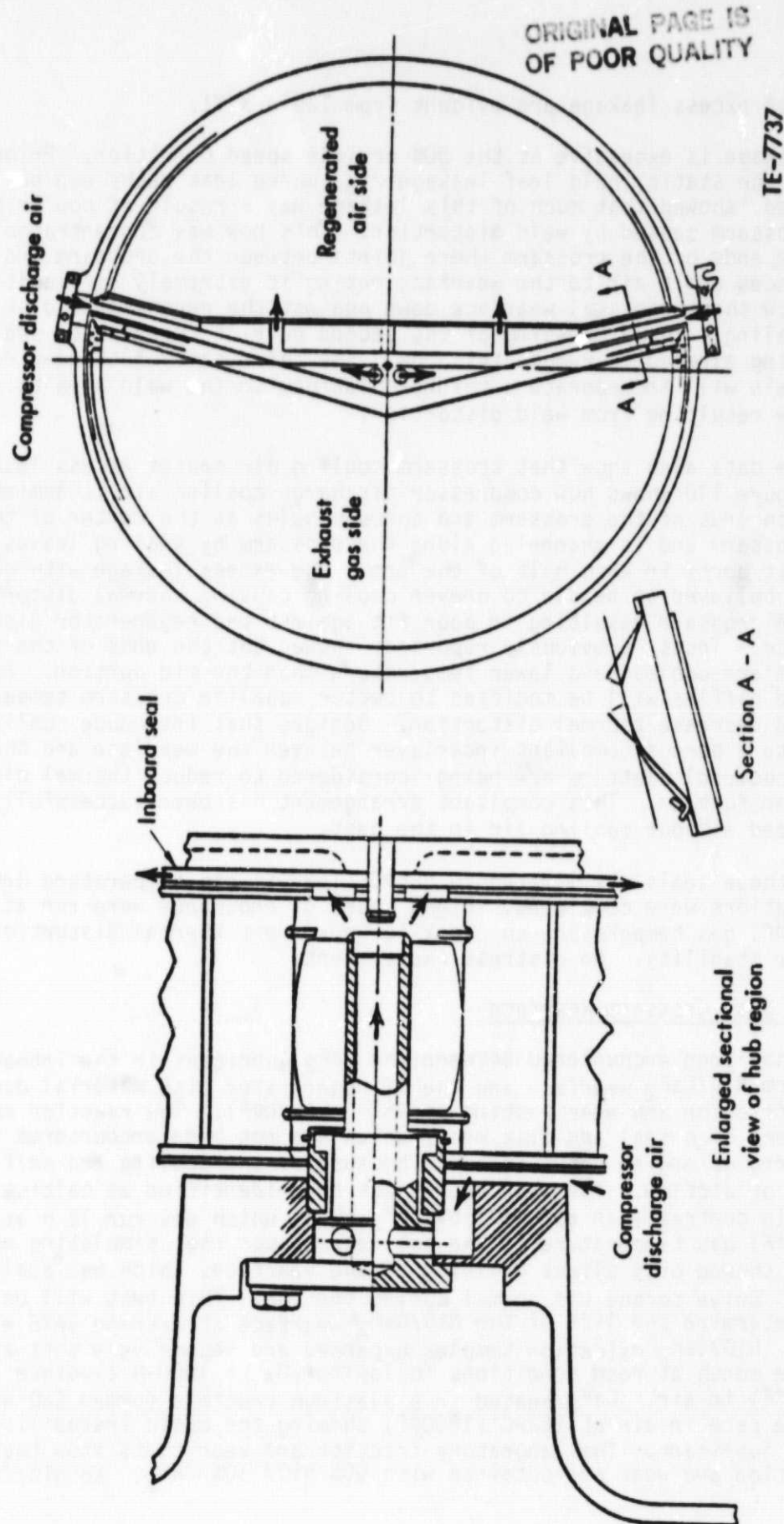
Figure 110. Regenerator inboard seal cooling air system.

mix performed satisfactorily at 982°C (1800°F) in the laboratory friction and wear rig. Specific data are included in the Materials Development section of this report. Laboratory friction and wear tests have typically produced higher wear rates than engine tests possibly because:

o Airflow in the engine and in the full-scale hot rig has two benefits that are not present in the laboratory friction and wear rig:
   o Airflow carries away excess heat generated by friction.
   o Airflow carries away reactive powdered wear debris.

o Seal samples in the laboratory wear rig receive radiative heating whereas in the engine and full-scale hot rig, seals experience radiative cooling.

A 500-h wear test has been completion on 90% NiO/10% CaF_2 wearface material at 871°C (1600°F) in the laboratory rig. Stabilized wear rate was 0.075 mm/1000 h (0.003 in./1000 h), which is quite acceptable. The temperature will be increased to 927°C (1700°F) to define the limit.

Tests for thermal expansion mismatch between the NiO/CaF_2 wearface have been completed. The 70% NiO/30% CaF_2 mixture proved to have the least permanent set after the first thermal cycle and the least bow at 982°C (1800°F). Increasing CaF_2 content up to 30% CaF_2 produced progressively less thermal bow at 982°C. The 30% CaF_2 is not acceptable for friction, wear, and chemical stability, so the poorer expansion match of 10% CaF_2 must be accommodated by other means.

HIGH-TEMPERATURE REGENERATOR RIG

The new high-temperature regenerator rig was operated for 15 h at the maximum design temperature at 982°C (1800°F). Modifications were made to the gas burner, fuel nozzle, and pipe liners to eliminate liner oxidation. Three new one-piece inboard seals, with standard outboard seals and regenerator, produced normal leakage, pressure drop, effectiveness, and torque data on the new rig.

SEAL PERFORMANCE TESTS

Apart from three-piece seal testing discussed earlier there were four other inboard seals tested in the new high-temperature rig this period. Three of these seals were standard construction single-piece seals: two with plasma sprayed crossarm wearfaces of 70% NiO/30% CaF_2 and the other with an 85% NiO/15% CaF_2 crossarm. Leakage performance of these seals is shown in Figure 111. The data shown in Figure 111 was taken while running on the 1900°F-configuration CATE cycle with a 774°C (1425°F) limit on the regenerator inlet temperature. the point at the left of the curve is the 50% freeshaft idle condition and the continuous part of the curve represents 60 through 100% power transfer conditions. The leakage of these seals compares favorably with previous inboard seals with 85% NiO/15% CaF_2 crossarm wearfaces, which were tested in the old rig. However, the new rig in itself appears to give slightly lower leakage values than the old one, making it hard to draw any firm conclusions about this data until more running experience establishes a better data base line for the new rig.

Inboard seal R82924-4 85/15 X-ARM
△ ⋯⋯⋯ S/N H3038
Inboard seal R82924-5 70/30 X-ARM
○ ---- S/N H3046
○ ——— S/N H3047
Outboard seal E76354A S/N C535
Disk E76790A S/N GM14A-04
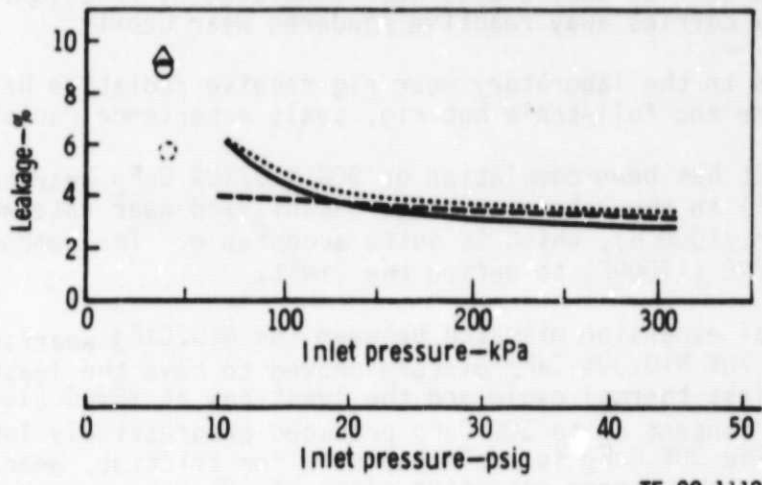
TE-80-1112

Figure 111. Leakage performance of standard construction single-piece seals.

CERAMIC REGENERATOR SEAL MATERIALS

Summary

The 2265°F engine configuration requires a regenerator/seal system capable of operating at maximum temperature of 982°C (1800°F). The current effort has concentrated on establishing the limitations of the NiO/ CaF_2 system. Based on an evaluation of friction/wear behavior and thermal distortion characteristics the 90% NiO/10% CaF_2 composition was found to be acceptable to temperature of at least 871°C (1600°F) and possible to 972°C (1700°F) and above. Since the ultimate temperature capability can only be established from full-scale rig testing, complete seals of this composition are now being fabricated.

Objective

The objective of this task is to develop a regenerator seal wearface material for application to temperature of 982°C (1800°F). Such a material must be compatible with the current thin wall AS matrix material (Corning 9461) and meet the following general requirements:

o Dynamic coefficient less than 0.6 from room temperature to 650°C (1200°F) and less than 0.4 from 650°C (1200°F) to 982°C (1800°F) at 34.5 KPa (5 psi) load

o An average seal wear rate less than 0.025 mm (1.0 mil)/200 h with a simultaneous disk wear rate of 0.025 mm (1.0 mil)/2000 h at 982°C (1800°F)

146

o Seal wearface thermal expansion to be compatible with a high metallic temperature substrate material

o Resistant to road salt and free of delaminations after 50 cycles from room temperature to 982°C (1800°F)

Discussion

The current effort is aimed at assessing the suitability as defined by friction/wear and thermal distortion characteristics of the NiO/CaF_2 for use to temperatures of 982°C (1800°F). Present seals are fabricated from a premixed blend of NiO and CaF_2 powders by plasma spraying. However, seals sprayed from such blends show significant stratification, which promotes spalling and delamination. To eliminate this difficulty in the current work composite powders were employed.

Composite powders with CaF_2 contents ranging from 0 to 40% by weight were prepared by Metco using a proprietary process. Electron microprobe photomicrographs (Figures 112 and 113) show typical distributions of CaF_2 for both the 80% NiO/20% CaF_2 and 60% NiO/40% CaF_2.
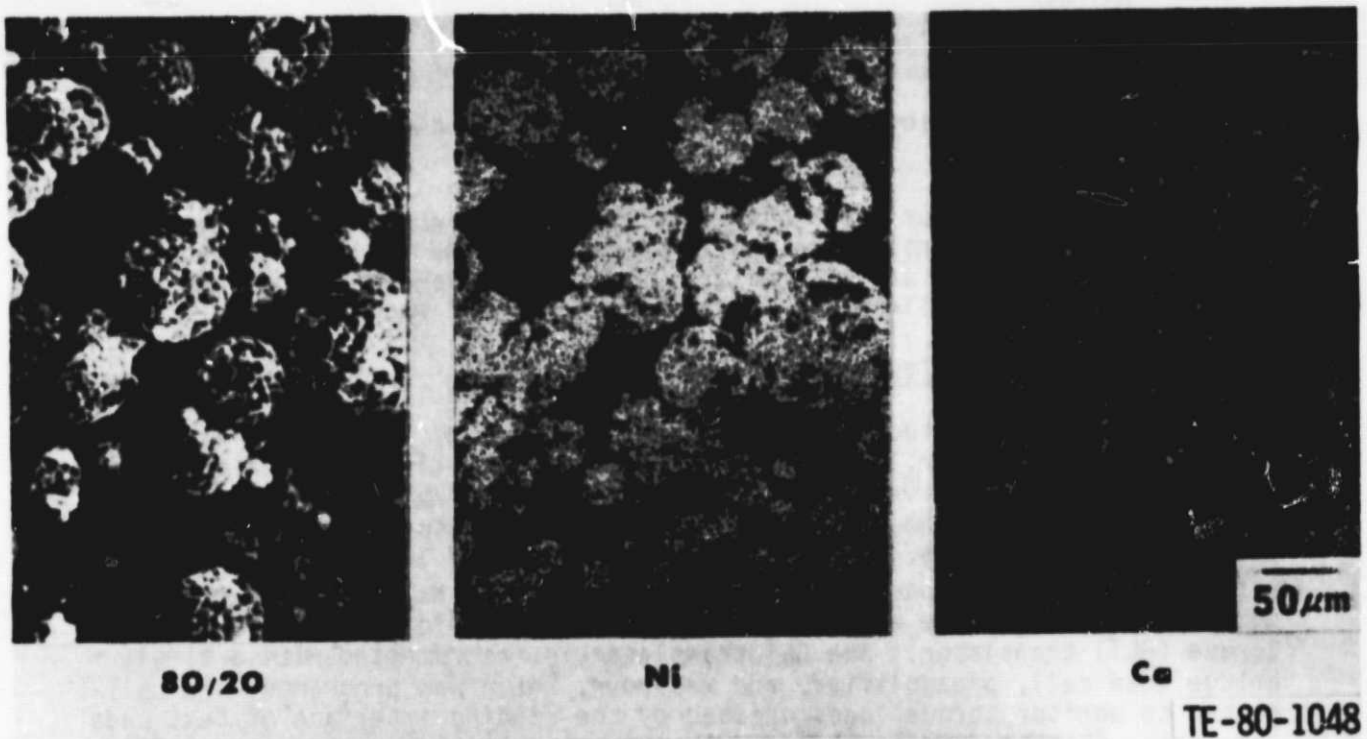

Figure 112. Distribution of Ni and Ca in composite powder, 80% NiO/20% CaF_2.
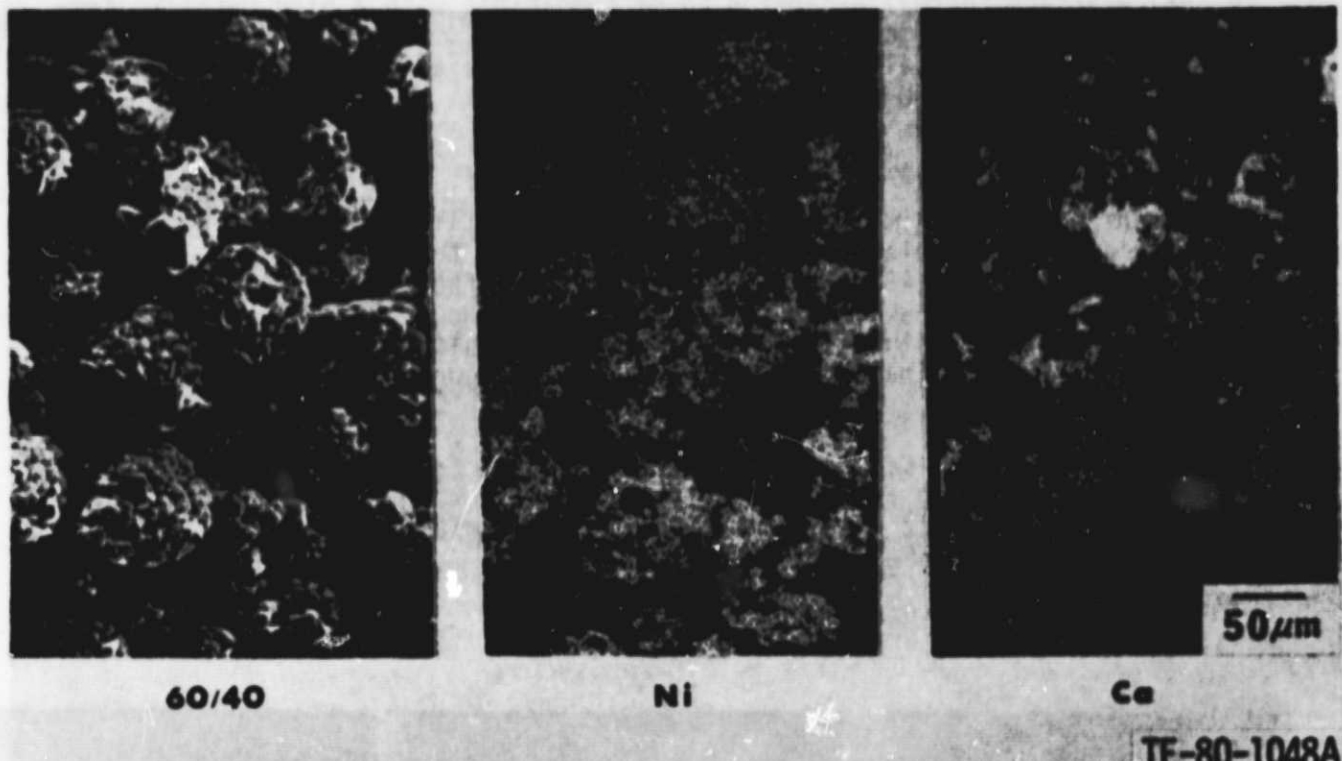
Figure 113. Distribution of Ni and Ca in composite powder, 60% NiO/20% CaF$_2$.

To determine the optimum ratio of NiO to CaF$_2$ test specimens were prepared for friction and distortion testing. All test specimens were prepared with a substrate material and an intermediate layer between the bond coat and composite layer. Figure 114 shows the microstructure of each coating.

Friction and Wear Testing

The test rig used to study friction and wear behavior, Figure 115, is comprised of 15.2-cm (6-in.) diameter test disk 2.54-cm (1-in.) thick of ceramic regenerator matrix, driven by a turntable by means of a variable speed electric motor and speed reducer. A range of rotational speeds equivalent to sliding velocities of 6.4, 13.7, 32 m/min (21, 45 and 105 f/min) were evaluated. Seal wearface pads, 2.54 x 3.81 cm (1 x 1.5 in.), are affixed and equally spaced onto the rotating disk by a gimbled spider and guide-load-torque (GLT) translator. The GLT translator is instrumented with a single bridge load cell, preamplifier, and recorder, which was programmed and calibrated to monitor torque loads created by the rubbing interface of test pads and disk. This reading is then simply converted to give continuous coefficients of friction. In addition, a simultaneous temperature recording is made adjacent to the torque traces indicating the temperature environment of the specimens.

Normally, the specimens are permitted to heat to 427°C (800°F) prior to starting the drive mechanism. Sufficient running time is then permitted at each

90/10   80/20

50μm
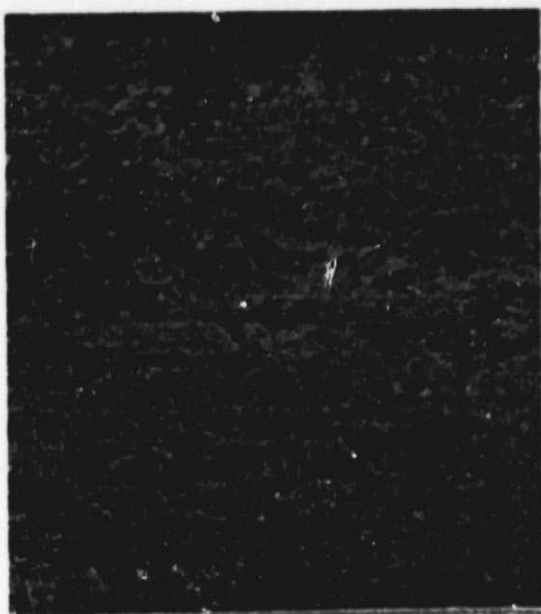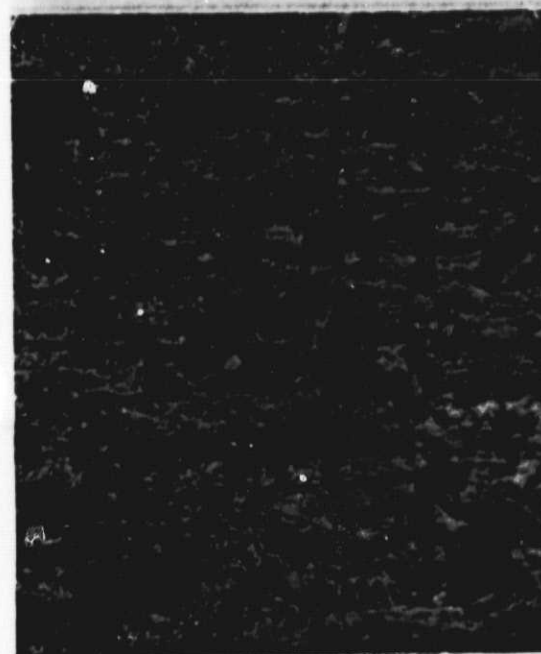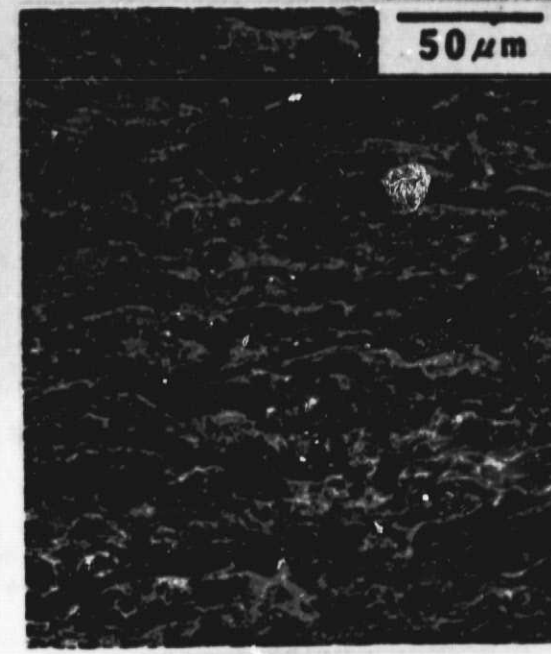
70/30   60/40   TE-80-1049

Figure 114. Typical microstructures of plasma sprayed NiO/CaF_2 wearface
materials. Ratios are weight percent NiO to CaF_2.
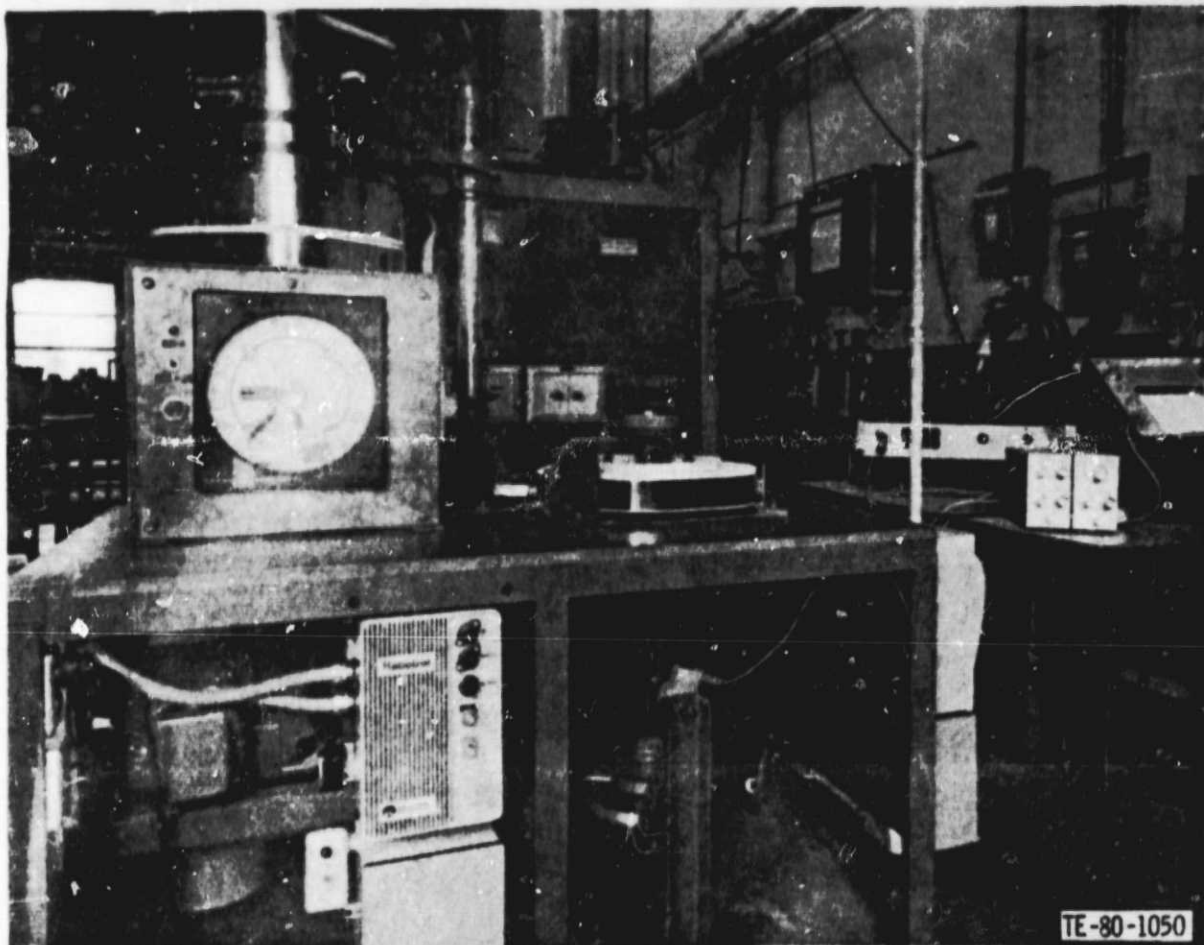
Figure 115. Friction/wear rig.

temperature (approximately 1 h) to ensure stabilized readings of friction and temperatures. All test specimens--pads and disk--are carefully examined and measured before and after each test to evaluate wear conditions and/or disk matrix damage.

The screening evaluation consists of three separate test runs totaling 72 h. Each involves 24 h of observation run at 871, 927 and 982°C (1600, 1700, and 1800°F). Test load and speed are 34.5 kPa (5 psi) and 13.7 m (45 ft)/min, respectively. In addition, sliding velocities of 6.4 and 32 m (21 and 105 ft)/min are monitored briefly to determine the slope of the friction vs speed curve. The seal pads and disk are stabilized at 427°C (800°F) before a run is started. After the temperature is stabilized, three sliding speed readings are taken to determine the friction coefficient. A friction coefficient is then obtained at 111°C (200°F) increments until the run temperature is reached. At temperature, the sliding speed and friction coefficient are checked periodically until 24 h time has elapsed.

150

Friction and Wear Behavior of NiO-Type Regenerator Seal Material

Initial friction and wear tests for various plasma-sprayed seal materials against a Cercor 9461 thin wall disk have been completed.

Results are shown in Table XXVII. From these test results the following can be concluded:

o Plasma-sprayed composite powders of 90% NiO/10% CaF_2 exhibited the least amount of seal and disk wear at test temperatures of 871°C (1600°F) and 927°C (1700°F).

o All seal samples experienced high friction and severe wear on disk and/or seal wearface at 982°C (1800°F). (In all cases, test parameters were modified to a lower sliding velocity or test was terminated because excessive rig chatter.)

o With the exception of 70% NiO/30% CaF_2, increasing the CaF_2 content increased the seal and disk wear rate at all temperatures tested. (70% NiO/30% CaF_2 seal pads had to be tested at a reduced sliding velocity of 10.7 m/min (35 ft/min) because of excessive rig chatter at 13.7 m/min (45 ft/min).)

Based on these initial test results the 90% NiO/10% CaF_2 composition was selected for additional long-term (500 h) wear testing at both 871°C (1600°F) and 972°C (1700°F). Both the pods and the disc were resurfaced prior to each test. The same incremental start up used in the preliminary testing was employed.

The results of the long term wear tests are shown in Figures 116 and 117. At 871°C (1600°F), the wear rate of the wearface seal material is almost twice that of the disk. Total wear of the seal material after 200 h of testing is 0.043 mm (1.7 mil), whereas the projected wear of the disk at 2000 h is approximately 1.14 mm (4.5 mil). At 927°C (1700°F), the wear rate of the disk is significantly higher than that of the seal material, increasing more rapidly after the first 225 h.

The observed wear levels at 871°C (1600°F) are higher than established goals described earlier. At 927°C (1700°F), the preferred disk material becomes limiting. However, previous experience has shown that wear rates are always significantly higher on the laboratory test apparatus as compared to the full-scale rig on the engine. Thus, it is expected that the 90% NiO/10% CaF_2 wearface composition will perform acceptably to temperatures of at least 871°C (1600°F) and perhaps to 927°C (1700°F) or slightly above.

Thermal Distortion Testing

The test rig is schematically illustrated in Figure 118. The test specimen, 2.54 x 15.24 x 0.43 cm (1 x 6 x 0.170 in.), used in the test rig is supported in a furnace by two quartz stands, 12.7 cm (5 in.) apart. Attached to the center of the test specimen is a small diameter quartz rod that connects to the core of a linear-variable differential transformer (LVDT). The LVDT is wired to a preamp recorder system wherein a calibration and subsequent measurements can be made. During the heating and cooling cycle any movement of the test specimen in a concave or convex mode normal to the coating is detected and plotted continuously over the test temperature sufficiently long to ensure stabilized readings for temperature and deflection.

TABLE XXVII. FRICTION AND WEAR RESULTS

Sliding velocity: 13.7 mpm (45 fpm) Load: 34.5 KPa (5 psi)
Test time: 24 hr/temp Disk material: Cercor 9461 thin wall

Composite	871°C (1600°F)	972°C (1700°F)	982°C (1800°F)
90% NiO/10% CaF_2			
Friction coefficient	0.41-0.48	0.47-0.53	0.44-0.63
Seal wear, μm (mils)	13.0 (0.51)	12.4 (0.49)	8.1 (0.32)
Disk wear, μm (mils)	1.9 (0.075)	3.8 (0.15)	Terminated after 9 h because of excessive seal chatter
80% NiO/20% CaF_2			
Friction coefficient	0.41-0.70	0.43-0.73	1.0
Seal wear, μm (mils)	45.7 (1.80)	14.2 (0.56)	8.9 (0.35)
Disk wear, μm (mils)	2.54 (0.10)	10.2 (0.40)	8.3 (0.325) Terminated after 6 h because of excessive seal chatter
70% NiO/30% CaF_2			
Friction coefficient	0.56-0.73*		
Seal wear, μm (mils)	16.5 (0.65)*		
Disk wear, μm (mils)	3.2 (0.125)*		
60% NiO/40% CaF_2			
Friction coefficient	0.21-0.27	0.43-0.53	
Seal wear, μm (mils)	56.9 (2.24)	28.4 (1.12)	
Disk wear, μm (mils)	5.1 (0.20)	3.1 (0.125) Terminated after 75 h because of excessive seal chatter	

*Due to excessive seal chatter. Test was conducted at a reduced sliding velocity of 10.7 m/min (35 ft/min); test terminated after 871°C (1600°F) run.

The thermal distortion rig is calibrated with a solid aluminum oxide test specimen to determine the error introduced by the expansion of the quartz push rod and specimen supports. The curves presented herein for the various seal wearface test specimens have been corrected.
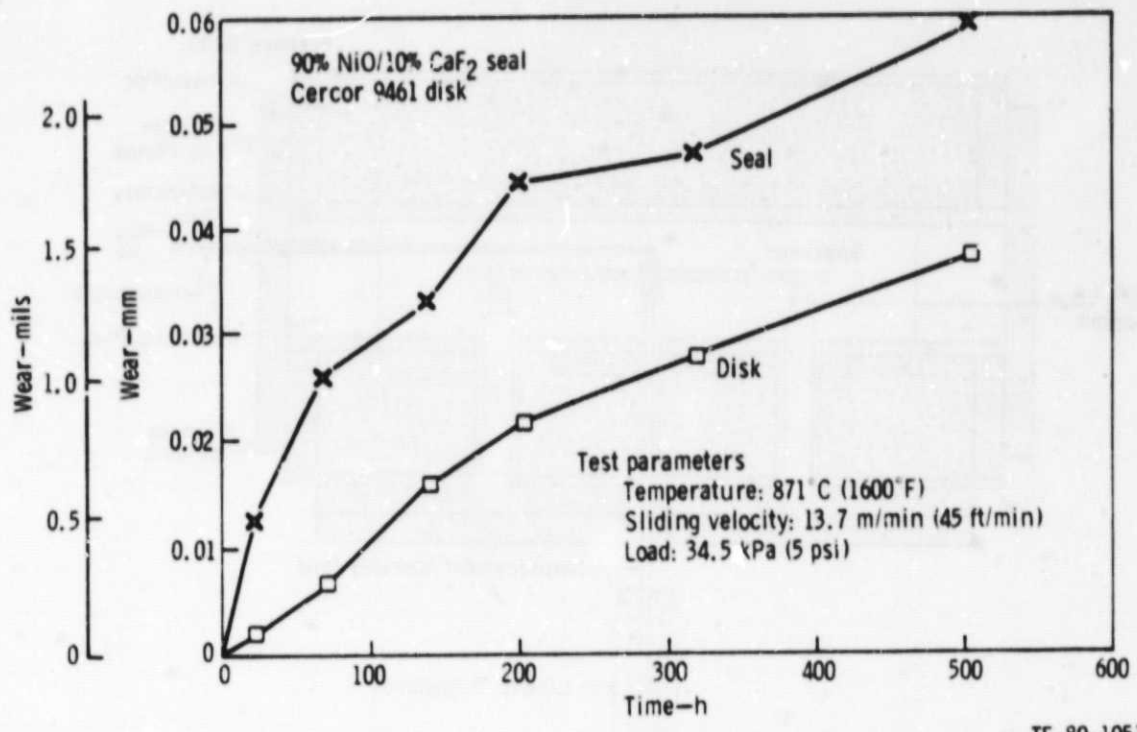
Figure 116. Long-range wear curves for regenerator seal and disk materials.
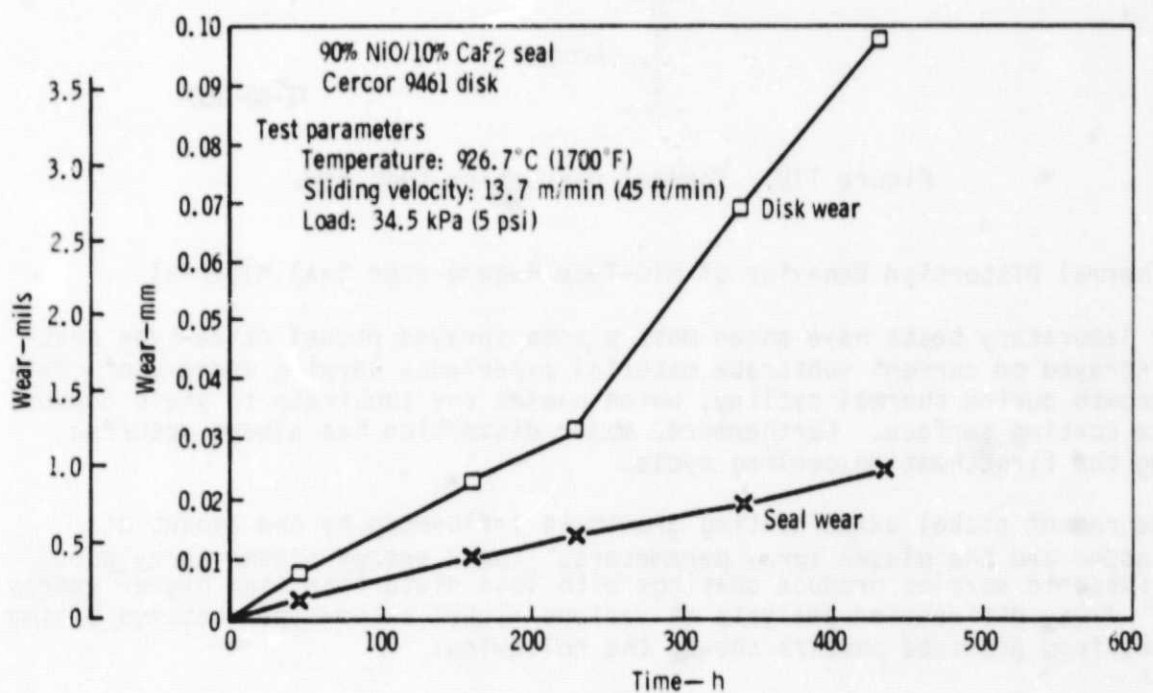
Figure 117. Long-range wear curves for regenerator seal and disk materials.

153
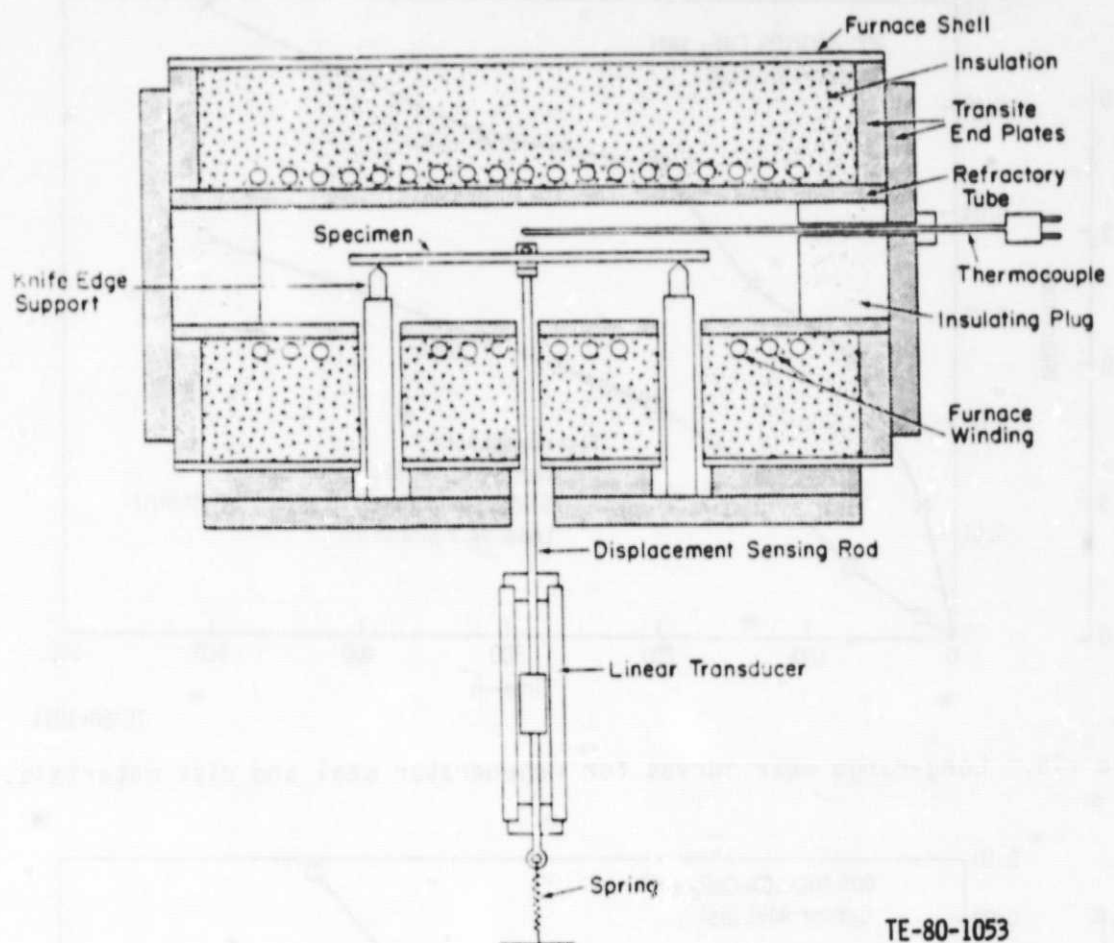
Figure 118. Thermal distortion test rig.

Thermal Distortion Behavior of NiO-Type Regenerator Seal Material

Prior laboratory tests have shown most plasma sprayed nickel oxide-type coatings sprayed on current substrate material experience varying degrees of coating growth during thermal cycling, which causes the substrate to yield convex to the coating surface. Furthermore, major distortion has always occurred during the first heating/cooling cycle.

The degree of nickel oxide coating growth is influenced by the amount of CaF_2 added and the plasma spray parameters. Lower energy plasma spray guns with subsonic nozzles produce coatings with less distortion than higher energy guns. X-Ray diffraction analysis of various nickel oxide-type coatings plasma sprayed from premixed powders showed the following:

o A degree of free nickel was always formed during the plasma spray process regardless of spray parameters tested and oxidized when thermally cycled in air.

o A measureable increase in the lattice parameters of the nickel oxide crystal structure was observed after thermal exposure in air at 871°C (1600°F).

Laboratory test to date shows that composite powders react chemically in the same manner as described for premixed powders. However, cross-sectional studies of the composite powders show a more uniform distribution of CaF_2 throughout the NiO matrix as compared to premixed powders.

Results of thermal distortion tests completed during this reporting period for various plasma-sprayed seal materials made from composite powder are illustrated in Figures 117 through 122. Two heating and cooling cycles were conducted on each seal wearface material in the as plasma sprayed condition. Generally major distortion occurred after the first heating and cooling cycle resulting in a degree of permanent set convex to the seal wearface. In addition, thermal mismatch is most severe between coating and substrate at temperatures of 216°C (600°F) to 538°C (1000°F).

TE-80-1055
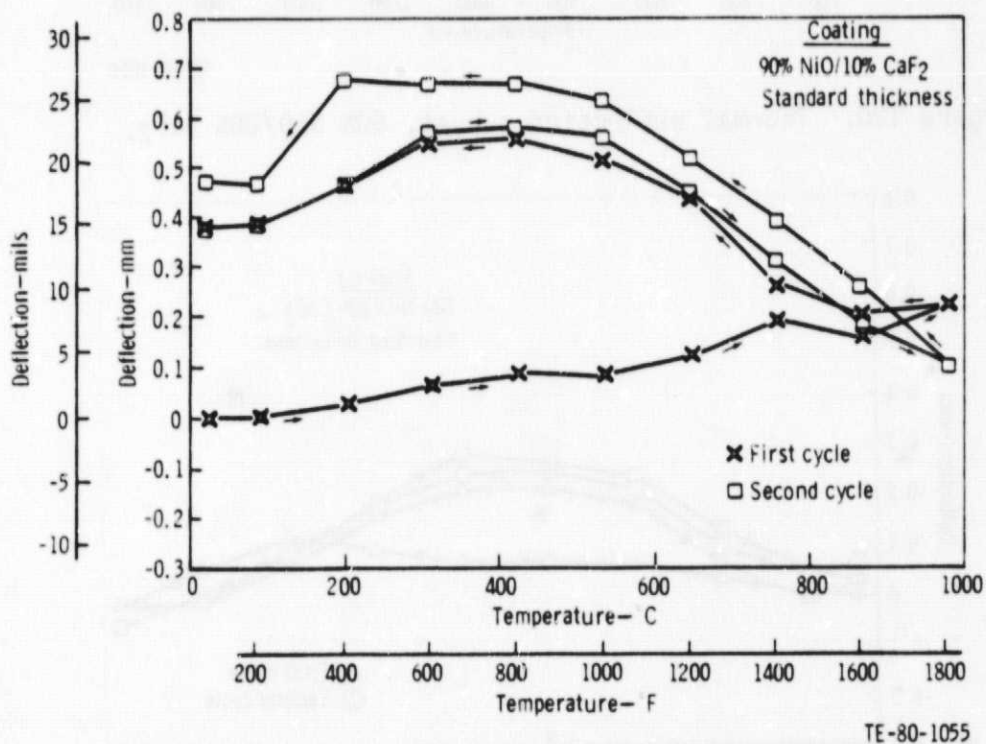
Figure 119. Thermal deflection curves, 90% NiO/10% CaF_2.

155

o A decrease in modulus as the coating ages would decrease the thermal stress properties of the coating as generated and installed when thermally cycled in air.

o A decrease in the ratio of the tensile-strength to the modulus could make the coating more sensitive to thermal stress should a crack propagate.

Laboratory tests to date show that composite powders have the ability to retain some amount of specific chemical product. However, not all the powders of the same composition will show a more uniform distribution throughout the structure as compared to premixed powders.

Results of the thermal deflection of the complete system have been determined for various plasma-sprayed configurations of the composite system as shown in figures 117 through 135. The heating and cooling of the coating and base metal is shown. The deflection behavior is the as-plotted. A second thermal cycle was conducted after the first. The cooling portion of the cycle in general showed a decrease from the maximum deflection as the coating and base metal returned to room temperature.

Figure 120. Thermal deflection curves, 80% NiO/20% CaF$_2$.
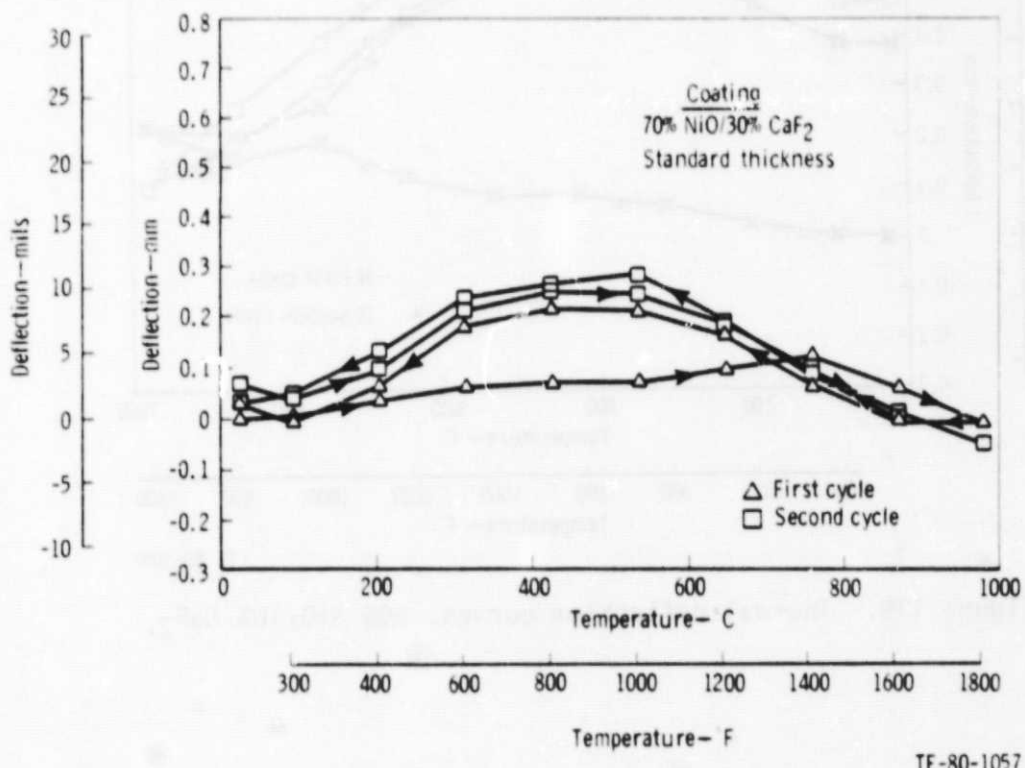

Figure 121. Thermal deflection curves, 70% NiO/30% CaF$_2$.

156
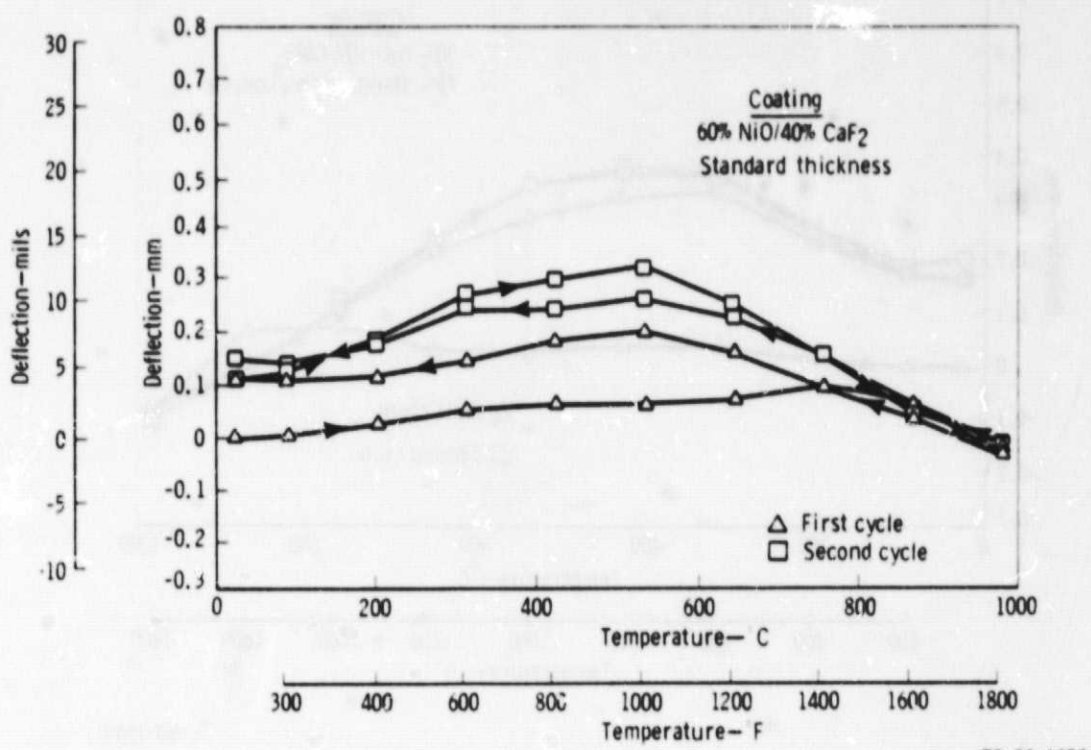
Figure 122. Thermal deflection curves, 60% NiO/40% CaF$_2$.

The 70% NiO/30% CaF$_2$ composition showed the least amount of distortion and permanent set of the materials tested. These results are consistant with previous experience using premixed powders which was the basis for using this composition on early full-scale seals operating at 788°C (1450°F). However, as discussed previously this material is not appropriate from a fracture/wear point of view for use at higher temperatures.

In an effort to use a composition of lower calcium fluoride, consideration was given to reducing the thickness of wearface material. The 90% NiO/10% CaF$_2$ composition was selected for initial testing. Substrate thickness was maintained, whereas the final wearface coating thickness was reduced. Figure 123 shows the resulting thermal distortion for this configuration. A significant improvement has been realized, and the result more nearly conforms to that obtained for the 70% NiO/30% CaF$_2$ composition.

Based on the results of the friction/wear and thermal distortion tests 90% NiO/10% CaF$_2$ has been selected for evaluation on full-scale seals in the regenerator seal rig. Two crossarms of this composition have been proposed. Fabrication and testing will be completed during the next reporting period.
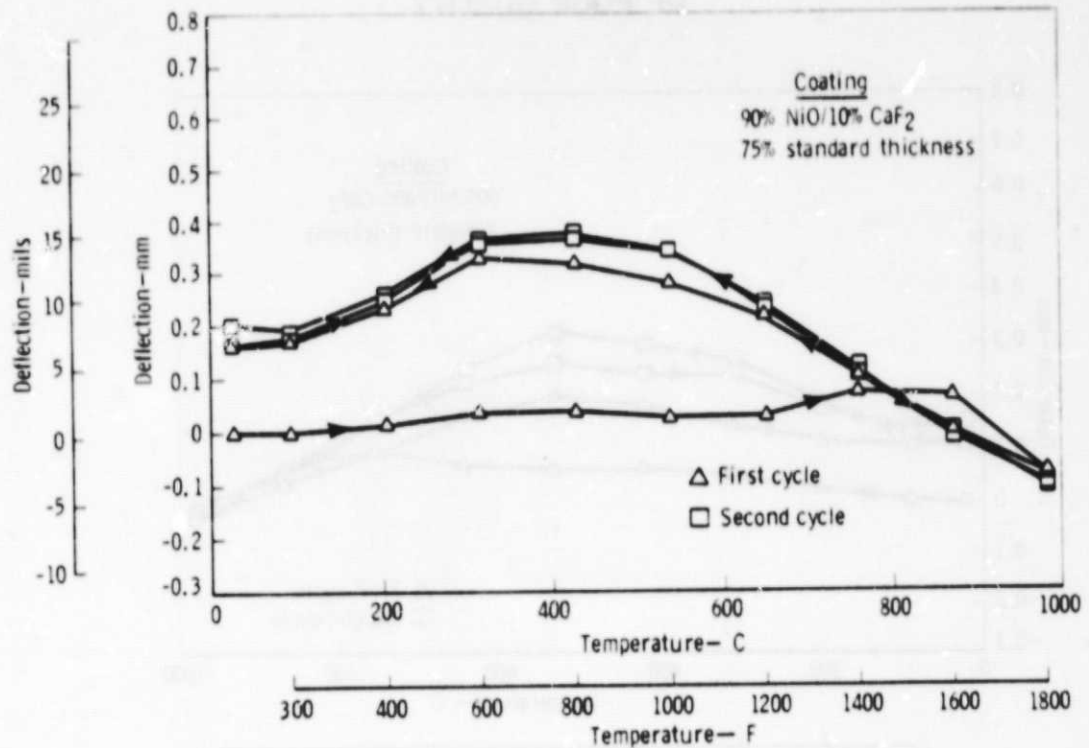
Figure 123. Thermal deflection curves, 90% NiO/10% CaF$_2$ (reduced coating thickness).

TE-80-1059

VI. GENERAL ENGINE DESIGN AND DEVELOPMENT

INTRODUCTION

General engine design and development continued with testing of an engine block cooling scheme, 2070°F-configuration hot engine simulator ring combustor, and T_6 thermocouples using a microprocessor control system.

ENGINE BLOCK COOLING

Summary

During this reporting period, the following items were accomplished with regard to cooling the engine block while running at the CATE increased temperatures:

- o The proposal to cool the cross-arm area of the block with ambient air from an external blower was tested on an engine and proved feasible.
- o A block modification to implement this proposal was completed, and the parts were ordered.
- o A theoretical analysis was conducted to evaluate the engine test to furnish design data for the modified block and to determine the requirements of the external blower.

Objective

The primary objective of this task is to develop a scheme to cool the engine block in order to operate at the elevated temperature as specified in the CATE project goals. The objective for this reporting period was to test the engine external blower cooling scheme for the block crossarm and to conduct an analysis for engine block modifications based on test data obtained.

Discussion

The critical area of the block, the cross-arm, must be kept under 538°C (1000°F) to prevent excessive thermal stress and distortion. The high-pressure section of the block containing burner inlet air is separated from the low-pressure exhaust section by a double-walled bulkhead. These two walls are connected at each side of the block by the cross-arm, which serves as a seal surface for the regenerator seal. Experience has shown that when the metal temperature of the cross arm exceeds 538°C (1000°F), the middle of the cross-arm deflects laterally outward taking a permanent set due to yielding and creep and interfering with the performance of the regenerator seal. Furthermore, analysis shows that at elevated cross-arm temperatures the thermal stress at the top and bottom of the cross-arm results in a potential low-cycle fatigue problem. Therefore, the design goal for the CATE program is to keep the block cross-arm temperature below 482°C (900°F). An analytical evaluation of a number of proposals to accomplish this goal has shown that the most practical method is to replace the present compressor discharge air cross-arm cooling method with a cooling circuit using ambient air supplied by an external blower.

Engine C-2 was modified to test the scheme to cool the block with ambient air. Shop air was piped to the cavity between the two walls of the double bulkhead adjacent to the cross-arms through the two casting core support holes at the top of the block and exhausted through the bottom two holes. These holes are

159

Thermocouple locations

—·— Ambient cooling test—left side (T$_4$ = 1065°C (1949°F), T$_6$ = 795°C (1464°F)
— — — Ambient cooling test—right side (T$_4$ = 1065°C (1949°F), T$_6$ = 795°C (1464°F)
——— Standard block cooling (T$_4$ = 1038°C (1900°F), T$_6$ = 774°C (1425°F)

TE-80-1113
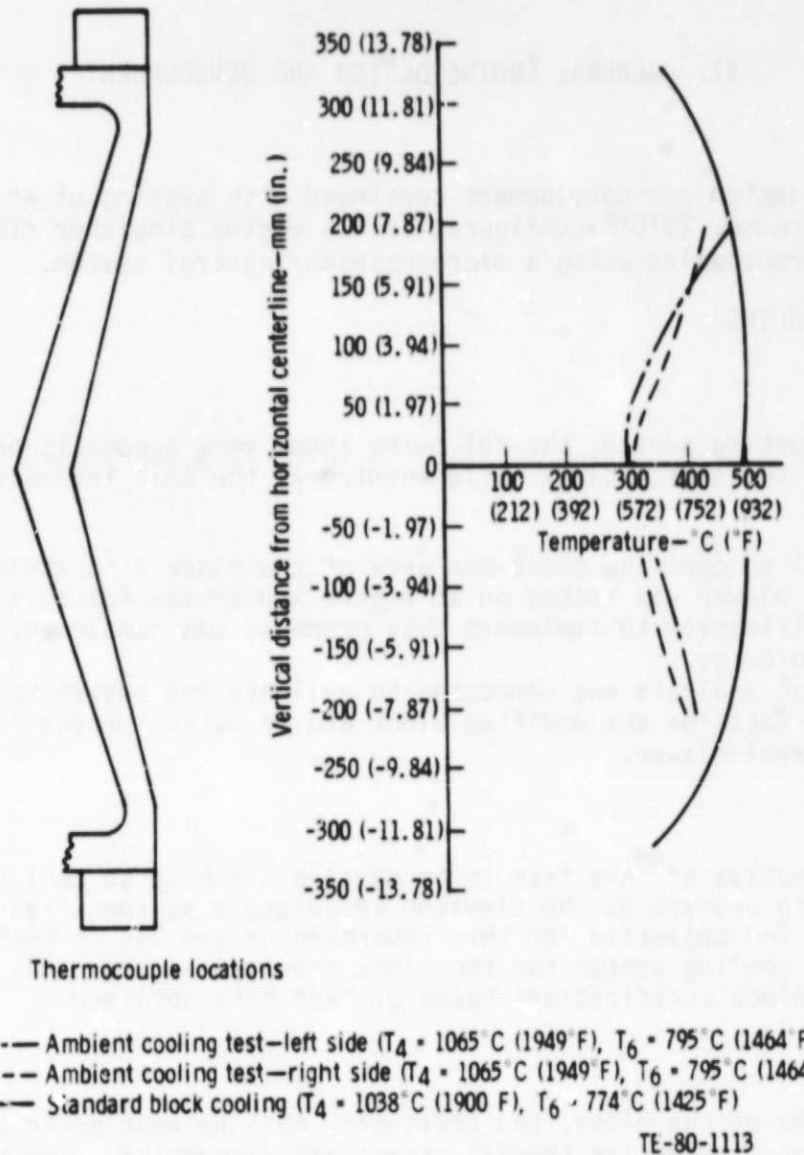
Figure 124.   Cross-arm temperatures for ambient air and standard cooling.

plugged in the basic engine. The flow path through the cross-arms was sealed
as well as possible from the interior flow path of the engine, and the cooling
circuit for the containment ring and outer muff, which is normally an exten-
sion of the block cross-arm cooling circuit, was supplied with compressor dis-
charge air from the front block through an external line. Figure 124 shows
the cross-arm temperatures measured in this test compared with an engine using
the standard cross-arm cooling with compressor discharge air. Over most of
the length of the cross-arm, the temperature is significantly reduced. The
higher temperatures near the top and bottom of the cross-arm are probably a
result of the restriction at inlet and discharge causing a high-velocity jet
not in contact with the cross-arm surface. At the middle, the flow path shape
puts the air in contact with the metal surface of the cross-arm. Figure 125
shows flow vs pressure for engine buildup 20, which had a flow path through
the cross-arm typical of a standard engine and buildup 20R in which the
restriction to flow at the middle of the cross-arm was opened up slightly.

Figure 125. Flow vs pressure drop for ambient air cooling tests.

Both hot flow and cold flow tests are plotted and compared with analytical results using a mathematical model to represent the flow path for each build condition. This comparison indicates that for the cold flow tests, run on a static engine, the cooling air leaked out of the flow path since the measured flow is greater than the analytical. However, when the flow measurements were made on a running engine the flow measured at the inlet was less than the analytical indicating that the higher pressure compressor discharge air leaked into the cross-arm flow path. This was probably detrimental to the cooling efficiency of the system because it caused hotter compressor discharge air to be mixed with the ambient air.

The test showed that while the ambient air cooling system was able to achieve the temperature goal the pressure drop across the flow path while flowing the required amount of air was significantly beyond the capability of a typical centrifugal blower. Therefore, the primary goal of the ambient air cooling redesign was to reduce the pressure drop across the system to below 10 cm H_2O (3.9 in. H_2O) while flowing 54.2 dm^3/s (115 ft^3/min) ambient air corrected to standard conditions, the maximum flow observed in the test. This was accomplished by removing the restrictions at inlet and discharge by counterboring the tapped holes for the casting core plugs and removing the restrictions at the horizontal centerline of the engine by redesigning the turbine containment ring and machining the inside surface of the block cross-arm. The mathematical model of the system was used to produce a flow vs pressure drop curve shown in Figure 126 for the redesigned system. It is compared with

161
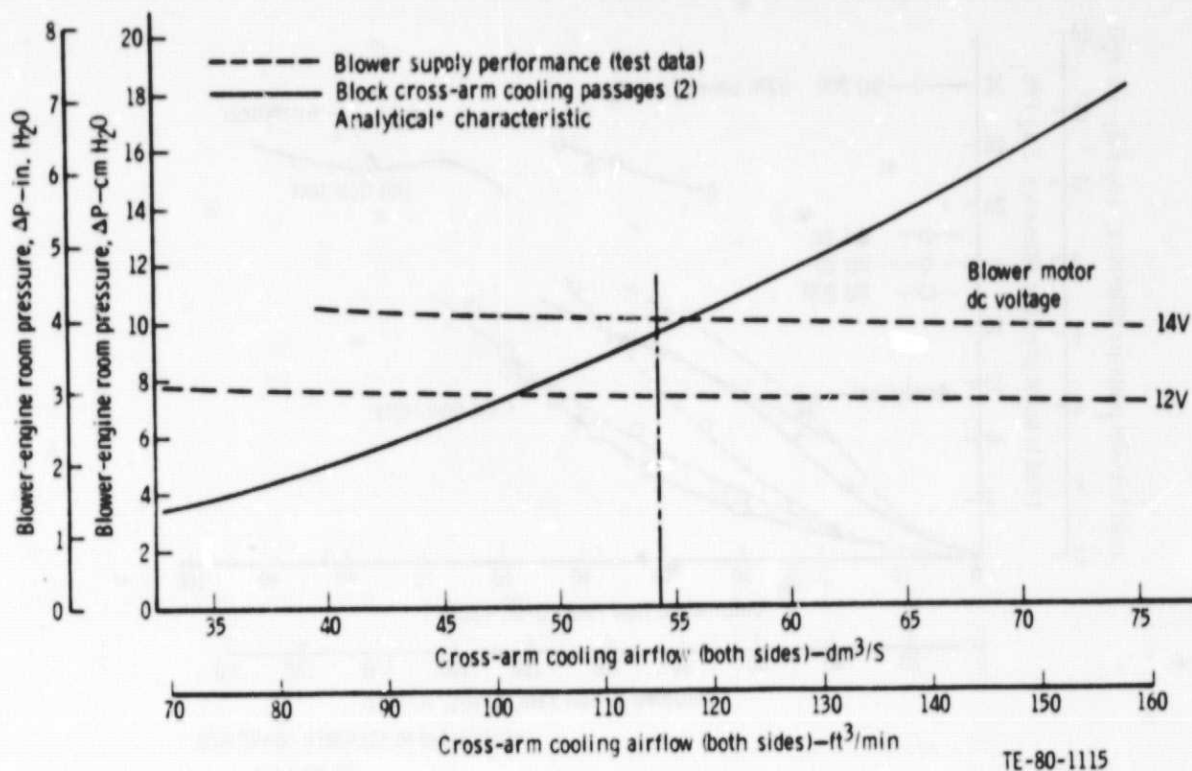
Figure 126. 2070°F CATE IGT 404-4 block cross-arm cooling with
ambient air from an external blower of deep wheel fan design.

curves of a typical automotive heater blower and shows that at the expected
requirement of 54.2 dm³/s (115 ft³/min) the blower would be adequate if
supplied with between 12 and 14 V. This is expected to be possible with the
engine 12-V battery system.

Parts for the internal engine redesign are currently being procured. The de-
sign for the externally mounted blower and ducting is near completion. The
first dynamometer testing on the ambient cooling air configuration will be
done using shop air instead of the blower. Measurements of cross-arm tempera-
ture, airflow, and pressure drop will be taken to further substantiate the
blower requirements.

2070°F-CONFIGURATION HOT ENGINE SIMULATOR RIG COMBUSTOR

Summary

The 2070°F-configuration hot engine simulator rig combustor, in conjunction
with CATE fuel injector and ignition systems, was tested on the combustor com-
ponent rig to determine starting characteristics, lean burning limits, low-
speed efficiency, and steady-state exhaust temperature pattern and radial
gradient.

162

This system performed satisfactorily except for higher than desired exhaust temperature pattern (T_{max}/T_{avg}) and the tip to root temperature gradient; however, further development effort is planned for improved exhaust pattern and profile.

Objective

The design objectives for the hot simulator rig combustor include:

o Combustor temperature pattern and profile must approximate 2070°F-configuration engine design goals.
o Combustor system must be easy to light-off and accelerate to idle.
o Pressure loss must be compatible with simulator rig cycle.
o Combustor must have adequate durability.

Discussion

The nonregenerative cycle for the hot simulator rig affects the combustor design by lowering the inlet temperature from 738°C (1360°F) to 213°C (415°F) and increasing the temperature rise from 40°C (55°F) to 937°C (1700°F). The design changes made to the 1940 CATE combustor consisted of increasing the primary zone airflow, decreasing total hole area to maintain design pressure loss, and changing combustor wall Lamilloy * to lower porosity providing proper cooling flow.

Lightoff Characteristics

Lightoffs were successful at airflows simulating cranking speeds up to 20% N_1 and fuel flows between 13.6 kg/s (30 lbm/sec) and 27.2 kg/s (60 lbm/sec). These results are typical for all CATE and IGT combustion systems.

Low-Speed Efficiency

Combustion efficiency in the starting "pull-away" range was evaluated and found to be adequate for good starting characteristics. The results were similar to CATE combustor data.

Exhaust Gas Temperature Pattern and Profile

The exhaust gas temperature pattern gradient measured was not as uniform as desired. A T_{max}/T_{avg} value of 1.11 K/K (1.13°F/°F) was obtained compared to a goal of 1.05 K/K (1.07°F/°F). The tip-root gradient of -161°C (-290°F) was obtained as compared to a design goal of approximately -47°C (-85°F). Additional development effort is planned to improve the exhaust pattern and profile.

T_6 ENGINE CONTROLS

Summary

The major accomplishment during this reporting period was to test successfully most of the engine operating modes using T_6 thermocouples (turbine exit tem-

---

*Lamilloy is a registered trademark of the General Motors Corporation.

perature). Testing was on engine C-1 using the supplier-owned prototype microprocessor control. Starting and full throttle accelerations were well behaved; however, acceptable automotic shutdown and power transfer operation could not be achieved during the report period. Cold start thermocouple compensation was added to improve the T_6 algorithm required for constant T_4.

Only one hardware problem was encountered when the unit was mistakenly connected to the bench test equipment while the power switch was on. This resulted in damage to three transitors. Otherwise all problems were software oriented.

Objective

The objective for the period was to complete the functional development of the control in preparation for dynamometer operation on a 1900°F-configuration engine. Function development was to include at least starting, accelerations and decelerations, power transfer, and automatic shutdowns.

Development testing was alternated between sessions at DDA on engine C-1 sessions at Woodward Governor Company on bench test equipment capable of dynamic simulation of the engine. Engine testing was aimed at problem definition and only minor software revisions were made at DDA using a PROM programmer. Major software development was conducted at Woodward using a Tektronics Development System.

Discussion

Engine testing at DDA was performed with four iterations. Initial testing was devoted to the automatic shutdowns and fuel control for starts, accelerations, and steady-state speed governing. After achieving good fuel control, the power er transfer clutch logic was added and first engine tested. Satisfactory clutch control was not achieved, partly because of difficulty discovered in the engine clutch where large temperature changes occur for small pressure changes. The digital control has not yet achieved the level of performance of the current analog control. Fuel and clutch loop interplay needs to receive further development as the new digital logic is better understood.

TWO-STAGE POWER TURBINE

Initial design studies for the two-stage power turbine applicable to the 2265°F-configuration engine have been initiated. Progress includes preliminary determination of rotor disk coolant flow requirements, the related secondary flow scheme, and the establishment of engine cycle conditions at design and several off-design points. Using a preliminary flow path, turbine general arrangement studies have been initiated and several concept sketches have been produced.

Early effort centered on rotor blade life determination. The proposal concept featured a two-stage all metal rotor with reduced speed to provide adequate blade life at the elevated temperatures necessary to obtain the desired 0.36 sfc. Current study indicates that desired turbine performance can be obtained with two stages and a 100% design speed of 25,000 rpm, which is a significant speed reduction from the current single stage with a 100% design speed of 34,117 rpm. It has now been determined that long life (18,000 h) metal turbine blading is not possible at required gas temperatures in spite of the

164

reduced rotor speed (and blade stress) based on stress rupture life properties of Mar-M246 cast material. Possible rotor configurations were studied and results are presented in Table XXVIII.

TABLE XXVIII. POWER TURBINE CONFIGURATION STUDY

Configuration	Remarks
Single-stage metal (2265°F-configuration)	Very short life
Two-stage metal (2265°F-configuration)	Limited life, acceptable performance (200.7 mg/W·h (0.3616 lb/hp-hr) sfc)
Two-stage metal (2200°F-configuration and increased power transfer)	Moderate life, reduced performance (225.1 mg/W·h (0.3716 lb/hp-hr) sfc)
Single stage with ceramic blades 2265°F-configuration, increased speed	Cannot provide satisfactory blade attachment
Two-stage turbine (2265°F-configuration)-- ceramic first stage, metal second stage	Acceptable first-stage reliability and engine performance Moderate second-stage life
Two-stage turbine (2265°F-configuration)-- ceramic blading both stages	Acceptable reliability and performance (increased program cost)

As a result of this preliminary study, the two-stage all metal turbine rotor with reduced speed has been selected for the CATE program and the 1241°C (2265°F) performance cycle, which provides 200.7 mg/W·h (0.3616 lb/hp-hr) is to be retained. This configuration will provide adequate life for all proposed test stand and vehicle demonstrations in the CATE program. Evaluation of selected power turbine ceramic configurations will be possible without developing a ceramic-bladed power turbine.

After selecting the power turbine concept, emphasis has been placed on completion of preliminary design of blade and rotor disk shapes. Although the rotor detailed design is not complete, a concept has been established.

Both stages have integrally cast blades and disks using Mar-M246 material. First-stage disk mounting is provided by through bolts that provide attachment to a flange on the second-stage wheel. The second disk is inertia welded to a steel shaft as in the current single-stage IGT power turbine. Rotating labyrinth seal members are also integrally cast with the wheel disks. Results and/or status of preliminary analyses pertaining to rotor design are outlined here:

o Blade shape (section area versus radius in particular) has been optimized to produce maximum stress rupture life at the maximum power design point, 1241°C (2265°F), and 100% rotor speed. In continuous operation at design point, the first-stage blade has a minimum life of 350 h, and the second-stage minimum life is 3003 h. This is based on minus 3 standard deviation properties of cast thin wall Mar-M246 material.

o A review of axial spacing allowance between vane and blade rows is ade-
  quate based on DDA experience with dynamic response stages levels in vari-
  ous engines.
o Blade frequencies have been computed, and this information is being re-
  viewed to determine the desired vane count on each sta
o Dynamic stress distributions are being determined for the first four vi-
  bratory modes in both stages.
o Preliminary disk stress analysis has been completed to establish prelimi-
  nary disk geometry. The shapes shown should provide desired cyclic life
  and overspeed burst margin, although a final and more detailed analysis is
  required.
o Rotor assembly dynamics also appear to be satisfactory using the existing
  engine bearing location and support system. First rotor critical speed is
  reduced by the increased rotor mass, but rotor speed is also reduced, and
  rotor first critical remains near 55% rpm as in the current engine.

The configuration will feature ceramic vanes in either the first or both power
turbine stages. This design also presents new challenges because these stator
airfoils must be cantilever supported from the outer flow-path structure as
opposed to the gasifier vane design, which provides support at inner and outer
flow-path locations. Several power turbine vane support concepts are cur-
rently being studied.

VII. ASSOCIATED ACTIVITIES--PAPERS AND EXHIBITS

During this reporting period, DDA participated in one exhibit, presented three papers, and staged a vehicle demonstration.

In February 1980, Mr. J. L. Wertz presented a paper entitled "Predicting the Reliability of Ceramic Turbine Components" at the National SAE Congress and Exposition, Detroit, Michigan. This paper discussed the elements of the established methodology for predicting component reliability and compared the predicted and measured reliabilities of a blade attachment spin test coupon to assess the validity of the analysis techniques.

In April 1980, DDA participated in the Fifth International Automotive Propulsion Systems Symposium at Dearborn, Michigan with a paper, exhibit, and vehicle demonstration. The paper, entitled "Ceramic Application in Turbine Engines," was presented by Mr. S. M. Hudson; focused on ceramic nozzle vane designs and applications, 2070°F-configuration ceramic nozzle configuration, ceramic support rings and shroud applications, ceramic blade process development, ceramic blade coupon spin testing, larger ceramic components such as the plenum and regenerator disks, 2265°F-configuration engine concept, and engine test results. The exhibit displayed the 1900°F ceramic components tested to date, 2070°F-configuration ceramic engine components which included a partially bladed gasifier turbine wheel, an exploded view of the 2070°F-configuration ceramic gasifier nozzle assembly, and a GT 404-4 engine mock-up which is the powerplant for testing ceramic components.

The 1979 GMC Astro 95 was available for demonstrating the 1900°F-configuration GT 404-4 engine with twelve ceramic components: eight silicon carbide turbine inlet vanes by Carborundum Company, two silicon carbide turbine inlet vanes from Pure Carbon Company, and two alumina silicate regenerator disks by Corning Glass and associated ring gear assembly and regenerator seals by Harrison Radiator Division--GM. Subsequent to the Automotive Propulsion System Symposium, this vehicle continued on a demonstration tour to NASA-Lewis Research Center, Cleveland, Ohio; Harrison Radiator Division--GM, Lockport, New York; Corning Glass, Corning, New York; and Pure Carbon Company, St. Mary's, Pennsylvania. A total of 3398 km (1895 mi) were driven and 63 h of operation were accumulated on this tour. This brings a total of 12,316 km (6650 mi) and 231 h of vehicular operation with ceramic components.

In May 1980, Mr. D. H. Jacobson participated in a series of conferences in Europe promoting ceramics in automotive applications. The paper presented at these conferences discussed ceramic component development, 1900°F ceramic components, ceramic materials development, abradability testing, ceramic regenerator development, 2070°F-configuration ceramic components, nondestructive inspections, and ceramic part development test results.

ACKNOWLEDGMENTS